technische universität
dortmund

Bipyridine modified DNA G-quadruplexes: From structure to function

This dissertation is submitted for the degree of
“Doctor rerum naturalium”

TU Dortmund
Fakultät für Chemie und Chemische Biologie

Armin Durmisevic

Dortmund, November 2025

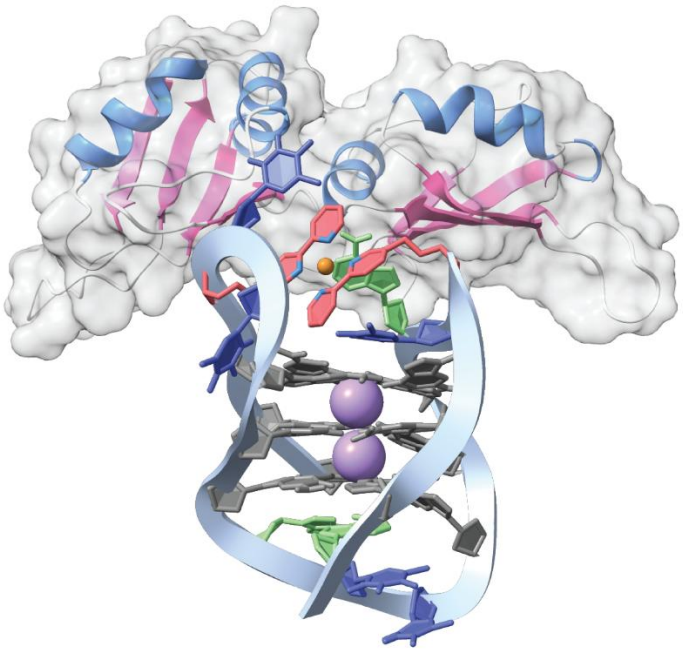

Principal advisor: **Prof. Dr. Guido H. Clever**
Faculty of Chemistry and Chemical Biology,
TU Dortmund University

Coexaminer: **Prof. Dr. Hannes Mutschler**
Faculty of Chemistry and Chemical Biology,
TU Dortmund University

Submission date: 05.11.2025

“Das Wahre ist das Ganze. Das Ganze aber ist nur das durch seine Entwicklung sich vollendende Wesen“

- *Georg Wilhelm Friedrich Hegel, Phänomenologie des Geistes*

Awards

2024 – Prize for the best oral presentation at the G4 Webinar Series hosted by Prof. Kathrin Paeschke

Conference Contribution

Oral presentations

June 2022 – 8th International Meeting on Quadruplex Nucleic Acids, Marienbad, Czech Republic

October 2022 – Deutsche Nukleinsäure Gesellschaft Meeting, Bad Herrenalb

April 2024 – G4 Seminar Series by Prof. Kathrin Paeschke, Uni Bonn

Poster presentations

September 2022 – RESOLV Klausurtagung, Bielefeld

September 2023 – RESOLV Klausurtagung, Bielefeld

August 2024 - 8th Cambridge Symposium on Nucleic Acids Chemistry and Biology

September 2024 – Tag der Chemie, TU Dortmund

Publications

A. Durmisevic, I. Regeni, M. E. Namoro, A. Baksi, G. H. Clever, „Phenazinium- and Malachite Green-Based Pd(II) Cages: Chiroptical Discrimination of Nucleoside Triphosphates" *Chem. Eur. J.* **2025**, 31, e202403679.

A. Durmisevic, J. Openy, A. Majid, M. Nanda, R. Vilar, G. H. Clever „Metal-triggered Topology Switching in Bipyridine-modified DNA G-Quadruplexes" – in submission

Zusammenfassung

DNA G-Quadruplexe sind viersträngige DNA Sekundärstrukturen, die durch Hoogsten H-brückenbindungen von vier einzelnen Guaninen gebildet werden und ein G-Tetrad bilden, wobei sich mehrere solcher Tetraden übereinander stapeln um den Quadruplex zu bilden. Diese Strukturen sind eng an der Regulierung verschiedener biologischer Prozesse wie Transkription und Translation beteiligt, den Kernmechanismen des Lebens auf der Erde. Dies macht sie zu primären Zielen für verschiedene therapeutische Ansätze. Dazu gehört die Entwicklung kleiner Molekül-Liganden, die in der Lage sind, G-Quadruplex Strukturen anzusteuern und zu stabilisieren oder zu destabilisieren. Dennoch bleiben ihr polymorpher Charakter und ihre komplexe Wechselwirkung mit anderen Biomolekülen, vor allem Proteinen, eine Herausforderung für das Verständnis der chemischen und biologischen Eigenschaften von G-Quadruplexen. Gleichzeitig macht dies sie zu einem interessanten Spielfeld für die Einführung von Modifikationen in diese Systeme, die möglicherweise neue Einsichten ermöglichen. In dieser Arbeit wurde ein neuartiges künstliches Bipyridin-Ligandosid kovalent in kurze DNA-Oligonukleotide eingebaut, die in der Lage sind, G-Quadruplex Strukturen zu bilden. Es wurde gezeigt, dass diese Modifikationen nur einen geringen Einfluss auf die ursprüngliche Struktur hatten und die ursprüngliche Topologie und thermische Stabilität beibehalten wurden. Obwohl fast alle Sequenzen durch die Komplexbildung der Bipyridin-Gruppen und zweiwertigen Metallkationen wie Cu^{2+}, Ni^{2+}, Zn^{2+}, Co^{2+}, Cd^{2+} und Fe^{2+} eine gewisse thermische Stabilisierung aufwiesen, kam es nur bei wenigen G-Quadruplexen zu einer strukturellen Umordnung, die zu einer neuartigen, eindeutigen Topologie führte. Bei diesen speziellen Beispielen zeigten kinetische Experimente, dass die Rückfaltung hauptsächlich durch H-brückenbindungen und π-wechselwirkungen der DNA-Struktur angetrieben wurde und lediglich kinetisch durch die anfängliche schnelle Bildung des Metallkomplexes ermöglicht wurde. Darüber hinaus wurde gezeigt, dass diese künstlichen G-Quadruplexe ihre Wechselwirkungsfähigkeit mit Proteinen und insbesondere mit den Helikasen Pif1 und DHX36 beibehielten. Für die besten Systeme konnten niedrige K_d-Werte im nM Bereich erzielt werden, während die thermische Stabilisierung durch den Metallkomplex genutzt wurde, wodurch die Entwindung der G-Quadruplex-Struktur, wie durch Luciferase-Assays nachgewiesen, stark behindert wurde. Schließlich wurden diese modifizierten Systeme in die menschlichen Krebszelllinien HeLa und U2OS transfiziert, wo ihre spontane Lokalisierung im Zellkern sowie die Beibehaltung ihrer durch Ni^{2+}-Kationen ideal stabilisierten Struktur durch fluoreszenzbasierte Mikroskopie nachgewiesen werden konnte. Insgesamt ermöglichten diese neuartigen modifizierten G-Quadruplex-Systeme mit Bipyridin-Modifikationen einen detaillierteren Einblick in die strukturellen Eigenschaften dieser DNA-Sekundärstrukturen und eröffneten vielversprechende neue therapeutische Ansätze sowie eine Anwendung als potenzielle molekulare Köder.

Abstract

DNA G-quadruplexes are four-stranded secondary DNA structures formed through Hoogsten hydrogen bonds of four individual guanines, creating a G-tetrad whereby several of such tetrads can stack on top of each other to create the final construct. They are closely involved in the regulation of several biological processes such as transcription and translation, core mechanisms of life on earth. This makes them prime targets for several therapeutic approaches. Amongst them is the development of small molecule ligands capable of targeting and stabilising or destabilising G-quadruplex structures. Yet their polymorphic character and their complex interaction with other biomolecules, primarily proteins, remains a challenging aspect of understanding G-quadruplex chemical and biological features. Concomitantly this renders them an interesting playground to introduce modifications into these systems that potentially offer a novel understanding of their characteristics. In this thesis, a novel artificial bipyridine ligandoside was incorporated covalently into short DNA oligonucleotides capable of forming G-quadruplex structures. It was shown that these modifications had little to no impact on the parental structure, retaining the original topology and thermal stability. Although almost all sequences showed thermal stabilisation to some degree through complex formation of the bipyridine moieties and divalent metal cations such as Cu^{2+}, Ni^{2+}, Zn^{2+}, Co^{2+}, Cd^{2+} and Fe^{2+}, only few G-quadruplexes experienced a structural reorganisation resulting in a novel distinct topology. Of these particular examples, kinetic experiments revealed how the refolding was mostly driven by hydrogen bond and π-stacking interactions of the DNA structure and merely kinetically enables through the initial fast formation of the metal complex. Furthermore, it was showcased that these artificial G-quadruplexes retained interaction capabilities with proteins and in particular helicases Pif1 and DHX36. As the topology of some modified G-quadruplexes was metal dependent, the resulting binding constants (K_d) where impacted as preferential interaction with either hybrid, antiparallel or parallel topologies was observed. For the best systems low nM K_d values could be obtained while taking advantage of the thermal stabilisation by the metal complex and thus greatly impeding the unwinding the G-quadruplex structure proven by luciferase assays. Lastly, these modified systems were transfected into human cancer cell lines HeLa and U2OS where their spontaneous localisation into the cell nucleus as well as the retention of their structure stabilised ideally by Ni^{2+} cations be proven by fluorescence based microscopy. Overall, these novel modified G-quadruplex systems bearing bipyridine modifications granted a more detailed insight into structural properties of these DNA secondary structures and also made for promising novel therapeutic approaches and an application as potential molecular decoy.

Table of Contents

1. Introduction

1.1 Deoxyribonucleic Acids

Deoxyribonucleic acids (DNA) are amongst the most important biological macromolecules as they not only serve as the storage of the genetic information of each individual living organism but also act as interactive partner for other biopolymers such as proteins or ribonucleic acids (RNA) in many cellular processes.[1] The linear DNA polymer consist of monomeric building blocks called nucleotides. Each nucleotide consists of three parts, the ribose sugar backbone, the nucleobase and the phosphate group, linking two nucleotides together in a phosphodiester bond. In DNA, the ribose sugar is missing a hydroxyl group (-OH) at the 2' position, whereas this is present in RNA. In total four canonical nucleobases can be found on the 1' position of the ribose: adenine (A), guanine (G), cytosine (C) and thymine (T). Structurally they can be further classified into purine (A, G) and pyrimidine (C, T) nucleobases (**Figure 1**).[2]

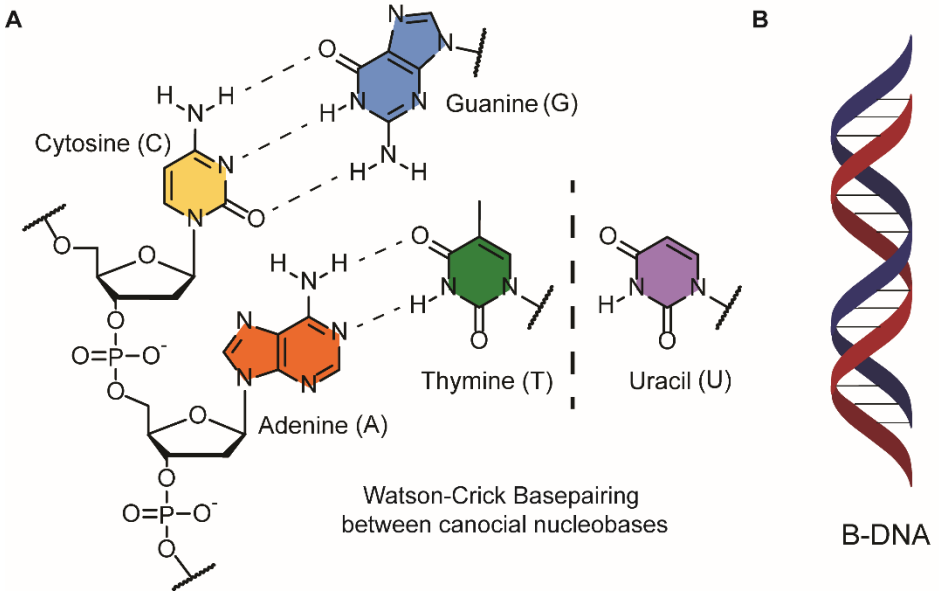

Figure 1. Basic DNA structure. A) DNA is a linear polymer of individual nucleotides as building blocks. A nucleotide consists of a deoxyribose sugar, a phosphate group and one nucleobase. These nucleobases engage in specific hydrogen bonds interactions, the classical Watson-Crick-Franklin basepairing. DNA consists of four canonical nucleobases guanine (G), cytosine (C), adenine (A) and thymine (T) and uracil (U) in RNA, substituting all thymine positions. B) Most common secondary structure of DNA is the double-helical B-type structure formed by two complementary single DNA strands.

Through the linear arrangement of these four nucleobases, information can be encoded for the generation of firstly carrier RNA molecules which either have a direct function themselves or translate their information into the creation of proteins. DNA rarely resides as

a single linear strand but adopts various different secondary structures either with itself or through interaction with a secondary (complementary) strand.[2–4] The most common secondary structure is that of the double helix, which arises when two complementary DNA strands come together and coil around a central axis through the formation of WATSON-CRICK-FRANKLIN interactions.[4–7] These hydrogen bond interactions between adenine and thymine as well as guanine and cytosine nucleobases were named after the researches who solved the crystal structure of DNA in 1953 and later crowned with the NOBEL prize in 1962. Additional π-stacking interactions between nucleobases further contribute to the stability of the double helix DNA. Two more helical motifs of DNA have been discovered since, leading to the classification into B-DNA, the most biologically relevant and most abundant, as well as A-[8] and Z-DNA[9,10], the latter possessing a left-handed twist (**Figure 2**).[6,7]

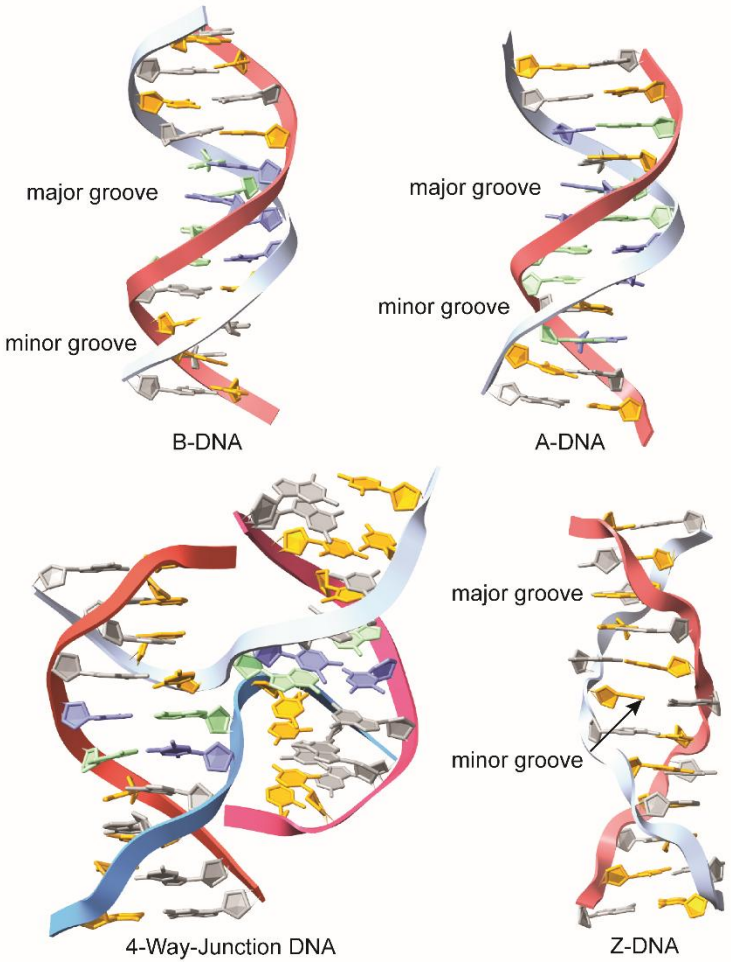

Figure 2. Further secondary structures adopted by DNA. Aside from the most representative B-type form (PDB: 1BNA)[11], other folds such as A-type (PDB: 1D28)[12] and Z-type (PDB: 1DCG)[13] DNA can be adopted. Structures of higher order, involving more than two DNA single strands can also be adopted as showcased by the four-way-junction (PDB: 1ZEZ)[14]. Strand A in pink, strand B in light blue. Nucleobases are colour coded as follows: guanines in grey, thymines in blue, cytosines in yellow and adenines in green.

Besides the double helix motif, DNA is known to adopt several other secondary structures both *in vitro* and *in vivo* which are involved in several different biological processes. Out of several possibilities, most commonly found are the hairpin loops, three- and four-way junctions and the cruciform DNA.[15,16] They are believed to be involved in genetic recombination and DNA repair mechanisms.[17–19] Although these structures are again achieved mainly through the Watson-Crick-Franklin base pairing, they are not the only contributing interaction in DNA secondary structures. In 1959 KARST HOOGSTEN visualized a non-canonical A-T base pair through X-ray crystallography using 9-methyladenine and 1-methylthymine, marking the first experimental evidence of an alternative interaction motif. In this case, the N7 atom of the purine base served as a hydrogen bond acceptor. More than two decades later this unusual base pairing pattern was shown in DNA through X-ray crystallography.[20] Furthermore, it was discovered that HOOGSTEN base pairing was not limited to A-T pairs but could also occur between guanine and protonated cytosines (G-C+) as well as between guanines themselves. If four guanines come together, they can form a G-quartet either in solution or in G-rich sequences of DNA and RNA. If multiple of such G-quartets can form in close proximity to each other, another secondary structure of DNA can be formed, the G-quadruplex (**Figure 3**).[21–23]

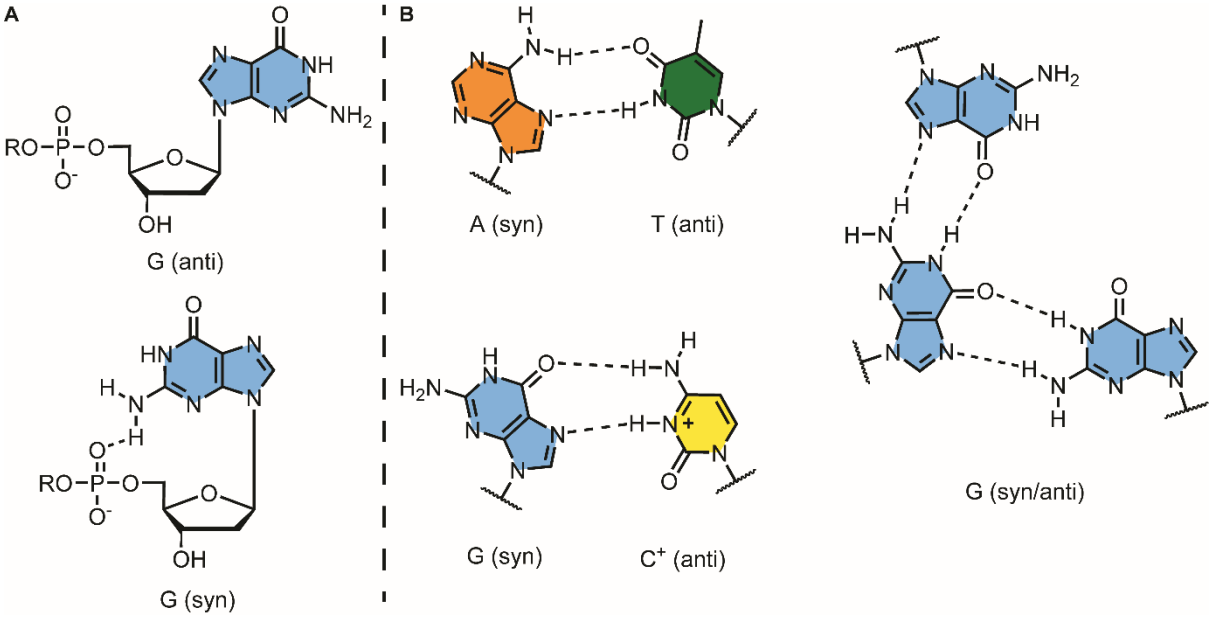

Figure 3. A) Anti- and syn-confirmations of nucleotides showcased on guanine as exemplary nucleotide. In syn-conformation additional hydrogen bonds between the amine group (-NH_2) and the phosphate group in the backbone. B) Hoogsten basepairing between canonical nucleobases with an alternative hydrogen bond pattern. This enables the formation of high-order structures and further DNA secondary structures such as i-motifs and G-quadruplexes.

1.2 DNA G-quadruplexes

First proposed by Gellert, Lipsett and Davies, the secondary structure of DNA G-quadruplexes is formed when multiple G-quartets (n ≥ 2) formed by G-rich DNA π-stack on top of each other, thus creating a four-stranded cuboid DNA structure.[24] The DNA sequence must follow the pattern of $G_{\geq 2}N_xG_{\geq 2}N_xG_{\geq 2}N_xG_{\geq 2}$, where N = A, T or C and x = 1 – 7.[25] It is then generally assumed that the DNA can fold into the secondary structure of a G-quadruplex. To stabilize the structure, monovalent cations are bound within the central core of the G-quadruplex structure, countering the high electron density created by the inward pointing carbonyl oxygen atoms of the guanines. Potassium and sodium cations are most commonly found within these cavities, yet examples with cations of similar size such as NH_4^+ or Tl^+ have been shown (**Figure 4**).[26,27]

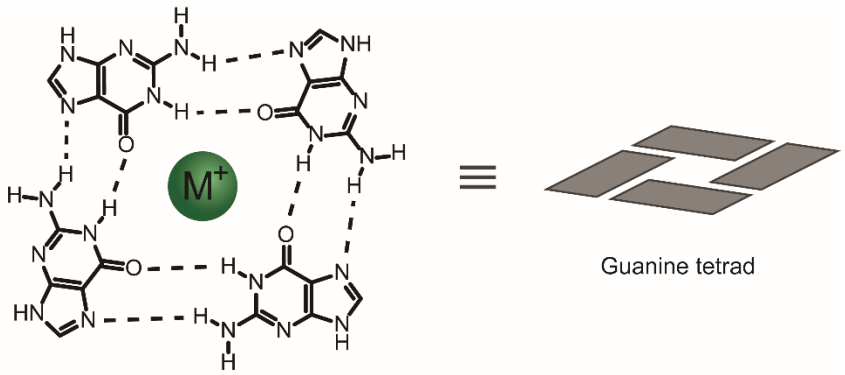

Figure 4. Structure of the planar guanine tetrad (G-tetrad) formed by Hoogsten basepairing between four guanines. Further stabilisation is achieved through coordination of a monovalent metal cation (M^+ = Na^+, K^+, NH_4^+, Tl^+) within the central channel, compensating extensive charge density of the inwards pointing carbonyl oxygen atoms of the individual guanines. Stacking of multiple (n ≥ 2) G-tetrads leads to formation of G-quadruplexes.[26]

Several possibilities of how each of the four strands is oriented relative to the others exist and is influenced by the DNA sequence, number of DNA strands, the solvating environment which includes the buffer, pH and present co-solutes as well as the central cation. Through this, G-quadruplexes possess a rich diversity in accessible topologies. Most G-quadruplexes consist of one single stranded DNA (ssDNA) folding back unto itself and are therefore classified as unimolecular. However, two or four strands can also spontaneously self-assemble into a G-quadruplex and are classified as bi- or tetramolecular respectively. When uni- or bimolecular quadruplexes are formed, the nucleotides between the guanine runs form loop regions which differ in length, composition and connectivity and adopt different forms themselves. These forms are distinguished in diagonal, lateral (edgewise) and propeller (double-chain-reversal) loops. The interplay between the G-quartets and loops formed lead

to different directionalities of the four strands on the edges of the G-quadruplex (**Figure 5**).[28–35]

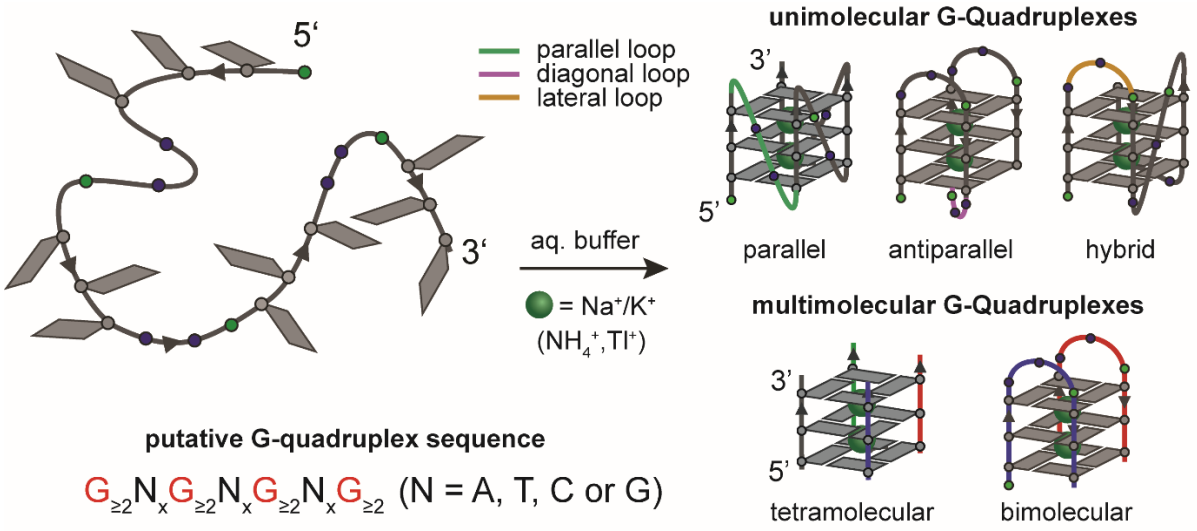

Figure 5. Formation of DNA G-quadruplexes from a guanine rich DNA strand obeying the minimal criteria of the putative sequence. Most G-quadruplexes require buffer at physiological pH (6.9 – 7.2) and presence of monovalent metal cations (green spheres) for successful formation. Different G-quadruplex structures can be achieved including most commonly unimolecular but also bi- and tetramolecular constructs. These structures can adopt different topologies termed parallel, antiparallel or hybrid, dependent on the relative 5’-to-3’ orientation of each G-run. Furthermore, nucleotides between G-runs involved in formation of the G-tetrads, form the loops of G-quadruplex, categorised into parallel, diagonal and lateral loops. To note is the schematic representation of these structures where their right-handed helical twist has been omitted.

If all four strands possess the same directionality when read from 3’ to 5’, then a parallel topology is achieved. If two strands possess the same directionality respectively, then an antiparallel topology is present. A third possibility exists when only one strand has a different orientation in respect to the others and this case is termed hybrid. A further differentiation of the antiparallel and hybrid topologies can be made, depending which of the four strands shows different orientation. When read from 3’ to 5’, if two adjacent strands show the same directionality in an antiparallel configuration the resulting structure will adopt a chair-like topology. If the strands are not adjacent but diagonal to each other, then a basket-type topology will be achieved. Two different examples of hybrid topologies exist, depending on if the single opposing strand is the second (hybrid-1) or the third (hybrid-2) when read from 3’ to 5’ direction.[36,37]

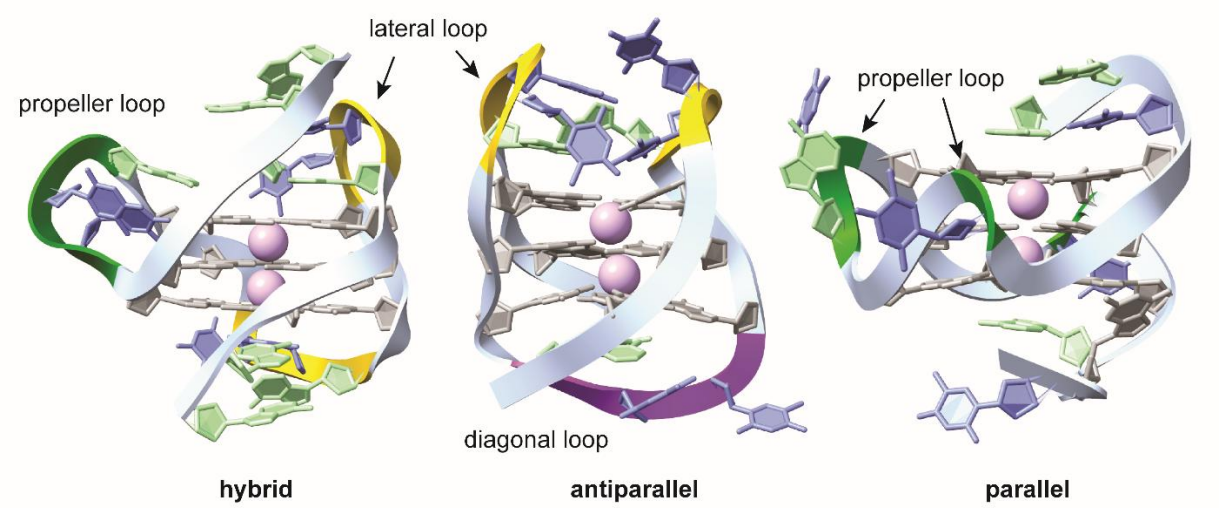

Figure 6. Solution structures of G-quadruplexes found in the human telomeric repeat (htel22) (PDB: 2HY9) in its hybrid topology or antiparallel topology (PDB: 143D) and in the promoter region of the c-MYC oncogene (pu22) (PDB: 1XAV). These structures showcase the large differences in G-quadruplexes and their spatial arrangement as well as size. Loop regions have been colour coded as following: propeller loops in green, lateral loops in yellow and diagonal loops in purple.

This complex landscape of G-quadruplex topologies can be elucidated through various spectroscopic techniques, most commonly by circular dichroism (CD) and UV-Vis spectroscopy. The latter is generally used to obtain the thermal denaturation behaviour as well as the thermal differential absorption spectra of G-quadruplexes. CD spectroscopy of G-quadruplexes mostly relies on the absorption of the abundantly present guanines and how they are spatially arranged relative to each other. This is important as changes in the *N*-glycosidic bond conformation of guanines from *syn* to *anti* or viceversa, will also change their CD signature. As the three possible topologies of parallel, antiparallel and hybrid will have a different constellation of *syn* and *anti* configured guanines at different positions, this results in unique CD spectra for each topology. Parallel G-quadruplexes will have maximum Cotton effect at ~260 nm and a minimum at ~240 nm, whereas antiparallel will show two maxima at ~295 nm and ~240 nm and a minimum at ~260 nm. Hybrid topologies generally show a broad maximum at ~295 nm and at minimum at ~240 nm, although smaller shoulder local maxima can be observed around ~270 nm. This allows a simple qualitative assessment of an unknown structure, whether it is capable of forming a quadruplex and which topology it adopts under the given conditions.[40,41] CD spectroscopy is an inherently low-resolution technique and does not allow to differentiate between mixtures of topologies or between subtypes of the above-mentioned topologies, such as hybrid-1 or hybrid-2 (**Figure 7**).[42,43] To achieve atomistic resolution techniques such as NMR for solutions structures or X-ray crystallography for solid- state structures are necessary for differentiating between these

subtle differences and have been used successfully on many occasions over the past decade.[44–46]

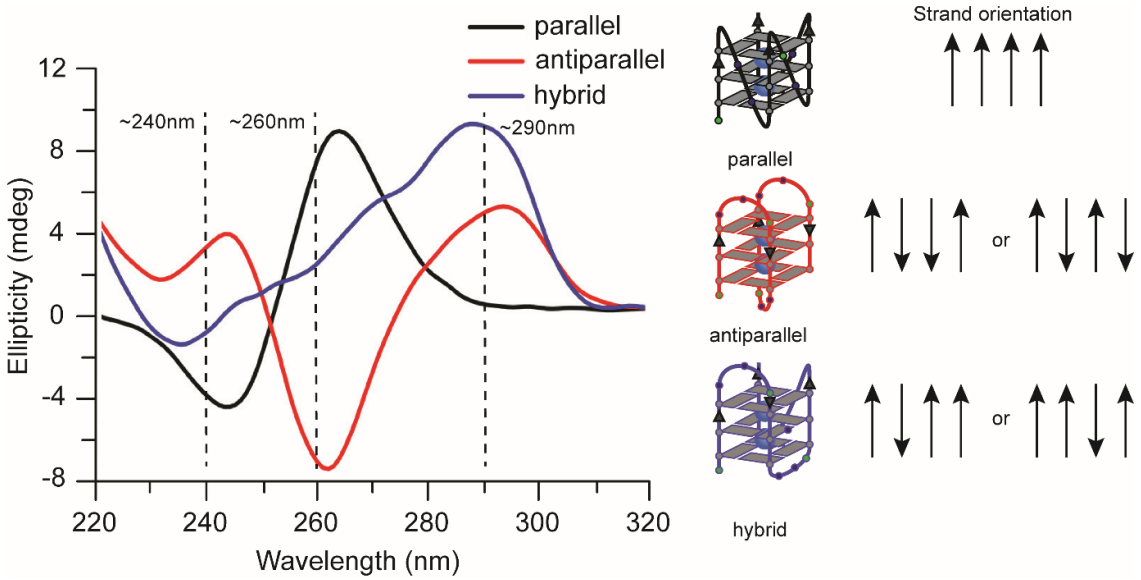

Figure 7. Identification of the individual G-quadruplex topologies can be achieved via CD spectroscopy. The strand orientation of the G-runs leads to a specific ratio between syn- and anti-guanosines of which the sum results in the corresponding signature in the CD between 220 nm and 300nm with characteristic minima and maxima.[38–41]

In thermal denaturation experiments, the stability of G-quadruplexes can be assessed by recording the changes in absorption at 295nm with increasing temperature. In contrast to double stranded DNA (dsDNA) a hypochromic shift is observed as the structure unfolds into linear DNA strands (ssDNA). The stability is expressed as the melting temperature T_m, which indicates when half of the DNA structure as unfolded. In addition to this TDS experiments are used to further confirm the presence of a G-quadruplexes. The absorption spectrum in the unfolded (high temperature) state is subtracted from the absorption spectrum in the folded (low temperature) state to obtain the characteristic signature. Many secondary structures of DNA then show a characteristics spectrum, amongst them G-quadruplexes. Regardless of the folded topology, a minimum at ~295 nm and a maximum at ~270 nm must be present to indicate an intact quadruplex structure. Differences in the range between ~260 – 220 nm in TDS of G-Quadruplexes can be attributed to the various topologies and difference in sequences (**Figure 8**).[48] The structural complexity and dynamic nature of G-quadruplexes underscore their functional significance in biological systems.[51–60] While their formation was initially debated as an in vitro artifact, advances in structural analysis and molecular recognition have confirmed their prevalence *in vivo*. The interplay between sequence-specific folding, cation-dependent stability, and environmental factors positions G-quadruplexes as key regulators of genomic processes. This structural versatility also makes

them attractive targets for chemical modification, enabling tailored manipulation of their stability and biological activity.[61–66]

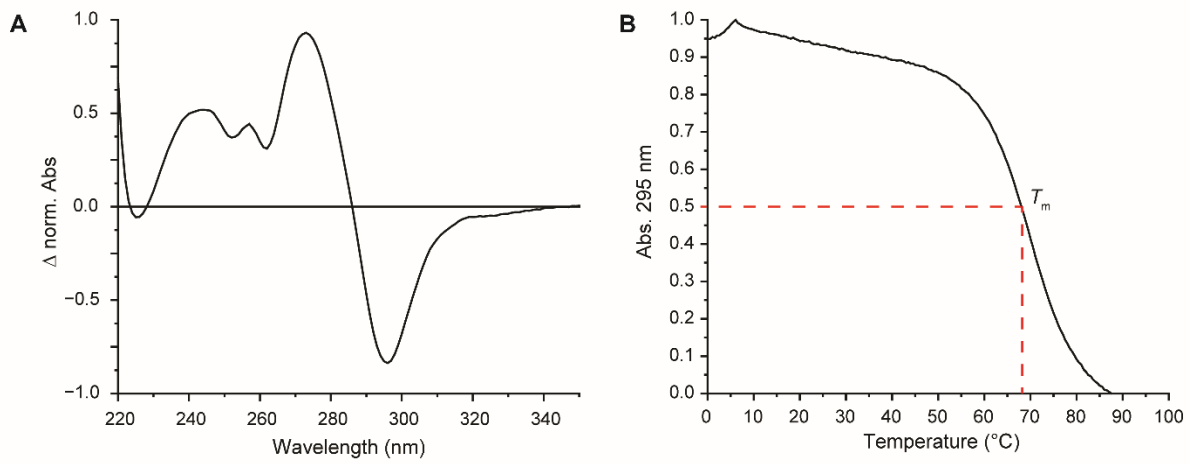

Figure 8. A) Exemplary thermal differential spectrum (TDS) of a G-quadruplex indicating successful formation through presence of a minimum at 290 nm and a maximum at 270 nm. B) UV-Vis melting curve of a G-quadruplex measuring thermal stability of the construct. To note here is the hypochromic shift of the absorption at 295 nm for melting of a G-quadruplex, in contrast to a hyperchromic shift of double-stranded duplex DNA.[47–50]

1.3 Biological Relevance

Initially dismissed as artifacts of isolated single-stranded DNA (ssDNA) in vitro, G-quadruplexes have emerged as critical regulators of genomic function in vivo.[65,67,68] Bioinformatic analyses estimate over 300,000 potential quadruplex-forming sequences (PQS) in the human genome, with enrichment in regions governing gene expression, replication, and chromosomal stability (**Figure 9**). [25,69]

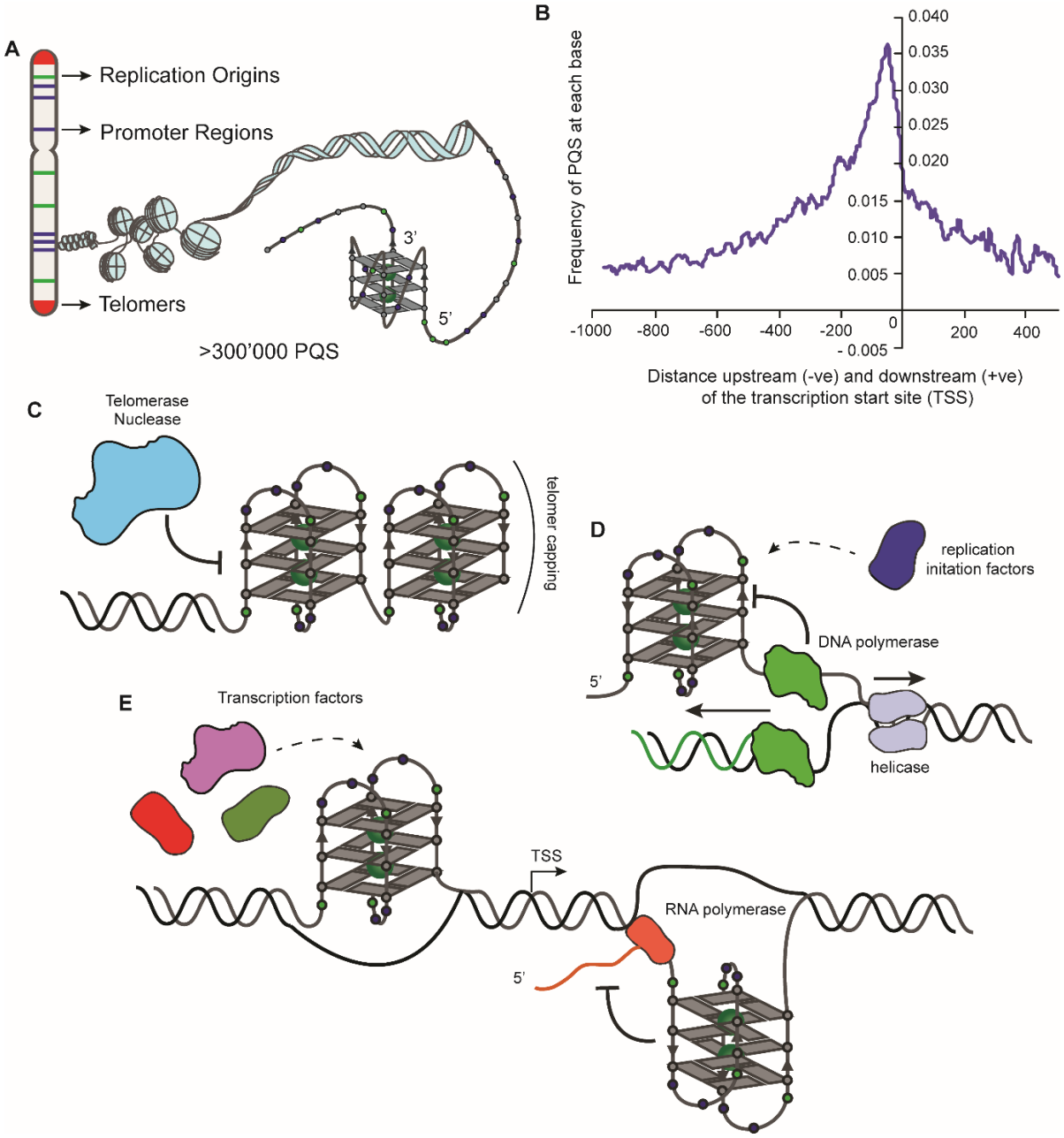

Figure 9. A) G-quadruplexes are abundant in the entire human genome and across all 23 chromosome pairs. They are found predominantly at the telomers, promoter regions and replication origins within a chromosome. Postulated amount of putative G-quadruplex forming sequences (PQS) within the human genome is >300000. B) Strong increase in PQS density can be found within 200bp of transcription start sites (TSS) indicating close involvement of G-quadruplexes in transcription and translation and therefore various diseases. Main interaction points of G-quadruplexes within the human body are C) the inhibition of telomerase and nucleases and telomer capping leading to telomer protection, D) recruitment of replication initiation factors and stalling of DNA polymerase and E) recruitment of transcription factors or inhibition of the RNA polymerase during transcription. [25,69–74]

While not all PQS adopt G-quadruplex structures under physiological conditions, their dynamic formation is tightly regulated by cellular factors such as helicases, cation

concentrations, epigenetic modifications and protein association. The breakthrough in validating their biological relevance came with the development of G-quadruplex-specific antibodies (e.g., BG4, 1H6, SG4) and fluorescent probes, enabling direct visualization in live cells. Confocal microscopy studies have localized G-quadruplexes to telomeres, oncogene promoters, and replication origins, particularly during S-phase, where they influence DNA synthesis and repair (**Figure 10**).[63,75–77]

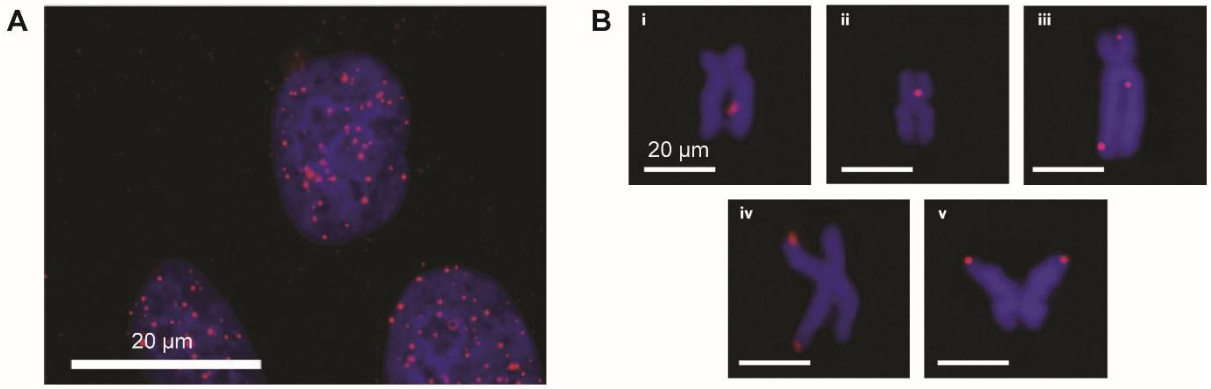

Figure 10. A) In vivo detection of DNA G-quadruplex through the use of specific antibodies (BG4) and fluorescence microscopy. Folded G-quadruplexes are indicated through the red fluorescence (MFC-7 cell line). B) Direct visualisation of folded G-quadruplexes through immunofluorescence with BG4 antibody on various human chromosomes. Reprinted with permission from Nature Chemistry. Copyright © 2013 Nature Publishing Group.[75]

G-quadruplexes have been prominently associated with telomeres, where the tandem repeats of $(TTAGGG)_n$ form highly stable DNA secondary structures which protect chromosome ends from degradation and fusion.[78] These telomeric G-quadruplexes can inhibit telomerase activity, a ribonucleoprotein enzyme that maintains telomere length in approx. 90% of cancer cells leading to immortalization of these malignant cells.[79,80] Targeting these structures with small-molecule ligands such as pyridostatin or BRACO-19 (**Figure 11**) can impair telomere maintenance leading to telomere dysfunction which concomitantly leads to the induction of senescence or apoptosis in cancer cells while sparing normal cells with inactive telomerase. G-quadruplexes are enriched not only in telomers but can be found in promoter regions of oncogenes such as c-MYC, BCL-2, KRAS, and VEGF, where they act in a dual role either as roadblocks for transcription or conversely as hubs for transcription factors.[81–84] For example, the c-MYC promoter contains a nuclease-hypersensitive element ($NHE\ III_1$) capable of forming multiple G-quadruplex structures due to its G-rich sequence. Stabilization of these structures represses c-MYC expression, a key driver of uncontrolled proliferation in cancers like breast carcinoma.[82,85–88] Likewise, G-quadruplexes in the KRAS promoter modulate its oncogenic activity, connecting structural dynamics to the progression and development of cancer.[89–91] Recent studies have

expanded the functional characteristics of G-quadruplexes to encompass roles in RNA metabolism, epigenetic regulation and viral pathogenesis. RNA G-quadruplexes in the 5' untranslated regions (UTRs) of mRNAs (FMR1, APP) regulate translation efficiency, with implications for neurodegenerative diseases like Alzheimer's disease. G-quadruplex motifs are essential for replication and latency in the genomes of several viruses, including examples like HIV-1[92,93] , SARS-CoV-2[94] , and Epstein-Barr virus (EBV)[95] . For example, the HIV-1 long terminal repeat (LTR) promoter contains a G-quadruplex structure that suppresses viral transcription thus making it a potential target for latency-reversing drugs or therapies in HIV cure strategies.[96] G-quadruplex stability can be further modulated by epigenetic modifications, such as DNA methylation and hydroxymethylation. The presence of 5-methylcytosine (5mC) in loops or flanking regions of these structures can either stabilize or destabilize quadruplexes, depending on sequence context, connecting these structures to imprinting disorders as well as cancer epigenetics.[97]

Formation and resolution of G-quadruplexes is tightly controlled by cellular machinery consisting of various components. Amongst them helicases play a crucial role. To aid in transcription and replication, helicases such as WRN (Werner syndrome helicase), BLM (Bloom syndrome helicase), and DHX36 selectively and efficiently unwind G-quadruplexes. Defects in these helicases correlate with genomic instability and diseases like Werner syndrome (premature aging) and Bloom syndrome (cancer predisposition).[98,99] In contrast to that, stabilization of G-quadruplexes by small molecules or mutations of protein sequences resulting in reduction or loss of function can induce replication stress, leading to DNA breaks and chromosomal rearrangements.[100] The accumulation of G-quadruplexes in for example oncogene promoters is linked to chromothripsis, a special case of chromosomal shattering observed in certain cancers.[101–103] As mentioned, the dysregulation of G-quadruplex dynamics are implicated in neurodegenerative diseases. It was shown that the C9ORF72 hexanucleotide repeat expansion in amyotrophic lateral sclerosis (ALS) and frontotemporal dementia (FTD) both can form DNA and RNA G-quadruplexes, which subsequently sequester RNA-binding proteins and can lead to the disruption of gene expression.[104–106] In a similar fashion, G-quadruplexes in mitochondrial DNA contribute to oxidative stress and mitochondrial dysfunction, which are both hallmarks of aging and metabolic disorders.[107–110]

The unique structural and functional properties of G-quadruplexes make them attractive targets for drug development. Over 100 G-quadruplex-binding ligands have been designed, including telomestatin derivatives, acridines, and porphyrins. The main goal of all so far developed small molecule ligands was to stabilize quadruplexes to ideally either inhibit telomerase or suppress oncogene expression.[111–113]

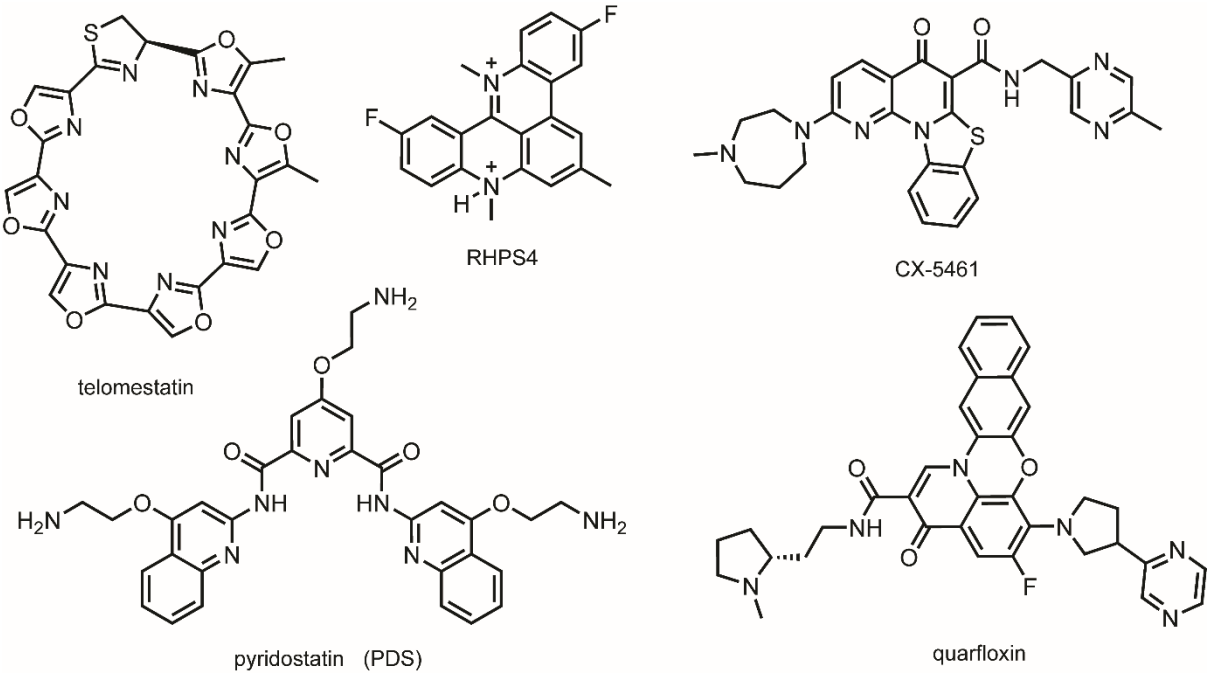

Figure 11. Exemplary G-quadruplex binding ligands used for stabilisation of these DNA secondary structures through Coloumb interactions and pi-stacking on G-tetrads. Common structural features include nitrogen heterocycles and extended pi-surface. Additional positive charges can be beneficial for interaction with the negatively charged phosphate backbone of the G-quadruplex.

Clinical trials are underway for compounds like CX-5461 (targeting ribosomal DNA G-quadruplexes in hematologic malignancies)[114–116] and quarfloxin (disrupting G-quadruplex–protein interactions in neuroblastoma)[117]. However, challenges persist, including ligand selectivity, off-target effects, and the need for high-resolution structural data to guide rational drug design.[81,118,119] These challenges are being addressed by novel emerging technologies like CRISPR-Cas9-mediated genome editing[120] and single-molecule fluorescence resonance energy transfer (smFRET). For example, CRISPR screens have made it possible to identify synthetically lethal genes with G-quadruplex stabilization, offering novel therapeutic approaches. The real-time monitoring of of G-quadruplex dynamics in live cells has been made possible by sophisticated smFRET experiments, revealing how environmental cues such as oxidative stress or hypoxia, modulate their structure formation.[121–123]

Beyond the double helix, G-quadruplexes represent a paradigm shift in understanding of the functional complexity of DNA. Their significance in human biology is highlighted by the plethora of roles in telomere maintenance, gene regulation, and disease pathogenesis, meanwhile their structural plasticity offers opportunities for targeted intervention and novel therapeutic approaches. However further research is required to fully understand the interplay between G-quadruplex formation, their cellular context, and environmental factors.

Chemically modified analogs and advanced imaging tools will be important to dissect their *in vivo* functions and translating this knowledge into precision therapies.

1.4 DNA G-Quadruplex Protein Interactions

G-quadruplexes have been shown to be not just static structures but dynamic platforms that engage in complex interactions with a diverse range of proteins. These interactions are crucial for important cellular processes such as replication, transcription, telomere maintenance and DNA repair. Their unique topological and physicochemical features enable binding partners such as proteins with specialized binding domains to selectively recognize them. These DNA-protein interactions can either have a stabilising or destabilising effect on G-quadruplexes which affects gene expression or resolution of these structures, underscoring their dual role as functional elements and potential sources of genomic instability.[124–131]

1.4.1 Helicases: Guardians of G-Quadruplex Resolution

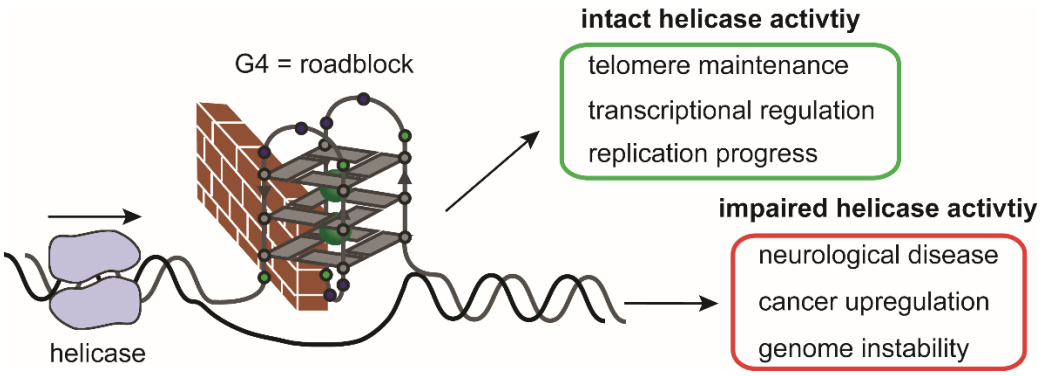

Figure 12. G-quadruplexes can act as molecular roadblocks needing to be unwound by specific motor proteins such as helicases. Intact helicase activity is generally associated with functioning telomere maintenance, transcriptional regulation and correct replication progress. Impaired helicases can lead to genomic instability and further negative consequences such as cancer upregulation.

Helicases are ATP-dependent motor proteins that unwind DNA secondary structures, including G-quadruplexes. This prevents replication fork stalling and transcriptional interference important for the overall cellular machinery.[132,133] Among the most investigated are the RecQ family helicases which exhibit high specificity and efficiency in binding and unwinding of G-quadruplexes. The aforementioned WRN and BLM helicase are two of the most prominent examples of this helicase family.[134–137] WRN helicase is defective in the premature aging disorder Werner syndrome. This enzyme shows 3'→5' helicase activity and is capable of resolving telomeric DNA G-quadruplexes thus ensuring correct telomere replication and granting telomeric stability.[138–140] In a similar fashion a deficiency in BLM helicase activity is observed in Bloom syndrome, a cancer-predisposing disorder. This

helicase preferentially targets and unwinds parallel folded G-quadruplexes in oncogene promoters in a 3'→5' directionality, preventing replication stress and chromosomal breakage during DNA replication.[141–144] Another key player, FANCJ (BRIP1), a component of the Fanconi anemia pathway, resolves G-quadruplexes during DNA repair and homologous recombination. Mutations in FANCJ are linked to breast and ovarian cancers, highlighting the pathological consequences of unresolved G-quadruplexes. Helicases beyond the RecQ family have been thoroughly studied in the context of G-quadruplexes amongst which Pif1 and DHX36 are two prominent targets of interest.

Pif1 is a dedicated replication fork guardian protein with very high specificity for G-quadruplex structures. Unlike RecQ helicases, Pif1 employs a unique 5'→3' translocation mechanism that directly interacts with the G-quartet core rather than loop regions thus facilitating the processive DNA unwinding even in K^+-stabilized G-quadruplex structures. Its N-terminal domain contains a conserved G4-binding pocket with high selectivity for the carbonyl oxygen arrangement found in G-tetrads. This allows Pif1 to resolve topologically diverse G-quadruplexes with high efficiency, not strongly differentiating between parallel, hybrid or antiparallel folds. Crucially, Pif1 deficiency leads to G-quadruplex dependent replication stalling at telomeric $(TTAGGG)_n$ repeats and at oncogene promoters, which leads to the induction of double-strand breaks as well as chromosomal rearrangements. More recent single-molecule analyses have confirmed Pif1 to be exquisitely sensitive to the G-quadruplex structure's thermal stability. Chemically modified G-quadruplexes with high thermal stability, achieved through ligand-induced π-stacking or cation substitution, inhibit Pif1-catalysed DNA unwinding to a significant degree (**Figure 13**).[145–150]

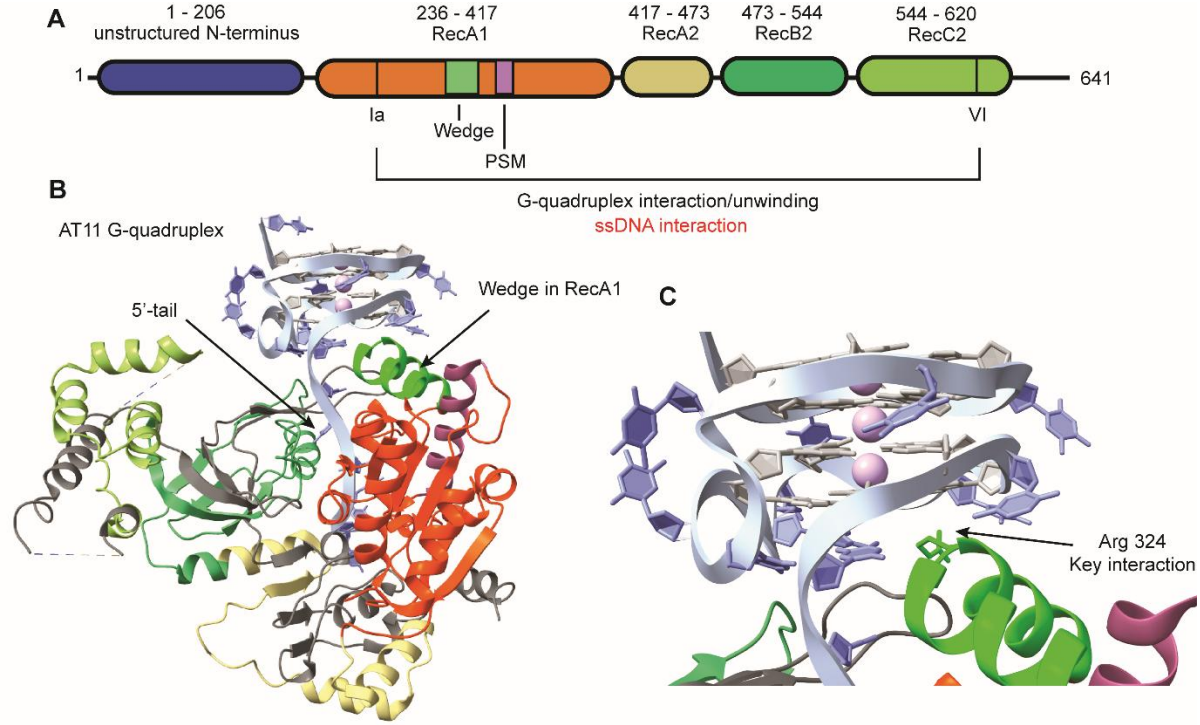

Figure 13. A) Protein domain structure of Pif1 helicase. The G-quadruplex interaction and unwinding is facilitated by various motifs from Ia within the RecA1 domain until the VI motif in the RecC2 domain. B) Crystal structure of AT11 parallel G-quadruplex with Pif1 from yeast cells (*S. cerevisae*). The extended 5'-tail of a G-quadruplex target is buried deep within the protein pocket between the various domains. C) The wedge region (green box) within the RecA1 domain is predominantly involved in G-quadruplex binding with a single arginine (Arg 324) as a key interaction point between Pif1 and the G-tetrad of a quadruplex..[151]

A second helicase, operating in the reverse direction than Pif1 is DHX36 (alternatively RHAU). This protein belongs to the family of DEAD/DEAH-box helicases.[152] This protein is the strongest known G-quadruplex resolving helicase to date, with combined ATP-dependent unwinding as well as an RNA/DNA chaperone function. In contrast to Pif1 a strong preference for binding parallel folded G-quadruplexes through the presence of its dsRBD domain which engages in minor groove insertion, while the helicase core disrupts G-quartets via a "wedge-and-pump" mechanism involving conserved motifs Ia and V. DHX36 binds unimolecular G-quadruplexes with nanomolar affinity and shows almost negligible activity toward bimolecular structures which highlights its topology-dependent recognition. The roles of DHX36 in a telomeric context is to resolve G-quadruplexes efficiently to prevent the formation and accumulation of R-loops and maintain telomere length homeostasis. The depletion or inhibition of this helicase triggers telomeric DNA damage responses detectable via γH2AX foci. It has been noticed that the activity of DHX36 is strongly influenced by loop composition of the respective G-quadruplex target. Chemical modifications within the loops, such as 8-oxoguanine substitutions or locked nucleic acids, influence resolution depending

on conformational flexibility.[153–157] Recent studies with cryo-EM structures of DHX36-G-quadruplex complexes reveal that the helicase induces a 30° bend in the G-quadruplex backbone during unwinding. This has been exploited as a novel targeting angle, whereby ligands that rigidify the G-tetrad core can disrupt this process and thus efficient unwinding of the DNA structure. This sensitivity to structural perturbations makes DHX36 an exceptional reporter for evaluating how chemical modifications alter G-quadruplex dynamics (**Figure 14**).

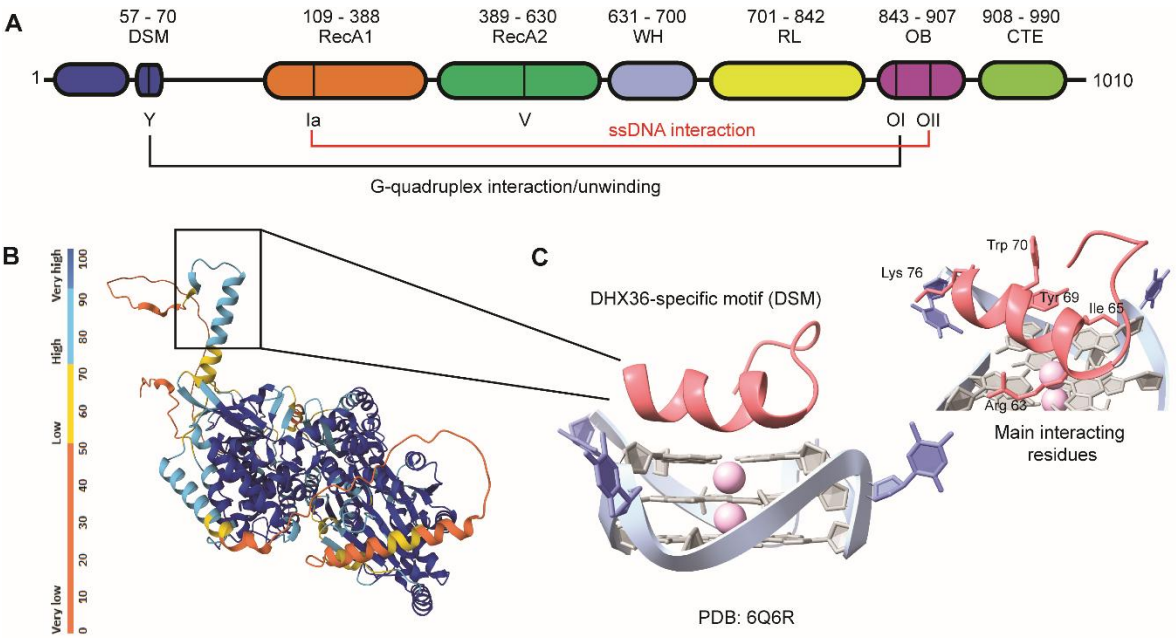

Figure 14. A) Protein domain structure of DHX36 helicase. G-quadruplex interaction and unwinding involves various domains from the DHX36-specific motif (DSM, Y), the RecA1, RecA2 up to the OB-fold domain. Main interaction point of DHX36 with G-quadruplexes occurs through the alpha helical DSM which engages with the G-tetrads though non-covalent interactions. B) AlphaFold3 prediction of the structure of DHX36 and the resulting confidence score. Unstructured regions are represented as random coils. The DSM sits outside of the protein core therefore facilitating efficient G-quadruplex binding. C) Co-crystal structure of a parallel G-quadruplex with the isolated DSM of DHX36 (PDB: 6Q6R). Aminoacid sidechains of Lys, Trp, Tyr, Ile and Arg are mainly involved in G-quadruplex binding.[153,158]

Structural studies of G-quadruplex-helicase complexes have furthermore shown that their interaction occurs through few key conserved motifs within the protein structure, such as the helicase OB-fold (HARP), RRM or RGG domains. These domains are crucial in the recognition of the terminal G-quartets and distinct loop compositions. For instance, the E. coli helicase RecQ binds to the lateral loops of G-quadruplexes, inducing conformational changes that destabilize the structure. In humans, the helicase DHX36 (RHAU) specifically binds RNA G-quadruplexes via its helicase domain, regulating their stability in mRNA untranslated regions (UTRs).[127]

1.4.2 Transcription Factors and RNA-Binding Proteins: Modulators of Gene Expression

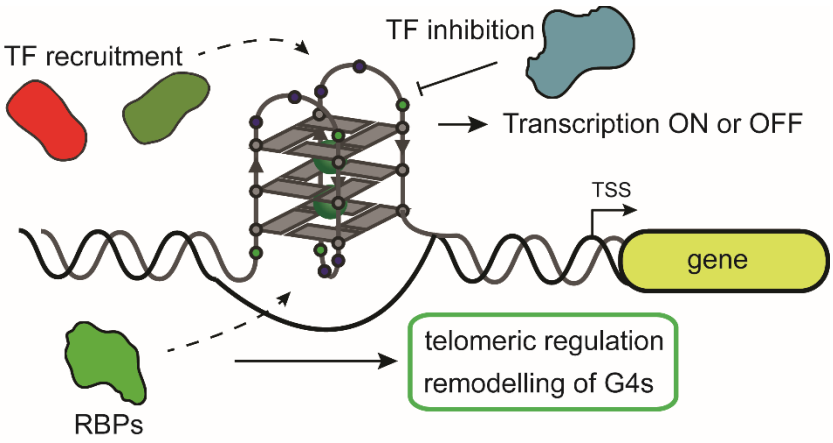

Figure 15. G-quadruplexes do not only act as recruitment hubs for transcription factors (TF) but can also regulate which TFs are bound or unbound, resulting in the control of gene transcription. RNA binding proteins (RBP) furthermore interact with G-quadruplexes in order to facilitate telomeric regulation and can potentially lead to remodelling of G-quadruplexes.

G-quadruplexes in promoter regions serve as binding sites for transcription factors (TFs) and RNA-binding proteins (RBPs), some of which recognize both RNA and DNA structures despite their nomenclature, which either stabilize or destabilize the structures to regulate gene expression (**Figure 15**). Nucleolin is a nucleolar protein overexpressed in cancer cells and binds to telomeric G-quadruplexes with high affinity, promoting their stabilization and inhibiting telomerase activity.[159–161] Conversely, MAZ (myeloid zinc finger 1) binds to G-quadruplexes in the c-MYC promoter, displacing the structure to enhance transcriptional activation.[162–164] This dual role of TFs—either suppressing or promoting gene expression—depends on the sequence context and cellular environment.[127] RBPs such as hnRNP A1 and FUS interact with RNA G-quadruplexes to regulate splicing, transport, and translation. hnRNP A1 destabilizes G-quadruplexes in the FMR1 mRNA UTR, preventing the sequestration of fragile X mental retardation protein (FMRP) in fragile X syndrome. In contrast, FUS binds to G-quadruplexes in neurodegenerative disease-associated transcripts (e.g., C9ORF72), contributing to pathological RNA foci formation in amyotrophic lateral sclerosis (ALS).[165–169]

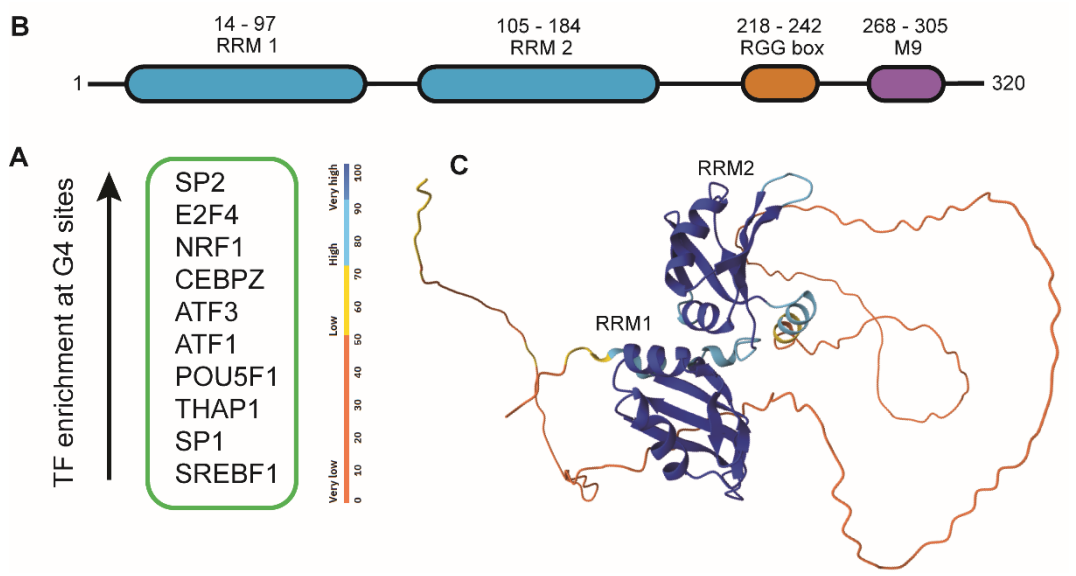

Figure 16. A) Selection of most enriched TFs at observed G-quadruplexes in promoter regions of various genes. B) Protein domain structure of RNA-binding protein hnRNP A1 with two RNA recognition motifs (RRM) responsible for the binding and unfolding of DNA G-quadruplexes in an ATP-independent manner. C) AlphaFold3 structure prediction of full length hnRNP A1 with unresolved C-terminus represented as low confidence random coil. Only the substructure of the two RRM domains is reported as crystal structure (PDB: 1UP1).

DNA polymerases encounter severe osbtacles when replicating through G-quadruplex-forming DNA sequences. The stable stacking of G-quartets can stall replication forks, leading to DNA breaks and mutations. Nonetheless biological systems have developed TLS (specialized translesion synthesis) polymerases like Pol η and Pol κ which can bypass G-quadruplexes through adoption of flexible active sites that accommodate the non-B DNA topology.[170] For example, Pol η is able to efficiently replicate past G-quadruplexes in genes coding for immunoglobulin to ensure somatic hypermutation and antibody diversity. Replication polymerases like Pol δ and Pol ε require the assistance of helicases to achieve their dedicated function as the G-quadruplexes need to be unwound before synthesis by the polymerase can occur. Failure to resolve these structures causes collapse of the DNA replisome and subsequent chromosomal instability, a common hallmark of cancer genomes. Interaction of viral polymerases, shown for example with the HIV-1 reverse transcriptase, can also engage in G-quadruplex interaction within the respective viral genome. This has lead to a targeted approach of HIV latency treatment, whereby stabilization of these G-quadruplex structures with small molecules (e.g., pyridostatin) could lead to reverse transcription inhibition.[171]

Exploiting G-quadruplex–protein interactions has emerged as a promising therapeutic avenue. Several approached have been investigated ranging from small molecules that stabilize G-quadruplexes (CX-5461, quarfloxin) and thus enhance their binding to nucleolin

or MAZ, suppressing oncogene expression or on the contrary, helicase inhibitors such as PBP1019, which block WRN or BLM activity, selectively killing cancer cells with high G-quadruplex content. CRISPR-Cas9 screens have identified synthetic lethal interactions between G-quadruplex stabilization and helicase deficiency, guiding personalized cancer therapies.[172] Chemically modified G-quadruplex analogs, such as 8-oxoguanine derivatives or locked nucleic acids (LNAs)[173–175] , are being developed to probe protein interactions with atomic precision. These tools enable the mapping of binding interfaces and the design of allosteric inhibitors that disrupt pathogenic interactions without affecting non-target proteins.

Despite the continued advancement in understanding G-quadruplex–protein interactions, their transient and context-dependent nature remains a challenging part especially for *in celluo* and *in vivo*. Methods such as chromatin immunoprecipitation (ChIP-seq)[77,176] and proximity labelling (BioID)[177] are currently being developed to define interactions at a genome-wide scale. Cryo-EM and crosslinking mass spectrometry (XL-MS) have shown promising results in delivering high-resolution insights into these dynamic complexes.[178,179] Ultimately, understanding how proteins recognize, stabilize, or resolve G-quadruplexes will illuminate their roles in health and disease. This knowledge can then be combined with chemical biology tools to develop targeted treatment strategies to harness such interactions for precision medicine purposes.

1.5 Metal-Mediated Base Pairing in Nucleic Acids

The canonical Watson-Crick-Franklin base pairing relies on hydrogen bonds to ensure the precise hybridization of complementary DNA strands.

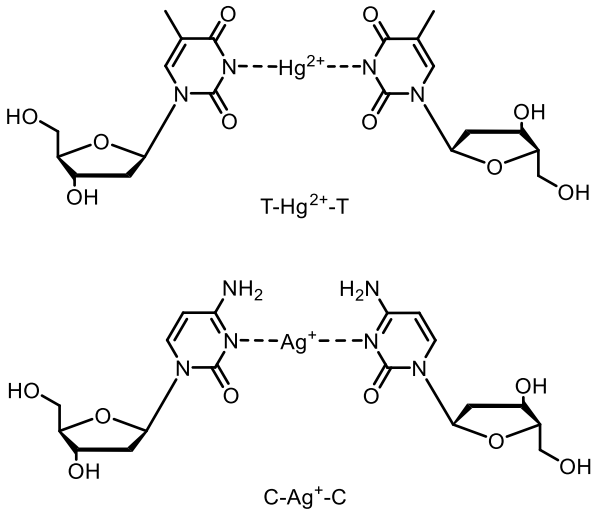

Figure 17. Metal-mediated base pairs of a T-T mismatch stabilised with Hg^{2+} and a C-C mismatch with Ag^{+}. These structures were among the first reported metal-mediated base pairs in nucleic acids.

Nevertheless, nature and synthetic chemistry have been able to expand this model to metal-mediated base pairing, wherein metal ions can substitute or augment the role of hydrogen

bonds to give rise to novel structurally and functionally distinct nucleic acid architectures.[180,181] This concept emerged in 1960 when Katz demonstrated that divalent mercury ions (Hg^{2+}) could be reversibly bound between thymine-thymine (T-T) mismatches, stabilizing a metal-complexed T-Hg^{2+}-T pair despite the absence of any canonical hydrogen bonding (**Figure 17**). The structural proof of this novel base pair was not achieved until modern X-ray crystallographic techniques had been developed. It nevertheless laid the foundation for a field now rich with examples of metal-dependent nucleic acid structures.[182] After this first T-Hg^{2+}-T prototype, several researchers identified diverse metal-complexed pairs, such as C-Ag^{+}-C and others involving Cu^{2+}, Ni^{2+}, or Pd^{2+}.[183,184] A historic breakthrough was achieved in 2017 with the first crystal structure of a DNA double helix entirely stabilized by Ag^{+}-mediated base pairs, revealing a linear "silver nanowire" threading through the duplex. This demonstrated that metal ions could not only mimic hydrogen bonds between isolated nucleobases but also be a core element of entire DNA secondary structural motifs (**Figure 18**).

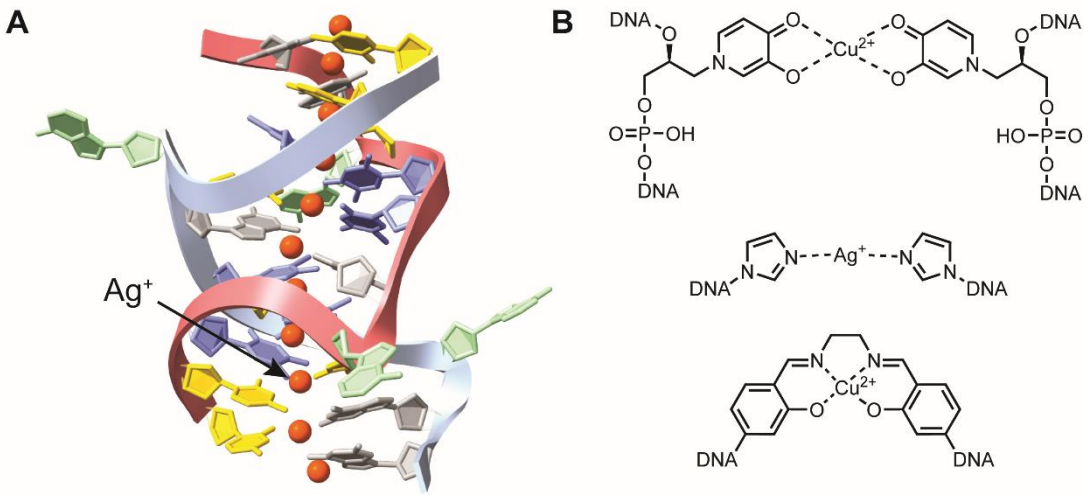

Figure 18. A) X-ray structure of duplex DNA containing canonical nucleobases exclusively forming metal-mediated basepairs (G-Ag+-G, G-Ag+-C, C-Ag+-C, T-Ag+-T). The close proximity of the Ag+ cations bound within the DNA form a Ag-nanowire (PDB: 5IX7).[185] B) Novel metal-mediated base pairs based on artificial nucleosides incorporated covalently into a DNA oligonucleotide strand (hydroxypyridine, imidazole, salen) capable of binding various transition metals.

The field advanced further with artificial nucleobase surrogates, designed to bind transition metals like Mn^{2+}, Zn^{2+}, or Cu^{2+}.[186] Another examples is showcased with hydroxypyridone ligandosides (HP) which form stable HP-Cu^{2+}-HP pairs and thus enhance duplex thermal stability by up to +13°C.[187] Methylated cytosine analogs (MeC-Ag^{+}-T) and palladacycle-based pairs expanded the toolkit for programmable metal-mediated DNA. That metal-mediated base pairing could be applied to structures beyond the classical double helical

structure was shown with the example of a Cu^{2+}-salen system, introduced in 2005, whereby metal coordination and covalent imine crosslinking was combined. This yielded an unprecedented thermal robustness and enabled programmable metal arrays within DNA.[188] Debates about metal-mediated conductivity where ignited, with studies suggesting that structural rigidification and not the direct metal ion conduction, enhanced the charge transfer between bases.[185,189–192] Applications for some of the systems has been exploited and few examples showcase heavy metal sensing (of Hg^{2+} via T-Hg^{2+}-T pairs) and templated synthesis of metal nanoclusters, where DNA-bound metal cations can be reduced into fluorescent or catalytic nanoparticles.[184,193]

While most studies focused on duplex DNA more recent work explores metal-mediated pairing in complex DNA architectures. Such a case can be found for three-way junctions, functionalized with bipyridine-Ni^{2+} motifs which offer nanoscale building blocks that can be dynamically reconfigured for DNA origami assemblies.[194,195] Pyridine-Ag^{+}-pyridine pairs enabled the first metal-wired DNA triple helices, while hydroxypyridone ligands supported Fe^{3+} arrays.[196] Making use of the chemical properties of some transition metals, such as Cu^{2+} and its redox-activity in i-motif DNA structures, demonstrated reversible switching between protonated and metal-bound states, opening avenues for dynamic biosensors (**Figure 19**).[197]

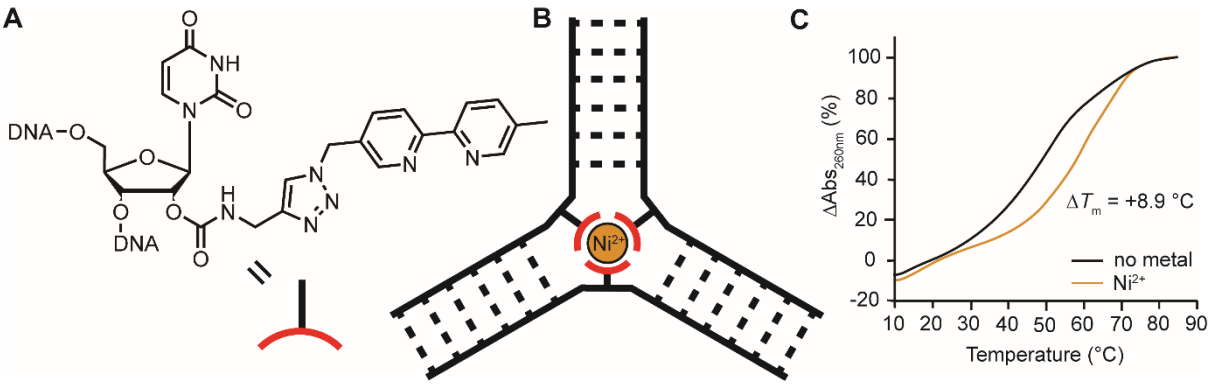

Figure 19. Metal-mediated base pairing was further expanded to different secondary DNA structures. A) A bipyridine modified thymine nucleoside, functionalising the 2'-OH group of ribose through a Click-reaction. B) Implementation of the bipyridine bearing thymine for the dynamic assembly of a DNA three-way junction through complexation of a Ni^{2+} cation. C) Formation of the metal complex leads to a significant thermal stabilisation of the three-way junction.[194,195]

1.5.1 Metal-Mediated Base Pairing in DNA G-quadruplexes

G-quadruplexes have become prime targets for metal-complexed modifications due to their inherent cation-binding pockets for monovalent cations such as Na^+ or K^+. Early work incorporated T-Hg^{2+}-T pairs into loop regions[198] , but recent advances replaced entire G-tetrads with Cu^{2+}-pyridine quartets. Clever demonstrated that tetramolecular G-quadruplexes with terminal pyridine ligandosides exhibited Cu^{2+}-dependent stabilization and reversible assembly via EDTA-mediated metal removal.[199,200] In tetramolecular G-quadruplex systems, pyridine substitutions enforced parallel topologies and enabled EPR-based distance measurements between Cu^{2+} centers as they possess unpaired electrons, aligning with molecular dynamics simulations.[201,202] A Cu^{2+}-stabilized thrombin-binding aptamer showed a notably enhanced clotting inhibition, highlighting potential therapeutic applications (**Figure 20**).[200]

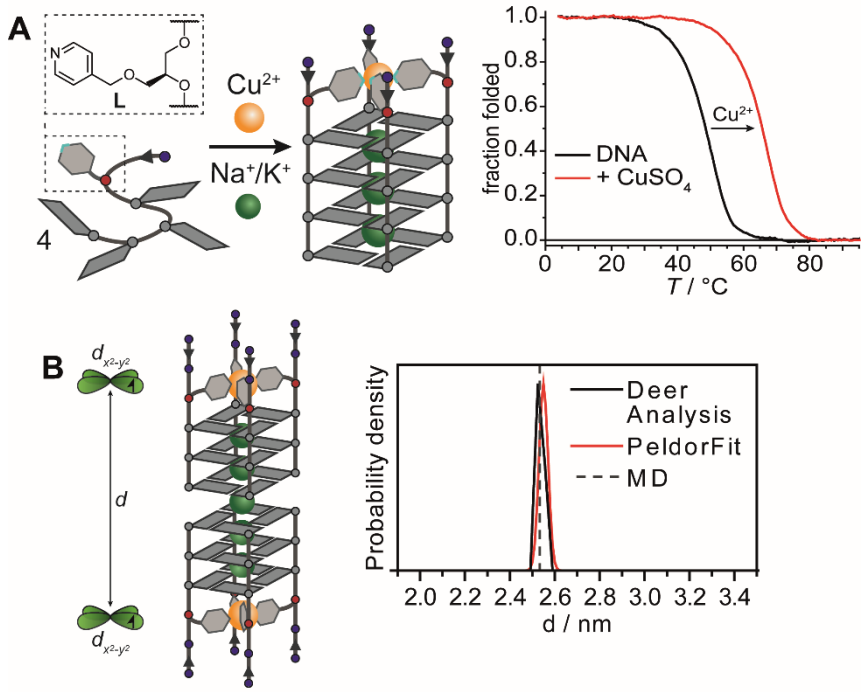

Figure 20. A) Formation of tetramolecular G-quadruplexes bearing four pyridine modifications per quadruplex capable of binding a Cu^{2+} which increases the thermal stability of the system by ΔT_m = 20°C. B) As the G-quadruplexes possess an exposed G-tetrad on their 3'-end π-stacking of two constructs is observed leading to a high-ordered structure. The unpaired electron of the individual Cu^{2+} cations, due to its d^9-electron configuration, enables the possibility of precise distance measurements between the two Cu-centers bound within the G-quadruplexes via electron paramagnetic resonance (EPR) spectroscopy utilising the double electron-electron resonance (DEER) method. A narrow distance distribution of the G-quadruplex dimer can be obtained corresponding to the theoretical distance between stacked basepairs (0.35 nm per basepair, $d_{theor.}$ = 2.45 nm, $d_{exp.}$ = 2.55 nm).[202]

These modified G-quadruplex system could furthermore take advantage of the chemical properties of the implemented metals and not only as structural elements or thermal stabilisation. The Lewis acidic nature of the Cu^{2+} cation was used to create a catalytically active G-quadruplex (DNAzyme) capable of facilitating a Michael addition in an enantioselective manner due to the inherent chiral nature of the DNA. Precise positioning of the imidazole modifications within the G-quadruplex loop regions made it possible to switch enantioselectivity with ee-values up to 99% (**Figure 21**).[203,204] Despite relentless effort and constant progress the control over metal selectivity, understanding of dynamic structural changes between G-quadruplex topologies and further exploiting interaction of these modified structures with other biomolecules such as protein remains challenging. The combination of chemical synthesis, structural biology, and computational modelling promises to unlock new functionalities—from redox-switchable aptamers, over metal-encoded DNA nanomachines and to molecular decoys. As metal-mediated base pairing bridges inorganic chemistry and nucleic acid biology, it redefines DNA's versatility beyond its genetic role, positioning it as a scaffold for smart materials and precision diagnostics.

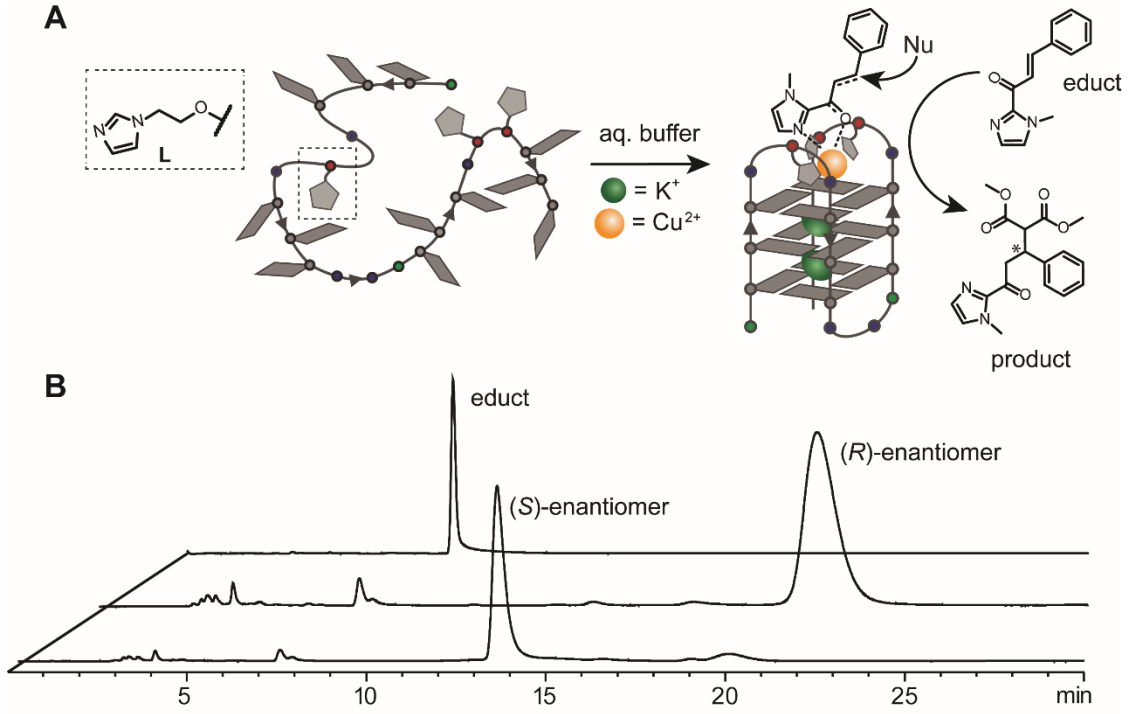

Figure 21. A) Implementation of an imidazole ligandosides within an oligonucleotide strand capable of folding into a unimolecular G-quadruplex. The imidazole modification is capable of binding a Cu^{2+} cation. Through implementation of just three ligands, one coordination site of the metal cation is left vacant, rendering it catalytically active. The G-quadruplex construct could be used as metallo DNAzyme for the catalysis of a Michael addition in an enantioselective manner. B) Chiral-HPLC traces of the educt and the two possible product enantiomers. Selectivity between enantiomers could be influenced by selective position of the imidazole modifications within the G-quadruplex structure.[204]

2. Motivation and Objectives

The aim of this thesis is to develop a novel bidentate ligand capable of forming various transition metal cations and build upon the previously reported monodentate systems of the Clever Lab. In previously reported systems, the bipyridine modification was introduced through either the 2'-OH group of a ribose backbone, as C-1' nucleoside or as double modified phosphoramidite with polyethylene glycol chains. Contrasting to this, we aim to attach the bipyridine unit to a flexible glycidol backbone, not only simplifying synthetic effort but also scalability which was deemed asit is the determining factor for the solid-phase oligonucleotide synthesis.

The goal is to access further transition metal cations beyond Cu^{2+} and its thermal stabilisation of previously reported system, but potentially employ Ni^{2+}, Zn^{2+}, Co^{2+}, Cd^{2+} and even octahedral metals such as Fe^{2+}. This would expand the toolbox of possible applications of these ligands modified DNA G-quadruplexes and not make use of the metal for just their thermal stabilisation. The precise control and switching of G-quadruplex topologies is a further goal we want to achieve through the implementation of novel bidentate ligands and their corresponding complexes. The driving force of the stable bipyridine metal complex is envisioned to be capable of overwriting G-quadruplex folding. This would not only allow to study the refolding of known polymorphic G-quadruplexes but also follow their behaviour in direct response to an external stimulus. Before studying these systems in a more biological context we will investigate their behaviour under varying solvation environments, specifically under the influence of molecular crowding reagents, organic solvents and hydrogen bond competitors. To complete the structural analysis, molecular dynamics simulations should be performed in order generate a better understanding of the spatial arrangement of the ligands and the DNA structure itself.

Lastly it will be interesting to investigate protein-DNA interactions with these modified G-quadruplexes and compare binding affinities with the natural counterparts. Ideally, we can create systems with similar or better binding affinities towards the proteins of interest (POI) that can resist unfolding by certain RNA binding proteins (RBP) or by helicases. This would allow the use of these artificial systems as potential molecular decoys, capable of interfering with malignant interaction cascades by binding critical proteins. With this interaction investigated we aim towards bringing these artificial DNA systems into living organisms by transfection and studying their impact on cell viability and their localisation within the cell via fluorescence microscopy. If successful, these modified G-quadruplexes could be employed as multipurpose therapeutic tools in the future.

3. Results and Discussion

3.1 New Ligand BiPy Ligandoside Synthesis

Results regarding **BiPy-L2** modifications in this chapter are partially found in the master thesis of Alexander Elmar Schneider.[205]

Prior studies demonstrated that monodentate ligands such as imidazole or pyridine can stabilize G-quadruplexes via coordination to transition metals like Cu^{2+} or Ni^{2+}. However, these systems often require multiple ligand copies to achieve robust stabilization, risking steric clashes or topological distortions. Punt observed that imidazole-based ligands with extended linkers were able to facilitate π-stacking with G-tetrads, yet this compromised metal-binding efficiency. Similarly, only tetramolecular pyridine-terminated G-quadruplexes of Engelhard exhibited substantial thermal stabilization through metal coordination (**L4**, ΔT_m = +15 – 20°C for Ni^{2+}/Cu^{2+}), highlighting the limitations of monodentate coordination (**Figure 22**).[199–201,203,204,206–208]

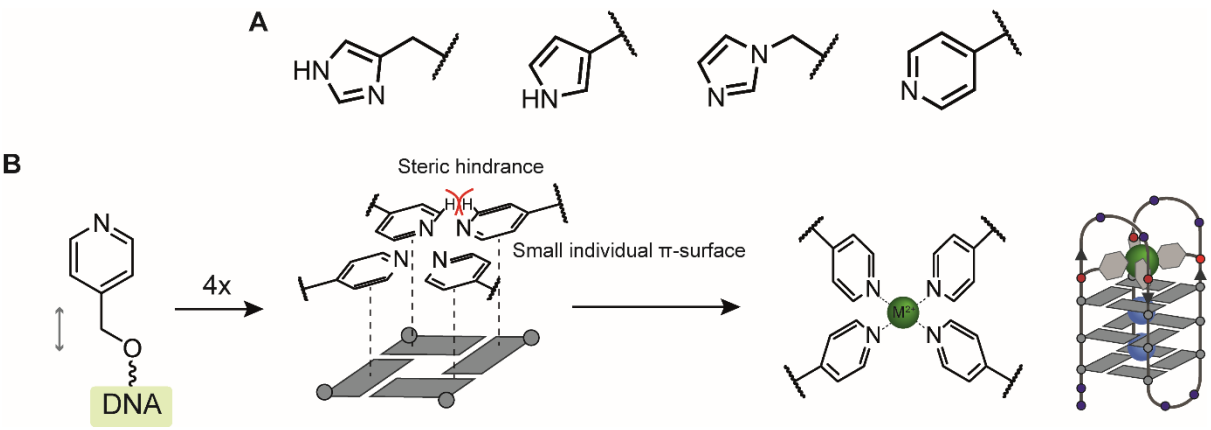

Figure 22. A) Previously reported monodentate ligands implemented into DNA oligonucleotides capable of forming G-quadruplexes. B) Implementation of 4 or more monodentate ligands to satisfy the coordination geometry of transition metals such as Cu^{2+}, could result in steric clashes between closely neighbouring ligands consequently reducing stabilisation of the G-quadruplex or possibly the formation of it in the first place.

A bidentate architecture would enable stronger metal binding with fewer ligands. This can be easily achieved with the incorporation of bipyridine as a novel ligand in DNA G-quadruplexes. Its two nitrogen donors are capable of chelating a single metal ion in a square-planar, octahedral or even tetrahedral geometry, enhancing thermodynamic stability while minimizing steric hindrance. This could overcome the ligand overcrowding observed by Punt, where excessive (n = 7) imidazole ligands within the G-quadruplex loops reduced Ni^{2+}-mediated stabilization.[207] As the pyridine units are covalently fixed in bipyridine's, it can impose a more fixed spatial arrangement on bound metal ions, aligning with the preferred

coordination environments of biologically relevant metals and showing less possibility for distorted orientations. For example, Cu^{2+} typically adopts a square-planar geometry, while Ni^{2+} favours tetrahedral or square-planar coordination. Bipyridine's inherent bidentate nature could synergize well with such systems by pre-organizing metal-binding sites within the folded G-quadruplex structure and thus enabling precise tuning of coordination numbers and geometries.[209] This contrasts with the flexibility of imidazole/pyridine ligands, which often adopt suboptimal orientations. Furthermore, complexes of bipyridine with a large amount of transition metal cations are literature known and exhibit high thermal stability and could enable an access to new tools harvesting the varying chemical properties of the metals and the respective complexes. The creation of stimuli-responsive G-quadruplexes that act as sensors, catalysts, or light-activated switches is intriguing. For example a Ru^{2+}-bipyridine complex within a DNA G-quadruplex could be used for its strong luminescence and electron-transfer capabilities, which could be in turn harnessed for DNA-based optoelectronics or catalytic DNAzymes.[210]

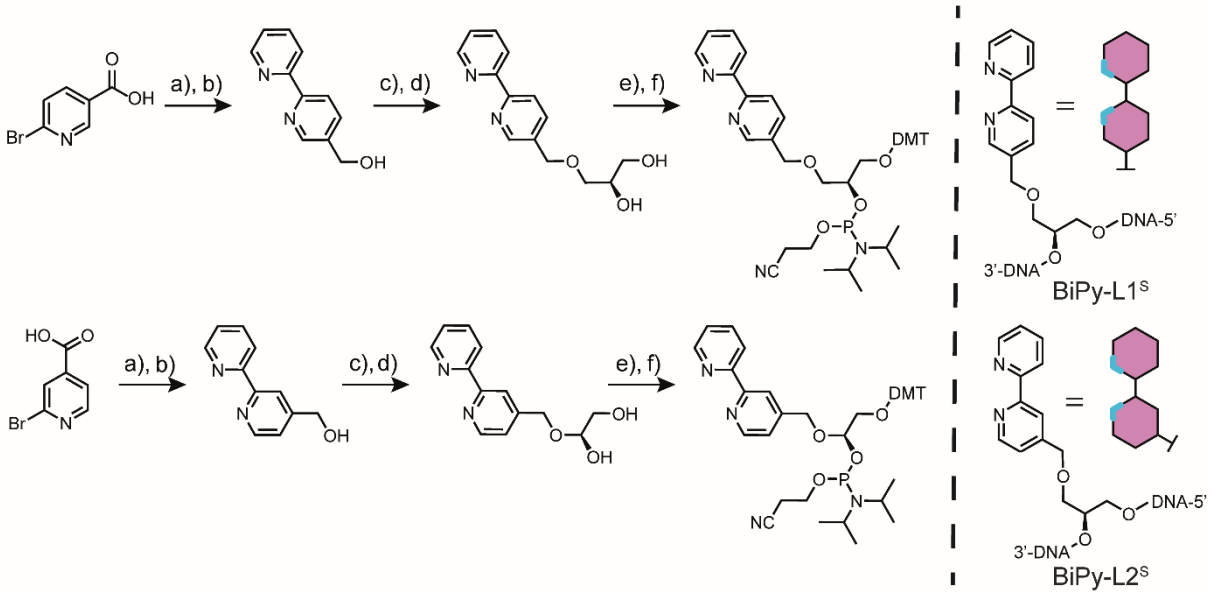

Figure 23. Synthesis of **BiPy-L1 and BiPy-L2** ligandosides starting from either 6-bromonicotinic acid or 2-bromonicotinic acid. a) 2-(tributylstannyl)pyridine, $Pd(PPh_3)_2Cl_2$, *m*-xylene, 110 °C, 16h; b) $NaBH_4$, THF, r.t., 24h; c) NaH, (*R*)-(2,2-dimethyl-1,3-dioxolan-4-yl)methyl-4-methylbenzenesulfonate, DMF, r.t., 24h; d) TFA, THF/water (1:1), 70 °C, 3h; e) DMT-Cl, DIPEA, DMAP, THF, r.t., 24h; f) CEP-Cl, DIPEA, THF, r.t., 3h.

To access the phosphoramidite building blocks for DNA solid-phase synthesis, a multi-step synthetic pathway had to be devised. Several options have been explored and consolidated into a final approach. As most commercially available bipyridines are bi-functionalised on both rings symmetrically, starting from a bipyridine scaffold was not feasible as a single-substituted unit was necessary for our design approach and later functionalisation into a

phosphoramidite building block. The easiest approach was to functionalise one pyridine ring and later joining the two heterocycles in a cross-coupling reaction (**Figure 23**). Bromonicotinic acid was chosen as a starting material where in a first step an esterification reaction was performed to prevent the carboxylic acid from engaging in side reactions in the following cross-coupling reaction. Methyliodide was successful in methylating the carboxylic -OH group of both 6-bromonicotinic acid and 2-bromoisonicotinic acid with excellent yields of up to 95%. A Stille cross-coupling reaction was chosen to fuse the second pyridine ring to the nicotinic ester, as it not only enables larger scale reactions but also the corresponding tri(butylstannyl)pyridine was commercially available and stable. Reactions with pyridines bearing substituents on the 2-position are difficult as these substrates either show strongly diminished reactivity compared to other positions or exhibit lower stability as showcased for pyridine-2-yl boronic acid or esters which are prone to hydrolysis or protodeboronation due to the interaction of the N → B dative bond formed. After successful cross-coupling and purification, the bipyridine carboxylates were reduced to the corresponding alcohol with $LiAlH_4$ in a quantitative reaction. In contrast to previously reported synthetic routes, the now -CH_2OH functionalised bipyridines were not further converted to the halogen analogs for the subsequent nucleophilic substitution reaction with the *S*-dioxolane as this was expected to have a low yield, losing previously synthesised material and decreasing the overall yield of the final building block. Instead, the commercially available dioxolane was converted to the electrophile with *p*-toluenesulfonyl chloride in a quantitative reaction. The nucleophilic substitution reaction of bipyridine-methanol and the now electrophilic S-dioxolane was performed under strong basic conditions with a NaH suspension in DMF at 0 °C. This was necessary in order to generate a strong nucleophile from the bipyridine-methanol. The product was obtained in low yield after purification. In order to obtain the corresponding 5'- and 3'-oxygen connections, the solketal was deprotected with trifluoroacetic acid (TFA) to obtain the corresponding bipyridine-diol in mediocre yield of 50%. To obtain the final building block the bipyridine-diol was then successfully functionalised with dimethoxytrityl chloride (DMTr-Cl) at the primary -OH group with a high yield (80%) and after purification converted to the phosphoramidite with CEDIP-Cl (**Figure 23**). The final product is not further purified as it is unstable in presence of air and moisture and a yield of 80% is assumed for the reaction. The success of the phosphitylation was proven by ^{31}P-NMR as the corresponding phosphorus signals of the product can be seen at 148.90 and 148.60 ppm and clearly distinguishable from either unreacted or hydrolysed reagent which shows ^{31}P-signals at 13.69 ppm (**Figure 24**).

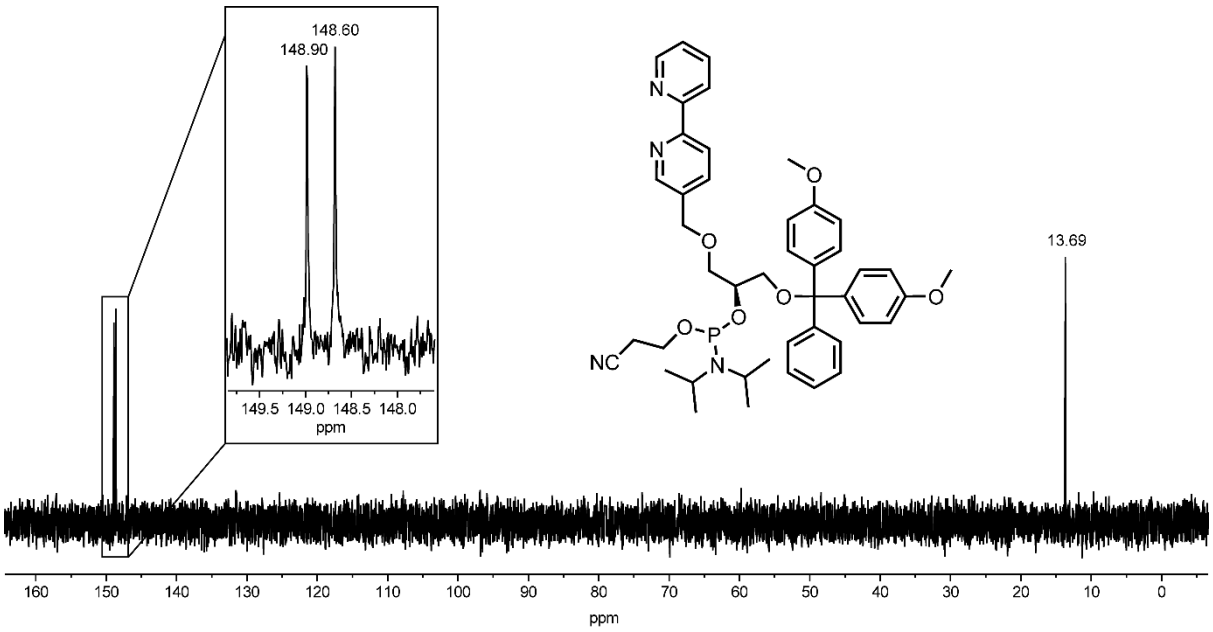

Figure 24. ^{31}P-NMR (202 MHz, 298 K, CD_3CN) spectrum of phosphoramidite of **BiPy-L1** in CD_3CN. The inset shows the diastereomeric pairs of the phosphorous atom. The signal at 13.69 ppm indicates oxidised or hydrolysed phosphitylating reagent.

For the following DNA solid-phase synthesis the phosphoramidites were dissolved in dry acetonitrile to a concentration of 0.1 M. In order to obtain higher yields with these artificial phosphoramidites, the coupling time was elongated to 10 min as compared to the 3 min for the standard phosphoramidite. Coupling efficiencies for the artificial phosphoramidites was 99% even with multiple incorporation.

3.2 BiPy-L modified G-quadruplexes

In an initial design, several sequences known to adopt unimolecular DNA G-quadruplexes - derived from the human telomeric region (htel), the promoter region of the Myc oncogene (pu22), and the Tetrahymena telomeric region (ttel) - were site-specifically modified with bipyridine ligandosides (**BiPy-L1/-L2**). Positions for nucleotide substitution were selected based on structural analyses of the native sequences and insights from prior studies on monodentate ligand incorporation. Nucleotides within loop regions or guanines in terminal tetrads were replaced with **BiPy-L**. Due to the absence of adjacent loops in parallel quadruplex topologies, **BiPy-L** was positioned before and after the first and last guanine runs, respectively, while the second loop was extended by up to two bases to enhance structural flexibility. The aim was to minimize disruption to the native structure while optimizing ligand placement for metal complexation, enabling both metal-induced thermal stabilization and stimuli-responsive control over G-quadruplex topology. The modified sequences were analysed via thermal differential spectra (TDS), UV-Vis melting

experiments, and circular dichroism (CD) spectroscopy after annealing in the presence or absence of divalent metal cations and buffers containing either K^+ or Na^+. The sequences will be discussed individually based on their parental sequences to highlight differences in G-quadruplex formation stability and the ability of the incorporated **BiPy-L** ligandosides to form metal complexes.

3.2.1 Telomeric sequences

3.2.1.1 Human telomeric sequence (htel)

Table 1. DNA sequence of modified htel22 G-quadruplexes. Positioning of the **BiPy-L1** and **-L2** ligands is indicated with **L**.

Name	Sequence (5'-3')
htel22[a)]	A GGG TTA GGG TTA GGG TTA GGG
htel22-L2a	A GGG **L**TA GGG TTA GGG TT**L** GGG
htel22-L2b	A GG**L** TTA GGG TTA GG**L** TTA GGG

a) natural G-quadruplex sequence

The human telomeric sequence $(TTAGGG)_n$ (htel) is critical for maintaining chromosomal stability, as it forms protective caps at chromosome ends to prevent degradation and fusion. These guanine-rich repeats are prone to forming G-quadruplex structures, which are four-stranded DNA motifs stabilized by stacked G-tetrads and monovalent cations like K^+. The dynamic interplay between telomeric G-quadruplexes and cellular machinery regulates telomere length, a key factor in cellular aging and cancer progression. The structural diversity of telomeric G-quadruplexes influences their recognition by helicases, ligands, and regulatory proteins, directly impacting telomere dynamics and cellular aging. This polymorphic behaviour also complicates therapeutic targeting, as small-molecule ligands must selectively stabilize specific conformations to inhibit telomerase activity or induce telomere dysfunction in cancer cells.[211] This polymorphic property of htel G-quadruplexes makes it a prime target for the implementation of artificial ligandosides in order to stabilize and control certain topologies and ideally switch dynamically between them. The parental sequence htel22 can adopt either a hybrid-1 topology in K^+ containing buffer or an antiparallel topology in Na^+ containing buffer. The **BiPy-L** modifications were implemented based on the hybrid-1 topology in order to position the ligands in close proximity to each other to either sit within the loop region or replace a guanine tetrade. After successful synthesis of all strands and characterisation by analytical HPLC and ESI-MS the oligonucleotides were annealed according to the standard protocol by heating to 90°C and

cooling down to 4°C with a cooling rate of 0.5°C/min to ensure proper folding. As buffer 4-(2-hydroxyethyl)-1-piperazineethanesulfonic acid (HEPES) set to pH 7.1 with LiOH was chosen as this does not interfere with metal complexation through chelation and is usable within a biological setting as will be important in further chapters. This allowed the addition of either KCl or NaCl as monovalent metal cations for the stabilisation of the G-quadruplexes, apart from the addition of a divalent metal cation such as Cu^{2+}, Ni^{2+} or Zn^{2+}.

Htel22-L2a

The TDS spectra of both **BiPy-L1** and **-L2** modified **htel22-L2a** and sequences are indicative of successful formation of G-quadruplexes as can been seen by the typical minimum showing a characteristic minimum at 295 nm and maximum at 273 nm in their respective spectra (**Figure 25**).

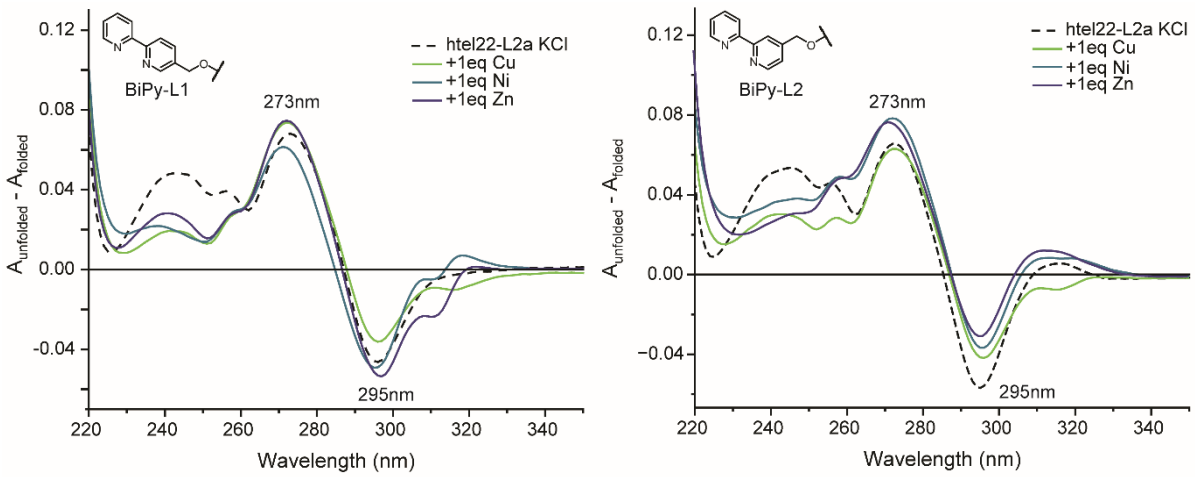

Figure 25. TDS spectra of **htel22-L2a** G-quadruplexes bearing either **BiPy-L1** or **-L2** modification. The oligonucleotide was annealed in absence or presence of M^{2+} (M = Cu, Ni, Zn) in 10 mM HEPES buffer (pH 7.1) and 100 mM KCl. In both cases successful G-quadruplex formation could be observed through the presence of the characteristic minimum at 295 nm and maximum at 270 nm. Minor spectral changes could be observed in presence of a stabilising metal cation M^{2+}.

This held true for sample in both Na^+ or K^+ containing buffer and in presence of M^{2+} (M = Cu, Ni, Zn) as metal cation for the **BiPy**-metal complex formation. Additionally, an absorption band at approx. 315 nm can be seen in presence of any M^{2+} which does not stem from the natural nucleobases or the single bipyridine units (**Figure 25**, **Figure 26**).

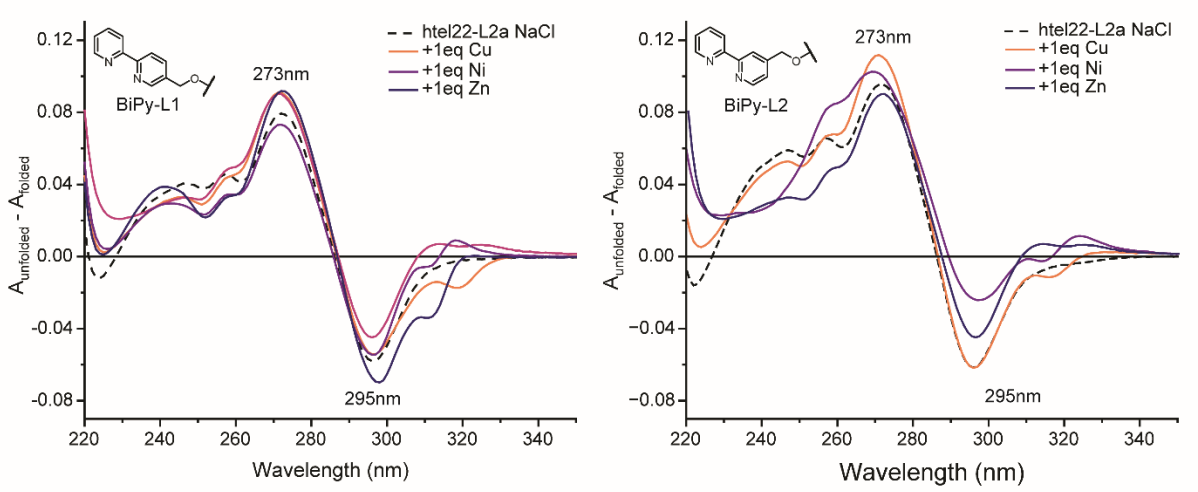

Figure 26. TDS spectra of **htel22-L2a** G-quadruplexes bearing either **BiPy-L1** or **-L2** modification. The oligonucleotide was annealed in absence or presence of M^{2+} (M = Cu, Ni, Zn) in 10 mM HEPES buffer (pH 7.1) and 100 mM NaCl. In both cases successful G-quadruplex formation could be observed through the presence of the characteristic minimum at 295 nm and maximum at 270nm. Minor spectral changes could be observed in presence of a stabilising metal cation M^{2+}.

This additional band originates from the redshift of the incorporated bipyridine ligands when forming a corresponding metal chelate complex as has been previously reported in literature (**Figure 27**).[212]

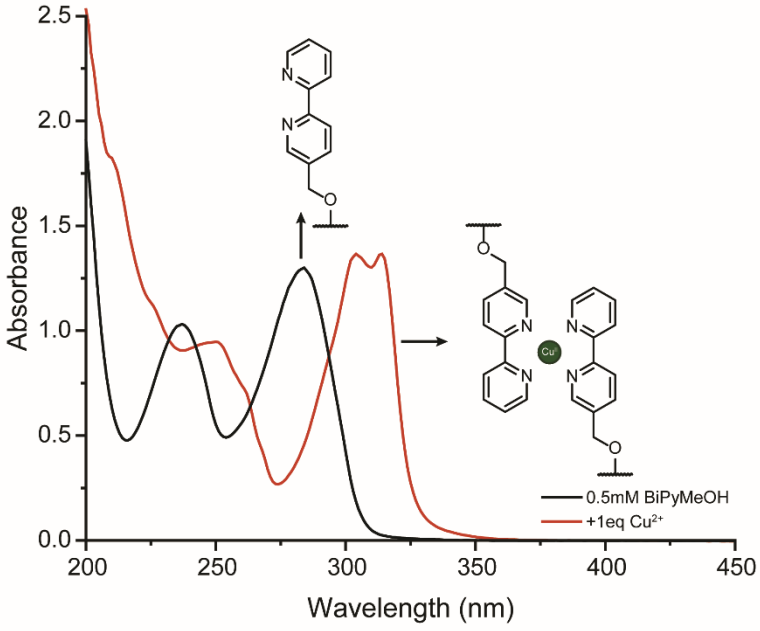

Figure 27. UV-Vis spectrum of the isolated bipyridine ligand ([2,2'-bipyridin]-5-ylmethanol) showcasing the redshift by 30nm in absorption upon complexation of Cu^{2+}. This behaviour renders it possible to detect successful complex formation within the modified G-quadruplex, visible as new absorption band in UV-Vis spectra or novel CD band.

UV-Vis melting curve analysis showed that all system in K^+ exhibited strong thermal stability with melting temperatures (T_m) between 68 – 70°C in absence of any M^{2+} (M = Cu, Ni, Zn), showing even greater stability than then unmodified parental sequence at T_m = 64°C. Additional favourable interactions of the bipyridine units with either the G-tetrads or surrounding nucleobases could explain this improved stability. This further increased to T_m = 80 – 83°C in presence of M^{2+}, showcasing a strong impact of the formed metal complex on the overall thermal stability. **BiPy-L2** modified sequences showed an additional melting point at 32°C possibly stemming from either a secondary event or a mixture of different systems. The system in Na^+ containing buffer showed expectedly lower melting points across all conditions with T_m = 40 – 53°C without M^{2+} and exhibiting much lower stabilisation by the metal complex to T_m = 62°C for the **BiPy-L1** modified sequence. Interestingly the **BiPy-L2** modified sequence could not be stabilised by addition of M^{2+} and showed even a destabilisation in the case of Zn^{2+} was added resulting in T_m = 37°C (**Figure 28**).

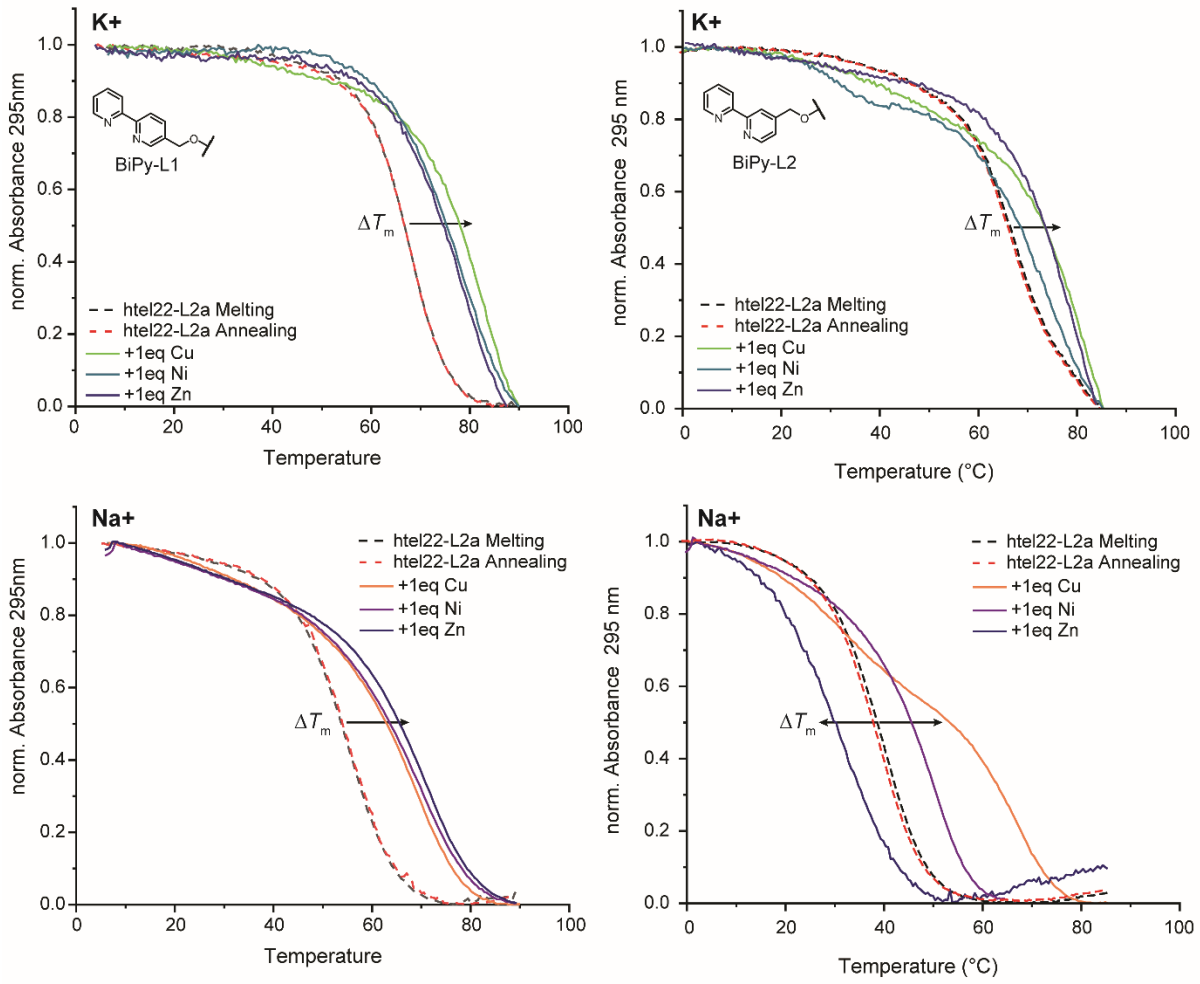

Figure 28. UV-Vis melting curve analysis of **htel22-L2a** bearing either **BiPy-L1** or **-L2** modification. Higher melting temperatures (T_m) were observed for systems in K^+ containing buffer. No hysteresis could be observed indicated by the exact overlap between recorded melting and annealing spectra

(dotted lines). In all cases a thermal stabilisation by presence of a divalent metal cation M^{2+} (M = Cu, Ni, Zn) could be observed, with the exception of **BiPy-L2** modified **htel22-L2a** in Na^{+} containing buffer, where Zn^{2+} lead to a significant destabilisation of the G-quadruplex. Absorption recorded at 295nm showing expected hypochromic shift of G-quadruplex unfolding.

The topology of the **htel22-L2a** systems was next determined through CD spectroscopy. **BiPy-L1** modified **htel22-L2a** showed a hybrid topology in K^{+} with the characteristic maximum at 295 nm and a minimum at 240 nm. However, when annealed in presence of M^{2+} (M = Cu, Ni, Zn) the spectrum completely changed and showed an antiparallel topology with maxima at 290 and 240 nm and a minimum at 260 nm. This was surprising as this topology was previously only achievable in Na^{+} containing buffer of the wild type G-quadruplex (**Figure 29**).

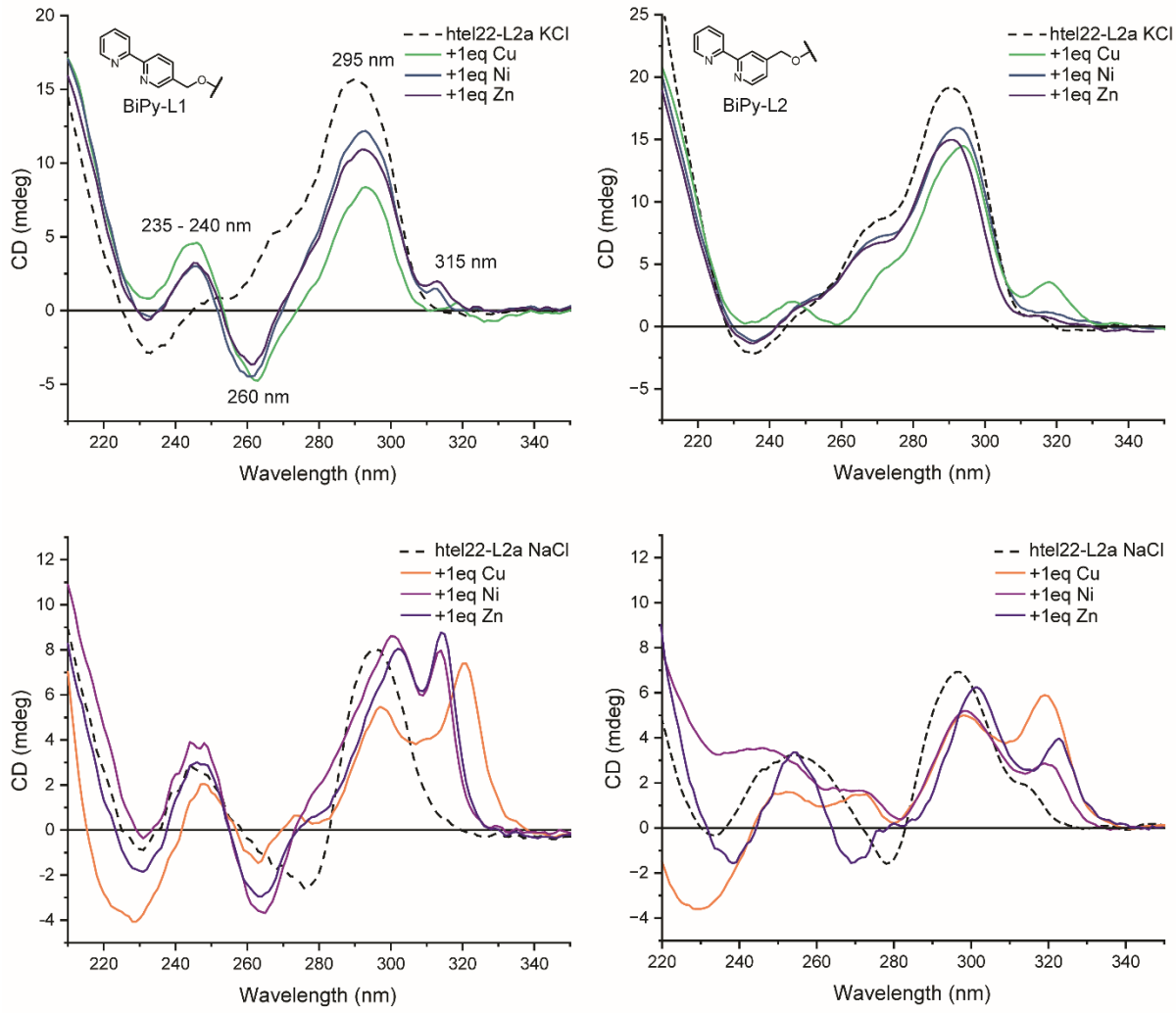

Figure 29. CD spectra of **htel22-L2a** bearing either **BiPy-L1** or **-L2** modification. In K+ containing buffer both version adopt a hybrid topology with the characteristic signature. Refolding was only observed for the **BiPy-L1** modified G-quadruplex upon addition of M^{2+} (M = Cu, Ni, Zn), adopting an

antiparallel topology. No clear topology could be identified for either system in Na^+ containing buffer although metal complexation was successful indicated by the novel CD band at 315 nm.

This demonstrated that the positioning of the ligandosides lead to at least a partial refolding of the structure likely driven by the metal complex formation. The formation of the complex was once again confirmed as an CD band at 315 nm could be observed which stems from the bipyridine-M^{2+} complex sitting within the chiral environment of the right-handed DNA G-quadruplex. In Na^+ the system adopts an antiparallel topology yet the minimum is shifted to 280 nm and shows a shoulder band at 260 nm. No large refolding could be observed through the addition of M^{2+}, only a small backshift of the minimum from 280 to 260nm. Additionally, the bipyridine-M^{2+} absorption band is strongly pronounced. We suspect that although a G-quadruplex might be formed under these conditions it is relatively unstable and distorted in its geometry thus leading to an unclear spectrum. For **BiPy-L2** modified **htel22-L2a** a completely different picture can be observed. Although the CD spectra in K^+ show a maximum at 290nm and a minimum at 240nm, a lack of a pronounced second maximum at 240 nm for an antiparallel topology is missing after the addition of M^{2+} indicating that no refolding of the G-quadruplex occured. Slight spectral changes could only be observed for the Cu^{2+}-complexed DNA, yet not clearly interpretable. The spectra in Na^+ look similar to the **BiPy-L1** system although here antiparallel characteristics are stronger pronounced with an identifiable albeit slightly shifted second maximum at 250nm. Similarly, the addition of M^{2+} does not induce a topological change and even completely disturbs a G-quadruplex formation when 2eq or more of M^{2+} are used (see SI).

Htel22-L2b

For the next iteration of htel modifications, the ligandosides were not placed within the loops but replaced two guanines that are involved in the formation of the upper G-tetrad when read from the 5'-end. The goal was to successfully form a G-quadruplex albeit a large disturbance had been introduced to the system. We chose diagonally sitting guanines to ensure optimal placement of the two ligandosides and facilitate complex formation. While for both **BiPy-L1** and **-L2** modified **htel22-L2b** sequences the TDS spectra again showed G-quadruplex characteristics in presence of either K^+ or Na^+ and M^{2+}, the thermal stabilities were drastically different. While both versions where stable in K^+ with melting points around T_m = 42°C which further increases with Cu^{2+} up to 72°C. All samples prepared in Na^+ containing buffer showed very low thermal stability with T_m values around 25°C and no stabilising effect of the added M^{2+} (see SI). The CD spectra again revealed a clearer picture for the **BiPy-L1** modified **htel22-L2b** where in all conditions a clear antiparallel topology of the folded G-quadruplex could be identified. The bipyridine-M^{2+} band is more prominent as

compared to **htel22-L2a** and shows significant differences depending on the employed metal. **BiPy-L2** modified **htel22-L2b** in K^+ showed no singular species as the characteristics of a parallel topology, with a maximum at 260nm and a minimum at 240nm, was accompanied by a large shoulder band at 290nm. Presence of M^{2+} only changes the relative intensities of these peaks which seem to indicate a shift to a hybrid topology, yet it remains difficult to entangle the spectrum. In Na^+ no G-quadruplex could be formed as there was a lack of an identifiable pattern within the spectrum. The other divalent metal cations were not tested for this htel22-L2b version akin to the previously presented argumentation for **htel22-L2a** (**Figure 30**).

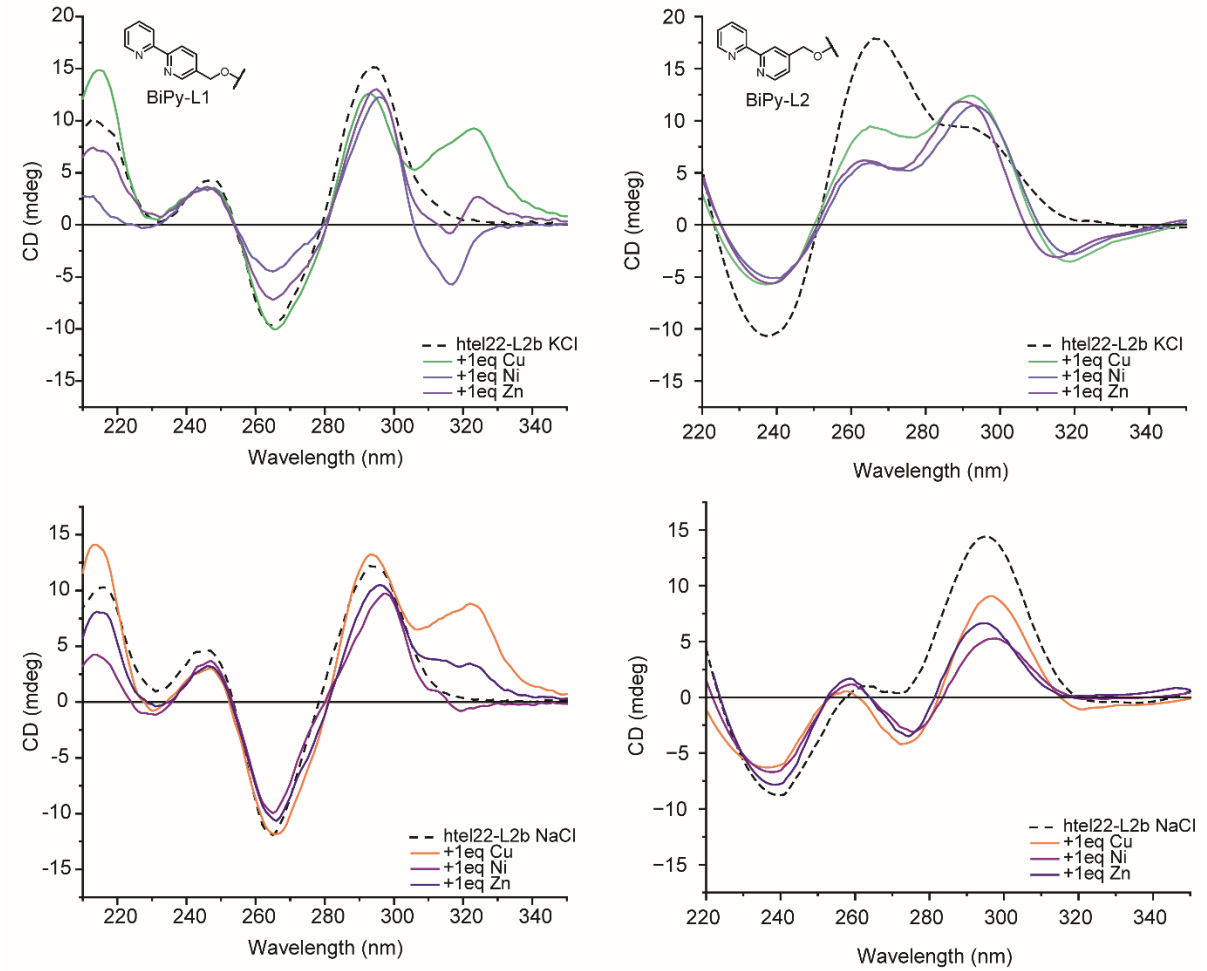

Figure 30. CD spectra of **htel22-L2b** bearing either **BiPy-L1** or **-L2** modification. **BiPy-L1** modified **htel22-L2b** adopts in both K^+ and Na^+ containing buffer a clear antiparallel topology and in absence and presence of stabilising M^{2+} (M = Cu, Ni, Zn). Additional CD band for the successful complex formation could be observed at 315 nm. **BiPy-L2** modified **htel22-L2b** adopts a mixed topology in K^+ buffer in absence and presence of stabilising M^{2+} (M = Cu, Ni, Zn). No clear G-quadruplex topology could be identified in Na^+ containing buffer.

3.2.1.2 Tetrahymena telomeric sequence (ttel)

Table 2. DNA sequence of modified ttel24 G-quadruplexes. Positioning of the **BiPy-L1** and **-L2** ligands is indicated with **L**.

Name	Sequence (5′-3′)
ttel24[a)]	TTG GGG TTG GGG TTG GGG TTG GGG
ttel24-L2a	TTG GG**L** TTG GGG TTG GG**L** TTG GGG
ttel24-L2b	TTG GGG TT**L** GGG TTG GGG TT**L** GGG

Ttel24-L2a

As last comparison for the differences between sequences modified with either **BiPy-L1** or **-L2**, the telomeric sequence of tetrahymena, an unicellular eukaryote, was chosen.[213] This sequence differs to that found in humans as no adenine (A) is present and the G-quadruplex forming sequence is 24 nucleotides (nt) long. As for the previous two sequences, both **BiPy-L1** and **-L2** modified **ttel24-L2a** showed TDS spectra that confirmed the formation of a G-quadruplex in a first instance with the characteristic signature (see SI). The samples prepared in K^+ exhibited a stronger thermal stability with $T_m \leq 73°C$ without any divalent metal cation added. The addition of M^{2+} then increased the melting points for both **ttel24-L2a** versions up to 85°C. Na^+ was less able to stabilise these structures and showed over melting temperatures of only up to $T_m \leq 64°C$. Although the TDS spectra of all oligonucleotides suggest that a G-quadruplex had been formed, their topologies differed as seen by the corresponding CD spectra (**Figure 31**). While the **BiPy-L1** modified **ttel24-L2a** folds into a mixture of hybrid and parallel topologies, it is capable of refolding into a predominantly hybrid topology when in presence of either Cu^{2+}, Ni^{2+} or Zn^{2+}. The **BiPy-L2** modification does not allow for a refolding as the G-quadruplex adapts a hybrid fold in absence of any M^{2+} and only changes its signature slightly when annealed in presence of either metal. In Na^+ containing buffer a clear topology could not be identified for this system although a change can be induced via the addition of M^{2+}, though not clearly assignable to an antiparallel fold. This is again different to the **BiPy-L1** modified system where initially no G-quadruplex structure could be observed. The stabilisation by Na^+ is likely too small to effectively hold the system together, as indicated by the TDS spectra beforehand (see SI). Addition of a source of M^{2+} facilitates a correct folding into an antiparallel G-quadruplex (**Figure 31**). To check if the placement of the individual modification impacted the topology and capability of refolding of **ttel24-L2a**, we designed a second iteration of the system.

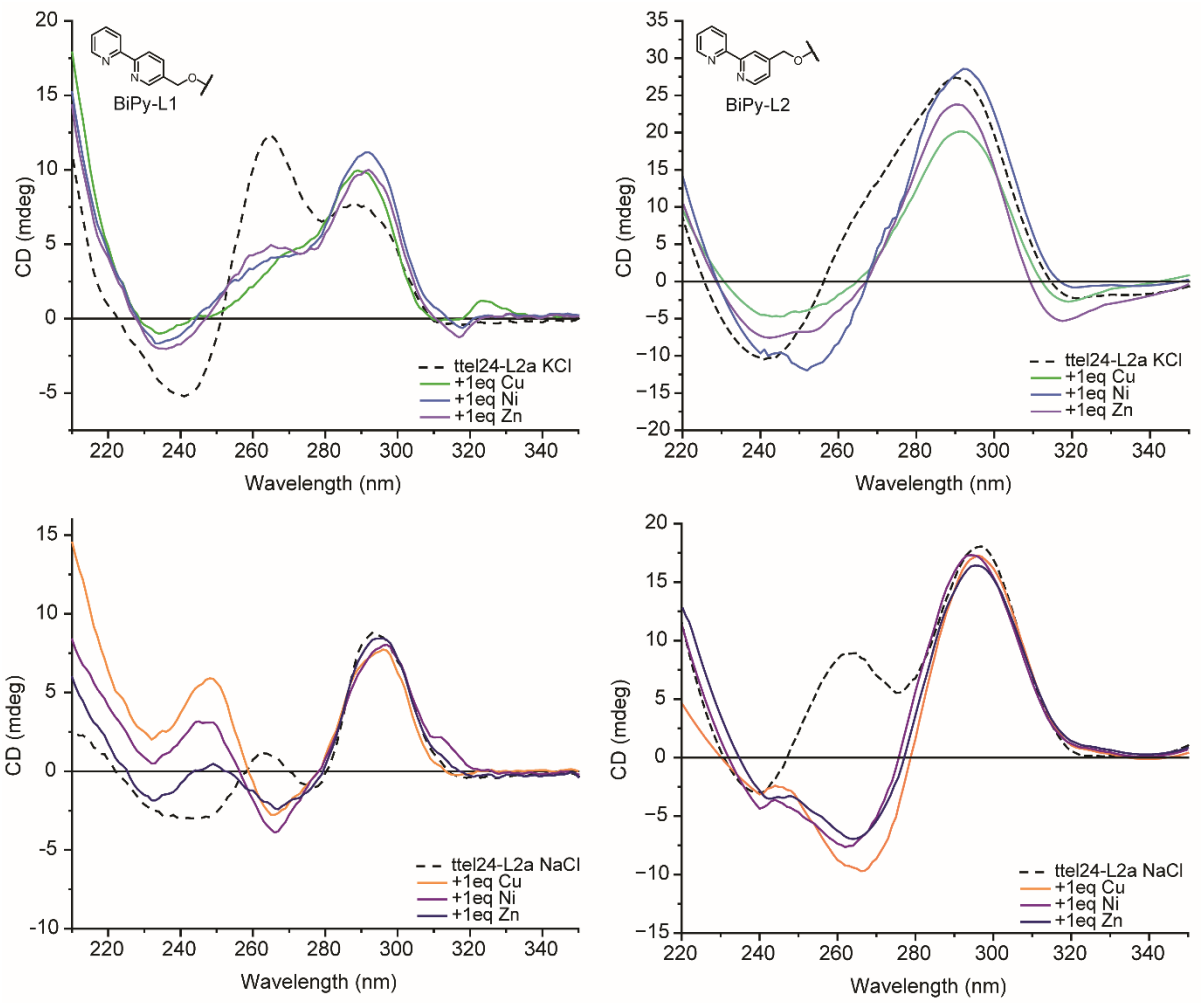

Figure 31. CD spectra of **ttel24-L2a** bearing either **BiPy-L1** or **-L2** modification. In K^+ containing buffer the **BiPy-L1** modified system adopts a mixed topology but refold into a hybrid form when in presence of a divalent metal cation M^{2+} (M = Cu, Ni, Zn). In presence of Na+, only the metal stabilised variants adopt a clearly identifiable antiparallel topology. **BiPy-L2** modified ttel24-L2a does not fold into a distinguishable G-quadruplex topology under neither condition.

Ttel24-L2b

After the unsuccessful employment of the **BiPy-L2** ligandoside and the lack of either defined G-quadruplex topologies or the formation of other secondary DNA structures with it, we decided to not further implement this bipyridine modification in the upcoming sequences of this work. An additional factor for this decision was the aforementioned low yield in synthesising this **BiPy-L2** ligandoside. All sequences discussed from here on are exclusively modified with **BiPy-L1**.

As the first version of ttel modification showed a mixture of topologies present in K^+ with some potential to fold into a defined singular topology with the addition of a M^{2+} source, it was of interest to test another position for the implementation of ligandosides at positons #9 and #21 within the sequence. The goal here was, similarly to **htel22-L2a**, to achieve a

refolding into an antiparallel topology upon metal complexation as has been shown by Engelhard.[200] Although TDS spectra and melting analysis confirmed that **ttel24-L2b** did form a stable G-quadruplex with T_m = 69°C, its CD signature in K^+ again showed a mixture of species as for the previous iteration. Notably the relative intensities of the two peaks at 260 and 290nm where inverted as compared to **ttel24-L2a**. Addition of M^{2+} lead to a stabilisation of the system overall yet failed to achieved the desired outcome, only slightly changing the signature of the G-quadruplex in the CD. In Na^+ again misfolding could be observed if the G-quadruplex was not stabilised by the presence of M^{2+} upon which it folded into an antiparallel topology for both Cu^{2+} and Ni^{2+}. Interestingly the Zn2+ stabilised species showed a more hybrid-type topology with the respective minima and maxima in the CD. This could originate from the slightly larger ionic radius of Zn^{2+} (r = 0.6 Å) and its lower ligand field stabilisation energy compared to the other two metals. With the lower stabilisation by Na^+ it could lead to a different or only partially correct folding of the G-quadruplex. (**Figure 32**).

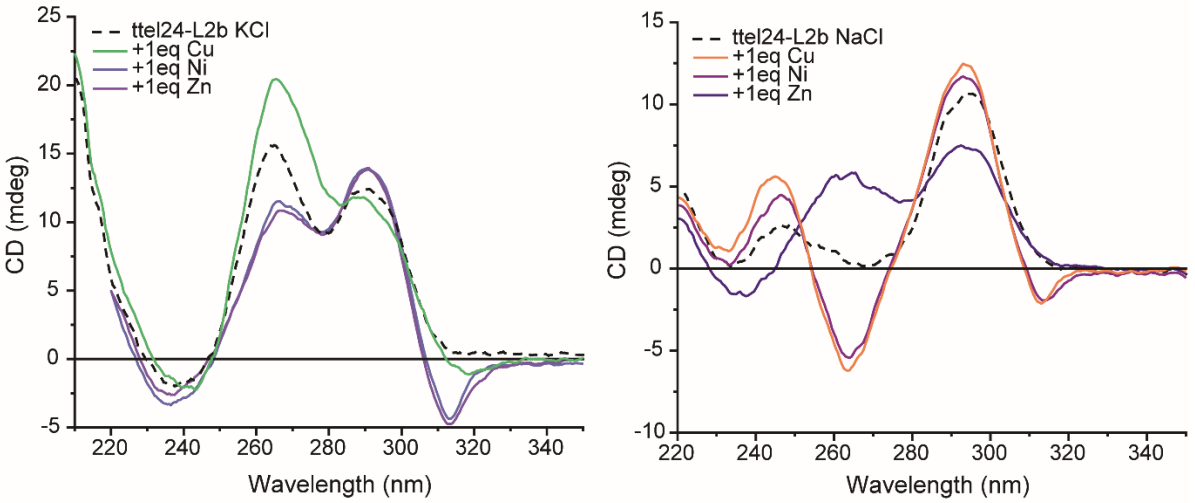

Figure 32. CD spectra of **ttel24-L2b** bearing the **BiPy-L1** modification. In K^+ containing buffer the system adopts a mixed topology similar to **ttel24-L2a**. No refolding into a hybrid topology could be observed when in presence of a divalent metal cation M^{2+} (M = Cu, Ni, Zn). Slight spectral changes between the different metals could be observed. In presence of Na^+, only the Ni^{2+} and Zn^{2+} stabilised variants adopt a clearly identifiable antiparallel topology.

Overall, the telomeric systems showed a diverse array of results highly dependent on the incorporated modification, the choice of electrolyte between K^+ or Na^+ and most importantly the presence of absence of stabilising M^{2+} cations which in a single case, for **htel22-L2a**, lead to a refolding of the G-quadruplex between to clearly identifiable topologies. The only unexplored topology was parallel, which neither of the system could fold into. For this we chose to modify a prominent G-quadruplex sequence found in the promoter region of the MYC oncogene, pu24.[214]

3.2.2 Promoter region sequences

As G-quadruplexes are not only found in the telomeric regions of chromosomes in various living eukaryotes but are involved in various different processes across the entire genome, we chose to expand the selection of parental sequences into which the bipyridine modifications were inserted. Particularly interesting are sequences found in the promoter regions of oncogenes as they are involved in the regulation of cancer disease. The MYC oncogene is dysregulated in >50% of human cancers and its overexpression correlates with aggressive disease progression.[82] Hence targeting G-quadruplex forming sequences in its promoter region is of such high interest. These sequences are of various lengths and are termed "putative" sequences (pu) and indicated by the number of nucleotides involved and all exclusively form parallel G-quadruplexes.

Table 3. DNA sequence of modified pu22 G-quadruplexes. Positioning of the **BiPy-L1** ligand is indicated with **L**. Additional modifications to the parental sequence are underscored.

Name	Sequence (5'-3')
pu22[a)]	TGA GGG TGG GTA GGG TGG GTA A
pu22-L2a	TGA GGG T**L**GG GTA GGG T**L**GG GTA A
pu22-L2b	TG**L** GGG T<u>T</u>GG GTA GGG TGG G**L**A A
pu22-L2c	TG**L** GGG T<u>TA</u>GG GTA GGG TGG G**L**A A

Putatitve sequence 22 (pu22-L2a)

The challenge with G-quadruplex sequences that naturally fold into parallel topologies was that in comparison to hybrid and antiparallel, no neighbouring loops exist on top of one of the terminal G-quartets into which the ligandosides could be placed. All loops, mostly 1-2 nt long, adopt the propeller-type and point away from the guanine core. Additionally, parallel G-quadruplexes tend to be highly thermally stable with melting points of up to 80°C for the pu22 sequence. In a first iteration of **BiPy-L1** modified **pu22-L2a** we sought out to place the modifications before guanine runs so that they possibly can form a metal complex on top of the upper G-tetrad or potentially engage in π-stacking interactions without any M^{2+} present for complex formation. The goal here was again to not only stabilise the system but potentially alter its topology. The TDS spectra in both K^+ and Na^+ showed the expected G-quadruplex signature albeit less pronounced on the minimum at 290nm. The stability of **pu22-L2a** in K^+ was remarkable with T_m = 69°C and further increasing in presence of M^{2+}, whereas Na^+ was not able to stabilise the system (see SI). The CD spectra revealed that no clear topology could be formed in Na^+ even in presence of M^{2+} as stabilising cation. In K^+ however the G-quadruplex formed into a predominantly parallel topology which is slightly

disturbed upon addition of M^{2+} and further changes with nature of the added metal. Successful formation of the complex could be observed with a weak band at 315nm yet no clear refolding took place. We hypothesise that the bipyridine positioning is suboptimal and the complexation can only take place with a higher M^{2+} concentration. This potentially exerts some sort of strain on the **pu22-L2a** system which leads to an undefined state with a possible mixture of topologies or partially unfolded structures (**Figure 33**).

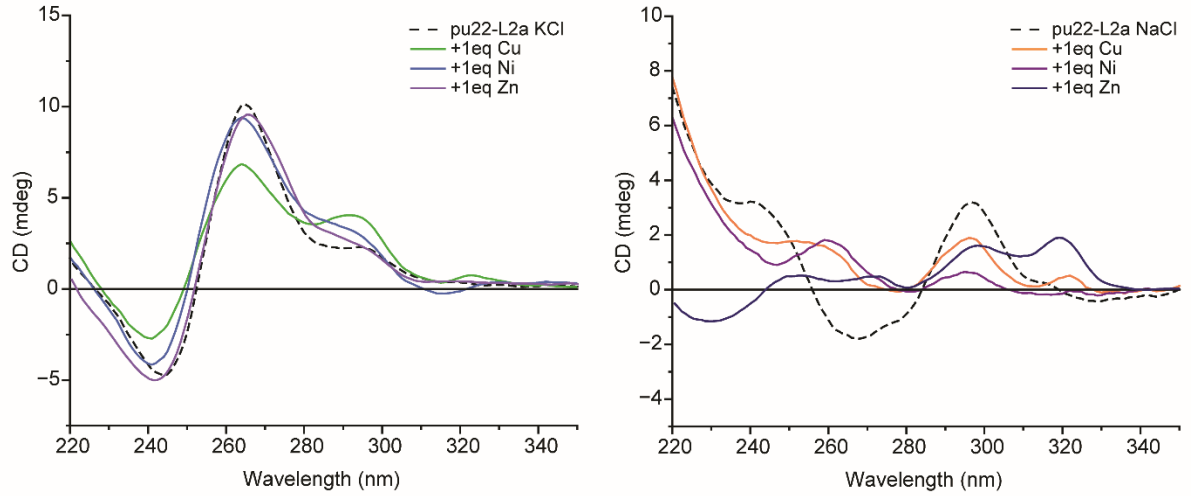

Figure 33. CD spectra of **pu22-L2a**. In K^+ containing buffer the system adopts a parallel topology. Binding of Cu^{2+} leads to increase in the shoulderband at 295 nm, indicating some structural changes of the G-quadruplex. In presence of Na^+ no G-quadruplex topology could be identified although metal complexation was confirmed by the additional bands at 315 nm.

Pu22-L2b and -L2c

For the second iteration of pu22 modifications (**pu22-L2b**) we took inspiration from the work of Klaus Weisz in characterisation of an originally parallel G-quadruplex which was able to adopt a unique hybrid topology due to Watson-Crick-Franklin basepairing of extended 5' and 3' ends (see figure).[215] Instead of implementing additional nucleotides we envisioned the placement of the **BiPy-L1** modification within the original short 5' and 3' overhangs with the goal of dynamically switching between topologies through metal coordination. As the G-quadruplex needs additional flexibility to perform this change, we elongated the first loop with either a single T (**pu22-L2b**) or TA (**pu22-L2c**). Making this loop any longer bore risks of altering the initial parallel topology and leading to a mixture of species. TDS spectra of both versions gave a first indication of a successful G-quadruplex formation. As expected for parallel G-quadruplexes, their thermal stabilities were high with melting temperatures at 80°C even without the stabilising effect of a divalent metal cation. In presence of Cu^{2+} seemingly two melting events can be observed with a slight change in absorbance at 37°C and the second event occurring above 85°C. The earlier melting event is difficult to

rationalise as the metal complex is expected to be thermally strong and should not fall apart at such low temperatures.

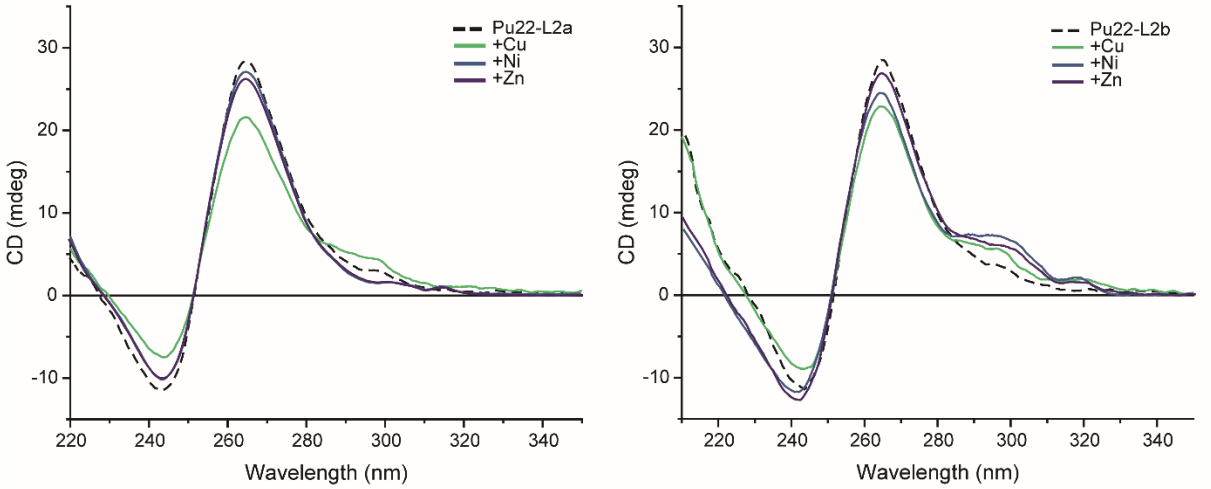

Figure 34. CD spectra of **pu22-L2b** and **-L2c**. In K^+ containing buffer the system adopts a parallel topology. Binding of M^{2+} leads to only minor spectral changes for **pu22-L2b** while a larger increase in the shoulder band at 295 nm for **pu22-L2c** could be observed, indicating some structural changes of the G-quadruplex.

A potential explanation is that a structural reorganisation takes places which impacts the absorbance of the G-quadruplex. Looking at the CD signatures, both **pu22-L2b** and **-L2c** adopt a parallel topology with a strong maximum at 260nm and a minimum at 240nm. The previously observed CD band at 315nm indicative of the successful formation of the bipyridine-metal complex was not present. A change in the spectra was however observable when annealed in the presence of M^{2+} with weak absorption bands at 310 and 325nm which indicate complex formation (**Figure 34**). The binding and thermal stabilisation of the divalent metal cations was confirmed by native ESI-MS measurements as well as thermal denaturation followed by UV-Vis (**Figure 35**). The goal of switching the parallel topology into a hybrid-3 topology was however unsuccessful. The flexibility of the ligandosides and the 5' and 3'-ends likely allows the two bipyridine units to come close enough together on the side of the parallel G-quadruplex and therefore not be capable of inducing a refolding. For a next iteration the 5' and 3' overhangs could be further elongated, similar to the example of Weisz, rendering the formation of Watson-Crick-Franklin base pairs as a secondary driving force for refolding, apart from the bipyridine complex formation.[215] It will be important to strike a balance for the additional base pairs as the G-quadruplex should not adopt the hybrid-3 topology without the addition of a M^{2+} source.

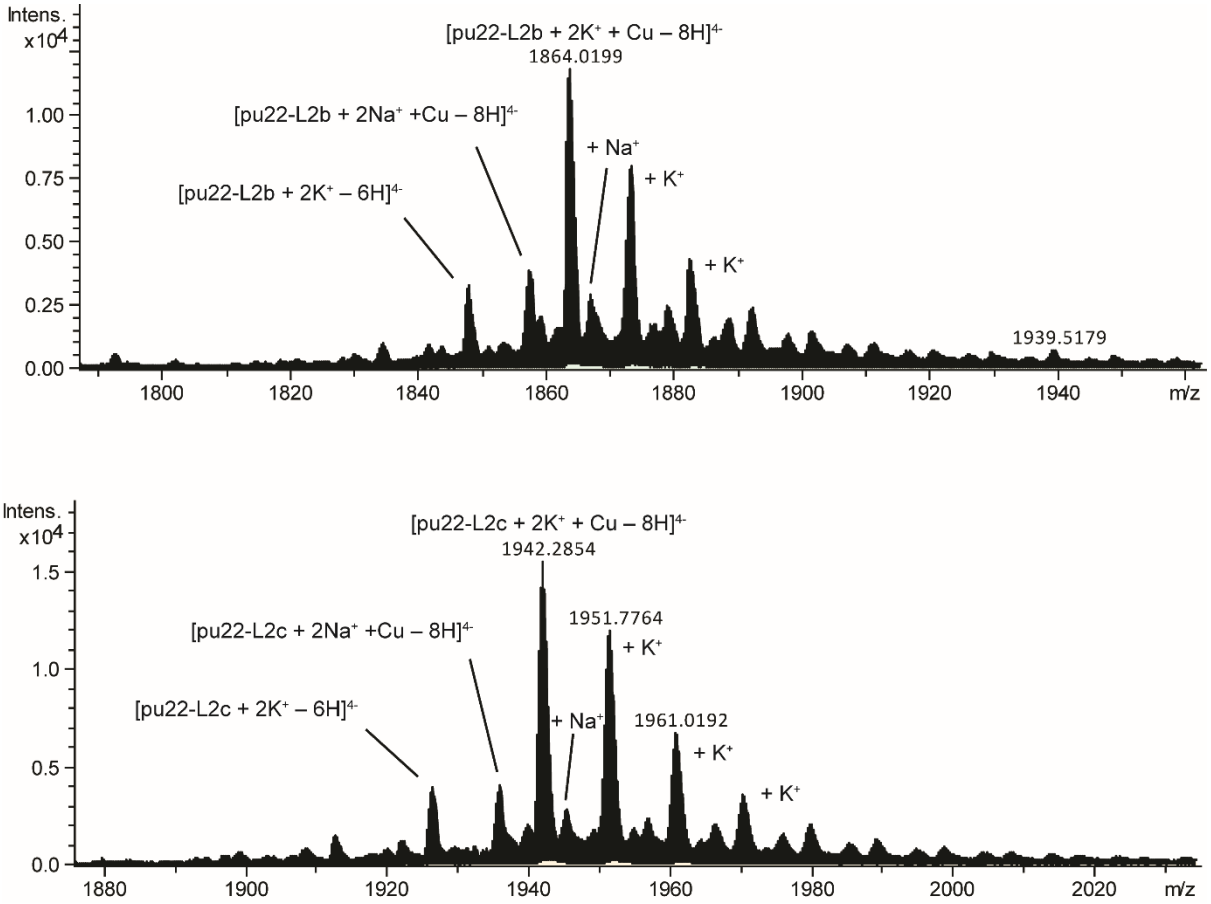

Figure 35. Native ESI-MS of **pu22-L2b** and **-L2c** in presence of Cu^{2+}. Both K^+ and Na^+ species are formed. Conditions: 12.5 µM DNA, 15 µM CuSO4, 0.5 mM KCl, 50 mM TMAA pH 7.1, H2O:ACN, 1:1.

3.3 MD Simulation

Out of the 6 synthesized sequences only those bearing the **BiPy-L1** formed G-quadruplexes with well-defined topologies as analysed by CD spectroscopy. Additionally, a single example of defined topological switching between defined states was found in **htel22-L2a**, being able to adopt either a hybrid topology in K^+ and switchting to antiparallel when either Cu^{2+}, Ni^{2+}, or Zn^{2+} are added into the mixture. To take a deeper look into this system and the closely related **htel22-L2b** system we prepared molecular dynamics simulations of the corresponding structures. We were particularly interested in comparing the two possible hybrid topologies (hybrid-1 and hybrid-2) which could be adopted by **htel22-L2a** as these cannot be differentiated by CD spectroscopy. The MD simulations enable the investigation of the time-dependent conformational change of the G-quadruplexes at hand, giving insight in how the systems may behave and adopt and compare stabilities in the form of total energies. In classical MD simulations a force field which contains all information about bonded and non-bonded interactions between individual atoms. The standard force field for

nucleic acids is AMBER parmbsc0 which fittingly not only describes double stranded DNA but also other secondary structures such as G-quadruplexes.[216,217] Included in this force field are only the standard bonds and structures of the 4 nucleotides A, G, T and C which necessitates the implementation of the bipyridine modification **BiPy-L1** into this by parametrisation of the individual atom charges, bond lengths, force constants, angles and dihedrals and torsions. This parametrisation has to be performed for the individual **BiPy-L1** ligandoside as well as the formed metal-complex as a DFT-level calculation. In summary, geometry-optimized structures of ligand **BiPy-L1** and the $M^{2+}(L2)_4$ complex were employed to derive structural parameters, including bond lengths, angles, and torsions. Atom-specific point charges were calculated using restricted electrostatic potential (RESP) fitting methods.[216,218] Force constants were either adopted from analogous parameters in the AMBER parmbsc0 force field or approximated based on literature values for Cu^{2+}-related interactions.[219] This adapted force field was subsequently applied in all molecular dynamics (MD) simulations. Notably, the inherent lability of the Cu^{2+}–N dative bonds in the $Cu^{2+}(bipyridine)_4$ motif could not be accurately modeled. Instead, these bonds were represented as inert covalent linkages. While this approach enforced a square-planar coordination geometry, it precluded dynamic sampling of dative bond dissociation or reformation events. A detailed explanation can be found in the appendix (see SI).[200]

3.3.1 Htel22

The initial models of **htel22-L2a** in absence of any M^{2+} were constructed from two NMR-derived structures, representative for the hybrid-1 and hybrid-2 topologies (PDB: 2HY9 and 2JPZ). Two nucleotides within the loops of either structure, specifically a thymine and an adenine in the respective positions #5 and #19 within the sequence were replaced by two **BiPy-L1** ligandosides. This was performed using the software Chimera 1.9X. After successful implementation these preliminary structures were imported into Gromacs, an MD simulation program, and placed within a box filled with explicit water molecules as well as potassium ions to represent the 100mM concentration used for the spectroscopic measurements beforehand. This system was then subjected to an iterative energy minimisation process until bond lengths and angles stabilised, no molecules or atoms clashed with each other and an overall equilibrium was reached. These initial structures were then subjected to a 100 ns MD production run simulation. In the hybrid-1 structure, the bipyridine in position #5 in the first loop adopted a stable position within the first 10ns and was found to interact with the upper G-tetrad of the G-quadruplex and situates itself on top of guanines G22 and G3 mainly. An additional interaction with the neighbouring thymine T5 in the loop can also be detected from the calculation (**Figure 36**).

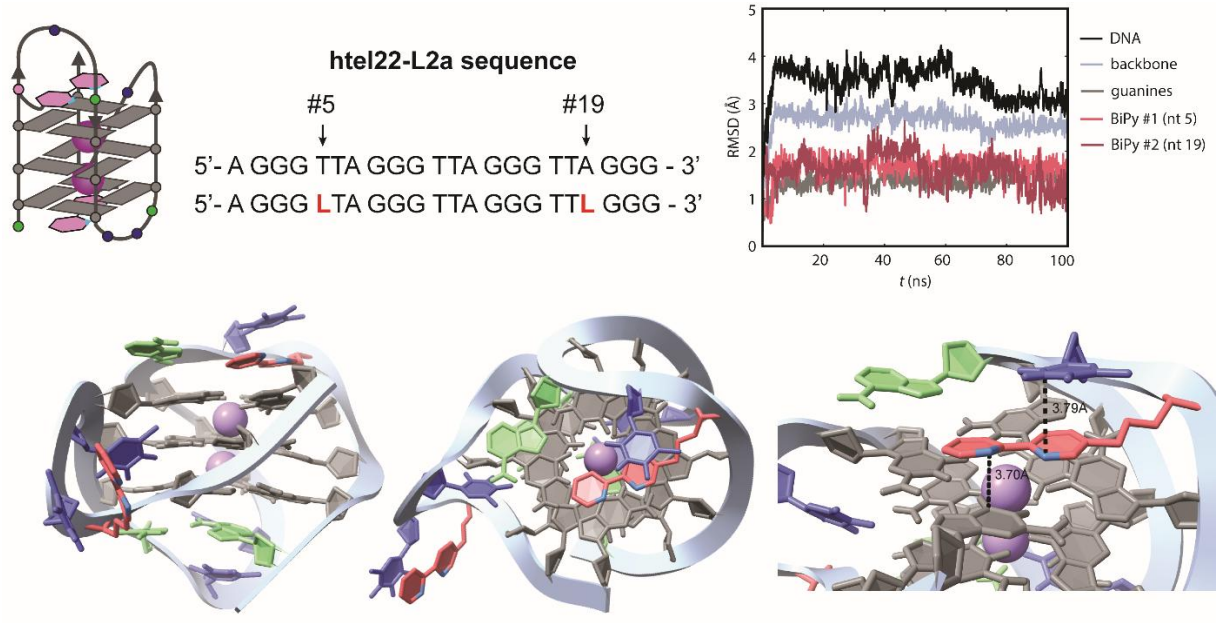

Figure 36. Molecular dynamics simulation of htel22-L2a based on starting structure of PDB: 2HY9. A) Schematic representation of **htel22-L2a** with **BiPy-L1** modification in hybrid-1 topology. The positions of the bipyridine ligands (#5, #19) are shown in the sequence. B) Representative structure determined from the 100 ns MD simulation with subsequent clustering. Side view from the 5'- and 3'-end of the structure. C) Top view. D) Zoom of the pi-stacking interaction of bipyridine at position #5 with the underlying G-tetrad. E) RMSD plot of selected structural parts (all guanines, individual bipyrdines, phosphate backbone, whole DNA construct) of the simulated structure over 100 ns. Colour coding: guanines in grey, thymines in blue, adenines in green, bipyridine in pink, potassium in violet.

The distances between the aromatic rings of this first ligandosides and G22, G3 and T5 were within the range of 3.7 – 4.2 nm, indicating potential π-π interactions between these heterocycles. The calculated RMSD values for the bipyridine in position #5 unit alone was approx. 1.8 Å without strong deviations over the whole run of 100ns. This indicates a rather stable state of this particular segment of the overall G-quadruplex structure. The second bipyridine unit, found at position #19 in the sequence, substituting an adenine from the wild type htel22 structure behaved very differently. As it is placed within a propeller loop of the structure, there exists no real possibility of interacting with the G-core and engaging in π-π interactions. This is reflected in the observed flexibility as the RMSD value fluctuates quite strongly within the first 50ns of the run before stabilising and engaging in interactions with the neighbouring thymine T18. Both the backbone and the whole DNA system showed stable RMSD values over the course of the simulation and slightly dropping towards the end of the run. The guanine core remained very unchanged throughout the 100ns without large deviations. Overall, this indicated a stable system and together with the π-interactions of the bipyridines could explain the slightly higher melting temperature in comparison to the wild type htel22 (delta T_m = +4 °C). To prevent biases in the ligand placement when constructing

the initial structure as well as confirming that the calculated structure is indeed the thermodynamically favoured one, we performed a second iteration of the MD simulation. This time the orientation of the bipyridine units was manually changed by rotation of the individual bonds (**Figure 37**).

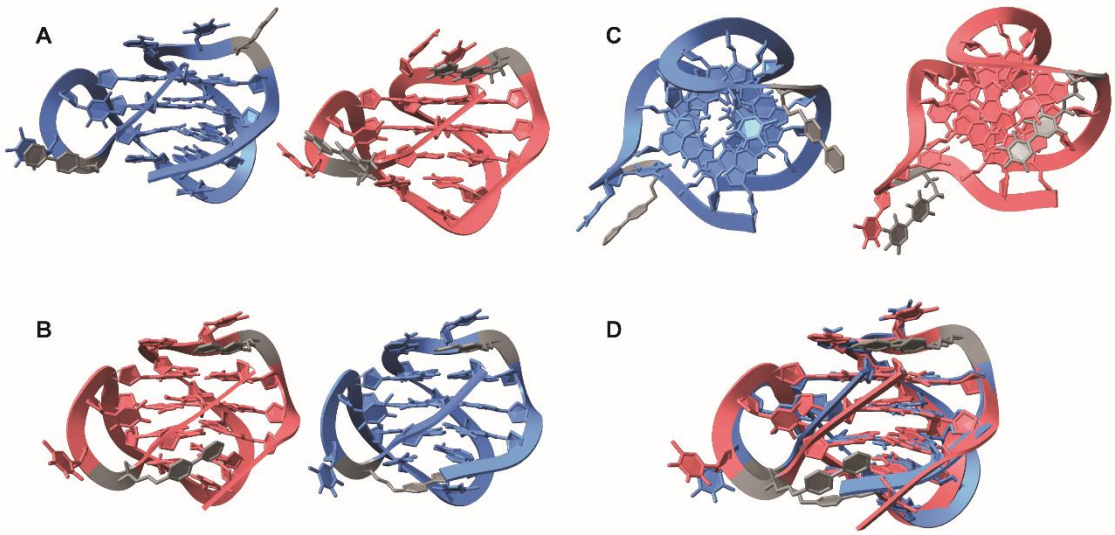

Figure 37. Molecular dynamics simulation results of **htel22-L2a** where orientation of the bipyridine units was altered after full completion of the simulation run and a secondary rerun was performed to check for arbitrary positioning of the bipyridine units. A) Side view from 5'-end of starting structure with manually altered position of bipyridine modification at nt position #5 (blue) resulting structure after rerunning simulation run over 50ns (red). B) Top view of starting structure with manually altered position of bipyridine modification at nt position #5 (blue) resulting structure after rerunning simulation run over 50ns (red). C) Side view from 5'-end of starting structure with manually altered position of bipyridine modification at nt position #20 (blue) resulting structure after rerunning simulation run over 50ns (red). D) Overlay of starting structure with manually altered position of bipyridine modifications and resulting structure after rerunning simulation run over 50ns (red).

The bipyridine unit at position #5 was twisted to point away from the G-tetrad, while bipyridine in position #19 was positioned to potentially engage in pi-interactions with the guanines of the lower tetrad. Indeed, the newly resolved structures exhibited high similarity to the originally observed conformation, with the 5'-end ligand consistently adopting a "swung-back" orientation to engage in π-π stacking interactions with the G-tetrad and the adjacent thymine T5. In contrast, the bipyridine ligand at the 3' terminus displayed an outward rotational displacement, avoiding direct stacking beneath the lower G-tetrad. While minor structural discrepancies were noted between the observed conformations, the overall architectures remained closely aligned, suggesting that the observed ligand arrangement likely approximates the thermodynamic minimum. This consistency in ligand behavior across structures underscores the inherent stability of this conformational motif in G-quadruplex-ligand interactions (**Figure 37**). For the hybrid-2 version of **htel22-L2a** G-quadruplex, a more

complex picture was encountered. The system was stable as can be seen from the obtained RMSD values for the whole 100ns simulation run. After an initial phase within the first 30ns, none of the selected components of the G-quadruplex show large structural changes (**Figure 38**).

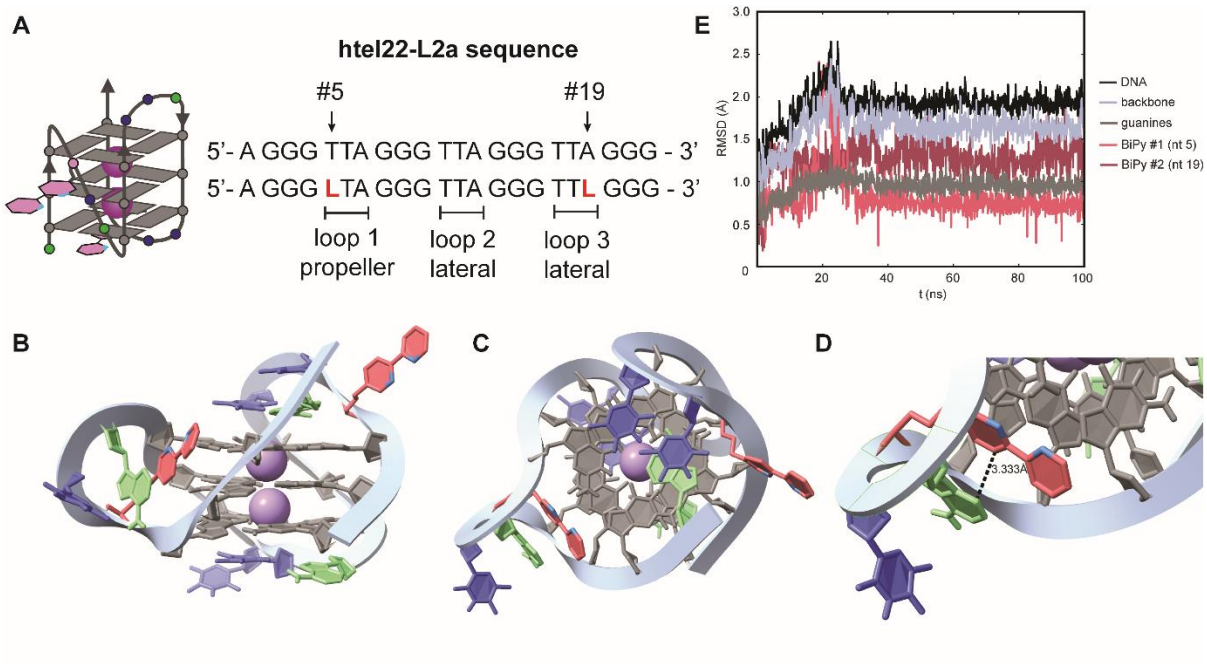

Figure 38. Molecular dynamics simulation of htel22-L2a based on PDB: 2JPZ. A) Schematic representation of **htel22-L2a** with **BiPy-L1** modification in hybrid-2 topology. The positions of the bipyridine ligands (#5, #19) are shown in the sequence. B) Representative structure determined from the 100 ns MD simulation with subsequent clustering. Side view from the 5'- and 3'-end of the structure. C) Top view. D) Zoom of the pi-stacking interaction of bipyridine at position #5 within the loop 1. E) RMSD plot of selected structural parts (all guanines, individual bipyrdines, phosphate backbone, whole DNA construct) of the simulated structure over 100 ns. Colour coding: guanines in grey, thymines in blue, adenines in green, bipyridine in pink, potassium in violet.

Again, here bipyridine at position #19 showed a higher flexibility throughout the run than the bipyridine unit in position #5 of the sequence. The orientation and placement of the two ligandosides was completely different in comparison to the hybrid-1 version. The first bipyridine, now situated in the propeller loop of the structure, is wedged between the G-core and the backbone of the loop in a perpendicular fashion. This creates a rather bulged propeller-type loop at the 5'-end as can be seen from the top-down view. This time potential π-interactions occur with the neighbouring adenine A7 as the ring-to-ring distance is 3.3 Å. The second bipyridine unit in the lateral loop does not engage in stabilising interactions with neither the neighbouring loop nucleobases nor the G-tetrad but is pointed away from the G-core. As this seemed strange initially, we again performed manual changes on the structure

by C-C or C-O single bond rotation of the two ligandosides. Similarly to the previous results of the hybrid-1 structure, we obtained again the almost identical structure after another 100ns run (see SI). This showcased that the initially obtained hybrid-2 structure of **htel22-L2a** was indeed close to the thermodynamic minimum. With the two structures at hand a direct quantitative comparison was possible as both simulation runs contain the same type and number of atoms.

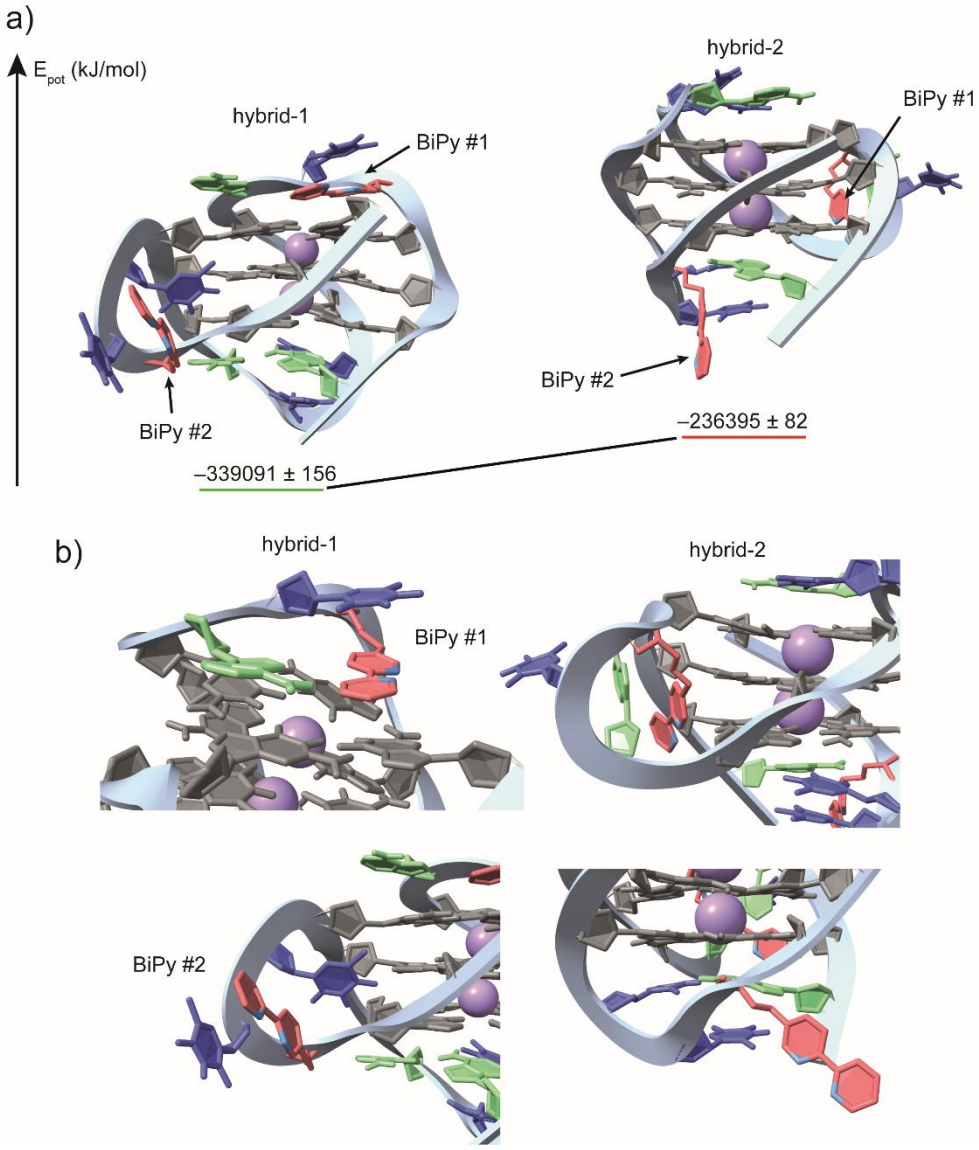

Figure 39. A) Comparison of potential energies of the modelled starting structures for **htel22-L2a** by modification of either a hybrid-2 (PDB: 2JPZ)[220] or hybrid-1 (PDB: 2HY9)[221] topology. b) Closer examination of **BiPy-L**, positioned in the two different hybrid topologies, reveals π-stacking of the bipyridine unit in the hybrid-1 structure, absent in hybrid-2. Closer examination of the interactions of BiPy #1 unit with the G-tetrad and the thymine T6 leading to potential additional stabilisation of the structure.

Since the systems contained the DNA constructs, water molecules and cations in the form of the K+, it was possible to compare various energy values that encompass either combination of these. Firstly, we extracted the potential energy of the DNA constructs. The energy for the hybrid-1 topology at E_{pot} = -13662 ± 1675 kJ/mol was similar to the of the hybrid-2 topology at E_{pot} = -14132 ± 565 kJ/mol. This indicated that the two constructs were closely matched when the DNA was isolated from all the other components of the calculation. This was at first hand unexpected as a qualitative observation of the two structures would have indicated a lower energy, therefore a more stable state, for the hybrid-1 topology with observed favourable interactions of the two bipyridine units. We then calculated the potential energy of the whole system for both hybrid-1 and hybrid-2, encompassing both water molecules as well as other ions such as K^+ and Cl^- and obtained a vastly different result. Here the hybrid-1 topology was clearly favoured with a difference of ΔE_{pot} = -102696 kJ/mol as compared to hybrid-2. Although these energy values are arbitrary and do not represent absolute energy values of each system, there is a non-negligible difference. It furthermore supports the hypothesis that the hybrid-1 is the preferentially adopted topology in solution. This highlights the importance of the solvent, water in this case, as well as the cations in accurately assessing the energic differences between systems. The orientation of water molecules around the structures can create areas of high- or low-energy contributing to the energy differences. To exclude any abnormal contribution of the kinetic energy to the difference of the two systems, we additionally extracted the E_{tot} values. This revealed a similar situation to the E_{pot} of the two total systems with a ΔE_{tot} = -84000 kJ/mol, again favouring the hybrid-1 topology. With the thermodynamically favoured topology of **htel22-L2a** in absence of a M^{2+} established, it was important to model and investigate the antiparallel topology of this G-quadruplex.

The starting structure was taken from the PDB 143D and no alterations of the sequence had to be performed apart from exchanging the nucleotides T and A at the respective positions #5 and #19 with the already preformed bipyridine-Cu^{2+} complex. Additionally, the present Na^+ cations in which the crystal structure was obtained had to be exchanged with K^+ at 100mM concentration.

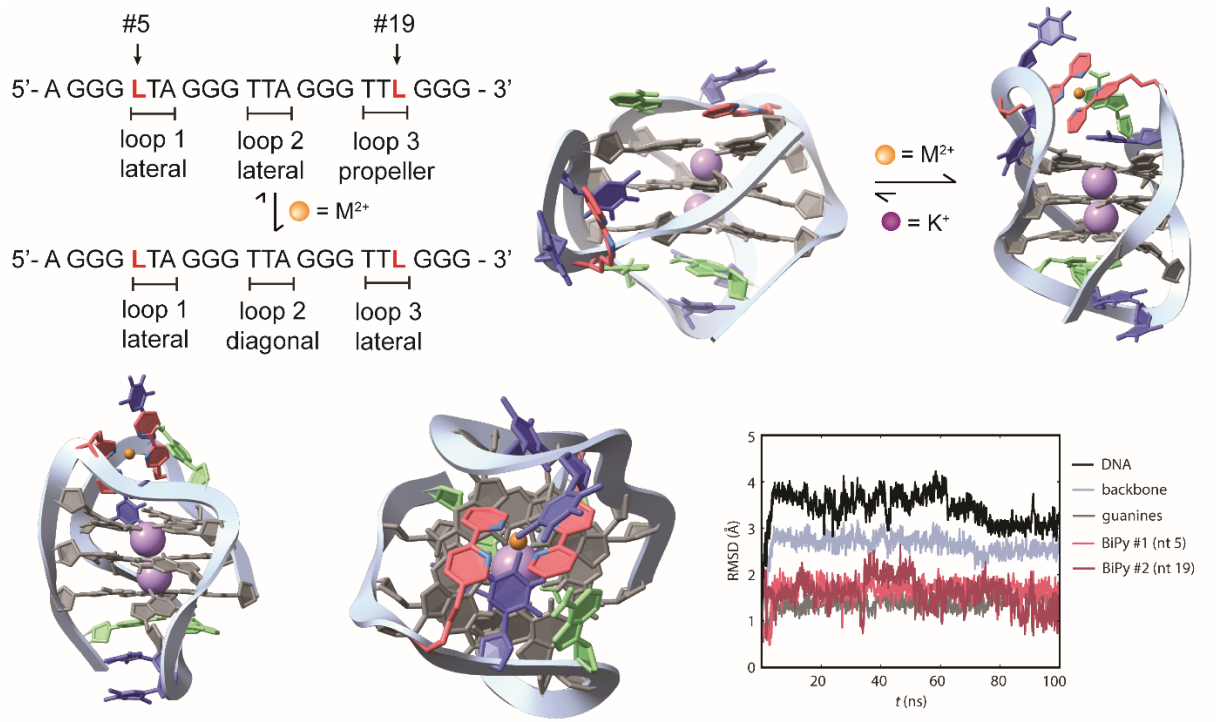

Figure 40. Molecular dynamics simulation of htel22-L2a stabilised by the bipyridine metal complex based on PDB: 143D for the antiparallel topology. A) Topological switch from hybrid-1 to antiparallel G-quadruplex structure. The metal complex is locate within the upper loop region between the two lateral loops. B) Side view of the representative structure determined from the 100 ns MD simulation with subsequent clustering. C) Top view showing the positioning of the metal complex centrally above the G-tetrad. D) RMSD plot of selected structural parts (all guanines, individual bipyrdines, phosphate backbone, whole DNA construct) of the simulated structure over 100 ns. Colour coding: guanines in grey, thymines in blue, adenines in green, bipyridine in pink, potassium in violet.

The MD simulation run was performed identical to the previous. The overall antiparallel character of the structure was preserved and did not deviate from the wild type structure in a significant manner. The positioning of the bipyridine-Cu^{2+} complex was interesting as it did not situate itself flat above the upper G-tetrad but occupied the area between the two lateral loops. The second bipyridine unit in position #19 points slightly outside of the G-quadruplex. No additional favourable interactions with loop nucleotides could be assessed qualitatively from this simulation. Positions of the individual bipyridine nitrogens coordinating to the metal center where not fixed in space as to allow free rotation of the two bipyridine ligands around the metal center during the simulation run. Restraints where only put on the relative orientation of the nitrogens as they had to obey a square planar coordination geometry. The RMSD values showed a remarkable stability of the system with minor fluctuations over the course of 100ns simulation time. When comparing the backbone flexibility in absence and presence of the metal complex, an overall decrease could be observed as reflected in the significantly lower RMSD values. Interestingly the second bipyridine unit in position #19

showed some structural fluctuations up to the 40ns mark but largely stabilised afterwards. The guanine core remained unchanged throughout the whole simulation run which further supported the hypothesis of a structurally sound G-quadruplex. From this modelled structure it was possible to see that the antiparallel folding observed in solution for **htel22-L2a** was indeed a reasonable assumption (**Figure 40**).

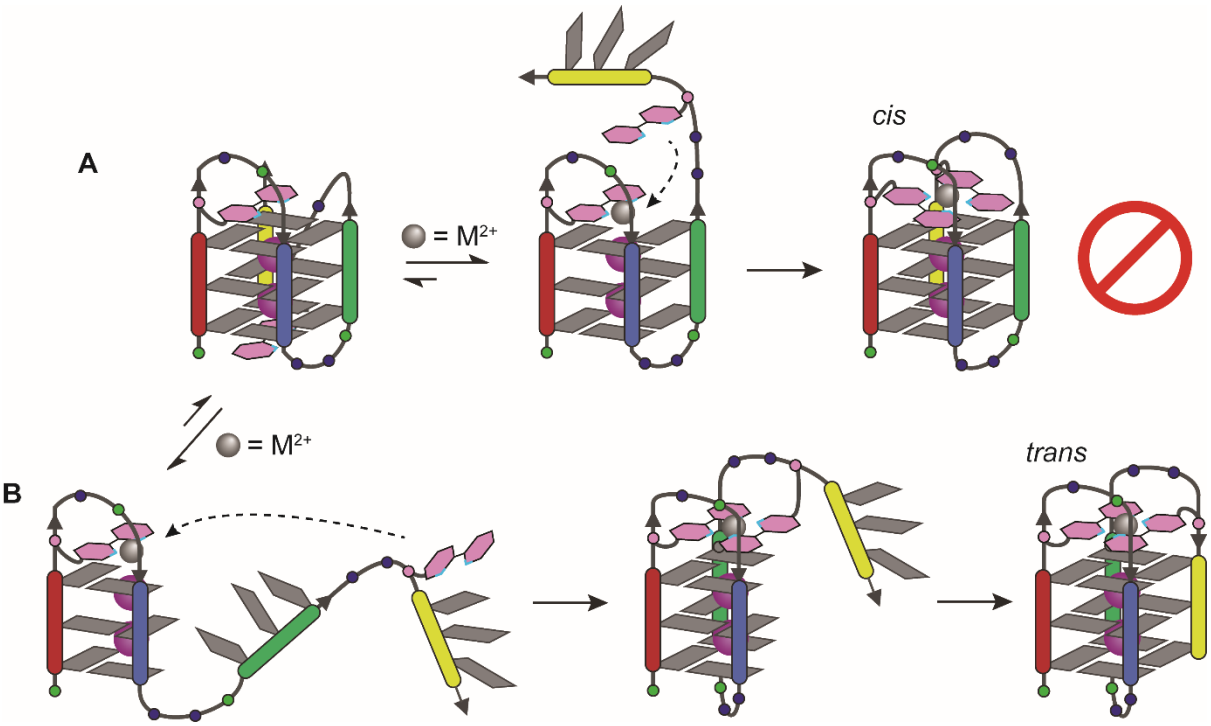

Figure 41. Schematic representation of the proposed refolding mechanism of htel22-L2a from a hybrid-1 to antiparallel basket type topology. A) Only the yellow G-run disengages from the G-quadruplex facilitated through the formation of the bipyridine metal complex resulting in a antiparallel chair type topology, not accessible for htel22 G-quadruplex. B) Both green and yellow G-runs disengage from the G-quadruplex core. The fast formation of the metal complex facilitates change in relative positioning of green and yellow G-run resulting in an antiparallel basket type topology.

This first 3D structural model, rather than schematic representation, visualises also the necessity of the refolding of the G-quadruplex if the formation of the bipyridine metal complex is induced. Additionally, it revealed how the G-quadruplex must refold to adopt this alternative topology when starting from the hybrid-1 topology, which was shown to be the energetically favoured one. To clarify the proposed mechanism based on these results, the G-quadruplex will be divided into four parts with each run containing three guanines (or “run” of guanines). The individual parts have been colour coded as can be seen in **Figure 41**. In order to adapt the basket-type antiparallel structure reported for the wildtype htel22 G-quadruplex it is not sufficient that strand 4 (yellow) inverses its directionality to create the upper lateral loop. This would result in a chair-type antiparallel topology, not observed for htel22 structures. Similar to previously reported wild type systems, strand 3 (green) and 4

(yellow) must switch positions relative to strands 1 (red) and 2 (blue). This results in the creation of the diagonally running loop 2 which is then followed by the inversion of the directionality of strand 4 (yellow). The **htel22-L2a** G-quadruplex must therefore undergo at least partially different folding pattern when annealed in the presence of M^{2+} as shown by the MD simulations. We were not able to model this full process especially in presence of the unnatural modifications and the metal complex formation as these interactions were not included in the AMBER force field. The folding and refolding mechanism of **htel22-L2a** will be discussed in more detail in the next part of this work.

After having analysed the **htel22-L2a** system in depth, next on the list was the alternatively modified **htel22-L2b**. Instead of nucleotides in the loops, here two guanines which form the third G-tetrad were substituted with the BiPy-L1 modification. In CD spectroscopy this G-quadruplex adopts an antiparallel topology in K^+ both in presence and absence of a M^{2+} source with only minor changes in the individual spectra.

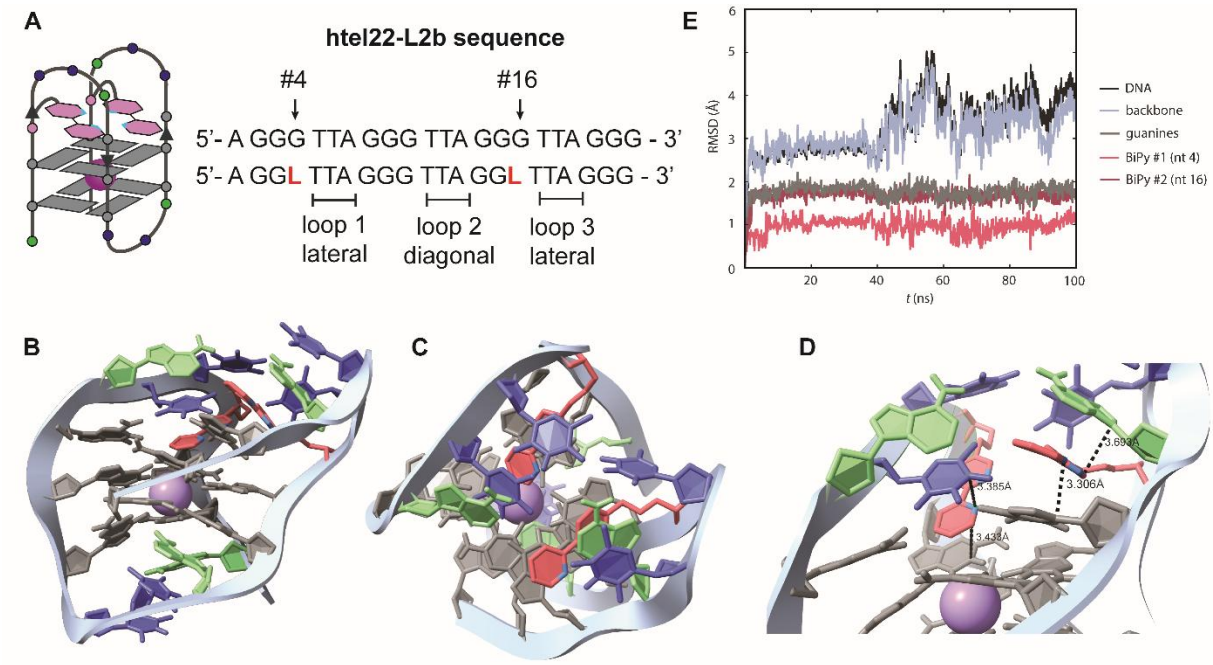

Figure 42. Molecular dynamics simulation of htel22-L2b in absence of any divalent metal cation M^{2+} (M = Cu, Ni, Zn). Starting structure used for modelling was PDB: 143D. A) Oligonucleotide sequence shown with placement of the bipyridine ligand modifications (BiPy) marked with L. B) Side-view of the representative structure from the 3'-end. C) Top-view of the representative structure. D) Zoomed view of the loop region with distances between selected nucleotides indicating possible ranges of pi-stacking interactions. E) RMSD plot of selected structural parts (all guanines, individual bipyrdines, phosphate backbone, whole DNA construct) of the simulated structure over 100 ns. Colour coding: guanines in grey, thymines in blue, adenines in green, bipyridine in pink, potassium in violet.

Again, 143D was chosen as the starting structure as this presented the ideal antiparallel topology and no alteration had to be performed except for the insertion of the **BiPy-L1** ligandosides. Contrary to **htel22-L2a**, or **htel22-L2b** guanines in position #4 and #17 were replaced instead of nucleotides in the loops of the G-quadruplex (**Figure 42**). In order to assess true representative structures from these simulations we again performed clustering of the entire simulation run and picked those with the highest population count. From a qualitative assessment of the 100ns simulation runs it's evident that both structures show a significant distortion of the G-tetrads regardless of the formation of the bipyridine-metal complex. This effect is slightly stronger pronounced in the non-metal stabilised **htel22-L2b** as here the guanines form an X-shaped arrangement around the central K+ cation when observed from one side of either lateral loop. The two now unpaired guanines in position #8 and #20 situate themselves above the upper G-tetrad and seemingly still engage in π-stacking interactions. The two bipyridine units also point to the inside of the G-quadruplex and arrange themselves within the loop region in such a manner that favourable π-π interactions seem possible. The distance between neighbouring nucleotides ranges from 3.4 – 3.6 Å, well within the expected limits. Bipyridine in position #4 creates a stack with the neighbouring G3, which forms one of the two G-tetrads, below it and thymine T6 and adenine A7 above it. A similar situation can be observed for the second bipyridine unit in position #17 where T18 and A19 from the later loop are arranged flat above one of the pyridine subunits of bipyridine and G20 found below the second pyridine subunit. These secondary interactions likely stabilise the positioning of the bipyridine ligandosides and prevent them from turning and twisting uncontrollably within the G-quadruplex. This can also be seen in the RMSD values of the run where both the guanines as well as the bipyridine units remain stable over the whole 100ns. Surprisingly the backbone as well as the entirety of the DNA construct is selected, large fluctuations after 40ns are recorded and do not stabilise until the end. In order to further investigate this behaviour and detect if there are any further changes after 100ns we performed a prolonged simulation run at 200ns (**Figure 43**).

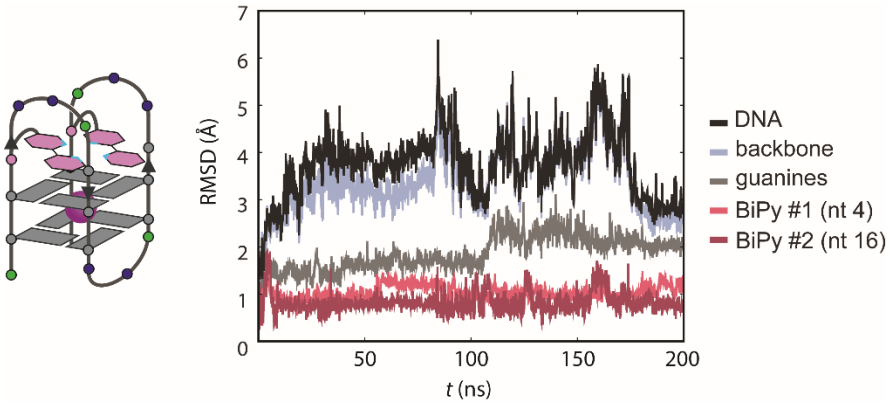

Figure 43. RMSD plof of htel22-L2b in absence of any divalent metal cation M^{2+} (M = Cu, Ni, Zn) over a 200 ns simulation period. System showed large structural fluctuations between 100 – 180 ns and only stabilising afterwards.

Although the guanines as well as the bipyridine remained stable over the first 100ns, large relatively large RMSD fluctuations of up to ΔRMSD = 1.5 Å of the phosphate backbone as well as the entire DNA constructs were observed. These further increased to approx. ΔRMSD = 2.5 Å from 100 – 185ns in the simulation run. In addition, the absolute RMSD value of the guanines jumped from 1.5 Å to 2.5 Å indicating a sudden structural change. The system seemed to reach a stable state after 185ns where the fluctuations of the backbone and DNA dropped significantly. Upon closer inspection of a representative structure at this point revealed no stark differences to the previously obtained structure, limited to 100ns. An overlay of both structures revealed that the guanines in the G-core remained slightly tilted but were in good accordance with the first structure. The largest difference was in the orientation of the bipyridines and their positioning in the loop region. Additionally, the spatial orientation of the third loop showed a more lateral configuration rather than pointing away from the G-quadruplex core. Thus, we deemed the second structure of **htel22-L2b** as more representative (see SI).

The situation for the metal stabilised **htel22-L2b** structure was very similar. The bipyridine complex moved away from the G-core and did not stack flat on top of the upper G-tetrad. There are no obvious π-stacking interactions observable for this structure due to its distance and position towards the other nucleotides. To our surprise the previously inserted *cis*-oriented bipyridine-Cu^{2+} complex did not retain this relative configuration but one of the bipyridine unit twisted to adopt a *trans*-configuration of the bipyridine units around the metal center (**Figure 44**).

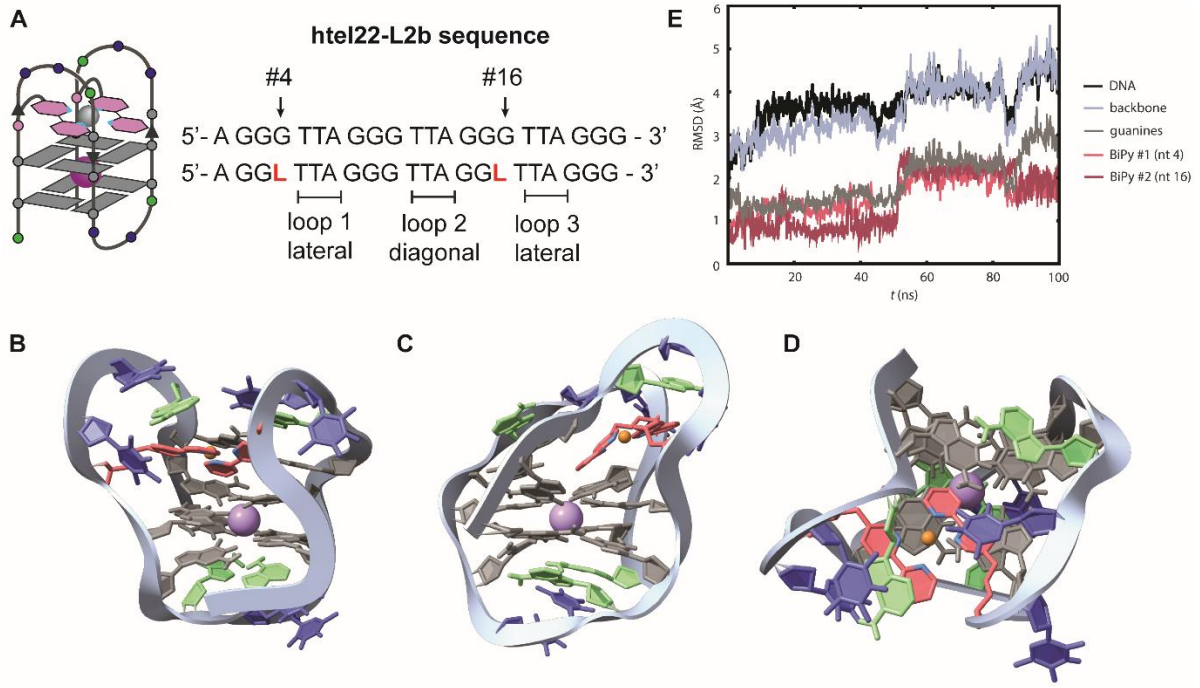

Figure 44. Molecular dynamics simulation of htel22-L2b in presence of a divalent metal cation M^{2+} (M = Cu, Ni, Zn). Starting structure used for modelling was PDB: 143D. A) Oligonucleotide sequence shown with placement of the bipyridine ligand modifications (BiPy) marked with L. B) Side-view of the representative structure from the 3'-end. C) Top-view of the representative structure. D) Zoomed view of the loop region with distances between selected nucleotides indicating possible ranges of pi-stacking interactions. E) RMSD plot of selected structural parts (all guanines, individual bipyrdines, phosphate backbone, whole DNA construct) of the simulated structure over 100 ns. Colour coding: guanines in grey, thymines in blue, adenines in green, bipyridine in pink, potassium in violet.

A frame-by-frame analysis of the simulation run was conducted and the twisting could be observed around the 50ns mark. This fell in line with the obtained RMSD values which show a positive jump at exactly this time stamp. The system quickly stabilises afterwards but again showed some deviations towards the end of the 100ns. Again we performed a longer simulation run of 200ns to further investigate the system. No large jumps in RMSD values could be observed for the longer simulation and overall values remained comparable to the initial run. We investigated several snapshots of the run to identify structural differences. While the main G-core remained in a similar position as well as relative orientation between individual guanines was retained, some minor changes in the loop arrangement was observed as well as the positioning of the bipyridine metal complex in reference to the previous run. As these structures are generated from the most populated clusters of the run, these minor differences could stem from inherent differences in snapshots between the two simulation runs and can therefore be neglected. Overall, the MD structures obtained for both **htel22-L2a** and **-L2b** structures support the characteristics observed in the spectroscopic

analysis and give a good insight in additional interactions between the artificial bipyridine and natural nucleotides. All structures showed a high structural fidelity.

3.3.2 Ttel24

As **ttel24-L2a** either presents a mixture of G-quadruplex topologies or adopts a predominantly hybrid form in presence of M^{2+} cations while **ttel24-L2b** remains in a mixed state, the modelling of these G-quadruplexes was not straightforward.

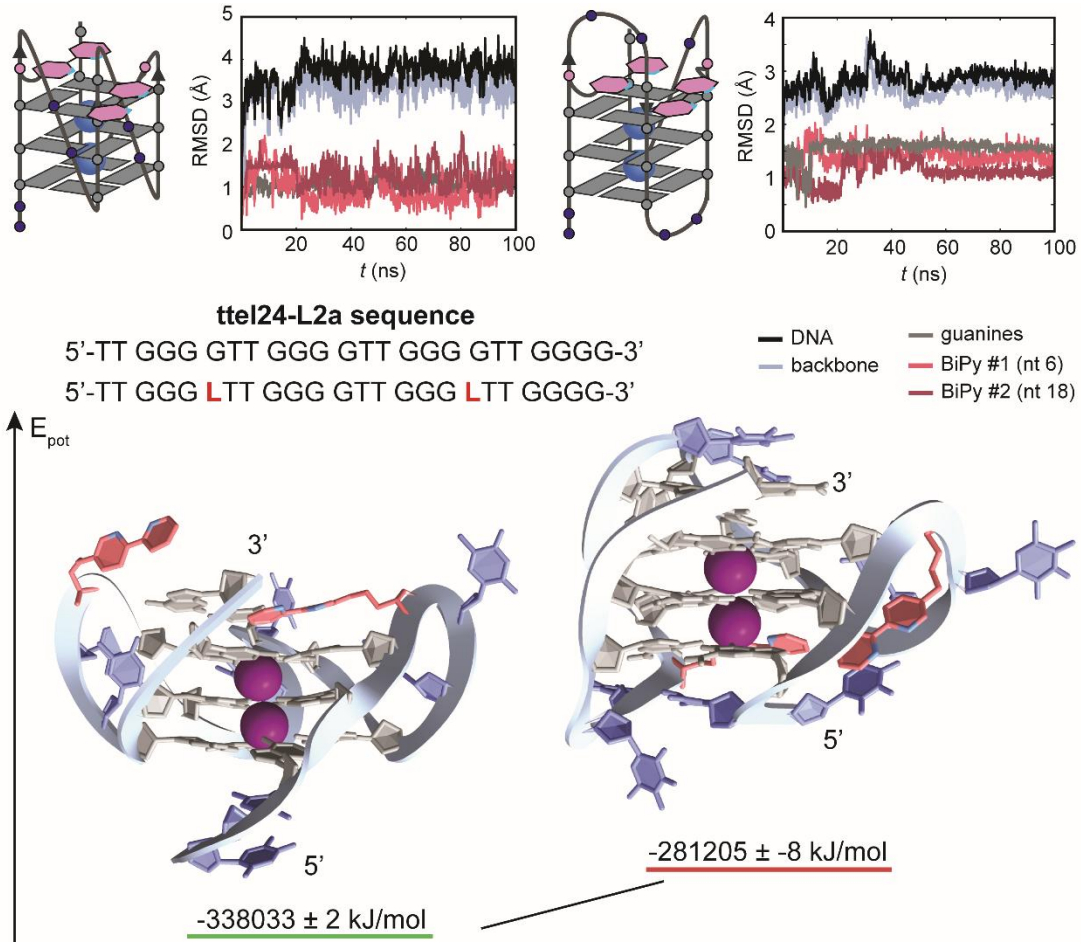

Figure 45. Molecular dynamics simulation of ttel24-L2a in absence of any divalent metal cations M^{2+} (M = Cu, Ni, Zn). A) As a mixture of topologies was observed in CD, two starting structures were chosen for the modelling in the form on an parallel fold (PDB: 6W9P) and a hybrid-2 fold (PDB: 6XT7). Oligonucleotide sequence shown with placement of the bipyridine ligand modifications (BiPy) marked with L. RMSD plots of selected structural parts (all guanines, individual bipyrdines, phosphate backbone, whole DNA construct) of the simulated structure over 100 ns. B) Comparison of potential energies of the simulated structures, indicating a preference for the parallel topology. Colour coding: guanines in grey, thymines in blue, bipyridine in pink, potassium in violet.

We opted to construct two initial structures based on a parallel folded structure (PDB: 6W9P) and a hybrid-2 topology (PDB: 6XT7) where either two bipyridine units or the corresponding metal complex were manually inserted and compare energies of these systems as well as qualitatively analyse their simulated stable geometries. In the parallel folded structure for **ttel24-L2a**, the two bipyridine units sit in position #6 and #18 substituting two guanines from the initial structure. Clustering of the 100ns simulation run in steps of 15ns revealed several possible structures of equal population, indicating that no large structural deviations across the run were observed. This was reflected in the RMSD analysis as well where, apart from the initial 15ns, the system retained stability with no large deviations in RMSD values.

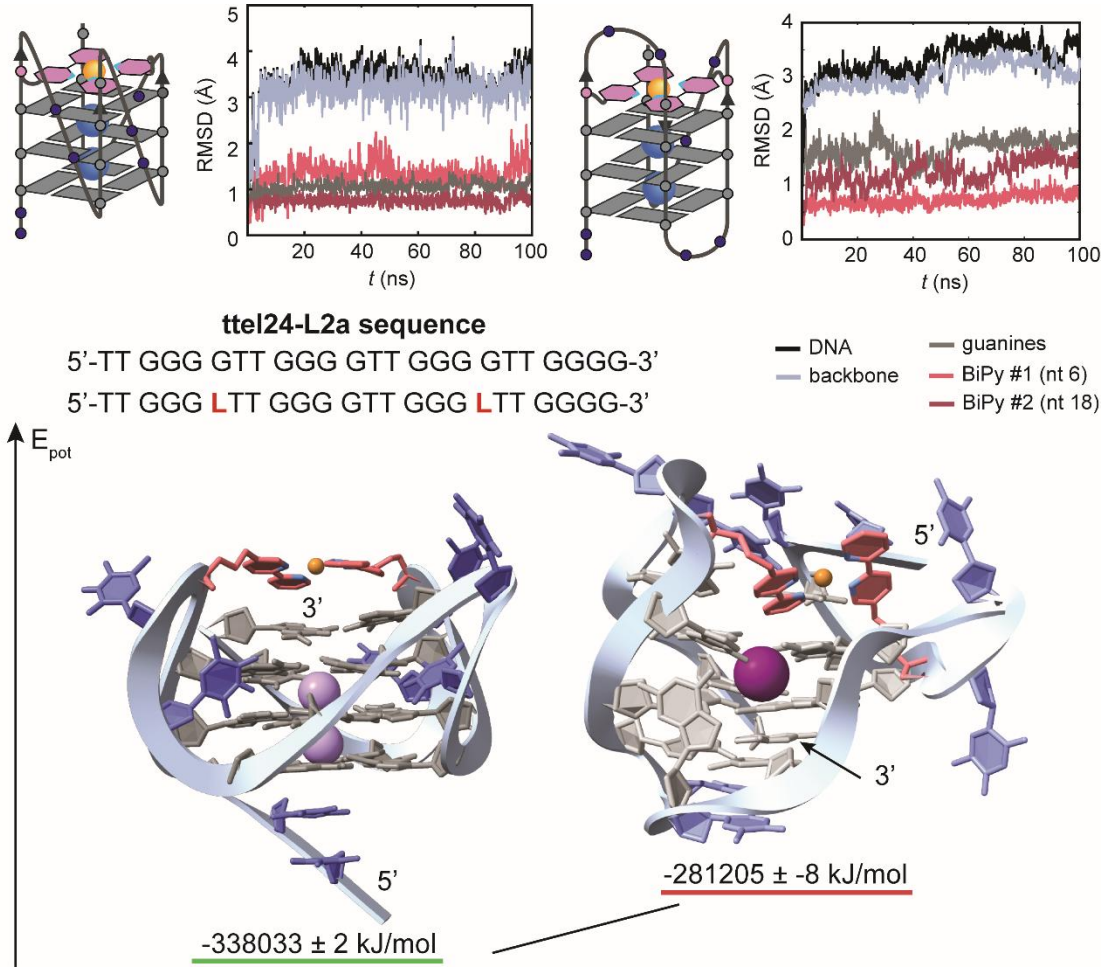

Figure 46. Molecular dynamics simulation of ttel24-L2a in presence of a divalent metal cations M^{2+} (M = Cu, Ni, Zn). A) As a mixture of topologies was observed in CD, two starting structures were chosen for the modelling in the form on an parallel fold (PDB: 6W9P) and a hybrid-2 fold (PDB: 6XT7). Oligonucleotide sequence shown with placement of the bipyridine ligand modifications (BiPy) marked with L. RMSD plots of selected structural parts (all guanines, individual bipyrdines, phosphate backbone, whole DNA construct) of the simulated structure over 100 ns. B) Comparison of potential energies of the simulated structures, indicating a preference for the parallel topology. Colour coding: guanines in grey, thymines in blue, bipyridine in pink, potassium in violet.

The guanine core remains stable over the entire simulation run yet intriguingly not all guanines participate in Hoogsten base pairing and are involved in the formation of G-quartets. In all of the most representative structures an additional triade of G24, G12 and one bipyridine unit towards the 3'-end of the structure was formed (**Figure 45**).

In contrast to the parallel topology, in the hybrid version we observed that above the upper G-tetrad (towards 5'-end) another triade is formed consisting of two guanines G3 and G21 and the bipyridine unit in position #18 and engaging in hydrogen bonding interactions as well as π-stacking with the underlying G-tetrad for additional stabilisation. Three other guanines namely G11, G15 and G24, are not participating in the formation of a G-quartet resulting in only two full G-tetrads. The distances are well within the range for π-interaction with values between 3.2 – 3.8 Å. The RMSD values of this bipyridine unit suggest that it is less flexible due to the possible secondary interactions with close by nucleotides and the G-tetrad. The bipyridine in position #6 adopts a strange configuration, folding back onto the phosphate backbone of the first loop and being stabilized by π-π interactions with the thymine T1 (2.9 Å). The first loop adopts a bulging propeller type configuration which is visible from the side view of the structure (**Figure 45**). The RMSD of the overall DNA constructs fluctuates initially but stabilises eventually after 60ns indicating that this strained loop orientation is not a structural outlier. The other loops of the G-quadruplex adopt a lateral orientation and no diagonal loop on the 3'-end is formed, thus retaining the overall hybrid topology of the starting structure.

We then compared the respective structures of ttel24-L2a in presence of the metal complex, starting of with the hybrid topology. Overall the system showed good stability across the 100ns simulation run with no large fluctuations of either guanines, the two bipyridine units or the DNA construct in its entirety. Clustering of the run to obtain most representative structures again showed similarly populated structures across the 100ns timescale. In combination with the RMSD plot we chose to consider a structure past the 60ns mark for a more in depth analysis as fluctuations were minimised in this region. The bipyridine metal complex is positioned above the upper G-tetrad but slightly off-centered and at an approx. 30° angle in relation to the guanines beneath, thus making unfavourable conditions for pi-interaction with the latter. Only two complete G-tetrads are formed with an additional G-triade on the 3'-end, very similar to the metal free structure of ttel24-L2a. While the overall hybrid topology is retained, loop1 twists in a seemingly unfavourable fashion in order to remain in its propeller type configuration. Neighbouring nucleotides around the bipyridine complex do not seem to engage in either hydrogen bonding or pi-stacking. When compared to the parallel topology derived from 6W9P clear differences can be observed. Firstly, three G-tetrads are formed in comparison to two for the hybrid topology, indicating a more stabilised structure. The RMSD values of the G-core reveal minor fluctuations across the 100ns

simulation run. The bipyridine complex is placed above the G-tetrads at the 3'-end but separated from it by two additional guanines, not engaging in tetrad formation. A low flexibility of either bipyridine unit can be deduced from the stable RMSD values, comparable to the hybrid topology. π-stacking interactions of the bipyridines with the guanines G24 and G12 in close proximity could contribute to further stabilising the structure. Similarly to the hybrid-topology, the propeller type loops need to adopt a strongly twisted configuration to accomodate the metal complex. We then compared energies of the two structures. Interestingly the parallel folded structure was energetically favoured in both total energy (E_{tot} = -279682 ± 16 kJ/mol) and potential energy (E_{pot} = -337931 ± 18 kJ/mol) compared to the hybrid structure (E_{tot} = -233140 ± 23 kJ/mol, E_{pot} = -281131 ± 14 kJ/mol) which is contrary to the spectroscopically obtained results showcasing a refolding of the **ttel24-L2a** G-quadruplex from a mixture to a predominantly hybrid topology. This trend reversal might stem from a wrong hybrid-2 starting structure used for the construction of the respective models. As here is no reported hybrid-1 solution or crystal structure of the ttel G-quadruplex, further comparison and validation of this hypothesis was not possible. The refolding of the G-quadruplex might be kinetically trapped through the quick formation the corresponding metal complex during the annealing process as the two bipyridine units are in close proximity, unlike in the case for **htel22-L2a**.

3.3.3 Pu22

Lastly the MD simulation for the parallel G-quadruplex of **pu22-L2c** was performed. As no success in formation of a correct structure was seen when the bipyridine ligands were placed in the loop regions of these parallel folded structures, no model of this was constructed. We concenctrated on those sequence bearing the two artificial ligandosides in the short overhangs on the 5'- and 3'-ends. For the construction of the starting structure the solution structure of natural pu22 G-quadruplex (PDB:1XAV) was manually modified as previously described. The sequence was further altered to correctly represent the elongation of the first loop by two additional nucleotides. A subsequent MD simulation run over 100ns was performed and analysed for both unbound bipyridine ligands and the corresponding metal complex.

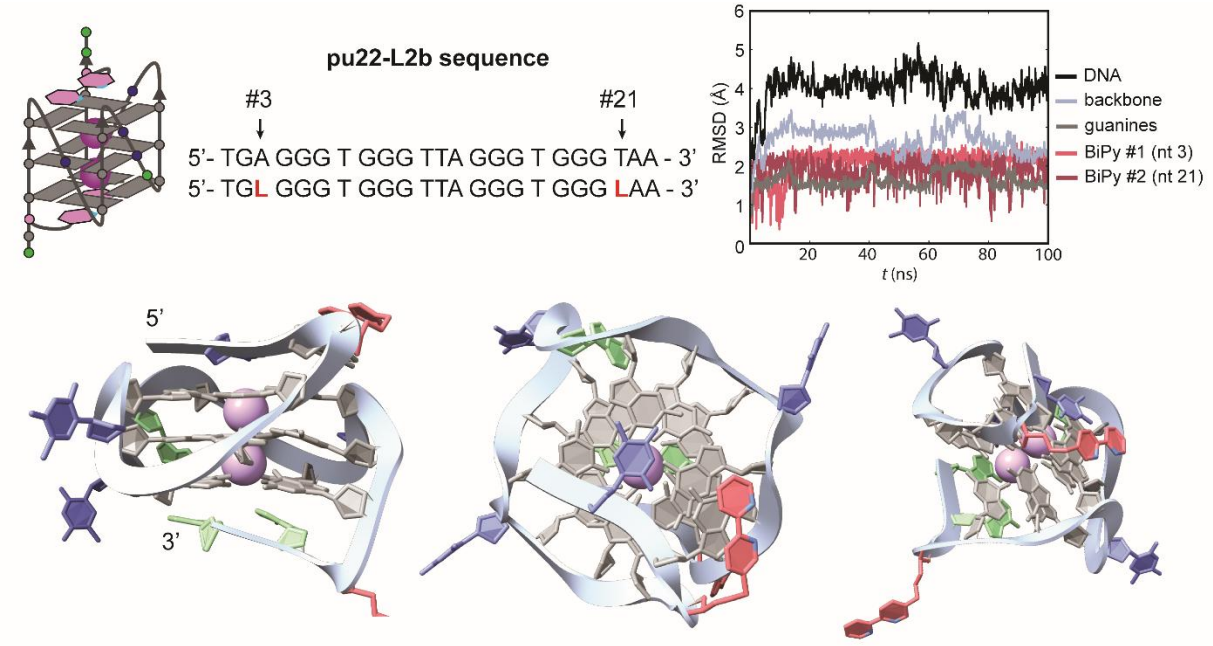

Figure 47. Molecular dynamics simulation of pu22-L2b based on PDB: 1XAV in absence of any divalent metal cations M^{2+} (M = Cu, Ni, Zn). A) Schematic representation of **pu22-L2b** with **BiPy-L1** modification in parallel topology. The positions of the bipyridine ligands (#3, #21) are shown in the sequence. B) Representative structure determined from the 100 ns MD simulation with subsequent clustering. Side view from the 5'- and 3'-end of the structure. C) Top view. D) Zoomed out view of the construct to visualise the positioning of the bipyridine unit in position #21. E) RMSD plot of selected structural parts (all guanines, individual bipyridines, phosphate backbone, whole DNA construct) of the simulated structure over 100 ns. Colour coding: guanines in grey, thymines in blue, adenines in green, bipyridine in pink, potassium in violet.

Overall, both systems achieved a stable state within the 100ns with low degrees of flexibility and variability of structures. For **pu22-L2c** in absence of any metal, the guanines involved in the formation of the G-tetrads show low flexibility with an $RMSD_{avg.}$ = 1.5 Å across the run and only minor jumps in this value were seen with one prominent period from 60 – 80ns. Qualitatively no large structural differences could be found between structures at varying RMSD values along the simulation run as the G-core remained stacked at all times with a strong parallel alignment of each G-tetrad. The two bipyridine units showed an overall similar $RMSD_{avg.}$ = 2.0 – 2.1 Å individually, with the second unit in position #21 experiencing larger short peaks to lower RMSD values. This similarity in RMSD is intriguing as in the representative structure, this bipyridine unit is pointing away from the G-quadruplex and does not engage in stabilising non-covalent interaction with either the phosphate backbone or neighbouring nucleotides or the G-tetrad towards the 3'-end. The position of the first bipyridine unit in position #3 is vastly different. As the short 5' overhand consisting of a thymine T1 and guanine G2 swing over the G-tetrad, the bipyridine engages in a secondary π-stacking with G2 and remains in this configuration throughout the run as demonstrated by

comparing several snapshots of the MD run. The parallel structure of the initial pu22 G-quadruplex was retained without strong twisting of the phosphate backbone and the presence of the propeller-type loops (**Figure 47**). This 3D model showcases why the placement of bipyridine units within the single or double nucleotide loops of pu22 could not lead to the formation of the corresponding metal complex as the orientation of the ligands would have pointed outside of the G-quadruplex and their spatial separation would have been too large to overcome. This is further supported when compared to the MD structure of the metal-stabilised **pu22-L2c** G-quadruplex (**Figure 48**).

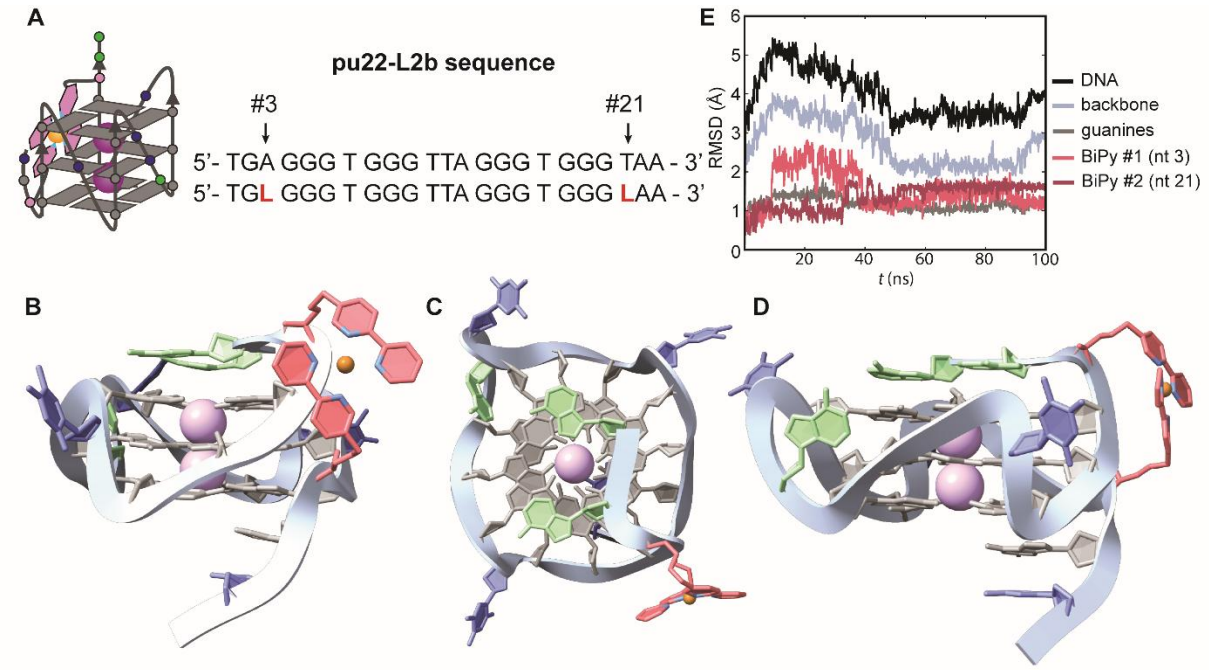

Figure 48. Molecular dynamics simulation of pu22-L2b based on PDB: 1XAV in presence of a divalent metal cation M^{2+} (M = Cu, Ni, Zn). A) Schematic representation of **pu22-L2b** with **BiPy-L1** modification in parallel topology. The positions of the bipyridine ligands (#3, #21) are shown in the sequence. B) Representative structure determined from the 100 ns MD simulation with subsequent clustering. Side view from the 5'- and 3'-end of the structure. C) Top view. D) Zoomed out view of the construct to visualise the positioning of the bipyridine unit in position #21. E) RMSD plot of selected structural parts (all guanines, individual bipyridines, phosphate backbone, whole DNA construct) of the simulated structure over 100 ns. Colour coding: guanines in grey, thymines in blue, adenines in green, bipyridine in pink, potassium in violet.

The system proceeded through unstable states within the first 50ns of the simulation run as can be seen by the overall flexibility of the phosphate backbone and the entire DNA constructs. The G-core remained stable over the entire simulation period, indicating that rearrangement of the structure is mainly driven by the short overhangs on both ends as well as the correct positioning of the bipyridine metal complex. A representative structure

(*t* = 79ns) reveals an interesting state of the structure where the metal complex is facing the G-core in an almost 90° angle and hovering above the phosphate backbone. In comparison to the metal-free **pu22-L2c** structure, in the 5'-overhang only the guanine engages in π-stacking the with underlying G-tetrad while T1 stacks on the corresponding G2. The first bipyridine unit (position #3) has twisted outside the interaction plane to be in close proximity to the second bipyridine unit. The 3' overhang adenines A21/22 have rearranged slightly in comparison with the metal-free structure in order to accommodate the successful formation of the complex. When comparing this stable structure to a prior snapshot (t = 22ns) a clear difference can be observed. Here the metal complex is lodged in between the phosphate backbones while the overhangs are twisted so that neither T1 nor A21 are engaging in stabilising interaction with the G-tetrad bur rather point away (see SI). The initial unstable nature of this particular G-quadruplex structure was therefore indeed correctly captured by the RMSD plot. The system nevertheless adopts a stable state over time. Overall, these simulations gave us important insight into the formation of bipyridine modified parallel folded G-quadruplexes and confirmed the potential for complex formation in these topologies when modified at the correct positions. Contrary to the telomeric structures, the ligand complexes in **pu22-L2c** do not form above or in close proximity to a G-tetrad but sit on the side of the G-quadruplex. These results show promise for further investigation of these system in presence of other biomolecular binding partners such as helicases and other proteins.

3.4 Refolding kinetics of BiPy-L1 modified G-quadruplexes

With the compounded knowledge of spectroscopic analysis as well as the MD simulation of the structures it was of interest to investigate if the multiple topologies, accessible through the addition or removal of a divalent metal cation M^{2+} (M = Cu, Ni, Zn) were not only a product of simple annealing and a thermally driven conversion but could be dynamically accessed at r.t. or below. Three constructs, namely **htel22-L2a** and **ttel24-L2a** and -**L2b** showed distinctive changes in their CD spectra when annealed in presence of M^{2+}. Out of these three only **htel22-L2a** could be identified as switching from a purely hybrid-1 to an antiparallel topology hence we chose to perform the first refolding kinetic experiments with this G-quadruplex. **Htel22-L2a** was pre-annealed under the standard conditions in 10mM HEPES buffer (pH 7.1) and 100mM KCl after which a first CD spectrum was recorded which showed the expected hybrid-1 topology as described previously. Then 1.1eq of $CuSO_4$, relative to the DNA concentration, was added to the sample without diluting it and the mixture quickly equilibrated by pipetting. This process took about 30s after which a second CD measurements was started, followed by a new measurement every 5min. During this a slow but strong change in the CD signature could observed at r.t. where the initial hybrid-1 topology was converted into the antiparallel topology (**Figure 49**).

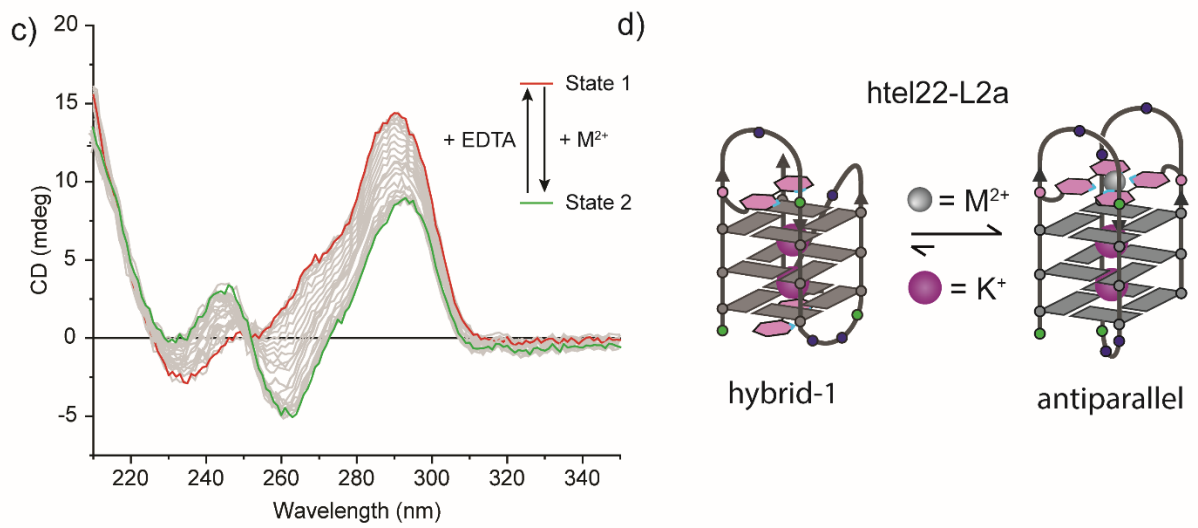

Figure 49. A) CD spectrum of **htel22-L2a** showcasing the slow refolding from hybrid-1 (red line) to antiparallel topology (green line) upon addition of $CuSO_4$ and reversal of the process by decomplexation with EDTA. B) Schematic representation of the suggested refolding mechanism, consisting of fast initial metal complexation by one bipyridine (here shown for the upper one), followed by slow refolding of the DNA and formation of the chelate complex.

This was accompanied by the rise of the band at 315nm indicative of the successful formation of the bipyridine metal complex. The transformation was concluded after 1.5h at which point no changes in the CD spectra could be observed. The presence of an isosbestic point in the overlayed spectra indicated that the refolding process took place from state 1, the hybrid-1 form, directly to state 2, the antiparallel form, without going through an intermediate structure or one that showed a half-life long enough to be recorded on the CD spectrum. We observe that the slow kinetics of this reaction, accompanied by pronounced alterations in the CD spectra, strongly suggest a substantial structural rearrangement of the G-quadruplex. In contrast, when metal ions bind to a preformed ligand environment without requiring conformational changes, CD spectral shifts occur rapidly and are typically minimal in magnitude. After this first qualitative assessment of the refolding process it was of interest to quantify this in detail by determining kinetic rate constants at different temperatures from which subsequently an Eyring-plot could be created which would give insight into the enthalpy and entropy of change (**Figure 50**).

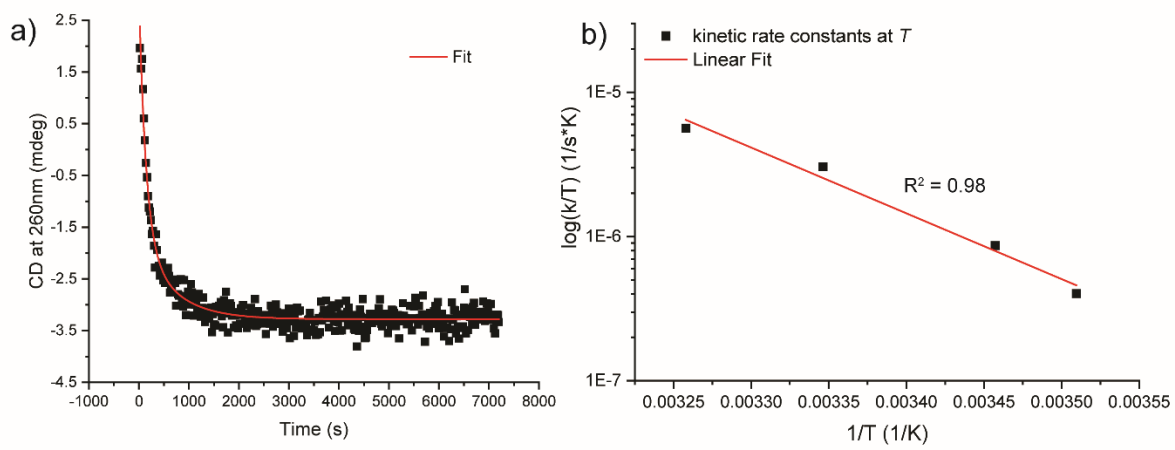

Figure 50. A) Decay of the CD signal of **htel22-L2a** at 260 nm over 7200 s at 306 K measured in intervals of 10 s. B) Eyring-plot for the determination of enthalpy and entropy of activation and Gibbs activation energy.

Instead of recording full spectra for each time point, the decay of the CD band at 260nm, which indicates the formation of the antiparallel topology, was followed over time in short steps of 10s. In order to create a reliable Eyring-plot afterwards, at least four kinetic rate constants, each measured at different temperatures, had to be determined. Limitations of the temperature range were determined by the freezing point of water at 273K and the speed of the reaction at elevated temperatures. Given that the refolding is fully completed after 1.5h at 298K, an increase of the reaction temperature by ΔT = 10K would increase the reaction speed by a factor of approx. 2.0 according to the Arrhenius equation. As the signal decays exponentially the resulting curvature at 318 K would result in a poor fit and the kinetic rate constant would be of poor significance (**equation 1**).

$$\frac{k_{308K}}{k_{298K}} = \exp\left[-\frac{E_a}{R}\left(\frac{1}{308} - \frac{1}{298}\right)\right] \quad (1)$$

We chose therefore 306K as the upper limit in order to obtain data that could accurately depict the beginning of the reaction which was fast and could be fit with a decay function with high fidelity. All decay curves for each temperature are shown in **Figure 51**. Different total times recorded for each temperature were chosen depending on how early a plateau was reached after which the measurement was stopped. We decided to include not only Cu^{2+} as metal source but also Ni^{2+} and Zn^{2+} as all three show very similar capacities to refold htel22-L2a from hybrid-1 to antiparallel as shown previously. Additionally, by comparing the rate constants of each metal we could support our argument that the rate determining step of this reaction is not the metal-complexation but the refolding of the DNA strands after. For further calculations it is assumed that the reaction proceeds fully from state 1 to state 2.

Converting the CD band intensity at 260nm to the concentration and subsequently plotting them on a logarithmic scale against the time a linear behaviour can be identified which shows first-order kinetics for the refolding process (see SI). This means the reaction is independent of the concentration of the added metal cation M^{2+}, but solely relies on the concentration of the DNA in solution. Fitting a linear function through the resulting logarithmic spectra (see appendix) results in the kinetic rate constants as slope thereof.

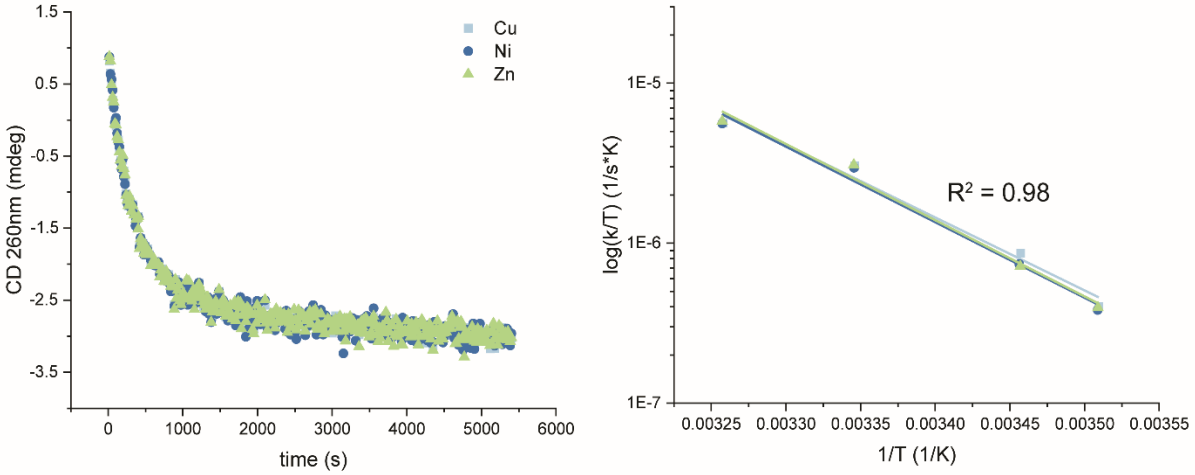

Figure 51. A) Decay of the CD signal of **htel22-L2a** at 260 nm over 7200 s at 306 K measured in intervals of 10 s after addition of either Cu^{2+}, Ni^{2+} or Zn^{2+}. B) Eyring-plot for the determination of enthalpy and entropy of activation and Gibbs activation energy.

All obtained values lied in the range of 10^{-3} to 10^{-4} s^{-1} which indeed is much slower than reported values for the bipyridine-metal complex formation.[222–224] The individual values can be found in **Table 1**. There were no large differences between the three metals employed for this reaction. With the kinetic rate constants at hand an Eyring plot could be created to determine the activation enthalpy ($\Delta H^{\ddagger}$) and entropy ($\Delta S^{\ddagger}$) as well as the resulting Gibbs energy of activation ($\Delta G^{\ddagger}$ or E_a). For all three metals the results were expectedly very similar with large enthalpic contributions ranging from +37.9 – 39.4 kJ/mol (**Table 5**).

Table 4. Kinetic rate constants of **htel22-L2a** refolding induced through addition of M^{2+}. All values are given in s^{-1}.

Metal	***k* @ 284K**	***k* @ 289K**	***k* @ 298K**	***k* @ 306K**
Cu^{2+}	$1.15 * 10^{-4}$	$2.51 * 10^{-4}$	$9.09 * 10^{-4}$	$1.73 * 10^{-3}$
Ni^{2+}	$1.11 * 10^{-4}$	$2.19 * 10^{-4}$	$9.05 * 10^{-4}$	$1.76 * 10^{-3}$
Zn^{2+}	$1.13 * 10^{-4}$	$2.04 * 10^{-4}$	$9.16 * 10^{-4}$	$1.76 * 10^{-3}$

This likely originates from the loss of stabilising interactions, mostly π-π and H-bonds within the initial hybrid-1 starting structure during the refolding process. To emphasize here is the distinction to the overall folding enthalpy which would reflect the net stabilisation in the final structure. A lowering of this enthalpic barrier therefore must be driven another process, in our case, the formation of the bipyridine-metal complex. While the argument cannot be made that the complex formation is the driving force in this kinetic analysis, it is still likely that the formation of the latter stabilises partially formed structures or even changes the path of refolding which would render the refolding of the G-quadruplex possible. We propose a schematic representation of the refolding process depicted below (**Figure 52**).

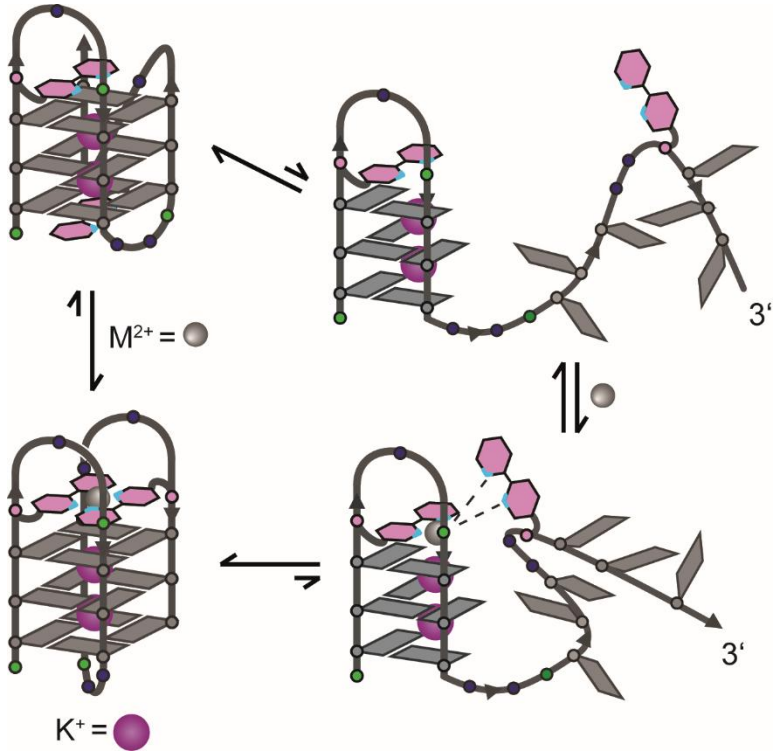

Figure 52. Schematic representation of the suggested refolding mechanism, consisting of fast initial metal complexation by one bipyridine (here shown for the upper one), followed by slow refolding of the DNA and formation of the chelate complex.

As the complexation of the metal cation M^{2+} to one of the bipyridines is very fast, it induces the formation of the whole complex. As the second bipyridine unit is not in close special proximity parts of the G-quadruplex needs to detach from the G-core after which the bipyridine-M^{2+} complex is rapidly formed. The dangling strands 3 and 4 now slowly arrange themselves in the most favourable fashion which according to our spectroscopic analysis is an antiparallel topology of the G-quadruplex of **htel22-L2a**. The negative activation entropy of –111 – –117 J/K·mol indicates that the system does not totally unfolded and refold but

retains likely some intermediate or even partially folded state throughout the entire process. This aligns with similarly flexible system reported by Schwalbe, where G-quadruplexes refold via transitory ensembles without totally unfolding.[225]

Table 5. Activation enthalpy ($\Delta H^{\ddagger}$) and entropy ($\Delta S^{\ddagger}$) as well as the resulting Gibbs energy of activation ($\Delta G^{\ddagger}$ or E_a) of **htel22-L2a** refolding.

Metal	$\Delta H^{\ddagger}$ (kJ/mol)	$\Delta S^{\ddagger}$ (J/K·mol)	$\Delta G^{\ddagger}$ (kJ/mol, 298.15 K)
Cu^{2+}	37.9 ± 3.5	-117.2 ± 12.1	72.85
Ni^{2+}	39.3 ± 3.2	-112.7 ± 10.8	72.88
Zn^{2+}	39.6 ± 3.3	-111.7 ± 11.3	72.89

For all three metals almost identical values at approx. $\Delta G^{\ddagger} \approx 72$ kJ/mol at 298.15 K was obtained. These values were in good accordance to the similar systems reported by Schwalbe and indeed seem representative of the refolding processes of G-quadruplexes.[225] These findings further supported our hypothesis and proposed mechanism of the refolding of **htel22-L2a**. Lastly the reversion of the folding from hybrid-1 to antiparallel was to be investigated. In order to achieve this, the dismantling of the metal complex was chosen as key interaction point holding. This could be easily facilitated by a competing ligand with a higher binding affinity for the divalent metal cations than the bipyridines and was found in the form of ethylenediaminetetraacetate, a standard reagent in biochemical analysis known to either stabilise interaction with Mg^{2+} or act as scavenger of toxic metals such as the here employed Cu^{2+}, Ni^{2+} and Zn^{2+} cations. Its reported affinities lie in the range of $K_a = 10^{18}$ M^{-1} for Cu^{2+} and are similar for the other metals as well, which is several magnitudes higher than the experimentally determined K_a of $10^{11\text{-}12}$ M^{-1} of the complexes formed in the bipyridine modified G-quadruplexes.[226] Albeit this stark difference, the addition of 1eq. EDTA had a remarkably small impact on the CD spectrum at first, showcasing a resilience of the G-quadruplex system and the metal complex against decomplexation. After 4h of no observed changes we opted to add another equiv. of EDTA and mix the system thoroughly and recorded full CD spectra in intervals of 2h over a period of 12h. To our surprise again no change could be identified although the CD band for the metal complex at 315nm was barely visible indicating at least partial decomplexation. Only after a total of 4eq. pf EDTA were added a concomitant change in the CD signature could be observed. The process for the entire reconstitution of the hybrid-1 topology of **htel22-L2a** was completed after 24h (**Figure 49**). These results indicate that this process likely follows a second-order kinetic, dependent not only on the concentration of the DNA but also the EDTA added. Overall, this process is much slower at room temperature (298K) than the folding from hybrid-1 to antiparallel in the first instance. We propose, similar to the results from

Engelhard, that a metal-free meta-stable state is created where the antiparallel topology is initially retained.[200] Yet, this topology does not seem thermodynamically stable under the given conditions and stabilised by the K^+ cation in the central channel. Possibly some repulsive forces and spatial constraints lead to the more favourable refolding of the **htel22-L2a**, not held together by the metal-complex anymore. In more simplistic terms, the bipyridine-metal complex could be envisioned as a ribbon indeed tying the G-quadruplex structure together and enforcing a structural rearrangement. Once the knot of the ribbon has been released that fragile structure collapses slowly back into its initial state. Overall, we were successful in characterising the refolding process of this artificial G-quadruplex **htel22-L2a** and compare it to more natural system which gained valuable insights for how G-quadruplex systems overall behave under different conditions. It furthermore underlines the polymorphic characteristics of this telomeric G-quadruplex and shows that under the given circumstances, previously inaccessible states are possible. This could have implications in a more biological setting and will be further explored in the next chapter of this work.

To expand on refolding G-quadruplexes we also wanted in investigate the systems of **ttel24-L2a**, which have been studied by Engelhard bearing simpler pyridine modifications.[200] Contrary to the pyridine modified systems, **ttel24-L2a** with the newly designed bipyridine modifications does not refold into an antiparallel topology but fold into a hybrid-resembling topology with the distinct maximum at 295nm and a minimum at 240nm. The other version of this second telomeric G-quadruplex, ttel24-L2b however did not adopt a clear new topology when annealed in presence of a divalent metal cation but rather changed just slightly the characteristics of the mixed topology in the CD. Nevertheless, it was of interest to investigate how these system adapt to the presence of a M^{2+} cation when they are already prefolded.

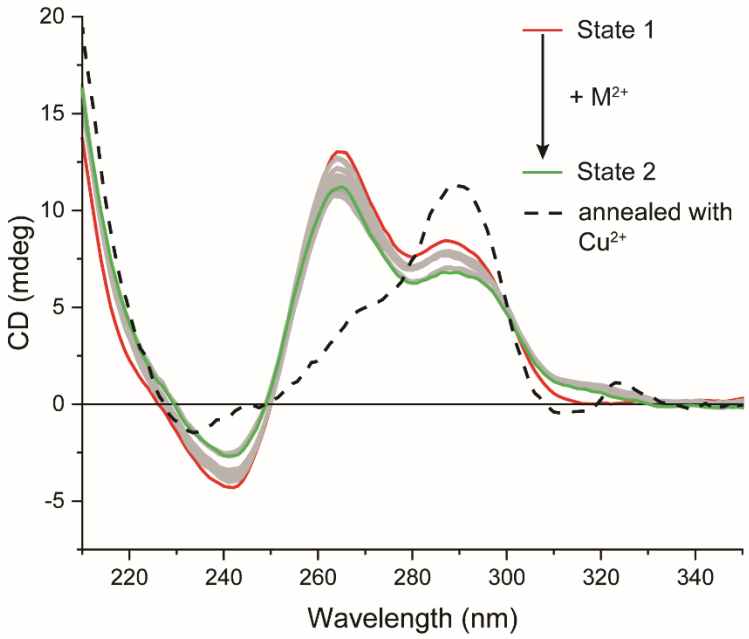

Figure 53. CD spectrum of **ttel24-L2a** showcasing the unsuccessful refolding from a mixed topology upon addition of $CuSO_4$ at 298 K.

All samples were prepared identical to **htel22-L2a** and a first CD spectrum was measured to verify the correct formation of the G-quadruplex. Subsequent addition of 1.1eq of $CuSO_4$ to either sample lead to significant change of the CD signature within the first 3h at 298K. Measurements were continued for a further 3h to exclude the possibility of a slow reaction process yet no changes in the CD bands could be observed for either G-quadruplex. To exclude the possibility of second-order reaction kinetics, new samples of the pre-folded G-quadruplexes and added increasing amounts of $CuSO_4$ in steps of 1eq up to a total of 10eq were prepared. In between each addition an equilibration time of 1h was chosen to give the system time to adapt and possibly start refolding, yet no change could be observed (see SI). After 10eq of $CuSO_4$ and a further 6h a last CD spectrum was recorded again showcasing no significant changes in the CD signature which would indicate the structural reorganization. Both of these ttel24 based system seemed to be highly resistant to a dynamic refolding under the formation of the bipyridine-metal complex and at room temperature. This was surprising as the thermal stabilities of both **htel22-L2a** and **ttel24-L2a** or **-L2b** are relatively similar (ΔT_m = 3 – 4°C) and would indicate some possibility of dynamic refolding. This behaviour points to a kinetic hinderance rather than thermodynamic one of **ttel24-L2a** and **-L2b** whereby the Gibbs activation energy $\Delta G^{\ddagger}$ cannot be lowered by the formation of the metal complex as to proceed at sufficient speed to be detected on a reasonable timescale (hours to days). This rendered both G-quadruplexes not suitable for a quantitative analysis and no kinetic rate constant or other parameters such as enthalpy and entropy of change could be determined. All other synthesised sequences in this work

showed no change in their topology when in presence of a M^{2+} cation. Those sequences showing a change upon M^{2+} addition in Na^+ containing buffer were unclear if the equilibrium between mixtures of topologies was affected or a refolding occurred and are therefore not further discussed in this work.

These results overall demonstrate that the systems need to exhibit a balance between structural flexibility—which enables adoption of distinct metal-triggered G-quadruplex topologies—and thermal stability, as evidenced by its resistance to exogenous chelating ligands. Additionally, the refolding of the individual G-quadruplexes follows different kinetic pathways and is difficult to accurately predict beforehand. Furthermore, we wanted to investigate other possibilities of impacting the topologies and refolding of these modified G-quadruplexes other than the presence or absence of the metal complex.

3.5 Refolding under external conditions

3.5.1 LiCl

Lithium chloride (LiCl) serves as a critical experimental tool for probing cation-dependent G-quadruplex stability due to its weak coordination with G-quartet cores. Unlike physiologically relevant cations (K^+, Na^+), Li^+ small ionic radius and high hydration energy prevent optimal insertion into the central channel, resulting in significantly reduced thermal stability ($\Delta T_m \approx -15$ to -25°C) and destabilization of folded topologies. This suboptimal stabilization often induces conformational shifts toward less compact structures or promotes unfolding, particularly in human telomeric sequences where LiCl favours hybrid-to-antiparallel transitions or partial denaturation. Consequently, studying the bipyridine modified G-quadruplex systems in presence of LiCl-containing buffers could provide essential insight for distinguishing cation-specific structural effects of G-quadruplex polymorphism and the possibility of accessing and tuning their topology and stability by formation of the respective metal complexes. For this we prepared samples of the respective G-quadruplexes annealed in 10mM HEPES buffer (pH 7.1) and 100mM LiCl and in presence or absence of 1.1 eq $CuSO_4$. We chose this high concentration of Li^+ cations to test the capabilities of the systems under the most extreme circumstances although this bears no physiological relevance as Li+ is a non-essential trace element. Neither of the three systems **of htel22-L2a**, **-L2b** and **ttel24-L2a** could form a stable G-quadruplex regardless of the possible stabilisation through the formation of the metal complex (**Figure 54**, **Figure 55**).

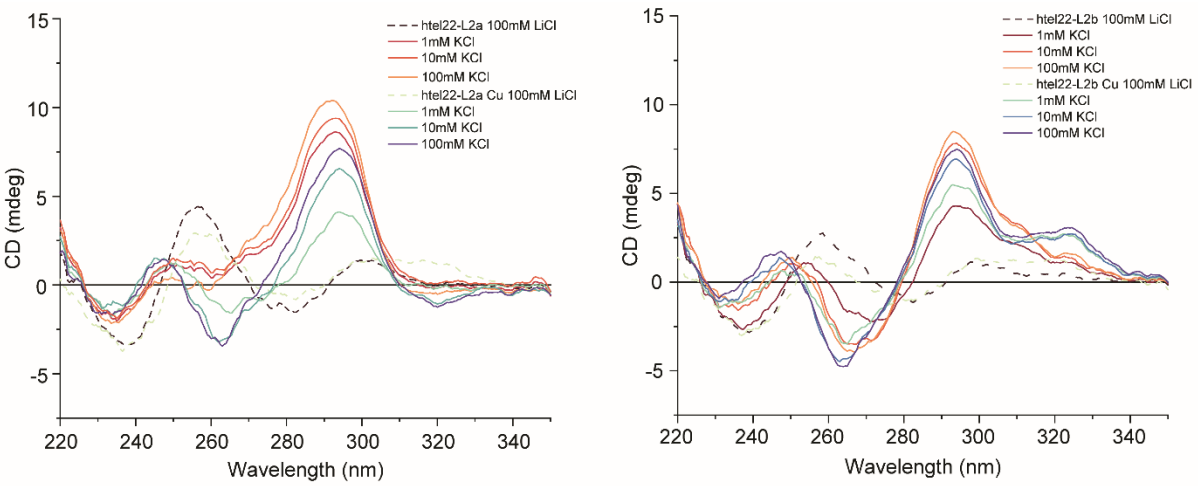

Figure 54. CD spectra of titration htel22-L2a and -L2b pre-annealed in 100 mM LiCl containing buffer (10 mM HEPES, pH 7.1) in absence and presence of Cu^{2+} with KCl to induce refolding. Measurements were performed at 298 K with 15min equilibration time between KCl additions.

In all recorded CD spectra a linear or unstructured DNA topology of the strands could be identified with minima at 240nm and 280nm and maxima at 260nm and 295nm. Interestingly for the htel22 G-quadruplexes the presence of Cu^{2+} and at least the partial formation of the complex could be identified as a weak and broad band at approx. 315nm could be detected. This was absent in the ttel24-L2a case. The high concentration of Li^{+} cations had a detrimental impact on the correct folding of the tested G-quadruplexes and the formation of the bipyridine metal complex could not overcome this destabilising effect.

In order to assess the possibility of overcoming this destabilisation we titrated KCl into the individual pre-annealed G-quadruplexes in steps of 1, 10 and 100mM of final KCl concentration. In all cases already the presence of 1mM K^{+} cations was enough to induce a structural change in respect to the spectra containing just 100mM Li^{+}. This was however not enough to fully restore the expected structure in the individual cases when 0mM Li^{+} and 100mM K+ cations were present. We observed an interesting trend for those G-quadruplexes already containing Cu^{2+} where the complex has potentially preformed. Here the structural reconstitution was stronger, judged by the CD signatures, than in those cases where the Cu^{2+} was lacking. This could indeed support the mechanistic idea where the metal-complex preforms the G-quadruplex and more efficient incorporation of the stabilising K^{+} into the central core. At 10mM K^{+} the destabilising effects of Li^{+} have been almost fully compensated as can be seen by the CD signatures of all systems, closely resembling the non-Li^{+} impacted topologies. One outlier could be identified in the case of **ttel24-L2a** in presence of Cu^{2+}. We expected this G-quadruplex to adopt a predominantly hybrid topology as previously described, yet the observed CD spectra showed an antiparallel topology being adopted. This behaviour could not be further elucidated. We hypothesise that the high

concentration of Li+ cations may destabilise one or multiple topologies in the mixed topology adopted by **ttel24-L2a**, giving the system access to another topology (**Figure 55**).

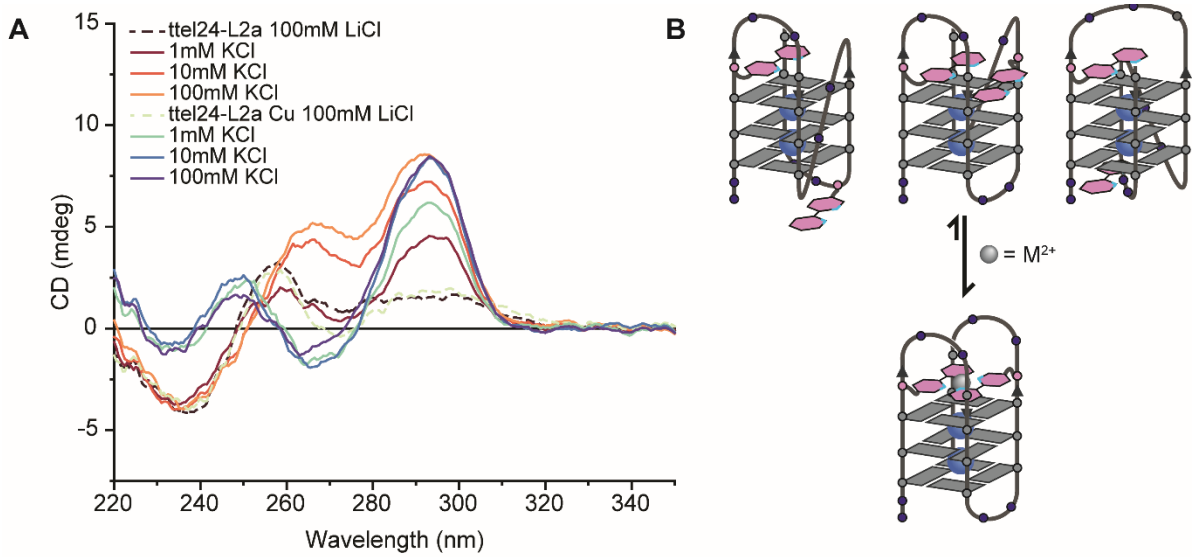

Figure 55. A) CD spectrum of KCl titration into ttel24-L2a pre-annealed in 100 mM LiCl containing buffer (10 mM HEPES, pH 7.1) in absence and presence of Cu^{2+} to induce refolding. Measurements were performed at 298 K with 15min equilibration time between KCl additions. B) Schematic representation of refolding from either an unstructured G-quadruplex or a mixture of various topologies into a predominantly antiparallel topology.

Overall, we could show that these bipyridine modified G-quadruplexes could overcome the destabilising effect of high Li^+ concentration with the addition of low mM K^+ after they have been pre-annealed.

3.5.2 PEG200

Molecular crowding agents such as polyethylene glycol 200 (PEG200) are widely employed to mimic the densely packed intracellular environment in in vitro studies of nucleic acid structures. At physiologically relevant concentrations (20–30% w/v), PEG200 induces an excluded volume effect that significantly enhances the thermal stability of G-quadruplexes by reducing water activity and favouring compact folded states. This crowding environment promotes conformational selection, often shifting equilibrium toward parallel or hybrid topologies while suppressing alternative folds observed in dilute buffer conditions. Critically, PEG200-mediated stabilization closely recapitulates the behaviour of G-quadruplexes in cellular contexts, where macromolecular crowding influences telomere maintenance and gene regulation. Consequently, it was of interest in the context of this work to analyse the impact of PEG200 on the artificial bipyridine modified G-quadruplexes given their dynamic

polymorphic behaviour. It would furthermore generate insight into how these artificial systems might behave when employed in a real cellular context for the last chapter of this work. We again started with the sequences based on the human telomeric G-quadruplex where both htel22-L2a and htel22-L2b were annealed in increasing concentrations of PEG200 (0 – 40% w/t) in 10mM HEPES buffered solution and in presence of the standard 100mM KCl to ensure maximum stability of the G-quadruplexes (**Figure 56**).

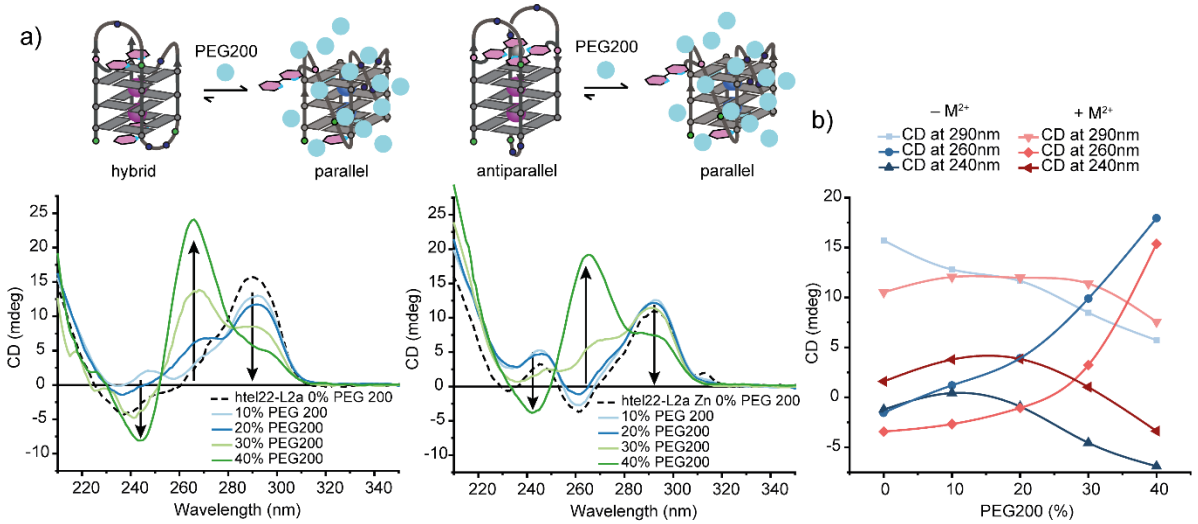

Figure 56. A) CD spectra of **htel22-L2a** in increasing concentration of molecular crowding reagent PEG200 (10 – 40%). PEG200 induces an earlier and stronger refolding of htel22-L2a into a parallel topology when not stabilised by the metal complex as indicated most prominently by the CD signal at 290 nm. B) Change of CD signal intensities of **htel22-L2a** in absence and presence of Zn^{2+} at various wavelengths with increasing PEG200 concentration.

Firstly the CD spectra of **htel22-L2a** without any stabilising metal complex formed showed an expected behaviour of the G-quadruplex where a swift refolding with increased concentration of PEG200 could be observed. Here the system changes from an initially hybrid-1 topology to a strongly parallel topology at 40% PEG200 with the clear maximum at 260nm and minimum at 240nm. Interestingly already at the half-way point at 20% PEG a strong shoulder band at 260nm can be detected and the ratio between hybrid-1/parallel is shifted in favour of the parallel topology at 30% PEG200. As there is no stabilising factor in the form of the metal complex, **htel22-L2a** behaves very similarly to the unmodified htel22 G-quadruplex. The refolding into a parallel topology by a molecular crowding agent such as PEG200 is caused by several factors but mostly through the change in water activity, mimicking a dehydrating osmotic stress. The nucleotides in the lateral loops of a hybrid topology expose a larger solvent accessible surface and are less stabilised in a low water activity scenario which would lead to a destabilisation of the system. This can be avoided if a parallel topology is adopted, where fewer nucleotides are exposed to the bulk solvent. Contrary to this the M^{2+} stabilised **htel22-L2a** experienced a different behaviour, and a

structural impact of the metal complex could be observed as the system remained resilient towards refolding from its antiparallel topology up to 20% PEG200. Only in presence of 30% PEG200 could a first change be initiated whereas a large part of the antiparallel topology was retained. At 40% PEG200 a similar parallel CD signature to **htel22-L2a** in absence of M^{2+} could be observed with the characteristic maximum and minimum at 260nm and 240nm respectively. Yet, a prominent shoulder band at 295nm remained which likely indicated that although the equilibrium was shifted in favour of the parallel G-quadruplex a non-insignificant part remains in its initial antiparallel topology. This behaviour can only be explained by the thermodynamic stability of the metal complex and its capacity to prevent total unfolding of the G-quadruplex in order for the whole G-quadruplex population to adopt a different topology.

PEG200 is also known to show an impact on the stability of G-quadruplexes. We therefore investigate its impact on the thermal melting profiles of **htel22-L2a** in presence and absence of the a priori stabilising metal complex. Without M^{2+} the G-quadruplex was highly destabilised with an increased amount of the molecular crowding agent and reached a maximum destabilisation of ΔT_m = - 16 °C (see SI).

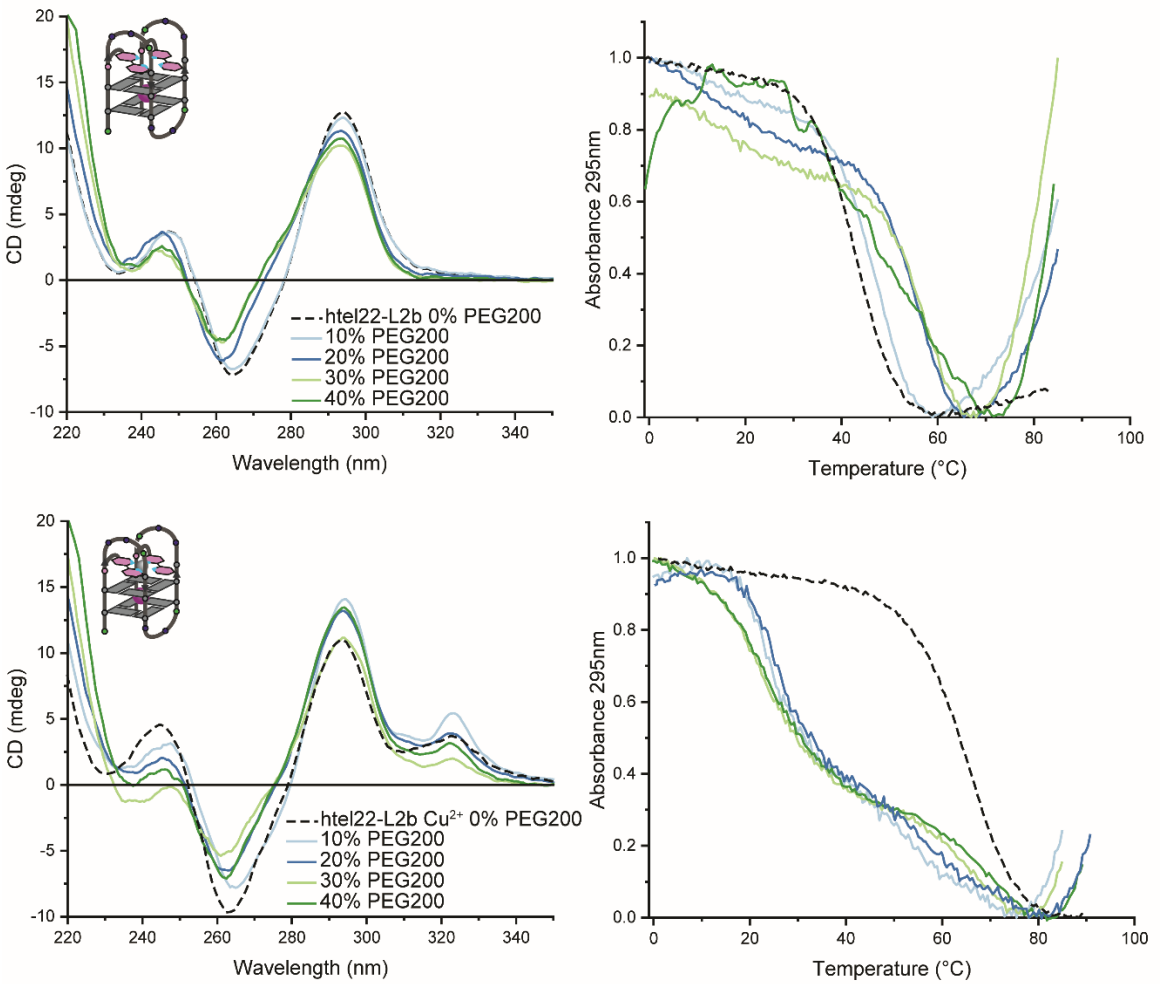

Figure 57. A) CD spectra of **htel22-L2b** in increasing concentration of molecular crowding reagent PEG200 (0 – 40%). PEG200 does not induce a refolding of htel22-L2a into a parallel topology both in absence and presence. B) UV-Vis melting curve analysis of **htel22-L2b** in absence and presence of Cu^{2+} with increasing concentration of PEG200 (0 – 40%).

Interestingly a second melting event at T_m = 82 °C could be detected at 30% PEG200, which is representative of the parallel folded **htel22-L2a**. Although the M^{2+} stabilised structure also showed structural refolding into a parallel topology by PEG200, no large impact on its thermal stability could be observed as the melting temperatures were only minimally lowered ΔT_m = -1 – 2 °C. The portion of the parallel folded G-quadruplexes might either be not large enough to exert a detectable second melting event or the melting points T_m of both metal stabilised **htel22-L2a** antiparallel and PEG200 refolded parallel topologies might lie close together. No melting profiled could be obtained for samples containing 40% PEG200. To better understand how PEG200 might impact the stability of the metal complex within the G-quadruplex of htel22-L2a we chose to investigate a system that did not show the possibility to refold into another topology regardless of the conditions. Therefore **htel22-L2b**, closely related to **htel22-L2a**, was chosen as ideal system. Firstly **htel22-L2b** needed to be

investigated without the stabilising M^{2+} and whether it adopts a different topology through the crowding effect of PEG200. Interestingly no structural impact could be observed even until 40% PEG200 where the system retained a fully antiparallel topology. An identical picture presented itself when the **htel22-L2b** was annealed in presence of M^{2+} and increasing amounts of the crowding agent. Again, the G-quadruplex retained its antiparallel topology. More interestingly the band at 315nm, indicative of the formed bipyridine metal complex only showed minor changes and overall decrease in intensity up to 40% PEG200 (**Figure 57**). This showed that the crowding conditions did not largely affect the metal complex which remains intact which retroactively explain the difference observed for the **htel22-L2a** system. We can concluded that the formed metal complex is indeed capable of partially retaining some structural integrity of the G-quadruplex and does not allow full unfolding and refolding of the system. The melting curve analysis of **htel22-L2b** in presence of PEG200 delivered different results compared to htel22-L2a. Here the non-complex stabilised G-quadruplex experienced an increase in thermal stability of up to ΔT_m = +14 °C at 30% PEG200 which is in expectation of literature reported effect of PEG200. The Cu^{2+} stabilised **htel22-L2b** samples however showed a strange behaviour which was difficult to interpret clearly. In all cases a first major melting event at approx. T_m = 24 °C could be observed which lies ΔT_m = – 44 °C under the melting point of **htel22-L2b** in absence of PEG200. Additionally, a second melting point could be identified at higher temperatures T_m = 67 °C as clearly visible at 20% PEG200. This melting event coincides with the metal-stabilised **htel22-L2b**. This behaviour cannot be fully explained but we hypothesise that the presence of PEG200 potentially prevents the formation of the bipyridine metal complex during the annealing process. As **htel22-L2b** always retains an antiparallel topology, the mixture of metal stabilised, and non-metal stabilised G-quadruplex could not be identified by CD spectroscopy.

3.5.3 Urea/Guanidium HCl

In contrast to molecular crowding reagents which largely impact the structure and energy of the surrounding bulk solvent, water in our case, there are other cosolutes capable of disturbing or altering the secondary structure of biopolymers including DNA and proteins. The main mode of action here is the disturbance of hydrogen bonds wherein the added cosolutes either compete with the surrounding bulk water for hydrogen bonds, effectively lowering the potential of hydrogen bonds formed between water and DNA, or they directly compete with hydrogen bonds between individual components of a biopolymers. In the case of DNA the formation of Watson-Crick-Franklin or Hoogsten basepairs is disturbed resulting in destabilisation or non-formation of the corresponding secondary structure. These agents

can also be classified as chaotropic in such a case and are often used to denature DNA or proteins chemically rather than thermally. The most common reagents used for this application are urea, thiourea or guanidinium hydrochloride. All three molecules share a very similar chemical structure with -NH_2 groups capable of engaging in hydrogen bonding. In some cases a hydrogen bond acceptor moeity, as in the case of urea or thiourea is the carbonyl oxygen or sulphur atom, is present additionally for a more effect H-bond network formation. These characteristics made this class of molecules interesting for us to investigate in the context of our artificial bipyridine-modified G-quadruplexes. Our goal was to observe the impact of urea and guanidinium hydrochloride on the formation and stability of the G-quadruplexes and if the topologies could still be dynamically accessed via metal-complexation, given then adverse circumstances.

In a first instance we prepared **htel22-L2a** under the standard conditions (10mM HEPES buffer pH 7.1, 100mM KCl, 4uM concentration) and measured a CD spectrum to ensure correct folding into the hybrid-1 topology. We then titrated an increasing amount of an 1M Urea solution to the preformed G-quadruplex until a total of 50eq and recorded a CD spectrum after an incubation time of 10min. No change in the CD signature of the G-quadruplex could be observed. This showcased a remarkable stability of the system towards a denaturing reagent. The main stabilising interactions, the Hoogsten basepairs between the guanines, are however heavily shielded from outside solvent and the central channel occupied by the K^+ cation which certainly contributes to the general stability of the G-quadruplex. To see if the system is still capable of refolding, given that is has to expose some the guanines and other nucleotides in the loop to the bulk solvent, we added 1.1eq of $CuSO_4$ to the **htel22-L2a** G-quadruplex and let the system incubate for 2h after which a CD spectrum was recorded. Indeed the system was capable of adopting the expected antiparallel topology despite the presence of 50eq of urea in the solution. To compare, we prepared the same G-quadruplex with Cu^{2+} preadded as to form the antiparallel topology, and then titrated urea in the same fashion. No impact could be detected here and even the metal-complex stays fully intact. To maximise the adverse effect of urea, we increased its concentration to 7M in which **htel22-L2a** was now prepared. To our surprise the G-quadruplex still adopted the hybrid-1 topology in absence of an M^{2+} cation to form the complex. Then 1.1eq of $CuSO_4$ was added, mixed and without incubation, CD spectra recorded in 20min intervals. We could nicely observe how the G-quadruplex refolds again into the antiparallel topology as if no urea were present in the solution. This feature is quite remarkable as 7M urea is considered strong enough to denature most proteins and DNA secondary structures.[227] The formation of the metal-complex is of high enough structural and thermodynamic impact to overcome the destabilising effect of the H-bond competing urea molecules.

We repeated the experiments in the identical fashion with guanidinium HCl. For the titration experiments, where guanidinium HCl was added to the prefolded G-quadruplex, very similar results could be obtained where the system showed no impact to the folding or refolding through addition of M^{2+}. When increasing the concentration to 7M the situation presented was however different from urea. Interestingly the starting structure of **htel22-L2a** was slightly impacted but still largely resembled a hybrid topology with a more pronounced shoulder band at 270nm. The minimum at 240nm could not be detected anymore due to the absorbance of the chaotropic agent from 254nm downwards. Addition of 1.1 eq $CuSO_4$ did induce some initial changes, expressed largely as a decrease in the overall intensity of the CD signature. Over the course of 2h no refolding into the antiparallel topology could be observed. The experiment was repeated with the same outcome to exclude any error in preparation. We then measured the pH of the final solution of DNA and 7M guanidinium HCl which resulted in a reading of pH 4.31, well below the neutral conditions usually needed for the correct formation of the G-quadruplex. This change could have an impact on the overall structure and stability of the system. We then neutralised the prepared the sample and remeasured the. Surprisingly a very similar result as to the acidic conditions was observed leading to the conclusion that the lowered pH had little to no impact on the hindered folding or refolding of **htel22-L2a**. It is proposed that due to its cationic nature, not only does the guanidinium engage in hydrogen bonds with parts of the G-quadruplex but also exhibits Coulomb interactions with the negatively charged phosphate groups in the sugar backbone of the DNA G-quadruplex. This could lead to a hindered flexibility of the overall system and its hindered capacity to adopt a different topology.

Overall, it could shown that guanidinium HCl but not urea could exert its destabilising characteristic as chaotropic reagent on the tested G-quadruplex of **htel22-L2a**. Other bipyridine modified system were omitted from further investigation as they either do not refold at all or there is no clear transition from two distinct topologies.

3.6 Binding of alternative transition metal cations

3.6.2 Triple modified G-quadruplex htel22-L3a

All G-quadruplexes sequences discussed thus far contain two bipyridine modifications at varying positions through which various topologies could be dynamically accessed through the formation of a corresponding metal complex.

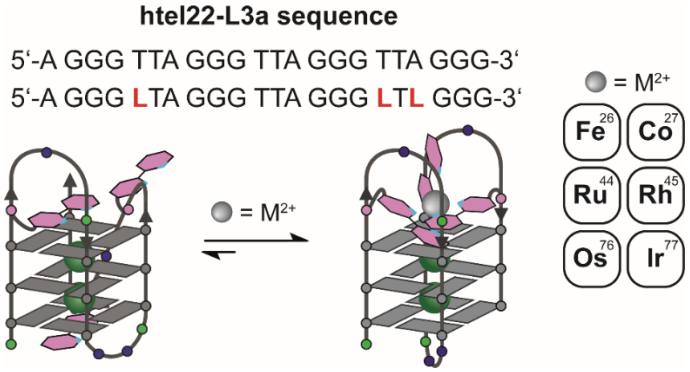

Figure 58. Schematic representation of htel22-L3a bearing three bipyridine modifications. Positions modified with **BiPy-L1** have been marked with L in the oligonucleotide sequence.

We showed that the toolbox of the transition metal cations exerting either topological change and/or thermal stabilisation could be expanded beyond just Cu^{2+} but included Ni^{2+}, Zn^{2+}, Co^{3+} and Cd^{2+}, yet binding of heavier transition metals or those adopting octahedral coordination geometries was unsuccessful. With the knowledge of spatial orientation of the bipyridine units within the G-quadruplex loop region, derived from the MD simulations, a new variant of **htel22-L2a** was synthesised bearing a third bipyridine unit in close proximity at position #17 in addition to those present at #5 and #19 in the sequence. Interestingly, **htel22-L3a** still folded into a hybrid-1 topology in presence of K^+ and showed no large differences identifiable to **htel22-L2a** by CD spectroscopy (**Figure 58**). The new system was capable of binding the already established transition metals and refolding into the expected antiparallel topology was also possible.

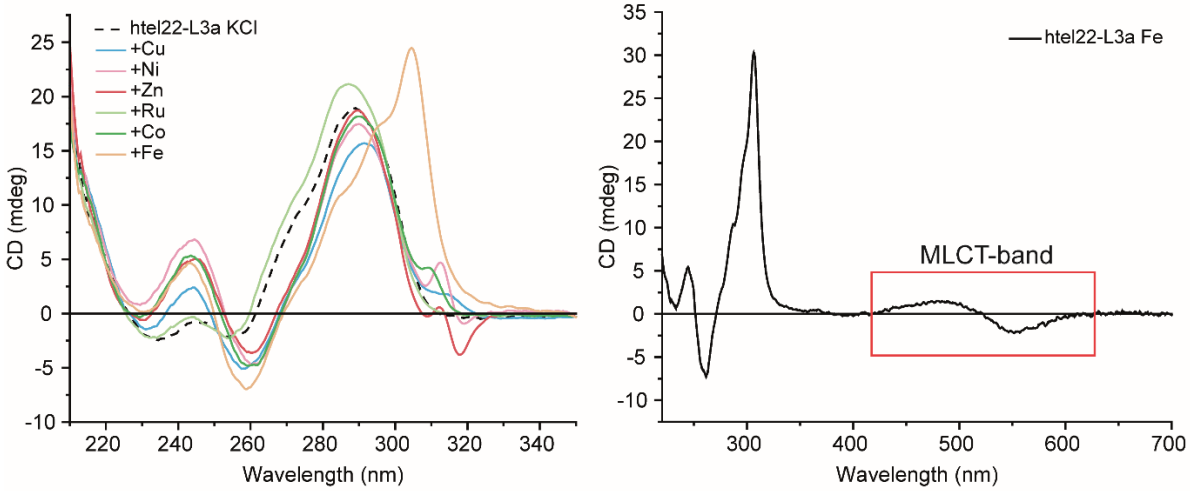

Figure 59. CD spectra of htel22-L3a in presence of various transition metal cations with either tetrahedral, square-planar or octahedral geometry. Formation of Fe-bipyridine complex identified by strong absorption band at 315 nm indicative of pi-pi* transition of the bipyridine ligand.[228] B) Extended CD spectrum of htel22-L3a with Fe^{2+} showing the MLCT band at 520 nm.

We measured CD spectra in a wider range up to 700nm in order to exclude the potential formation of octahedral complexes with either of the divalent metal cations which would lead to absorption bands due to the formation of metal-to-ligand-charge-transfer (MLCT) bands. Yet none of the tested metals showed indications of the formation of an octahedral trisbipyridine complex (**Figure 59**). We then employed Fe^{2+} and Ru^{2+} as these two predominantly form octahedral complexes due to their d6-electron configuration. Although Ru^{2+} seemed to have no impact and did not lead to a refolding of htel22-L3a, Fe^{2+} was capable of being bound by the ligands within the G-quadruplex and induce the expected structural change. From the CD signature it was immediately obvious that indeed the octahedral complex was formed as a large CD band at 305nm for the ligand centered π-π* transition as well as a weaker MLCT band at 450nm were observed. The MLCT band was in good accordance with the isolated $[Fe(bipy)_3]^{2+}$ complex by. Native-MS measurements confirmed the formation of a G-quadruplex bound Fe^{2+} complex (**Figure 60**).

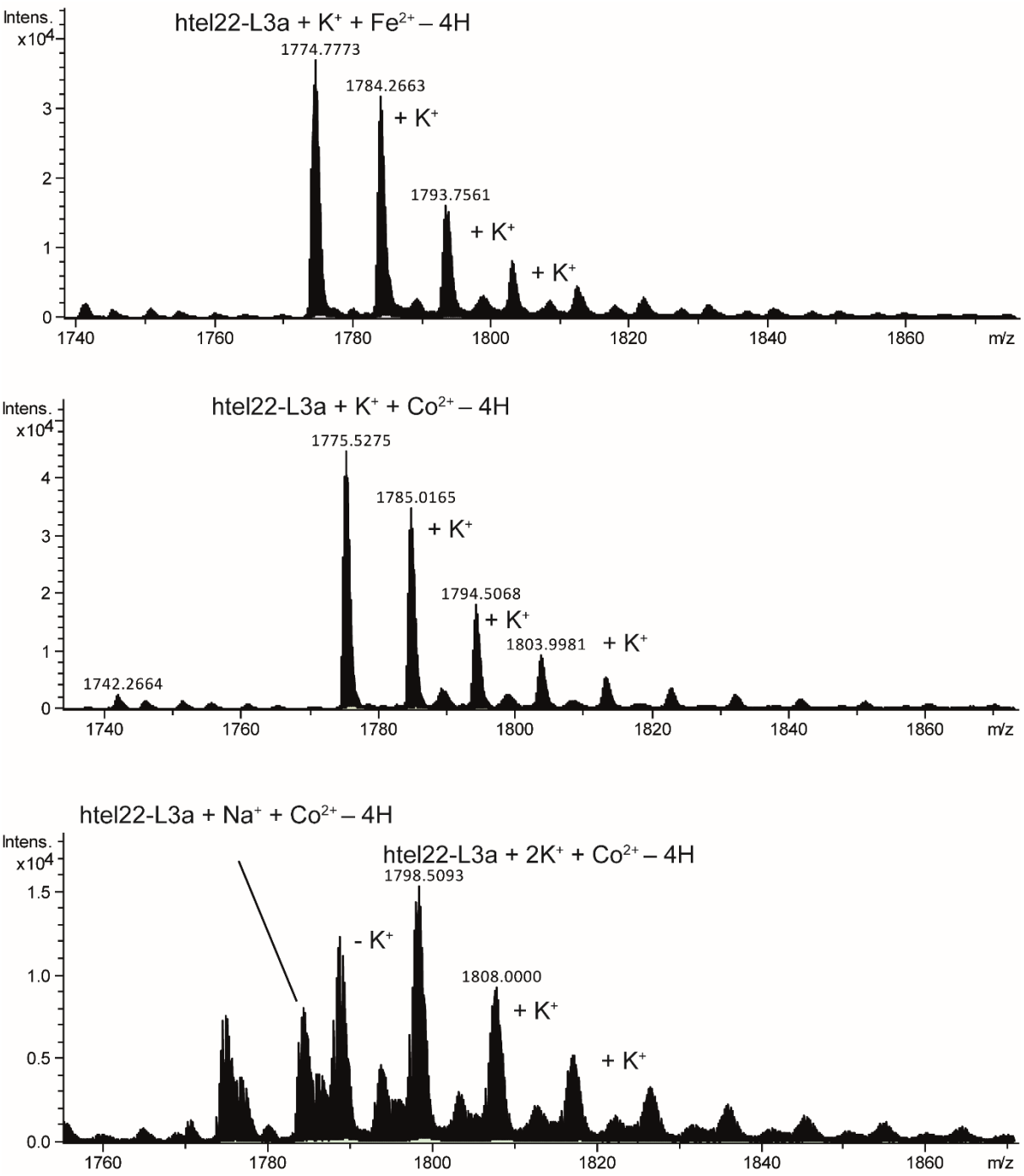

Figure 60. Native ESI-MS spectra of htel22-L3a annealed in presence of Fe^{2+}, Co^{2+} or Cd^{2+}. All spectra have been zoomed into the 4- species to visualise the isotopic pattern.

Although the isolated $[Fe(bipy)_3]^{2+}$ complex is not fluorescent as the excited state is extremely short-lived through intersystem crossing (ISC) from single $MLCT^1$ to triplet $MLCT^3$ followed by transition into a low-lying metal-centered (MC) state within <130 fs followed by non-radiative decay to the groundstate (GS), we nevertheless further explored its photophysical properties. Excitation and emission spectra were recorded and confirmed the MLCT absorption band with a maximum at $\lambda_{max, exc.}$ = 495nm. Interestingly an emission could

be recorded showing a maximum at $\lambda_{max, em.}$ = 520nm and a small Stokes shift of $\Delta\lambda$ = 25 nm. This small Stokes shift present in **htel22-L3a**-Fe^{2+} complex is atypical for octahedral complexes. Contributing factors to a diminishing Stokes shift are geometrical rigidity, intersystem crossing mechanism upon excitation and solvent reorganisation around the excited complex.[229–231] As the complex is buried within the crowded loop region of the G-quadruplex it seems likely that structural reorganization, for example metal-nitrogen bond elongation or contraction, are very limited without leading to the destabilisation of the G-quadruplex. As the complex is only partially exposed to the bulk solvent within the loop, while being shielded from it on the side oriented towards the hydrophobic G-core, the lack of solvent reorientation around the excited complex could additionally contribute to the stark differences of the $[Fe(bipy)_3]^{2+}$ complex covalently bound within the **htel22-L3a** G-quadruplex and isolated complex in solution (**Figure 61**).

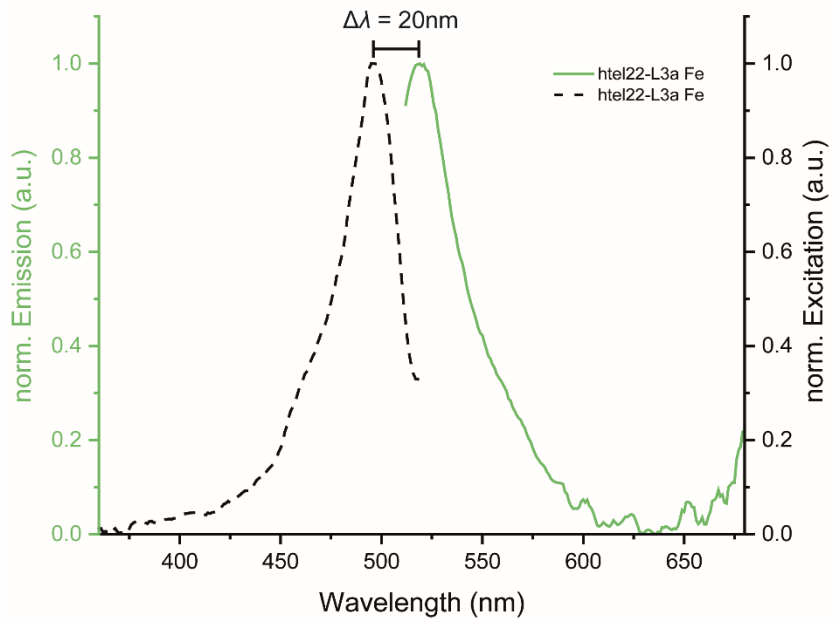

Figure 61. Excitation and emission spectrum of htel22-L3a in presence of Fe^{2+}. Emission was recorded after excitation at 520 nm (MLCT band).

The observed fluorescence could be caused by several factors. Strong structural rigidity could render MC states less accessible as less geometric distortion is possible or an overall pseudo-octahedral geometry.[232,233] Additional shielding effects of the Fe-complex by the DNA structure from the bulk solvent could lower vibrational dissipation pathways, as has been shown that solvation environment impacts lifetime and energy of the MLCT state.[233] Direct proof is however still missing and constitutes an objective beyond this work.

3.7 G-quadruplex Protein Interaction

The dynamic interplay between G-quadruplexes (G4s) and regulatory proteins represents an important layer of genomic control, with hnRNP A1, Pif1, and DHX36 as exemplary proteins where their respective activities directly influence G4 stability, topology, and biological processes. These proteins possess specialized recognition mechanisms for G4 structures, with implications for telomere integrity, replication fidelity, and transcriptional regulation, which are all highly sensitive to chemical modifications of the G-quadruplex scaffold. Many more proteins exist that have been closely linked to engage in G-quadruplex regulatory interplay, yet the focus of this work will remain on the above mentioned examples.[127]

As mentioned in the introduction of this work, hnRNP A1 serves as a master regulator of telomeric G-quadruplex dynamics through its dual RNA/DNA-binding domains. Its N-terminal intrinsically disordered region (IDR) facilitates rapid diffusion along single-stranded DNA, while tandem RNA recognition motifs (RRMs) selectively engage the loops of G-quadruplexes via π-stacking and electrostatic interactions. The core structure of this motif consists of four β-sheets with two α-helices embedded within an approx. 90 amino acid long stretch for each RRM unit (β1-α1-β2-β3-α2-β4). Main interaction with ssDNA occurs through π-stacking interaction of aromatic amino acid residues (Phe, Tyr, Trp) within a β-sheet and exposed nucleobases of the target as well as electrostatic and hydrogen bond interactions, rendering the presence of the 2'-OH group of RNA not necessary to facilitate binding and recognition.[234–236] Critically, hnRNP A1 resolves telomeric G4s (e.g., human htel sequences) by destabilizing parallel topologies through loop displacement, thereby enabling telomerase access—a process compromised in aging and cancer where hnRNP A1 dysregulation correlates with telomere fragility, meaning that the telomeric regions can become prone to increased replication stress, an abnormal G-quadruplex accumulation and DNA breakage at the chromosome ends. Recent structural studies reveal that its binding affinity is exquisitely topology-dependent, with antiparallel G4s exhibiting 5-fold higher dissociation constants than parallel folds, suggesting that chemical modifications altering loop conformation (e.g., ligand-induced rigidity) could profoundly modulate this interaction.

The Pif1 helicase operates as a replication fork guardian, resolving G-quadruplexes as they represent obstacles during DNA synthesis through a unique 5′→3′ translocation mechanism. Pif1's specificity arises from its N-terminal domain, which recognizes the G-core rather than loops, enabling processive unwinding even in K^+-stabilized structures, usually extremely thermally and mechanically stable. The deficiency of this helicase leads to G-quadruplex dependent replication stalling, double-strand breaks, and genomic rearrangements. These phenotypes are exacerbated in htel regions where G-quadruplex polymorphism creates heterogeneous replication barriers. The activity of Pif1 can be altered by quadruplex binding

ligands such as pyridostatin, implying that potentially the chemically modified G-quadruplexes in this work, with their enhanced thermal stability may evade resolution. This helicase's sensitivity to G-quadruplex structural nuances positions it as an ideal probe for assessing the functional consequences of synthetic modifications.

As described in detail in the introduction, DHX36 (RHAU) is the most potent G4 resolvase known. In a telomeric contexts, important in this work as mostly telomeric G-quadruplex structures are discussed, DHX36 resolves G-quadruplexes to prevent R-loop accumulation and maintain telomere length homeostasis. The depletion of this helicase can trigger telomeric DNA damage responses. More importantly, DHX36 exhibits nanomolar affinity for unimolecular G-quadruplexes but negligible activity toward bimolecular structures thus highlighting topology-dependent recognition. Recent work by Wu *et al.* demonstrates that DHX36-mediated resolution is impeded by loop-embedded modifications (e.g., 8-oxoguanine), suggesting that certain strategic chemical alterations could result in G-quadruplexes resistant to this cellular resolution machinery. This is a key consideration for therapeutic G4-stabilizing ligands.[237]

Altogether these proteins exemplify how G-quadruplex–protein interactions are regulated by structural context: hnRNP A1 targets loops, Pif1 engages the core, and DHX36 discriminates topology. Their varying sensitivity to G-quadruplex stability, cation dependence and conformational dynamics underscores why chemically modified G-quadruplexes, in particular those bearing a modification to their loop flexibility or quartet planarity, can potentially elicit protein-specific responses. As our experimental results demonstrate, such modifications can decouple thermal stability from biological function, revealing that metal complex-induced topological shifts may paradoxically enhance or suppress protein binding independent of melting temperature. This context-dependent interplay necessitates direct interrogation of protein–G-quadruplex interfaces when designing targeted structural modulators and give a direct access point for our metal-complex stabilised G-quadruplexes.

3.7.1 Synthesis of FAM labelled G-quadruplexes

In order to investigate DNA G-quadruplex-protein interactions and specifically binding constants (K_d) several methods of analysis were possible, among them electrophoretic mobility shift assay (EMSA) or fluorescence polarisation (FP) both requiring fluorescent labelling of either interaction partner. As modifying the proteins would include extensive adaptation of the expression process and potentially genetic engineering of the plasmid, we chose to modify the artificial G-quadruplexes, as fluorescent modifications are readily available as phosphoramidites.

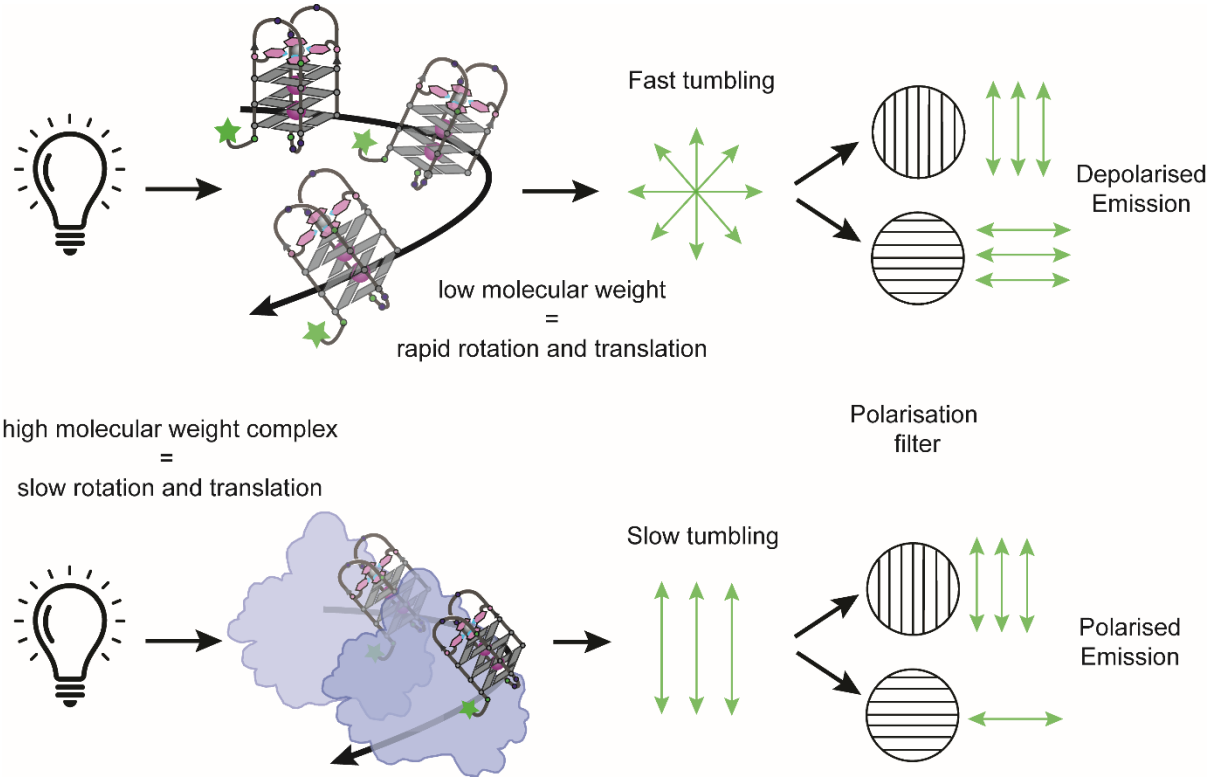

Figure 62. Principle of fluorescence polarisation (FP) assay. A) Polarized excitation light is depolarized by rapidly rotating small molecules bound to a fluorophore. B) Larger complexes rotate slower and hence emit prevalently polarised light.

All sequences were resynthesized with the bipyridine modifications and an additional fluorescein modification (FAM) at the 5'-end. This fluorescent tag is commonly used in biochemical applications and does not interfere with interactions. To exclude any structural changes to the G-quadruplexes we performed both CD and UV-Vis spectroscopy experiments. All sequences were prepared under identical conditions (10mM HEPES pH 7.1, 100mM KCl or NaCl). CD spectroscopy revealed that all sequences formed G-quadruplexes with identical CD signatures and therefore topologies as without the FAM modification. What was crucial was if the dynamic access to other topologies was still possible under the addition of M^{2+} which could be confirmed. Both annealing in presence of M^{2+} or addition of M^{2+} to the preformed G-quadruplex lead to the refolding of **htel22-L2a** from hybrid-1 to the expected antiparallel topology. The other sequences, namely **htel22-L2b** and **ttel24-L2a**, also showed very similar results with their topologies retained even in presence of the additional modification. The thermal stabilities of the G-quadruplexes was also not affected as proven by UV-Vis melting curve analysis with identical values for all systems. Overall, no structural impact of the FAM modification could be detected and therefore further interactions with proteins could be performed (see SI).

3.7.2 hnRNP A1

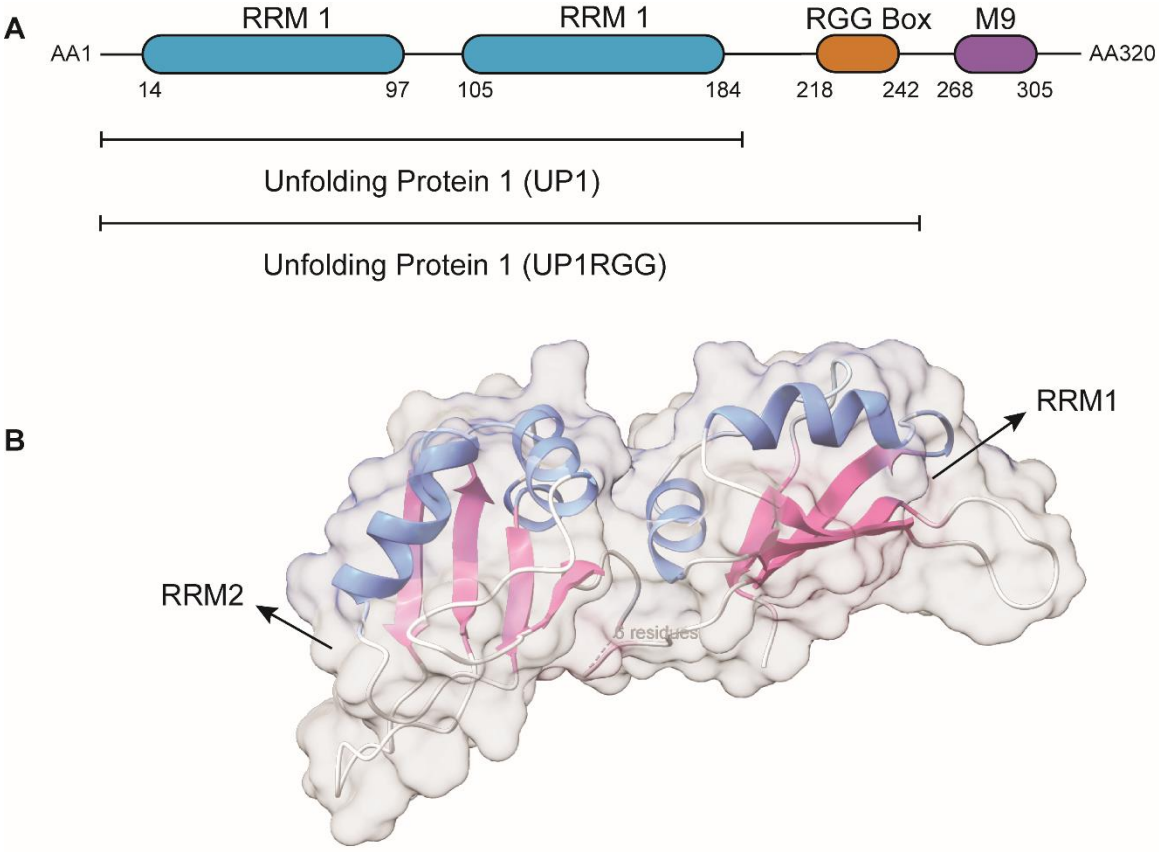

Figure 63. A) Protein domain structure of RNA-binding protein hnRNP A1 with two RNA recognition motifs (RRM) responsible for the binding and unfolding of DNA G-quadruplexes in an ATP-independent manner. The two protein constructs of UP1 and UP1RGG are indicated and include different domains of the full length protein. B) X-ray structure of UP1 with the two RRM domains (PDB: 1UP1). α-helix colour in blue, β-sheet in pink, unstructured parts in white random coil.

As elaborated beforehand, hnRNP A1 is heavily involved in the regulation of telomeric G-quadruplexes and unfolds these DNA secondary structures through an ATP-independent mechanism. Additionally, it showed differentiation between the different topologies and showing the highest binding constants towards antiparallel G-quadruplexes. This made it a prime candidate for investigating its interaction with the bipyridine modified G-quadruplexes, in particular **htel22-L2a**, capable of adopting both hybrid-1 and antiparallel topologies. In addition, **htel22-L2b** and **ttel24-L2a** were included in this first protein interaction study. The full-length protein of hnRNP A1 was not used for these experiments since the G-quadruplex interacting parts lie on the N-terminus to position #249 in the amino acid sequence (AA249) with two RNA recognition motifs (RRM domain) found at AA14 – 97 and AA105 – 184. In addition to that an repeat of arginine and glycine (RGG box) is found further down at AA218 – 249 and is hinted at showcasing favourable interactions with G-quadruplexes. The majority of the C-terminus of hnRNP A1 is disordered with only a nuclear targeting sequence (M9)

present at AA320 – 357 but not involved in any DNA interaction.[234–236] We therefore chose to express two protein constructs from hnRNP A1. The first one was UP1 ranging from AA1 – 196 and containing both RRM domains important for G-quadruplex interaction. The second construct was UP1RGG where the RGG box was added to UP1 and a total length of AA1 – 249 (**Figure 63**). Notable here is that both proteins are relatively small with 22.3 kDA and 27.0 kDa respectively, in stark difference to large helicases usually responsible for the resolving of DNA secondary structures. After successful expression and purification from E.coli bacteria we first investigated the binding affinity of the two proteins towards the three telomeric G-quadruplexes **htel22-L2a**, **-L2b** and **ttel24-L2a** under several conditions bearing different stabilising M^{2+} cations. As method of choice we chose fluorescence polarisation as the smaller interaction partner was our fluorescently labelled DNA.

In this assay the smaller binding partner is fluorescently labelled and in absence of the larger binding partner can freely perform rotation and translation in solution, resulting in low directionality or low anistropoy of the emission. If the larger binding partner is added, as a complex is formed, the overall molecular weight of the pair increases and rotation and translation are slowed down. This results in an increase in anisotropy of the emission (**Figure 62**). When performed over a concentration series, the concentration dependent change of the fluorescence anisotropy can be plotted resulting ideally in a sigmoidal binding curve. Some caveats need to be regarded to the experimental setup. A general estimate of the expect K_d value(s) needs to performed as the concentration of the limiting factor, in our case the DNA needs to be significantly lower than the K_d. If the concentration of the DNA is close to the K_d or even above it, the resulting titration curve merely indicates when a 1:1 complex is formed. As we expected the K_d to lie within 10-100 nM, we chose a starting concentration of the DNA G-quadruplex of 1nM per well in a 384-well plate. The protein concentration added to this ranged from 1uM to 0.03uM over 15 wells. All conditions were performed in triplicates to give statistical significance.

For **htel22-L2a** the calculated binding constants for UP1 were between K_d = 120.5 - 507.6 nM with the lowest value recorded for the Ni^{2+} stabilised species. All other conditions with no M^{2+} or either Cu^{2+} or Zn^{2+} were in a similar range of approx. 120nM. We could not explain the rather extreme outlier of the Ni^{2+} sample except for some unfavourable electrostatic interactions. This pattern repeated when investigating the interaction with UP1RGG, although the K_d values were much lower, indicating a stronger binding. Again, the NI^{2+} stabilisied **htel22-L2a** showed the weakest binding with K_d = 119.5 nM compared to the other conditions where a range from K_d = 37.8 – 79.6 nM was recorded. No large differences between the two adopted topologies, hybrid-1 and antiparallel, could be detected in the case for **htel22-L2a** (**Table 6**). The presence of the metal complex did also not influence the binding of the G-quadruplex to the protein. A larger difference between the two topologies

was expected given the preference of UP1 to bind to antiparallel G-quadruplexes more favourably. This however could indicate that either **htel22-L2a** does not fully convert to an antiparallel topology upon metal binding, or that the protein already starts unfolding the G-quadruplex at such a rapid rate that the structural differences are negated. The presence of the RGG-box in UP1RGG showed an overall increase in binding affinity towards all **htel22-L2a** topologies, indicating its involvement in binding. Likely the positively charged arginine residues add electrostatic interactions with the G-quadruplex, in particular with the polyanionic phosphate backbone, stabilising the overall interaction. While the RRM domains may interact more sequence dependent with the loops of the G-quadruplex, the RGG-box could interact with partially exposed guanine surfaces through cation-π interactions.

Table 6. Dissociation constants (K_d) for UP1 and UP1RGG proteins for **htel22-L2a** and non-quadruplex forming **mut-htel22-L2a** in presence and absence of stabilising divalent metal cations M^{2+} (M = Cu, Ni, Zn) obtained from fluorescence polarisation assays. All experiments performed in triplicates. Experimental conditions: DNA (1 nM) annealed in presence or absence of M^{2+} cations (M = Cu, Ni, Zn; 1.1 eq, 1.1 nM final concentration). Protein concentrations in descending order per well: 5, 2.5, 1.25, 6.25 x 10^{-1}, 3.13 x 10^{-1}, 1.56 x 10^{-1}, 7.81 x 10^{-2}, 3.90 x 10^{-2}, 1.95 x 10^{-2}, 9.76 x 10^{-3}, 4.88 x 10^{-3}, 2.44 x 10^{-3}, 1.22 x 10^{-3}, 6.10 x 10^{-4}, 3.05 x 10^{-4}, 1.52 x 10^{-4} µM.

Topology	Sequence	K_d (UP1) (nM)	K_d (UP1RGG) (nM)
hybrid	htel22	5221 ± 22	4826 ± 26
hybrid-1	htel22-L2a	120.5 ± 11.9	52.5 ± 7.9
antiparallel	+ Cu	126.4 ± 9.5	37.8 ± 4.8
antiparallel	+ Ni	507.6 ± 23.8	119.5 ± 7.6
antiparallel	+ Zn	128.5 ± 8.4	79.6 ± 11.9
non-G4	mut-htel22-L2a	>10000	>10000
non-G4	+ Cu	>10000	>10000
non-G4	+ Ni	>10000	>10000
non-G4	+ Zn	>10000	>10000

In the comparison with **htel22-L2b** we could indeed see that the RGG-box is indeed a larger factor for binding affinity when possible, a mixture of topologies is present as in the case for

htel22-L2a. As **htel22-L2b** can only fold into a fully antiparallel G-quadruplex due to the absence of a third G-quartet, the obtained binding constants are in the low nM range with K_d = 12.4 – 16.6 nM. We suspect that due to the more exposed lateral loops, showcased by the MD simulations, the two RRM domains are predominantly involved in the binding of this G-quadruplex. The G-quartets are blocked by the presence of the bipyridine units and diminish the impact of the RGG box interactions. The presence of the metal complexes did not impact the binding towards the protein in a positive or negative fashion. These K_d -values were compared to the literature reported values for the natural htel22 at K_d for UP1 = 5.2uM and UP1RGG = 4.8uM. Since these values were obtained in K^+ containing buffer, direct comparison only to htel22-L2a was possible. The bipyridine modified system showed an increased binding by several orders (10-50x) compared to the natural system for both UP1 and UP1RGG protein constructs. As natural htel22 folds into an antiparallel topology in presence of Na^+, we compared these binding constants with the htel22-L2b adopting the same topology. Although K_d values for wt htel22 drop to 0.6 – 1.0 uM, they are still weaker by a factor of 100x compared to the artificial **htel22-L2b** (**Table 7**). This remarkable behaviour of the htel-derived sequences could originate from several factors, all stemming from the presence of either the bipyridine modifications themselves or the corresponding metal complexes. The bipyridine units might present additional aromatic surfaces for π-π or cation-π interactions with the protein or even bind within a pocket of the protein as small molecule ligands as the protein approaches from the loop region of the G-quadruplex where the bipyridine modifications are located. The overall stabilisation of the ligands and the complex may lead to a more rigid G-quadruplex and thus to more favourable interactions, especially in regard to the two RRM domains attaching through the lateral loops.

Table 7. Dissociation constants (K_d) for UP1 and UP1RGG proteins for **htel22-L2b** in presence and absence of stabilising divalent metal cations M^{2+} (M = Cu, Ni, Zn) obtained from fluorescence polarisation assays. All experiments performed in triplicates.

Topology	Sequence	UP1 (nM)	UP1RGG (nM
antiparallel	htel22-L2b	12.4 ± 1.0	16.6 ± 0.8
antiparallel	+ Cu	15.9 ± 1.2	14.3 ± 1.8
antiparallel	+ Ni	13.4 ± 1.1	12.8 ± 1.2
antiparallel	+ Zn	13.9 ± 1.0	13.6 ± 2.8

In addition, we investigated the affinity of UP1 and UP1RGG to another telomeric G-quadruplex. **Ttel24-L2a** showed comparable binding results to **htel22-L2a** with K_d values ranging from 72.3 – 124.4 nM for UP1. Also here the presence of the metal complex did not largely influence the binding or make it more favourable. As **ttel24-L2a** changes its topology from a mixture or mixed-hybrid-parallel to towards stronger presence of hybrid no changes in affinity could be observed. In comparison to UP1RGG much stronger binding could be detected once again leading to the conclusion that the RGG-box exert a larger influence when the G-quadruplex does not adopt a full antiparallel topology. Overall, the K_d values for UP1RGG were lower by a factor of 2x and reflected the behaviour of **htel22-L2a**. In order to exclude false positive interactions driven purely by interactions with the bipyridine modifications and the proteins, we repeated the experiments with a mutated **htel22-L2a** (**mut-htel22-L2a**) sequence where all central guanines in a G-stretch where replaced with a thymine. This ensured that no G-quadruplex could be formed while maintaining the incorporated bipyridines. Binding strength of this DNA construct could only be estimated at >5uM showing very low preference to either protein construct. This **mut-htel22-L2a** could still form the corresponding metal complexes, yet no effect on binding reflected in the K_d values could be observed.

Table 8. Dissociation constants (K_d) for UP1 and UP1RGG proteins for **ttel24-L2a** in presence and absence of stabilising divalent metal cations M^{2+} (M = Cu, Ni, Zn) obtained from fluorescence polarisation assays. All experiments performed in triplicates.

Topology	Sequence	UP1 (nM)	UP1RGG (nM
mixed	ttel24-L2a	124.4 ± 25.1	56.5 ± 6.8
hybrid-1/2	+ Cu	109.6 ± 19.6	47.6 ± 3.8
hybrid-1/2	+ Ni	100.1 ± 10.3	72.1 ± 5.7
hybrid-1/2	+ Zn	72.3 ± 12.3	34.1 ± 2.0

Overall the preference of the hnRNP A1 derivates used in this work, UP1 and UP1RGG, towards antiparallel G-quadruplexes could be confirmed. We could show that binding is indeed sequence and salt independent as in the case for **htel22-L2a** and **ttel24-L2a** different topologies in the same salt (K^+) were accessible and did not largely impact the binding strength. The modified G-quadruplexes showed a higher affinity for both proteins than their natural counterparts. As these proteins are both capable of unfolding G-quadruplex structures we needed to investigate the stability of the modified **htel22-L2a**, **-L2b**

and **ttel24-L2a** when exposed to these proteins. CD spectroscopy was chosen as analysis tool as to give insight when and how a G-quadruplex is structurally disintegrating. The initial fold of each G-quadruplex was confirmed by CD spectroscopy after which an increasing amount of the corresponding protein was added up to a total of 5eq. After each titration step, the sample was incubated at 37°C for 15min before a CD spectrum was recorded. This experimental setup was inspired by previous results of Singh.[169]

It was observed that the hybrid-1 topologies of **htel22-L2a** were relatively slow to unfold in presence of UP1 and UP1RGG with a remaining G-quadruplex band at 295nm still present at 5eq. In a fully unfolded state no CD band in this region should be observable as it is representative of the guanine Hoogsten base pairing. We compared these results to the unmodified htel22 G-quadruplex to quantify the extent of unfolding. At the maximum concentration of 20uM protein (5eq), wt htel22 is fully unfolded as no 295nm band is detectable. Although UP1RGG showed significantly stronger binding to **htel22-L2a**, its capability of unfolding the G-quadruplex were similar when comparing relative foldedness. In addition the unfolding proceeds without the formation of intermediate DNA-protein structure with long lifetimes as indicated by the isosbestic point at 260nm.

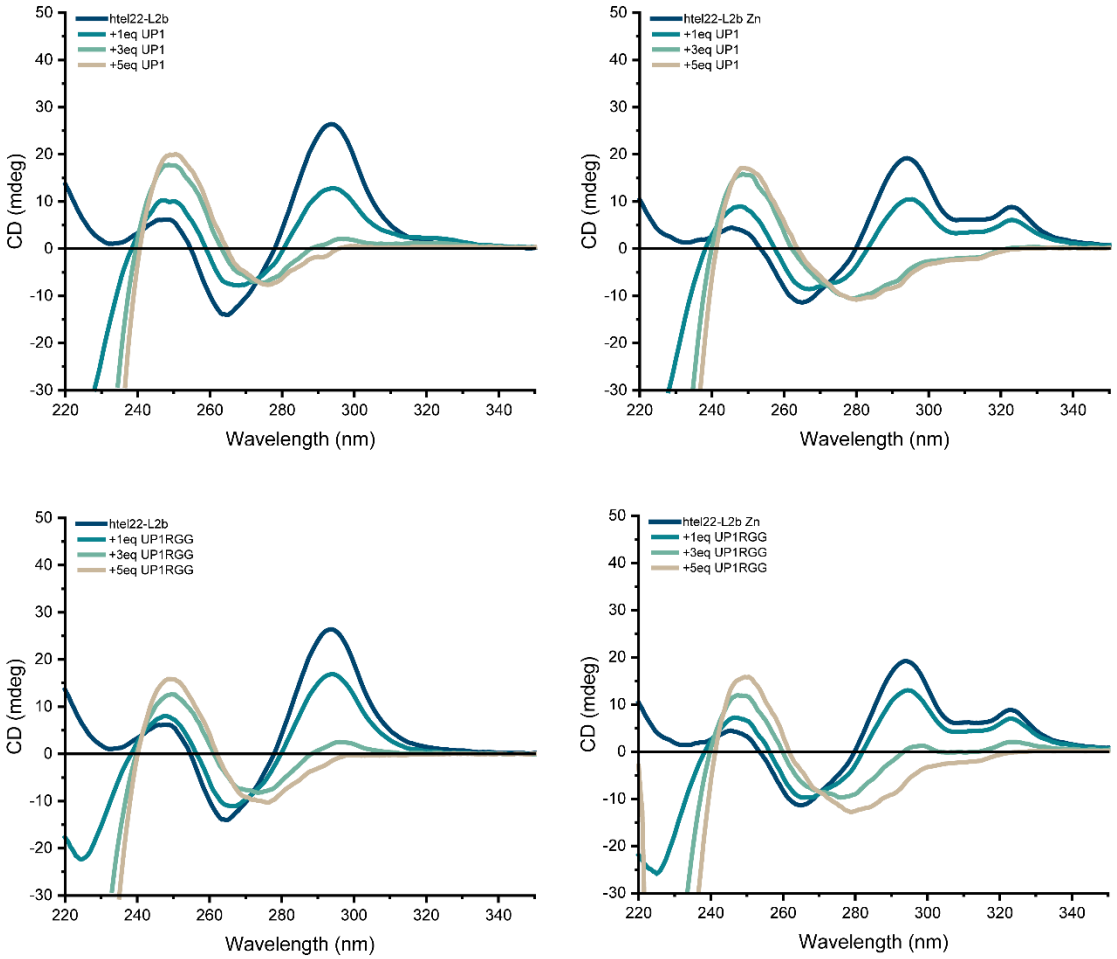

Figure 64. CD spectra of unfolding experiments of **htel22-L2b** in presence and absence of stabilising divalent metal cations M^{2+} (M = Cu, Ni, Zn) with UP1 and UP1RGG proteins. Protein was titrated to a prefolded G-quadruplex solution and equilibrated between each step for 15min between each step. Conditions: 4µM DNA annealed in 10 mM HEPES buffer (pH 7.1) and 100 mM KCl. Protein titrated into DNA solution to final concentration of 4, 12 and 20 µM with 15 min equilibration time in between each step.

The metal-stabilised and now antiparallel versions of **htel22-L2a** showed an overall stronger resilience against unfolding. In the case of UP1, the relative foldedness was still 40 %. This is good accordance with previously reported results of the unwinding G-quadruplexes by hnRNP A1 or its derivatives. Here the two RRM domains bind to the loop regions, in particular lateral loops to initiate the unfolding through breakage of hydrogen bonds between the guanines of the G-core. Since the bipyridine complex sits above the first G-tetrad within the loop region where UP1 approaches from, the unfolding is hindered in its initation through the thermally stable bipyridine metal-complex. This process is rendered more efficient in presence of the RGG-box, which should facilitate not only binding but also unfolding of the G-quadruplex as suggested by Singh.[169] The relative foldedness at the final protein concentration was indeed lower at 20 %, comparable to the hybrid-1 topology. When

compared to the **htel22-L2b** an impact of the increased binding strength could be noticed. Under all conditions the G-quadruplex was fully unfolded at 12uM protein concentration (3eq) as no band at 295nm could be detected. This held true for both UP1 and UP1RGG treated samples. The overall lower thermal stability of **htel22-L2b** in comparison to **htel22-L2a** could be a contributing factor as less guanine Hoogsten basepairs need to be disturbed to achieve full unwinding of the DNA (**Figure 64**).

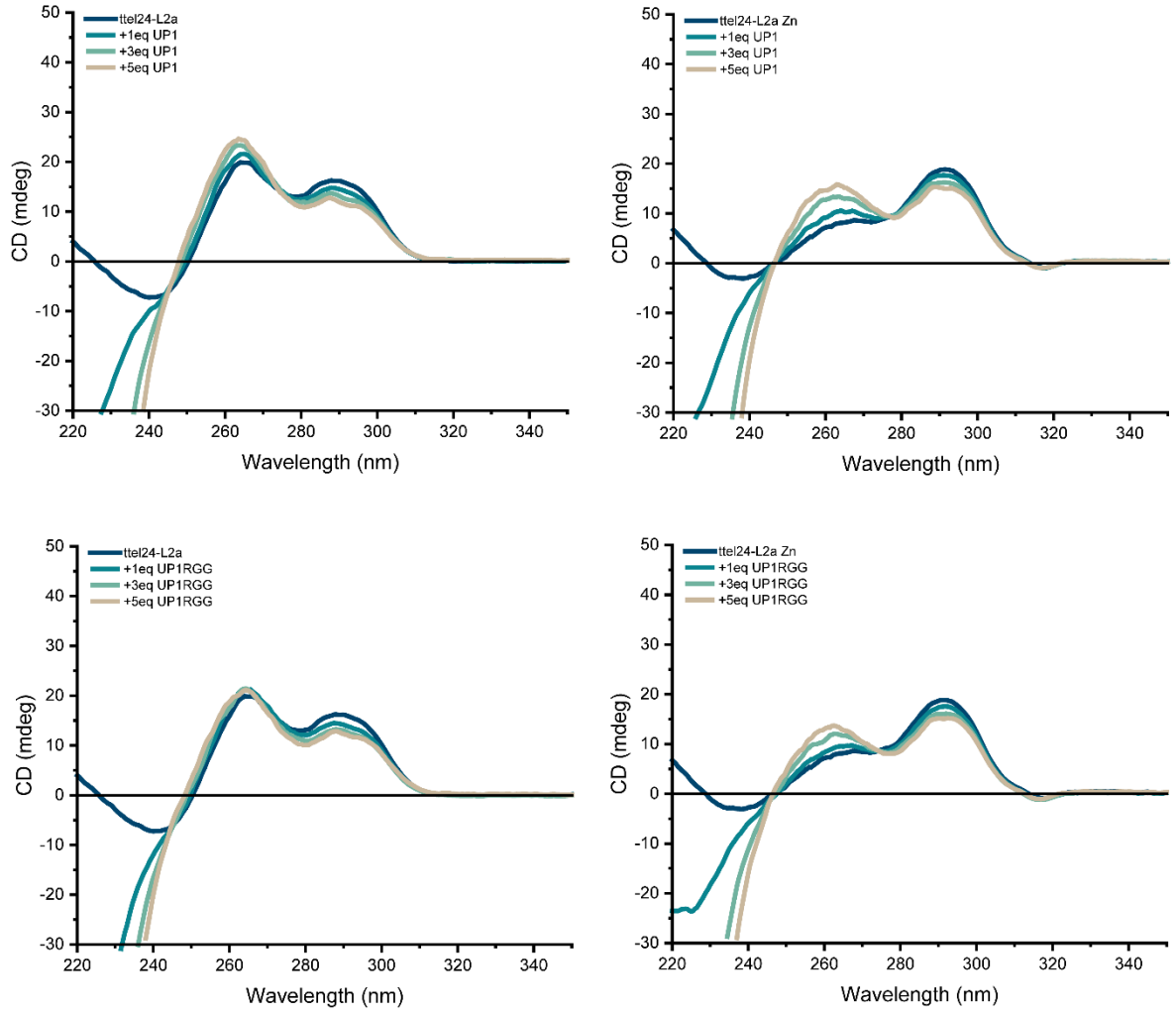

Figure 65. CD spectra of unfolding experiments of **ttel24-L2a** in presence and absence of stabilising divalent metal cations M^{2+} (M = Cu, Ni, Zn) with UP1 and UP1RGG proteins. Protein was titrated to a prefolded G-quadruplex solution and equilibrated between each step for 15min between each step.

The efficiency of the two proteins could be enhanced since the two lateral loops are stronger exposed and are spatially more separated from the G-core. Interestingly we could observe that the metal-complex does not directly dissociate in the presence of up to 1eq of either protein. These results further support the hypothesis of interaction and unfolding mechanism proposed in literature and could be reproduced with natural htel22 in Na^+ containing buffer, adopting an antiparallel topology. The unfolding efficiency is comparable to **htel22-L2b**.

Lastly the resilience of **ttel24-L2a** was tested in presence of both UP1 and UP1RGG proteins. Although binding strength was comparable to **htel22-L2a**, the extent to which both proteins were capable of unwinding the formed G-quadruplex was of minor extent. As **ttel24-L2a** is likely a mixture between parallel and hybrid topologies in absence of the stabilising metal complex, only the CD band at 295nm indicative of the hybrid topology showed some decrease at 5eq of either UP1 or UP1RGG. The band at 260nm showed increased intensity but stems largely from the DNA-protein complex forming and the CD signature of the protein itself (see appendix). This unexpected behaviour translated to the M^{2+} containing samples of **ttel24-L2a** now predominantly folded in a hybrid topology due to the formation of the metal-complex. Only minor decrease in the 295nm band could be observed while the 315nm, representative of the metal-complex, remained unchanged throughout, further supporting that the G-quadruplex only partially unwinds through UP1 or UP1RGG actions. Although the influence of the RGG-box lead to a significant increase in binding strength, it could not assist the protein in resolving the ttel24-L2a G-quadruplex. When compared to the unmodified ttel24 sequence which adopts a similar mixed topology as ttel24-L2a in K+, the extent of unwinding was much stronger with a relative foldedness of 80 % remaining at 5eq of both UP1 and UP1RGG. Thus **ttel24-L2a** represented a bipyridine modified G-quadruplex that both express strong binding in the low nM range towards UP1RGG yet remained in its folded state in presence of increasing concentration of the protein (**Figure 66**).

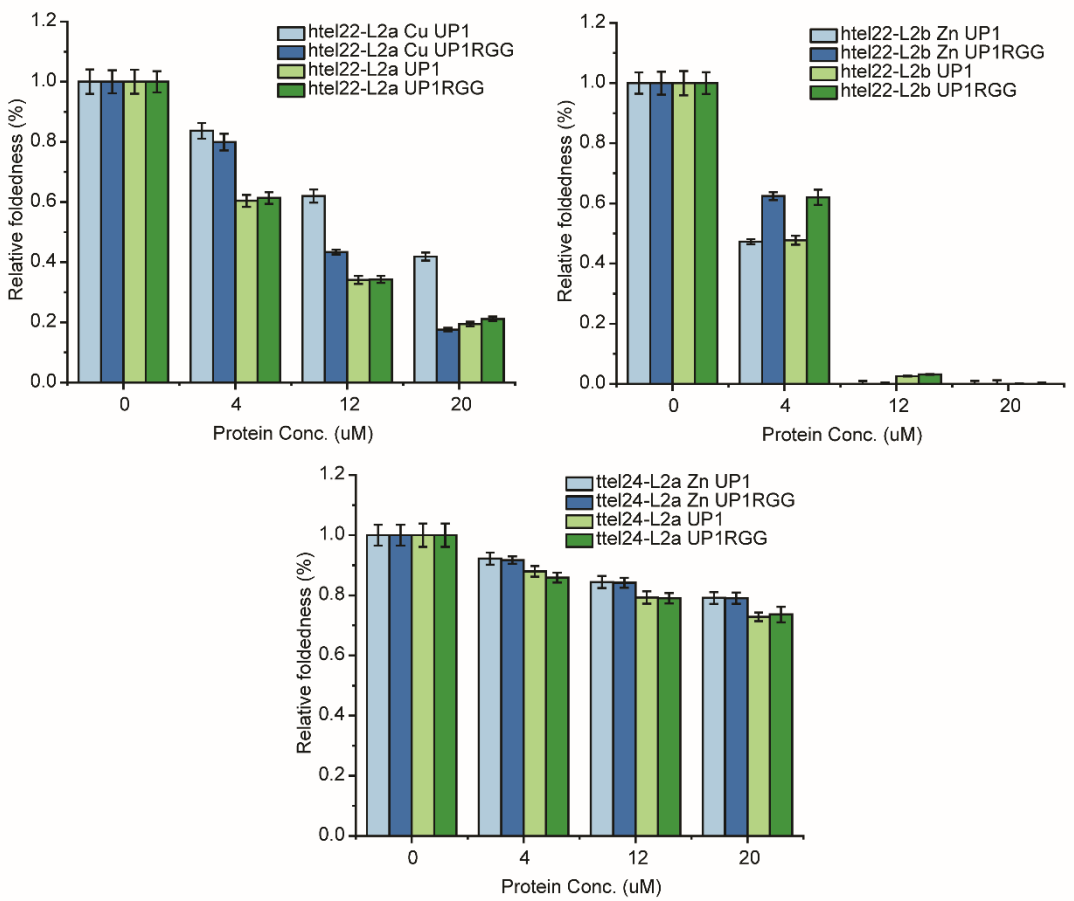

Figure 66. Relative foldedness of G-quadrupelxes htel22-L2a, -L2b and ttel24-L2a calculated from the intensity of the CD band at 295 nm upon unfolding by increasing concentrations of UP1 and UP1RGG.

Overall these results were the first proof of interaction between ligand modified G-quadruplexes and natural proteins and showcases that binding affinities were either retained or improved compared to the natural unmodified counterparts. We were successful in creating a system in the form of **ttel24-L2a** that combined high affinity towards the POI and resilience against their mode of action thus creating potential for the creation of the envisioned molecular decoy. To further extend the capabilities and potential target proteins we employed to more examples, heavily involved in the regulation of G-quadruplexes in the human body.

3.7.3 Pif1

As discussed in the introduction to this chapter, Pif1 is involved in resolving G-quadruplex structure in a 5'→3' fashion and is ATP dependent. In contrast to hnRNP A1 helicases cannot spontaneously attach to G-quadruplex structures but need a single- or double stranded overhang as additional structural feature to letch onto. In previous studies, the

minimal structural element determined for efficient binding was a poly thymine or adenine overhang of 9 nucleotides. This overhand only ensure that Pif1 can interact with the isolated G-quadruplex and has no effect on binding strength. An extended design of the modified G-quadruplexes was necessary bearing a poly-thymine (15nt) 5'-end single stranded overhang. In total four sequences were equipped with this feature: **htel22-L2a**, **-L2b**, **pu22-L2a** and **cmyc-L2a**. These G-quadruplexes cover all three topologies of hybrid, antiparallel and parallel in the form of pu22 and cmyc-L2a and make for a possible differentiation of structural preferences of Pif1 binding. To ensure that the G-quadruplexes are not impacted by the additional overhang CD spectroscopy was performed. All sequences were prepared in the standard conditions with 100mM KCl. UV-Vis thermal analysis was also performed to investigate the stability of these newly modified bipyridine and T15 bearing structures. A clear impact on the CD spectra on telomeric sequences **T15-htel22-L2a** and **-L2b** could be observed as the 295nm band broadened significantly and retained this feature even in presence of M^{2+}. This spectral change is however expected and could be observed for the natural htel22 sequences bearing 5`-end polyT overhangs as shown by Raney.[238] It originates from an increase in structural heterogeneity and tail-quadruplex interactions through stacking or backfolding of the polyT tail. Refolding of **T15-htel22-L2a** was unaffected as the characteristic minimum/maximum at 260nm and 240nm for the antiparallel fold were detected (see SI). The parallel G-quadruplexes of **T15-pu22-L2a** and **T15-cmyc-L2a** showed no large differences as structural changes are less likely for these thermodynamically more stable G-quadruplexes. As no lateral loops are present for parallel structures the polyT tail has less possibilities of transient interaction. Importantly, in all cases thermal stability was not affected by the thymine overhang as T_m values were unchanged compared to previously obtained results (see appendix).

FP assays of these G-quadruplexes with Pif1 were performed in an identical fashion as for hnRNP A1 in a 384-well plate. As lower K_d values were expected, the concentration of the DNA was reduced to 0.1nM. All binding curves showed a strong affinity of the protein towards all four G-quadruplexes with K_d values in the range of 2.5 – 5.1 nM. Binding strength was not affected by the presence of the metal complex, the bipyridine ligands nor the different topologies adopted by the individual modified G-quadruplexes. Binding strength values for natural G-quadruplexes are only reported for parallel topologies are in a similar range, showcasing that the substantial modification of the bipyridine ligands are not detrimental to the DNA-protein interaction.

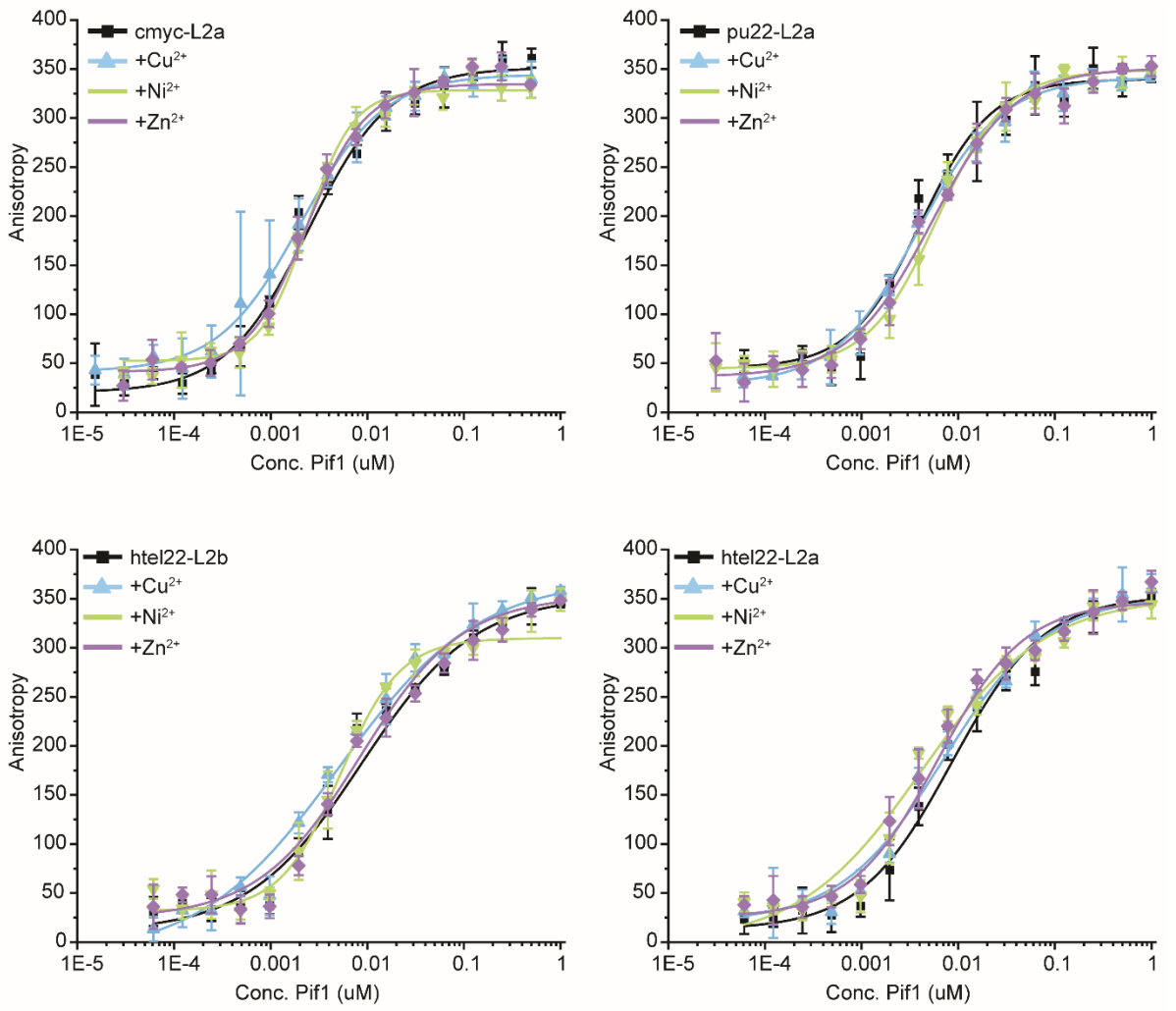

Figure 67. Binding curves from fluorescence polarisation assays of different modified G-quadruplexes in absence and presence of divalent metal cations M^{2+} (M = Cu, Ni, Zn) with increasing concentrations of Pif1. Incubation time of DNA-protein complex was 1h at 37°C before measurements. Obtained data was fit with a Hill function. K_d-values were obtained from the second derivative of the fitting function.

The lack of structural differentiation of Pif1 is interesting when comparing recently reported crystal structures of Pif1:G-quadruplex complexes. In the study of Raney[151] the eukaryotic Pif1 (ScPif1) found in yeast cells (Saccharomyces cerevisiae) binds G-quadruplexes through a wedge region in the N-terminal 1A domain of the protein. This requires an exposed G-tetrad on the 5'-end of the G-quadruplex as well as the additional polyT tail deeply buried inside of the protein. While ScPif1 differs in a longer N-terminus than human Pif1 (hPif1), the additional unstructured region is mainly responsible for the regulation of nuclear or mitochondrial localisation of the protein in yeast cells. Therefore, the interaction of hPif1 and ScPif1 in resolving G-quadruplex structures can be assumed to be similar. The modified **T15-htel22-L2a** and **-L2b** sequences do not possess such an exposed G-tetrad as shown by MD simulations where either thymine or adenine hover above the guanines or, in the case

for the antiparallel folded structures, a diagonal loop is present blocking access of the Pfi1 wedge. Given the high binding strength for these less favoured structures, an additional interaction pathway of Pif1 must contribute to the binding process.

As the neither metal stabilisation nor different topologies affected the binding, we sought to investigate the unwinding capabilities of Pif1 with the goal of achieving a retardation through the additional stabilisation of the metal complex. For this we performed a firefly luciferase assay through which the indirect consumption of ATP could be detected. Firefly luciferase catalyses the oxidation of its substrate, D-luciferin, in an ATP-dependent reaction that produces oxyluciferin, AMP, PPi, CO_2, and visible light. The emitted luminescence is directly proportional to the ATP concentration present in the sample, enabling highly sensitive and quantitative detection of ATP.

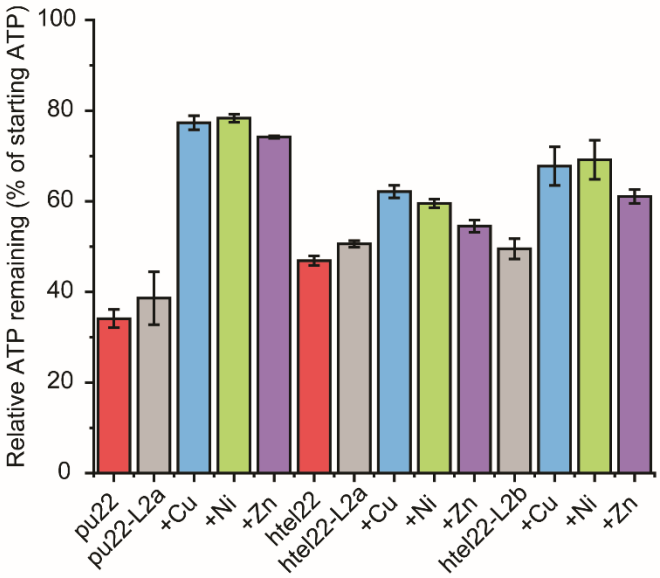

Figure 68. Luciferase assay for the determination of consumed ATP in the ATP-dependent unfolding of G-quadruplexes by Pif1 helicase. Consumption was referenced to a set amount of ATP from which the remaining ATP concentration was calculated correlated with the observed luminescence.

An expected preference for the parallel folded G-quadruplexes of **pu22** and the corresponding bipyridine modified **pu22-L2a** could be observed as the largest amount of ATP was consumed in the unfolding of these structures, thus giving the lowest amount of remaining ATP capable of being used in the luciferase reaction. it was observed that after the chosen time period of 5 min for the unfolding event, the metal stabilised G-quadruplexes lead to a significant increase in unfolding resistance and less ATP was consumed in the process. This held true for both **htel22** and **pu22** based G-quadruplexes structures, independent of their topology. A much stronger impact on metal stabilisation could be observed for **pu22-L2a** which coincides with the positioning of the bipyridine modifications within this particular G-quadruplex as showcased in the MD simulations prior. As Pif1

approaches from the 5'-end and unfolds the G-quadruplex in a nucleotide-by-nucleotide fashion, it immediately encounters the metal-complex and likely is perturbed and hindered by its presence. Thus, unfolding is rendered less efficient which leads to a stalling of the helicase function. We cannot exclude that in this process the helicase does not disengage from the substrate after multiple failed unfolding attempts. When compared to **htel22-L2a** and **-L2b**, where the bipyridine complex is placed within the loop region, the impact of the modification is much lower compared to the metal free counterpart. We speculate that as the G-quadruplex is partially unfolded, the additional stabilisation provided by the metal complex is not strong enough to cause a similar helicase perturbation and stalling as in the case for **pu22-L2a**. These results align with the observed characteristics of the bipyridine modified G-quadruplexes and showcase their capability of potentially being used as helicase perturbators. Additionally, it emphasizes the importance of G-quadruplexes within a cellular context and how healthy helicases function, thus leading to successful unfolding of G-quadruplexes is crucial. As we saw no stark binding differences or preferences in unfolding efficiencies for Pif1 for these modified G-quadruplexes we repeated the experiments with the 3'-to-5' helicase DHX36 (**Figure 68**).

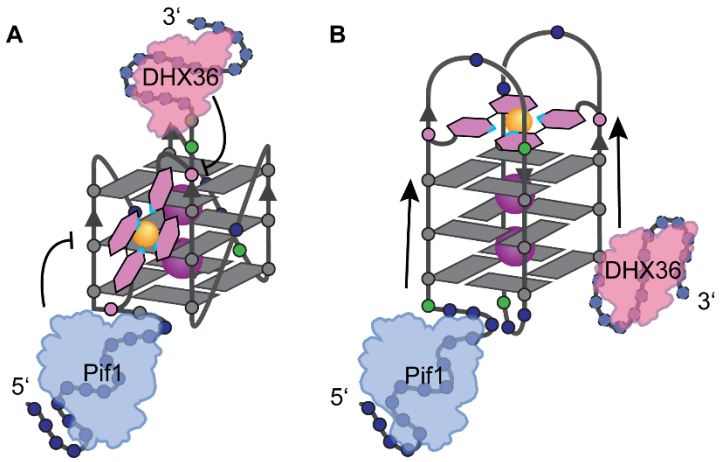

Figure 69. A) Unfolding of parallel folded pu22-L2c G-quadruplex through either Pif1 or DHX36 in either 5'→3' or 3'→5' obstructed through the positioning of the bipyridine metal complex at the end of the polyT overhangs. B) For G-quadruplexes with hybrid or antiparallel topologies the bipyridine metal complex sits on top of a G-tetrad and thus is unable to immediately block the unfolding by either Pif1 or DHX36.

3.7.4 DHX36

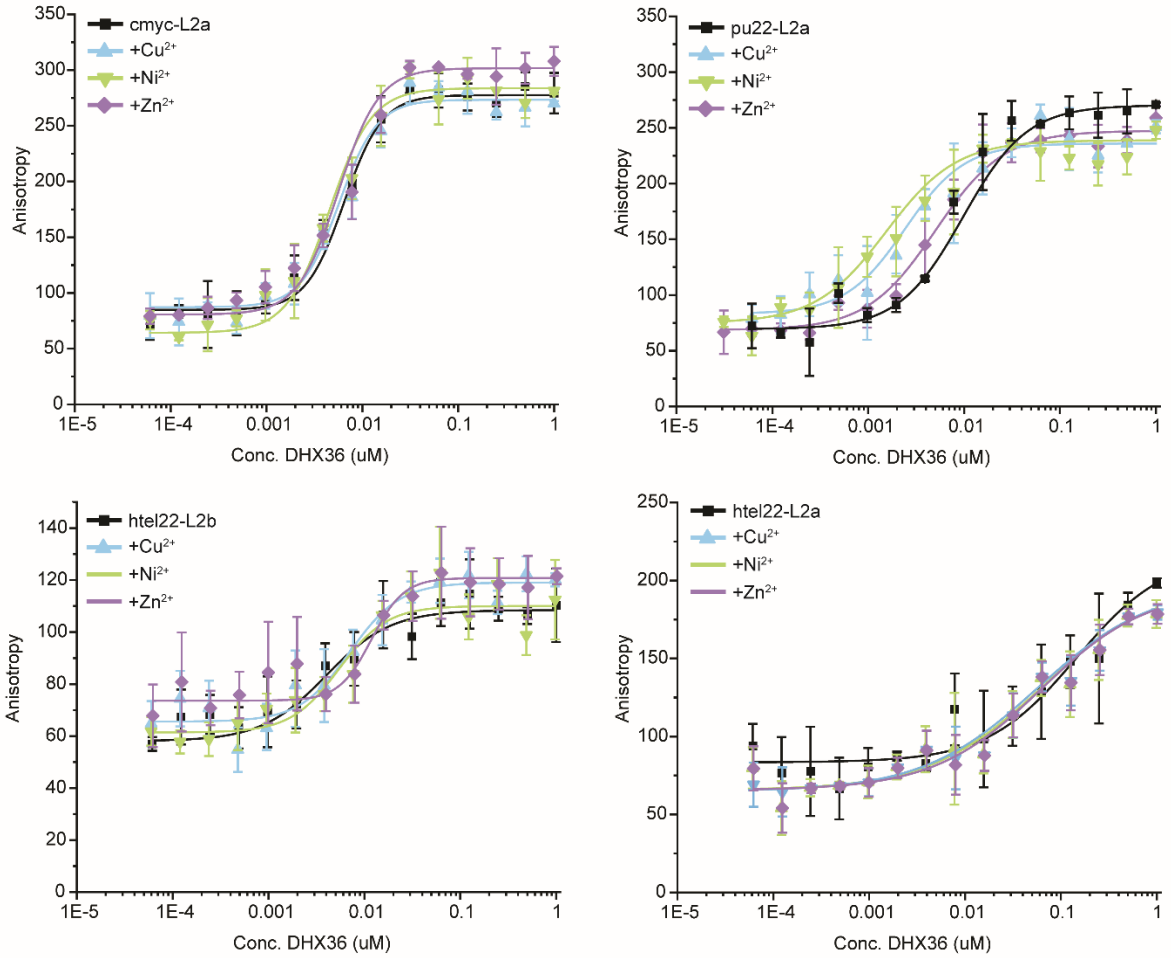

Figure 70. Binding curves from fluorescence polarisation assays of different modified G-quadruplexes in absence and presence of divalent metal cations M^{2+} (M = Cu, Ni, Zn) with increasing concentrations of DHX36. Incubation time of DNA-protein complex was 1h at 37°C before measurements. Obtained data was fit with a Hill function. K_d-values were obtained from the second derivative of the fitting function.

The second helicases we investigate for the interaction with artificial G-quadruplexes was DHX36, also known as RHAU. As stated in the introduction this protein is the main helicase responsible for the unwinding of G-quadruplexes and shows a very high preference for parallel G-quadruplexes. This helicase operates in an opposite direction as Pif1, resolving structures from 3' to 5'-end in an ATP-dependent mechanism. As this helicase requires a loading sequence, similar to Pif1, the bipyridine modified G-quadruplexes had to be resynthesized with a 15nt long polyT tail on the 3'-end. The standard protocol of CD spectroscopy and UV-Vis melting curve analysis was performed to ensure correct folding of the four G-quadruplex structures. Similar CD signatures for **htel22-L2a-T15** and **-L2b-T15** could be observed as for the sequences bearing the polyT tail at the 5'-end. The parallel pu22 and cmyc based G-quadruplexes showed no change in the CD spectrum, while no

thermally destabilising effect could be identified for either bipyridine modified G-quadruplex. Further characterisation of these structures can be found in the appendix. We proceeded to perform FP assays in order to determine the binding strength of DHX36 towards the different constructs of G-quadruplexes and potential impact of the metal complex or the bipyridine ligands. Contrary to the Pif1 results, a strong dependence of the binding strength on the G-quadruplex topology could be observed for DHX36. The hybrid-1 folded **htel22-L2a-T15** showed the weakest binding with a K_d = 144nM, which in comparison to natural parallel G-quadruplexes is weaker by a factor of 2-4x. The metal triggered transformation to the antiparallel topology of this system showed an increase in binding affinity as the calculated values dropped to K_d = 64nM. These results were unexpected as the 3'-end G-quartet is blocked by the diagonal loop, decreasing the potential interaction surface of the DSM. We propose an additional interaction of the closely neighbouring OB-domain and leading to preferential binding of an antiparallel G-quadruplex over a hybrid-1. This is supported when employing the smaller **htel22-L2b-T15** quadruplex as this showed antiparallel characteristics. Indeed, the binding strength towards the protein drastically increased to K_d = 4nm. The presence of the metal complex did not influence the binding as binding remained similarly strong towards the G-quadruplex, excluding any potential electrostatic or non-covalent interaction with the bipyridine ligands or the metal complex. This confirms that DHX36 preferably approaches the G-quadruplex from the 3'-end through loading onto the polyT tail and does not engage in interactions with the oppositely positioned loop region housing the bipyridine modifications.

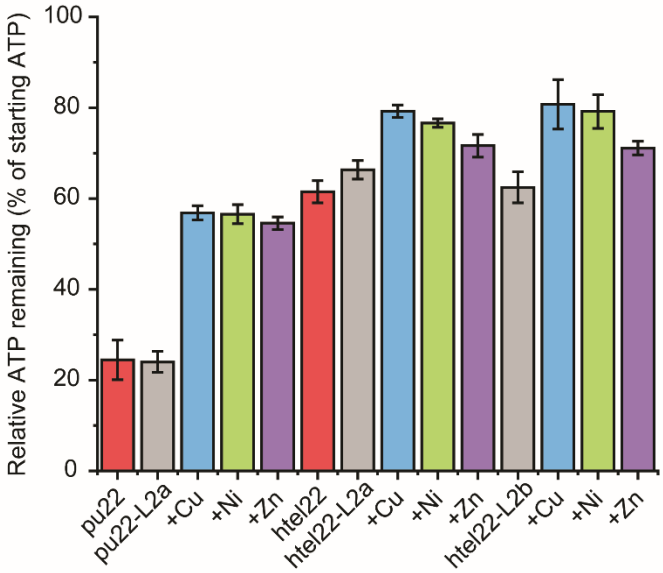

Figure 71. Luciferase assay for the determination of consumed ATP in the ATP-dependent unfolding of G-quadruplexes by DHX36 helicase. Consumption was referenced to a set amount of ATP from which the remaining ATP concentration was calculated correlated with the observed luminescence.

When compared to the parallel G-quadruplexes of pu22-L2a-T15 and cmyc-L2a-T15 low K_d values in the range K_d = 2.5 – 6.7 nM could be obtained, indicating very strong binding comparable to the natural counterparts of these sequences. As these systems possess an exposed G-tetrad, the main interaction is likely driven through the DSM and less by the OB domain. A full explanation for the comparatively high preference for the antiparallel G-quadruplex could not be found.

Next we performed firefly luciferase assay to investigate if the metal complex stabilised G-quadruplexes could withstand or retard the unwinding by DHX36. Similar results to Pif1 were obtained. As DHX36 has a stronger preference for parallel G-quadruplexes we observed an increased consumption of ATP in the unfolding of **pu22** and **pu22-L2a** while little ATP was consumed in presence of G-quadruplexes of other topologies as could be observed for **htel22-L2a** and **-L2b**. Again here the largest stalling was observed for **pu22-L2a** in presence of M2+ (M = Cu, Ni, Zn) as the stabilising metal complex sits very close on the 3'-end of the G-quadruplex (omitted the thymine overhand at the 3'-end) thus leading to an early disabling of the helicase activity. We could observe that DHX36 was much less capable of unfolding hybrid or antiparallel folded structures of **htel22-L2a** and **-L2b** where the additional stabilisation through metal complexation did not harbour an even further decreased unfolding efficiency (**Figure 71**). Overall we were successful in not only generating bipyridine modified G-quadruplexes of different topologies capable of effectively binding two helicases, but could showcase that the metal mediated dynamic topology switching could alter binding affinities and in addition lead to an increased stalling of the helicases progression in unfolding these secondary DNA structures. This makes for promising results in the creation of molecular decoys for direct application in regulating helicase activity.

3.8 In cellulo investigations of bipyridine modified G-quadruplexes

Having shown how these bipyridine modified G-quadruplexes not only exhibit large thermal stabilisation but also a strong resistance towards external influences such as crowding, chaotropic agents or even pH against their correct folding or refolding, our next goal was to investigate these systems within a cellular environment. The long-term goal, which lies beyond the scope of this work, is to develop new highly stabilised and metal-dependent G-quadruplexes as decoys for not only sensing but also modulating *in vivo* DNA-protein interactions. We could show that not only do these artificial G-quadruplex still interact with some proteins of interest (POI) (e.g Pif1 and DHX36) which are heavily involved in the regulation of healthy tissue or play a role in the progression of diseases, but in some cases affinities of the metal-stabilised G-quadruplexes was higher than the literature reported values of the unmodified sequences. Additionally, we saw that the presence of the metal-

complex could indeed hinder the progression of the ATP-dependent helicases to some degree, rendering them more stable than their natural counterparts. These first protein studies were however conducted in isolated conditions in an Eppendorf tube. Our studies regarding the molecular crowding on our artificial G-quadruplexes gave a first idea on how these system might behave under more crowded cellular conditions and if it would be even feasible to administer them into living cells. With the positive results gained from these crucial experiments we aimed towards the examination of the uptake, stability and potential toxicity as well as cellular localisation within living cells by fluorescence microscopy. The following results were achieved in collaboration with Prof. Ramon Vilar from the Imperial College London.

3.8.1 Cellular toxicity and transfection into HeLa and U2OS cells

A total of four sequences were chosen for these experiments as they showed the most promising results in the previous experiments showcased in this work, namely htel22-L2a, -L2b and ttel24-L2a, and a mutated mut-htel22-L2a, bearing the bipyridine modification but incapable of forming a G-quadruplex. All sequences were of telomeric origin. We chose these G-quadruplexes as they not only gave us the possibility to study discrete topological switching within a cellular context but also covered a range of thermal stabilities which could give us a deeper understanding of how artificial G-quadruplexes behave. We chose to exclude pu22 based G-quadruplexes as they showed a low impact of the metal-complex formation on their structure and stability, therefore closely resembling the natural version.

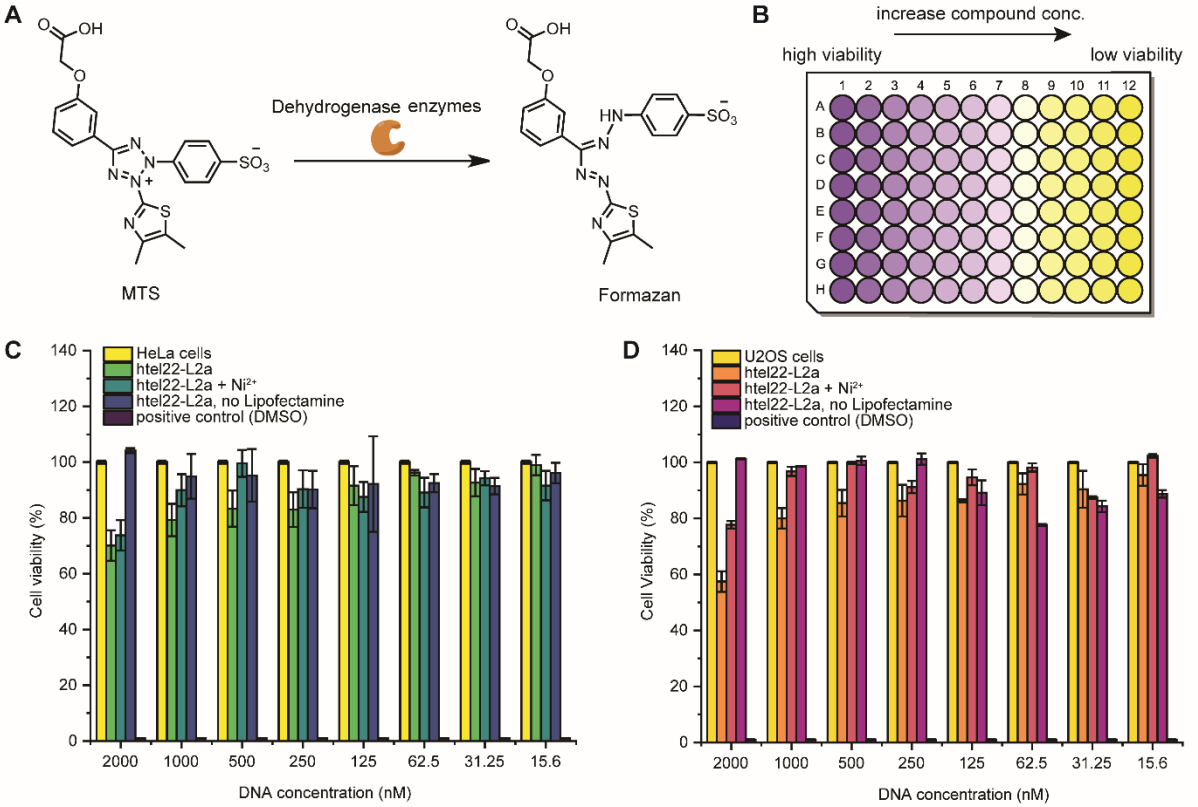

Figure 72. MTS Assay of FAM-htel22-L2a in absence or presence of Ni^{2+} and in absence or presence of Lipofectamine2000. A) Chemical reaction of MTS to formazan by dehydrogenase enzymes of living cells. B) Schematic representation of the experimental setup for MTS assay in 96-well plate and the change in colour from violet (formazan) to yellow (MTS) dependent on the viability of cells. C), D) Cell viabilities of htel22-L2a in HeLa and U2OS cells. Negative control: 10000 cells per well in growth medium. Positive control: Incubation in medium with 50% DMSO over 16h at 37°C and 5% CO2.

To investigate localisation and speed of the transfected oligonucleotides, as well as their toxicity the single fluorescently labelled G-quadruplexes bearing the FAM modification were chosen. As transfection of short single stranded oligonucleotides is relatively uncommon it was paramount to first establish a working protocol which included the choice of a fitting transfection method. Generally, transfection of DNA into a living organism can be performed either by chemical or physical means. The most common chemical transfection reagents are cationic lipids, which form a DNA-lipid complex which can penetrate the cell membrane, or calcium phosphate which enables the entry of DNA via endocytosis. Physical transfection is mostly limited to electroporation which creates transient cell membrane opening through electrical pulses. Another method is microinjection where the DNA of choice is directly injected into the cell or their nucleus via a syringe, though this method requires an extensive setup. We chose not to use electroporation as the strong electrical field might not be suitable for the combination of polycationic DNA and cationic metal ions, potentially ripping the M^{2+} ion out of the complex. Before exposing the system to yet another cation in the form of Ca^{2+},

we chose to test out a common lipid transfection reagent, Lipofectamine 2000. Only a few examples in literature exist where this reagent was used for the transfection of short (<50nt) oligonucleotide fragments which served as starting points for our protocol.

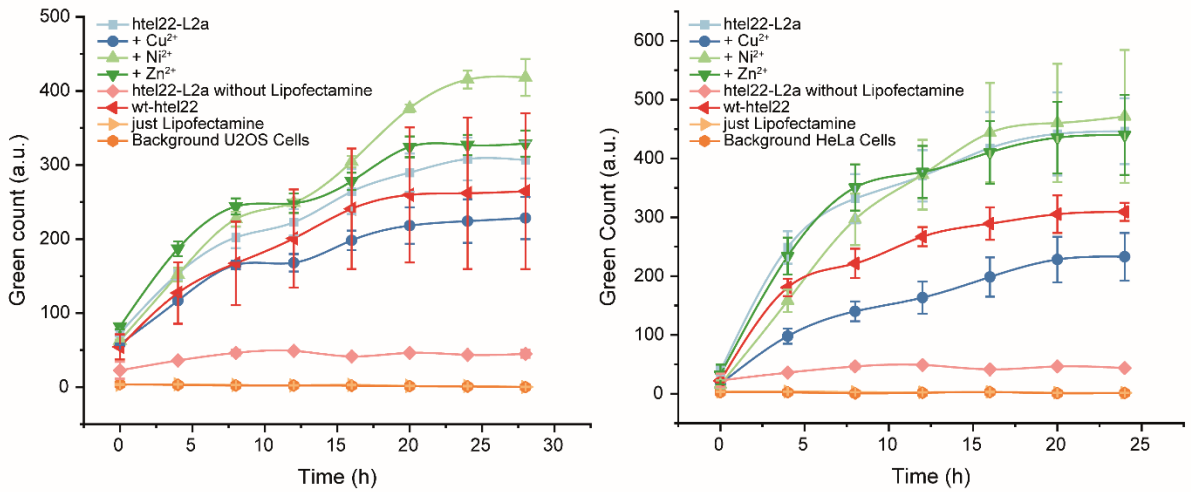

Figure 73. Green fluorescence count ($\lambda_{ex.}$ = 490nm, $\lambda_{em.}$ = 520nm) of the cells transfected with htel22-L2a in absence and presence of M^{2+} (M = Cu, Ni, Zn) and in absence and presence of Lipofectamine2000 into both HeLa and U2OS living cells.

As cell targets, we chose two cells lines, HeLa and U2OS. Both lines are immortalized human cell lines are well characterised, show good cell permeability and overall robustness. In both cases, G-quadruplex processing proteins such as the aforementioned Pif1 and DHX36 are endogenously expressed, rendering them interesting for further applications in the future. All cells were grown under the literature reported conditions of DMEM supplemented with 10% FBS at 37°C and 5% CO2 over night until the reached 80% confluency. After this they were plated into 96-well plates at 10000 cells per well in a total medium volume of 100uL. To this the mixture of the transfecting reagent and DNA G-quadruplex was added to a final total volume of 110uL per well.

In preparation of the complex between the cationic lipids of Lipofectamine 2000 and the DNA G-quadruplexes several ratios of the two components could be employed. The standard ratio of 3:1 lipofectamine/DNA was tested as well as 1:1 and 10:1 ratios to observe differences and ideal conditions. All G-quadruplexes were annealed under the standard conditions (10mM HEPES pH 7.1, 100mM KCl, (4uM MSO_4)) in presence or absence of a M^{2+} source for the formation of the corresponding complex. We tested a total of three metals, Cu^{2+}, Ni^{2+} and Zn^{2+}. These metals cover a range of highly cytotoxic, in the form of Cu^{2+}, to non-cytotoxic, in the form of Zn^{2+}, characteristics and could potentially gives us insight if they were retained within the transfected G-quadruplex or not. Only the ratio of 3:1 lipofectamine/DNA gave satisfactory transfection as could be seen by fluorescence

microscopy. We then proceeded to investigate the optimal transfection time as well as a first visualisation of the localisation of the transfected G-quadruplexes and potential differences between the different conditions using the automated fluorescence microscopy feature of an Incucyte S3 Live Cell Analysis. Here, images of up to 40x magnification of each individual well could recorded over a given time period and an adjustable interval.

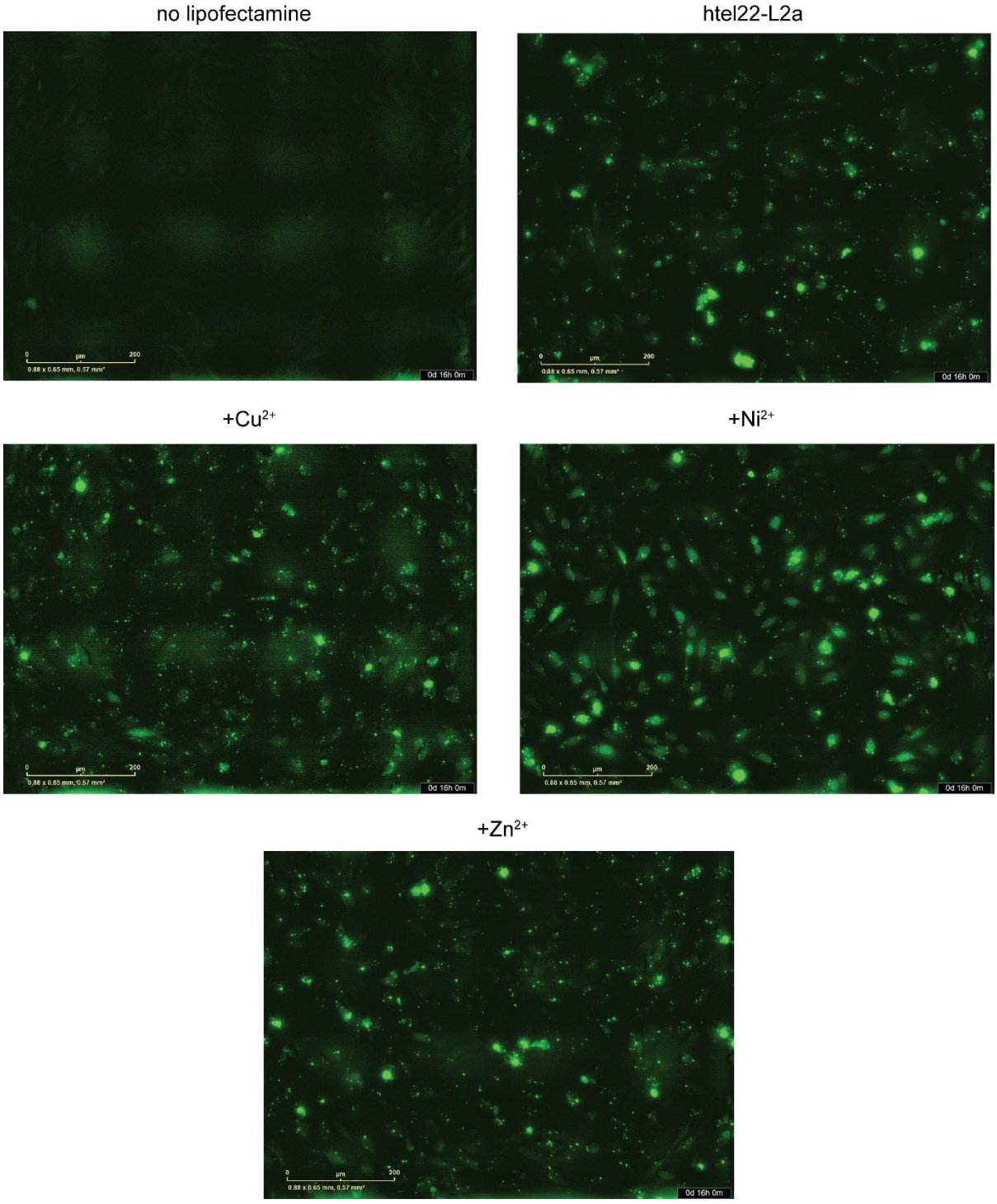

Figure 74. Fluorescence microscopy of HeLa cells transfected with **htel22-L2a** in presence of divalent metal cations M^{2+} (M = Cu, Ni, Zn) after 16h incubation.

We devised a maximum incubation time of 24h over which images were taken every 4h of each well. All conditions were performed in triplicates to gain statistical significance. Total green count of the selected cell area of the FAM fluorescence (exc. wavelength: 490nm, em. wavelength: 520nm) was taken to estimate the optimal incubation time after which no further increase was observed or the transfection was slowed down. As control experiments we added to the cells either just the lipofectamine mixture without DNA or the DNA without the lipofectamine. We could observe that without lipofectamine no fluorescence could be detected as the added G-quadruplexes are evenly distributed within the well and the volume. This meant that an efficient transfection would lead to a localised increase in the fluorescently labelled G-quadruplexes and a detectable signal. Indeed we observed exactly this behaviour.

Sample to which the lipo-DNA mix was added showed a total increase of green fluorescence over time reaching an plateau after approx. 18h for both HeLa and U2OS cells independent of the administered G-quadruplex of the presence/absence of an M^{2+} cation (**Figure 73**). The overall intensity between G-quadruplexes and the metals, as well as their localisation was however very different. We observed that Cu^{2+} showed the lowest total intensity which may originate from its capacity to quench the fluorescence of the FAM label, being a paramagnetic d9 metal. This has been shown by in vitro fluorescence spectroscopy and is an expected behaviour of open-shell transition metals. Interestingly, those G-quadruplexes stabilised by Ni^{2+} cations showed a strong fluorescence signal despite the d8 electron configuration of the transition metal cation. This d^8 electron configuration of nickel can adopt two ligand arrangements, either square-planar or tetrahedral/octahedral which depends on the number of ligands and their respective ligand field strength. With bipyridine only square-planar or tetrahedral are possible, though an octahedral complex with two water molecules in the apical positions cannot be excluded. However, both tetrahedral and octahedral Ni^{2+} complexes show strong quenching properties as they possess two unpaired electrons and are in most cases in a high-spin configuration. Here low energy spin-allowed d-d transitions are possible. As this behaviour is neither observed *in vitro* nor *in cellulo* we conclude that the Ni^{2+} cation must form a square-planar complex with the two bipyridine units. This also indicates that the conditions within the transfected cells do not affect the coordination geometry of the metal complex in the G-quadruplexes. Zn^{2+}, being a close-shell d10 transition metal, showed similar fluorescence intensities as those G-quadruplexes stabilised with Ni^{2+}. We cannot exclude that those G-quadruplexes bearing a Cu^{2+} complex show an overall lower transfection efficiency due to other interactions and properties of the metal.

Next we tested for the cytotoxicity of the administered DNA G-quadruplexes through Methylthiazolysulfophenyl tetrazolium (MTS) assays. Here, varying concentrations of each DNA were added to cells in a 96-well plate format and incubated for 18h at 37°. After this a

reaction mixture containing the MTS was added to the wells and incubated for another 4h at 37°C. The dehydrogenase enzymes in the living cells are capable of transforming the pale yellow MTS (λmax = 490nm) to the dark purple formazan, making a readout of the remaining viable cells possible through simple UV-Vis spectroscopy through quantification of the intensity of the 490nm absorption band. As positive control we had cells in fresh media and as negative control cells to which 50% DMSO was added. Overall the assay revealed an optimal final concentration of administered oligonucleotide at 1 µM where cell viability of both HeLa and U2OS cells was > 80% over the spectrum of all sequences and their respective combination with M^{2+} ions. Adding an increased concentration of 2 µM lead to a decreased cell viability of <80% yet no IC_{50} value was determined. This value is well within the realm of similar oligonucleotide systems and their corresponding toxicity in human cancer cell lines.[239] This enabled us to work with a sufficiently high concentration for further fluorescence microsopcy experiments (**Figure 72**).

Having established an ideal transfection time for these modified G-quadruplexes as well as a safe concentration range with viability >80%, it was of further interest to establish a qualitative overview of localisation of the transfected DNA and potential differences **htel22-L2a**, **-L2b** and **ttel24-L2a** and the different metals. In most cases an overall penetration of the cytoplasm concomitant with a green staining of it could be observed, indicating indeed a successful transfection. For samples containing either no M^{2+}, Cu^{2+} or Zn^{2+}, a large amount of fluorescing aggregates could be observed forming within the cells cytoplasm over the course of 24h. This punctuate objects if varying size could have various origins, ranging from intracellular agglomeration of the polyanionic oligonucleotides in combination with the polycationic transfecting reagents, endosomal compartmentalisation or cytoplasmic aggregation with proteins as these modified G-quadruplexes have been shown to have the general ability to retain their affinity towards them. Some of the small aggregates can also be found within the nucleus as shown by the microscopy images. In stark contrast to this were those G-quadruplexes stabilised by Ni^{2+} prior to transfection. Transfection into the nuclei of both HeLa and U2OS was so successful that no nuclear stain was necessary to visualise the cells nucleus. The extent at which punctuate fluorescent aggregates were formed was much lower compared to the other conditions although still present. A clear impact of the Ni^{2+} on either cellular uptake or the overall stability of the G-quadruplex was observed but no direct explanation was possible (**Figure 74**). Given these results it seemed however unlikely that the transfected G-quadruplexes in their pre-annealed state either completely unfold or are digested by exonucleases. The conditions within a cellular environment are different to the isolate *in vitro* conditions which makes these results not directly transferable. In order to test if the Ni^{2+} stabilised G-quadruplexes remained in a folded state **htel22-L2a** and **-L2b** were double modified with two fluorophores as Förster resonance energy transfer (FRET) pairs.

On the 5'-end the FAM modification remained while on the 3'-end a cyanine3 (Cy3) modification was installed in a newly synthesised batch of oligonucleotides. The emission and excitation spectra of these two fluorphores overlap in such a manner that emission of the donor (FAM) will be absorbed by the acceptor fluorophore (Cy3) which consequently will result in the emission of the latter. Because the emission of photons is directional and distance dependent by r/R0^6 only when both donor and acceptor are on close proximity, can this energy transfer occur and a high FRET efficiency be obtained. Through *in vitro* experiments of the doubly labelled G-quadruplexes we showed that indeed there are two states can be accessed. In their unfolded state, here induced by thermal denaturation, both htel22-L2a and -L2b show both donor and acceptor fluorescence thus creating a low FRET state. For comparison the melting point of htel22-L2b obtained through this FRET melting experiments coincided with the UV-Vis spectroscopy obtained results ($^{UV}T_m$ = 44°C; $^{FRET}T_m$ = 42°C). To note here is that both fluorophores used, show thermal degradation which additionally contributes to the obtained spectral behaviour. As the unfolded ssDNA does not form a perfect linear shape but behaves like a worm-like chain through still present secondary interactions, the distance between the fluorophores does not exceed the effective FRET range of approx. 2 – 8 nm. We can calculate the root-mean-square distance of the present 22nt long oligonucleotides of **htel22-L2a** and **-L2b** to be approx. 4.2 – 6.0nm from the FAM to the Cy3 fluorophore using the equation given below (**equation 2**)

$$R_{RMS} = \sqrt{2l_pL - 2l_p^2(1 - e^{-\frac{L}{l_p}})} \quad (2)$$

Where *lp* is the persistence length of the ssDNA and *L* the maximum contour distance, i.e. if the DNA strand would be maximally mechanically stretched. The persistence length *lp* is influenced by the ionic strength, i.e. K^+ or Na^+ concentration, resulting in a range of theoretical distances. This explains why the denaturation of either G-quadruplex does not lead to a vanishing of the Cy3 emission, just an overall lowering in intensity since the FRET pair is now further apart. In the folded state the FRET efficiency is maximal as the two fluorophores are in close proximity. We were unable to observe differences in FRET efficiency between the different topologies as in all cases the spatial distance is very similar between hybrid-1 or antiparallel. For these experiments, a new design of G-quadruplexes would be necessary to create a larger spatial difference between the topologies, shown by Sugimoto.

These results were crucial in order to correctly interpret the *in cellulo* experiments with **htel22-L2a** and **-L2b**. The transfection conditions were identical to the singly FAM-labelled G-quadruplexes. The results in HeLa cells were contrary to prior experiments and those

results obtained in the 96-well format. Again, we excited at 490nm exclusive for the FAM donor. For htel22-L2a the Ni^{2+} free conditions showed very low FAM emission, only high in some punctuate formations in the cells while the Cy3 emission was much higher and showing that the administered G-quadruplex had successfully entered the cell nucleus. This was a strong indication that the **htel22-L2a** indeed remained at least partially folded under the cellular conditions. Surprisingly the presence of Ni^{2+} resulted in an overall quenching of the fluorescence, contrary to the *in vitro* results. Due to time constraints these experiments could not be repeated. Similarly dissatisfying were the results obtained with **htel22-L2b**. In neither case a strong fluorescence could be detected in either metal stabilised or non-stabilisied. This could be either due to a quenching of the fluorphores through secondary processes in the cell, indeed digestion of the articifial DNA by nucleases or an insufficient transfection efficiency due to the additional modification in the form of the Cy3. We performed these experiments in U2OS cells to identify potential differences and cell constituency between these two cells lines is different and might affect G-quadruplex stability and transfection efficiency (**Figure 75**).

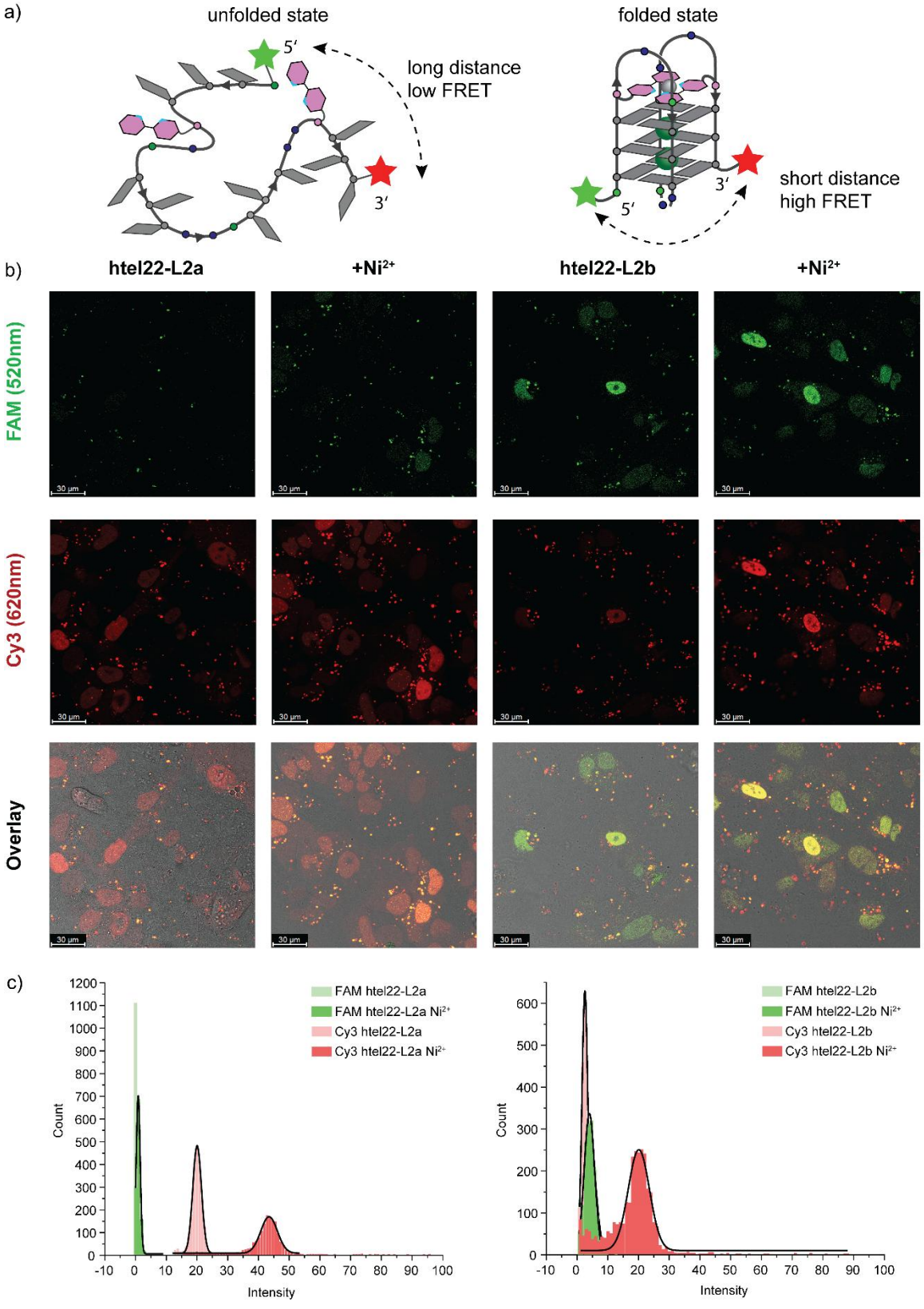

Figure 75. A) Schematic representation of the FRET experiments. Low FRET efficiency is observed when the G-quadruplex is unfolded as donor and acceptor are further away. High FRET efficiency is observed when the G-quadruplex is folded as donor and acceptor are in close proximity. B) Fluorescence microscopy of **htel22-L2a** without and with Ni^{2+} as well as **htel22-L2b** without and with

Ni^{2+} transfected U2OS cells. Images show filters applied for the individual fluorophores (FAM 520nm, Cy3 595nm) as well as the overlay with the brightfield image. Excitation wavelength corresponding to the excitation maximum of FAM donor (495nm). C) Green count of fluorescence intensities of FAM and Cy3 fluorophores of htel22-L2a and -L2b in presence and absence of Ni^{2+}.

Overall, we observed a slight change in both FAM and Cy3 fluorescence for the Ni^{2+} containing samples as compared to the metal-free systems, likely originating from the overall stabilisation and better transfection into the nuclei, which we determined as region of interest (ROI) as they showed little to no punctuate fluorescence formation, of the metal complexed G-quadruplexes. By plotting the counts of individual intensities (max intensity value: 255), we create a histogram of the two emission wavelengths for the donor FAM and the acceptor Cy3. Overall **htel22-L2a** shows FAM donor emission with extremely low intensity (<5) both in presence and absence of Ni^{2+}. The Cy3 acceptor emission intensity increased from a mean value of 20 to 44 when the G-quadruplex was stabilised with Ni^{2+}, yet a lower maximum count was concomitant which can be due to the quenching of the present metal. We conclude however that **htel22-L2a** remains partially folded even in the absence of Ni^{2+} and is further stabilised, as proven in vitro by it leading to a string FRET effect. The case is similar for **htel22-L2b** where FAM donor fluorescence does not decrease in presence of Ni^{2+} but shows higher intensities (<10) than **htel22-L2a**. Contrary to the previous strand, Cy3 acceptor fluorescence shows very low intensities in absence of Ni^{2+} (<5) for **htel22-L2b** indicating that the G-quadruplex was either transfected improperly due to the lacking stabilisation of Ni^{2+} or is unfolded in the absence of it. Similarly, we see that the metal stabilised G-quadruplex shows an increased Cy3 donor fluorescence with a mean value of 20. Again, partial quenching due to Ni^{2+} may explain a lower count. We were overall successful in bringing these ligand-modified structures into live cells for the first time and could show that they sustain under cellular environments. This paves the way for further applications of these biomimetic G-quadruplexes as potential interaction partner for proteins, possibly acting as molecular decoys capable of binding to proteins involved in certain diseases.

4. Summary

In summary we were successful in developing a novel ligandoside bearing a bipyridine moiety and the necessary synthetic route and installed it via SPPS into DNA oligonucleotides capable of forming G-quadruplexes. In most cases the initial G-quadruplex topologies were left undisturbed and could be thermally stabilised through the formation of corresponding bipyridine metal complexes with divalent transition metal cations M^{2+} (M = Cu, Ni, Zn, Co, Cd, Fe). The most stable systems showed melting temperatures of Tm ≥85 °C. Apart from the stabilisation, we could exert a structural change of **htel22-L2a** in particular which showed a hybrid-1 topology in K^+ containing buffer and could be dynamically switched to an antiparallel topology through the addition either Cu^{2+}, Ni^{2+}, Zn^{2+}, Co^{2+} or Cd^{2+} to the already preformed G-quadruplex at r.t. The kinetic analysis of this refolding process was then investigated and kinetic rate constants as well as the enthalpy and entropy of change determined, showcasing that the rate-determining step is constituted by the DNA restructuring and not the metal complex formation. MD simulations of major structure covering all G-quadruplex topologies showed that in certain scenarios positive interaction between the bipyridine moieties and the metal complex with the G-tetrad or the surrounding nucleotides in close proximity do exist and potentially contribute to preferences of certain topologies.

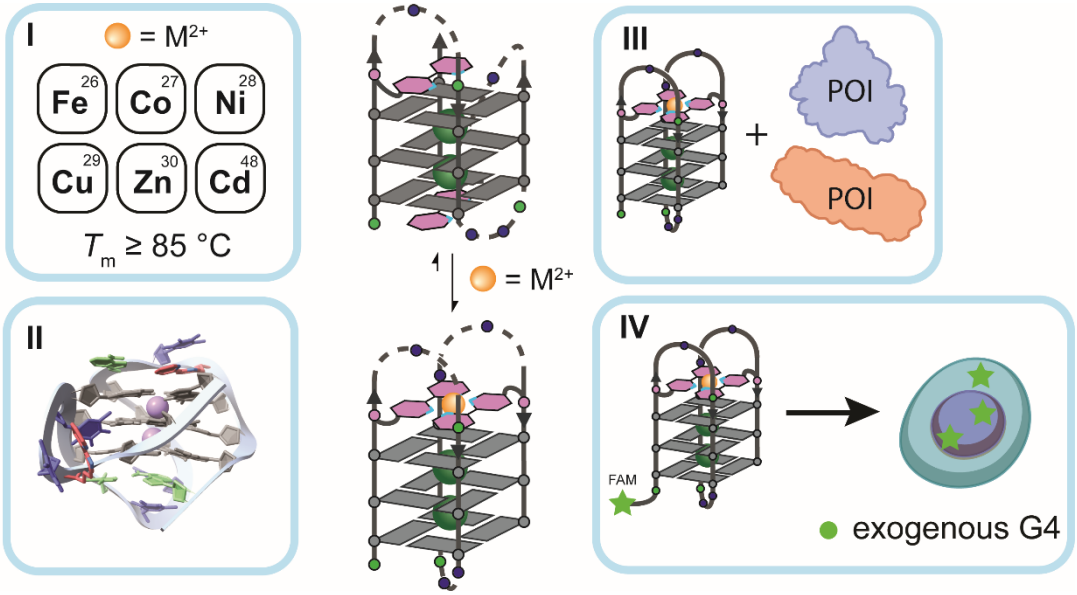

Figure 76. Summary of various parts covered in this thesis with bipyridine modified unimolecular G-quadruplexes. I) Binding and stabilisation with various divalent metal cations rendering the G-quadruplexes highly thermally stable and partially inducing structural refolding into other topologies. II) Structural analysis of MD simulations. III) Investigation of G-quadruplex protein interactions. IV) Transfection of bipyridine modified G-quadruplexes into HeLa and U2OS cells.

Studying these bipyridine modified G-quadruplex under different solvation conditions, specifically under high Li^+ content, or molecular crowding through PEG200 and hydrogen bond competitors like Urea gave us insight into how they behave in suboptimal environments. In all cases the stabilisation through the presence of the metal complex lead to either overcoming of the destabilising conditions or a retardation in forced refolding as in the case with PEG200.

As it was our goal to employ these artificial systems for more biological interactions firstly, we investigated their potential to engaging with G-quadruplex binding proteins. We chose three proteins directly involved in resolving these peculiar secondary DNA structure namely hnRNP A1, Pif1 and DHX36 with the latter two being ATP-dependent helicases. In all cases not only could we show high binding affinities of up to K_d = 2 nm for DHX36 but also a dependence of affinity and G-quadruplex topology. Thus, we could dynamically switch the proteins affinity through the formation of the metal complexes. For actual applications as potential molecular decoys in living organisms, we transfected these bipyridine modified G-quadruplexes into HeLa and U2OS cells, both known to express an abundance of G-quadruplex binding proteins. We showed that our modified systems show very little toxicity with IC50 > 2uM and could even facilitate the uptake in presence of toxic divalent metal cations such as Cu^{2+} and Ni^{2+}. The best transfection and penetration into the cell nuclei was achieved with Ni^{2+} stabilised G-quadruplexes **htel22-L2a** and **-L2b**. Double fluorescently labelled G-quadruplexes allowed us to prove that these systems remained at least partially folded through fluorescence microscopy and calculating the FRET efficiency.

5. Outlook

These bipyridine modified G-quadruplexes could be further explored in various ways. As we were able to bind novel metal cations such as Co^{2+} and Fe^{2+}, both of which show redox potential, direct application for catalysing chemical reactions could be explored. Apart from oxidation and peroxidase-like reactions, both metals could generate reactive oxygen species (ROS) through electronic interplay with the closely neighbouring guanines. The advantage of such systems over commonly used inorganic complexes as ROS-probes would be their low toxicity as well as biocompatibility. Subsequent investigation into cancer treatment of these G-quadruplexes would need to be performed.

Furthermore, building on the evidence of the protein interaction with hnRNP A1, Pif1 and DHX36 it would be highly interesting to expand the number of investigated G-quadruplex-protein interactions. A high throughput method like pulldown assays with whole cell lysates with subsequent proteomics analysis could potentially show which proteins and protein

classes show preferential binding to these artificial G-quadruplexes. Probes with varying metals and topologies could be prepared and thus interactions mapped out to find ideal candidates for which selective molecular decoys could be developed. Cellular studies with cell lines overexpressing the protein(s) of interest could be administered with the G-quadruplex probes and their cellular fate observed with the potential upside of a rescuing effect of the DNA oligonucleotide on it. Additionally, exact location of the transfected G-quadruplexes inside various cell lines could be investigated through immunofluorescence staining using either BG4 or SG4 anti-/nanobodies. This would give further insight into where the ideal mode of action and ideal cellular targets are.

6. References

[1] E. Bencurova, A. Akash, R. C. J. Dobson, T. Dandekar, "DNA storage—from natural biology to synthetic biology" *Comput. Struct. Biotechnol. J.* **2023**, *21*, 1227–1235.

[2] J. M. Berg, J. L. Tymoczko, G. J. G. jr., L. Stryer, *Stryer Biochemie*, **2018**.

[3] M. H. F. Wilkins, A. R. Stokes, H. R. Wilson, "Molecular Structure of Nucleic Acids: Molecular Structure of Deoxypentose Nucleic Acids" *Nature* **1953**, *171*, 738–740.

[4] J. D. Watson, F. H. C. Crick, "Molecular Structure of Nucleic Acids: A Structure for Deoxyribose Nucleic Acid" *Nature* **1953**, *171*, 737–738.

[5] M. H. F. Wilkins, W. E. Seeds, A. R. Stokes, H. R. Wilson, "Helical Structure of Crystalline Deoxypentose Nucleic Acid" *Nature* **1953**, *172*, 759–762.

[6] R. E. Franklin, R. G. Gosling, "Molecular Configuration in Sodium Thymonucleate" *Nature* **1953**, *171*, 740–741.

[7] R. E. Franklin, R. G. Gosling, "The structure of sodium thymonucleate fibres. I. The influence of water content" *Acta Crystallogr.* **1953**, *6*, 673–677.

[8] M. C. Wahl, M. Sundaralingam, "Crystal structures of A-DNA duplexes" *Biopolymers* **1997**, *44*, 45–63.

[9] V. I. Ivanov, E. E. Minyat, "The transitions between left- and right-handed forms of poly(dG-dC)" *Nucleic Acids Res.*. **1981**, *9*, 4783–4798.

[10] A. Rich, S. Zhang, "Z-DNA: the long road to biological function" *Nat. Rev. Genet.* **2003**, *4*, 566–572.

[11] H. R. Drew, R. M. Wing, T. Takano, C. Broka, S. Tanaka, K. Itakura, R. E. Dickerson, "Structure of a B-DNA dodecamer: conformation and dynamics." *Proc. National Acad. Sci.* **1981**, *78*, 2179–2183.

[12] N. Narayana, S. L. Ginell, I. M. Russu, H. M. Berman, "Crystal and molecular structure of a DNA fragment: d(CGTGAATTCACG)" *Biochemistry* **1991**, *30*, 4449–4455.

[13] R. V. Gessner, C. A. Frederick, G. J. Quigley, A. Rich, A. H.-J. Wang, "The molecular structure of the left-handed Z-dna double helix at 1.0 angstrom atomic resolution. Geometry, conformation, and ionic interactions of d(CGCGCG)" *J. Biol. Chem.* **1989**, *264*, 7921–35.

[14] F. A. Hays, A. Teegarden, Z. J. R. Jones, M. Harms, D. Raup, J. Watson, E. Cavaliere, P. S. Ho, "How sequence defines structure: A crystallographic map of DNA structure and conformation" *Proc. Natl. Acad. Sci.* **2005**, *102*, 7157–7162.

[15] J. Choi, T. Majima, "Conformational changes of non-B DNA" *Chem. Soc. Rev.* **2011**, *40*, 5893–5909.

[16] N. Saini, Y. Zhang, K. Usdin, K. S. Lobachev, "When secondary comes first – The importance of non-canonical DNA structures" *Biochimie* **2013**, *95*, 117–123.

[17] B. F. Eichman, M. Ortiz-Lombardía, J. Aymamí, M. Coll, P. S. Ho, "The Inherent Properties of DNA Four-way Junctions: Comparing the Crystal Structures of Holliday Junctions" *J. Mol. Biol.* **2002**, *320*, 1037–1051.

[18] C. Altona, J. A. Pikkemaat, F. J. Overmars, "Three-way and four-way junctions in DNA: a conformational viewpoint" *Curr. Opin. Struct. Biol.* **1996**, *6*, 305–316.

[19] D. R. Duckett, D. M. Lilley, "The three-way DNA junction is a Y-shaped molecule in which there is no helix-helix stacking." *EMBO J.* **1990**, *9*, 1659–1664.

[20] K. Hoogsteen, "The crystal and molecular structure of a hydrogen-bonded complex between 1-methylthymine and 9-methyladenine" *Acta Crystallogr.* **1963**, *16*, 907–916.

[21] J. Spiegel, S. Adhikari, S. Balasubramanian, "The Structure and Function of DNA G-Quadruplexes" *Trends Chem.* **2019**, *2*, 123–136.

[22] J. T. Davis, "G-Quartets 40 Years Later: From 5′-GMP to Molecular Biology and Supramolecular Chemistry" *Angew. Chem. Int. Ed.* **2004**, *43*, 668–698.

[23] T. M. Bryan, P. Baumann, "G-quadruplexes: from guanine gels to chemotherapeutics." *Mol. Biotechnol.* **2011**, *49*, 198–208.

[24] M. Gellert, M. N. Lipsett, D. R. Davies, "HELIX FORMATION BY GUANYLIC ACID" *Proc. Natl. Acad. Sci.* **1962**, *48*, 2013–2018.

[25] A. K. Todd, M. Johnston, S. Neidle, "Highly prevalent putative quadruplex sequence motifs in human DNA" *Nucleic Acids Res.*. **2005**, *33*, 2901–2907.

[26] D. Bhattacharyya, G. M. Arachchilage, S. Basu, “Metal Cations in G-Quadruplex Folding and Stability” *Front. Chem.* **2016**, *4*, 38.

[27] E. Largy, J.-L. Mergny, V. Gabelica, “The Alkali Metal Ions: Their Role for Life” *Metal Ions Life Sci.* **2016**, *16*, 203–258.

[28] S. Burge, G. N. Parkinson, P. Hazel, A. K. Todd, S. Neidle, “Quadruplex DNA: sequence, topology and structure” *Nucleic Acids Res.*. **2006**, *34*, 5402–5415.

[29] A. N. Lane, J. B. Chaires, R. D. Gray, J. O. Trent, “Stability and kinetics of G-quadruplex structures” *Nucleic Acids Res.*. **2008**, *36*, 5482–5515.

[30] H. J. Lipps, D. Rhodes, “G-quadruplex structures: in vivo evidence and function” *Trends Cell Biol.* **2009**, *19*, 414–422.

[31] J. L. Huppert, “Structure, location and interactions of G-quadruplexes” *FEBS J.* **2010**, *277*, 3452–3458.

[32] M. L. Bochman, K. Paeschke, V. A. Zakian, “DNA secondary structures: stability and function of G-quadruplex structures” *Nat. Rev. Genet.* **2012**, *13*, 770–780.

[33] S. Zhang, Y. Wu, W. Zhang, “G-Quadruplex Structures and Their Interaction Diversity with Ligands” *ChemMedChem* **2014**, *9*, 899–911.

[34] D. Rhodes, H. J. Lipps, “G-quadruplexes and their regulatory roles in biology” *Nucleic Acids Res.*. **2015**, *43*, 8627–8637.

[35] H. L. Lightfoot, T. Hagen, N. J. Tatum, J. Hall, “The diverse structural landscape of quadruplexes” *FEBS Lett.* **2019**, *593*, 2083–2102.

[36] Y. Ma, K. Iida, K. Nagasawa, “Topologies of G-quadruplex: Biological functions and regulation by ligands” *Biochem. Biophys. Res. Commun.* **2020**, *531*, 3–17.

[37] P. Hazel, G. N. Parkinson, S. Neidle, “Topology Variation and Loop Structural Homology in Crystal and Simulated Structures of a Bimolecular DNA Quadruplex” *J. Am. Chem. Soc.* **2006**, *128*, 5480–5487.

[38] D. M. Gray, C. W. Gray, T.-C. Mou, J.-D. Wen, “CD of Single-Stranded, Double-Stranded, and G-Quartet Nucleic Acids in Complexes with a Single-Stranded DNA-Binding Protein” *Enantiomer J Sterochemistry* **2002**, *7*, 49–58.

[39] S. Nagatoishi, Y. Tanaka, K. Tsumoto, “Circular dichroism spectra demonstrate formation of the thrombin-binding DNA aptamer G-quadruplex under stabilizing-cation-deficient conditions” *Biochem. Bioph. Res. Co.* **2007**, *352*, 812–817.

[40] R. del Villar-Guerra, J. O. Trent, J. B. Chaires, “G-Quadruplex Secondary Structure Obtained from Circular Dichroism Spectroscopy” *Angew. Chem. Int. Ed.* **2018**, *57*, 7171–7175.

[41] R. del Villar-Guerra, R. D. Gray, J. B. Chaires, “Characterization of Quadruplex DNA Structure by Circular Dichroism” *Curr. Protoc. Nucleic Acid Chem.* **2017**, *68*, 17.8.1-17.8.16.

[42] S. Beychok, “Circular Dichroism of Biological Macromolecules” *Science* **1966**, *154*, 1288–1299.

[43] S. R. Martin, M. J. Schilstra, “Circular Dichroism and Its Application to the Study of Biomolecules” *Methods Cell. Biol.* **2008**, *84*, 263–293.

[44] G. N. Parkinson, G. W. Collie, “G-Quadruplex Nucleic Acids, Methods and Protocols” *Methods Mol. Biol.* **2019**, *2035*, 131–155.

[45] R. K. R. Sannapureddi, M. K. Mohanty, A. K. Gautam, B. Sathyamoorthy, “Characterization of DNA G-quadruplex Topologies with NMR Chemical Shifts” *J. Phys. Chem. Lett.* **2020**, *11*, 10016–10022.

[46] J. Dickerhoff, J. Jang, D. Yang, “Best method to determine DNA G-quadruplex folding: The 1H–13C HSQC NMR experiment” *Methods* **2024**, *221*, 35–41.

[47] J.-L. Mergny, J. Li, L. Lacroix, S. Amrane, J. B. Chaires, “Thermal difference spectra: a specific signature for nucleic acid structures” *Nucleic Acids Res.*. **2005**, *33*, e138–e138.

[48] Y. Luo, A. Granzhan, J. Marquevielle, A. Cucchiarini, L. Lacroix, S. Amrane, D. Verga, J.-L. Mergny, “Guidelines for G-quadruplexes: I. In vitro characterization” *Biochimie* **2023**, *214*, 5–23.

[49] V. Singh, M. Azarkh, M. Drescher, J. S. Hartig, “Conformations of individual quadruplex units studied in the context of extended human telomeric DNA” *Chem. Commun.* **2012**, *48*, 8258–8260.

[50] V. Singh, M. Azarkh, T. E. Exner, J. S. Hartig, M. Drescher, “Human Telomeric Quadruplex Conformations Studied by Pulsed EPR” *Angew. Chem. Int. Ed.* **2009**, *48*, 9728–9730.

[51] G. N. Parkinson, M. P. H. Lee, S. Neidle, “Crystal structure of parallel quadruplexes from human telomeric DNA” *Nature* **2002**, *417*, 876–880.

[52] D. Sen, W. Gilbert, “Novel DNA superstructures formed by telomere-like oligomers” *Biochemistry-us* **1992**, *31*, 65–70.

[53] Y. Wang, D. J. Patel, “Guanine residues in d(T2AG3) and d(T2G4) form parallel-stranded potassium cation stabilized G-quadruplexes with anti glycosidic torsion angles in solution” *Biochemistry* **1992**, *31*, 8112–8119.

[54] Y. Krishnan-Ghosh, D. Liu, S. Balasubramanian, “Formation of an Interlocked Quadruplex Dimer by d(GGGT)” *J. Am. Chem. Soc.* **2004**, *126*, 11009–11016.

[55] Y. Kato, T. Ohyama, H. Mita, Y. Yamamoto, “Dynamics and Thermodynamics of Dimerization of Parallel G-Quadruplexed DNA Formed from d(TTAG $_n$) (n = 3−5)” *J. Am. Chem. Soc.* **2005**, *127*, 9980–9981.

[56] V. Kuryavyi, A. T. Phan, D. J. Patel, “Solution structures of all parallel-stranded monomeric and dimeric G-quadruplex scaffolds of the human c-kit2 promoter” *Nucleic Acids Res.*. **2010**, *38*, 6757–6773.

[57] N. Q. Do, K. W. Lim, M. H. Teo, B. Heddi, A. T. Phan, “Stacking of G-quadruplexes: NMR structure of a G-rich oligonucleotide with potential anti-HIV and anticancer activity” *Nucleic Acids Res.*. **2011**, *39*, 9448–9457.

[58] N. Q. Do, A. T. Phan, “Monomer–Dimer Equilibrium for the 5′–5′ Stacking of Propeller-Type Parallel-Stranded G-Quadruplexes: NMR Structural Study” *Chem. Eur. J.* **2012**, *18*, 14752–14759.

[59] M. Adrian, D. J. Ang, C. J. Lech, B. Heddi, A. Nicolas, A. T. Phan, “Structure and Conformational Dynamics of a Stacked Dimeric G-Quadruplex Formed by the Human CEB1 Minisatellite” *J. Am. Chem. Soc.* **2014**, *136*, 6297–6305.

[60] S. Kolesnikova, E. A. Curtis, “Structure and Function of Multimeric G-Quadruplexes” *Molecules* **2019**, *24*, 3074–3074.

[61] E. Henderson, C. C. Hardin, S. K. Walk, I. Tinoco, E. H. Blackburn, “Telomeric DNA oligonucleotides form novel intramolecular structures containing guanine·guanine base pairs” *Cell* **1987**, *51*, 899–908.

[62] D. Sen, W. Gilbert, “Formation of parallel four-stranded complexes by guanine-rich motifs in DNA and its implications for meiosis” *Nature* **1988**, *334*, 364–366.

[63] S. Galli, L. Melidis, S. M. Flynn, D. Varshney, A. Simeone, J. Spiegel, S. K. Madden, D. Tannahill, S. Balasubramanian, “DNA G-Quadruplex Recognition In Vitro and in Live Cells by a Structure-Specific Nanobody” *J. Am. Chem. Soc.* **2022**, *144*, 23096–23103.

[64] A. Ghosh, M. Trajkovski, M.-P. Teulade-Fichou, V. Gabelica, J. Plavec, “Phen-DC3 Induces Refolding of Human Telomeric DNA into a Chair-type Antiparallel G-quadruplex through Ligand Intercalation” *Angew. Chem. Int. Ed.* **2022**, DOI 10.1002/anie.202207384.

[65] F. Kouzine, D. Wojtowicz, A. Yamane, R. Casellas, T. M. Przytycka, D. L. Levens, “G-Quadruplex Nucleic Acids, Methods and Protocols” *Methods Mol. Biol.* **2019**, *2035*, 369–382.

[66] Z.-H. Zhang, S. H. Qian, D. Wei, Z.-X. Chen, “In vivo dynamics and regulation of DNA G-quadruplex structures in mammals” *Cell Biosci.* **2023**, *13*, 117.

[67] W. I. Sundquist, A. Klug, “Telomeric DNA dimerizes by formation of guanine tetrads between hairpin loops” *Nature* **1989**, *342*, 825–829.

[68] S. Neidle, “Quadruplex nucleic acids as targets for anticancer therapeutics” *Nat. Rev. Chem.* **2017**, *1*, s41570-017–0041.

[69] J. L. Huppert, S. Balasubramanian, “Prevalence of quadruplexes in the human genome” *Nucleic Acids Res.*. **2005**, *33*, 2908–2916.

[70] S. Roy, P. Pramanik, S. Bhattacharya, “Exploring the role of G-quadruplex DNA, and their structural polymorphism, in targeting small molecules for the design of anticancer therapeutics: Progress, challenges, and future directions” *Biochimie* **2025**, *234*, 120–145.

[71] F.-Y. Teng, Z.-Z. Jiang, M. Guo, X.-Z. Tan, F. Chen, X.-G. Xi, Y. Xu, “G-quadruplex DNA: a novel target for drug design” *Cell. Mol. Life Sci.* **2021**, *78*, 6557–6583.

[72] T. Tian, Y.-Q. Chen, S.-R. Wang, X. Zhou, “G-Quadruplex: A Regulator of Gene Expression and Its Chemical Targeting” *Chem* **2018**, *4*, 1314–1344.

[73] H. Masai, T. Tanaka, “G-quadruplex DNA and RNA: Their roles in regulation of DNA replication and other biological functions” *Biochem. Biophys. Res. Commun.* **2020**, *531*, 25–38.

[74] J. L. Huppert, A. Bugaut, S. Kumari, S. Balasubramanian, “G-quadruplexes: the beginning and end of UTRs” *Nucleic Acids Res.* **2008**, *36*, 6260–6268.

[75] G. Biffi, D. Tannahill, J. McCafferty, S. Balasubramanian, “Quantitative visualization of DNA G-quadruplex structures in human cells” *Nat. Chem.* **2013**, *5*, 182–186.

[76] R. Hänsel-Hertsch, M. D. Antonio, S. Balasubramanian, “DNA G-quadruplexes in the human genome: detection, functions and therapeutic potential” *Nat. Rev. Mol. Cell. Biol.* **2017**, *18*, 279–284.

[77] R. Hänsel-Hertsch, D. Beraldi, S. V. Lensing, G. Marsico, K. Zyner, A. Parry, M. D. Antonio, J. Pike, H. Kimura, M. Narita, D. Tannahill, S. Balasubramanian, “G-quadruplex structures mark human regulatory chromatin” *Nat. Genet.* **2016**, *48*, 1267–1272.

[78] M. A. Blasco, “Telomeres and human disease: ageing, cancer and beyond” *Nat. Rev. Genet.* **2005**, *6*, 611–622.

[79] A. L. Moye, K. C. Porter, S. B. Cohen, T. Phan, K. G. Zyner, N. Sasaki, G. O. Lovrecz, J. L. Beck, T. M. Bryan, “Telomeric G-quadruplexes are a substrate and site of localization for human telomerase” *Nat. Commun.* **2015**, *6*, 7643.

[80] T. M. Bryan, “G-Quadruplexes at Telomeres: Friend or Foe?” *Molecules* **2020**, *25*, 3686.

[81] J. Figueiredo, J.-L. Mergny, C. Cruz, “G-quadruplex ligands in cancer therapy: Progress, challenges, and clinical perspectives” *Life Sci.* **2024**, *340*, 122481.

[82] C. Esnault, A. Z. E. Aabidine, M.-C. Robert, A. Cucchiarini, T. Magat, A. Pigeot, S. Bouchouika, E. Garcia-Oliver, K. Gawron, E. Basyuk, M. A. Karpinska, A. Kozulic-Pirher, Y. Luo, D. Verga, R. Mourad, O. Radulescu, J.-L. Mergny, E. Bertrand, J.-C. Andrau, “G-quadruplexes are promoter elements controlling nucleosome exclusion and RNA polymerase II pausing” *Nat. Genet.* **2025**, *57*, 1981–1993.

[83], “G-quadruplexes define promoter identity in mammals” *Nat. Genet.* **2025**, *57*, 1798–1799.

[84] L. Chen, J. Dickerhoff, S. Sakai, D. Yang, "DNA G-Quadruplex in Human Telomeres and Oncogene Promoters: Structures, Functions, and Small Molecule Targeting" *Acc. Chem. Res.* **2022**, *55*, 2628–2646.

[85] R. Chaudhuri, S. Bhattacharya, J. Dash, S. Bhattacharya, "Recent Update on Targeting c-MYC G-Quadruplexes by Small Molecules for Anticancer Therapeutics" *J. Med. Chem.* **2021**, *64*, 42–70.

[86] L. Chen, J. Dickerhoff, K. Zheng, S. Erramilli, H. Feng, G. Wu, B. Onel, Y. Chen, K.-B. Wang, M. Carver, C. Lin, S. Sakai, J. Wan, C. Vinson, L. Hurley, A. A. Kossiakoff, N. Deng, Y. Bai, N. Noinaj, D. Yang, "Structural basis for nucleolin recognition of MYC promoter G-quadruplex" *Science* **2025**, *388*, eadr1752.

[87] I. Esain-Garcia, A. Kirchner, L. Melidis, R. de C. A. Tavares, S. Dhir, A. Simeone, Z. Yu, S. K. Madden, R. Hermann, D. Tannahill, S. Balasubramanian, "G-quadruplex DNA structure is a positive regulator of MYC transcription" *Proc. Natl. Acad. Sci.* **2024**, *121*, e2320240121.

[88] W. Wang, S. Hu, Y. Gu, Y. Yan, D. B. Stovall, D. Li, G. Sui, "Human MYC G-quadruplex: From discovery to a cancer therapeutic target" *Biochim. Biophys. Acta (BBA) - Rev. Cancer* **2020**, *1874*, 188410.

[89] K.-B. Wang, Y. Liu, J. Li, C. Xiao, Y. Wang, W. Gu, Y. Li, Y.-Z. Xia, T. Yan, M.-H. Yang, L.-Y. Kong, "Structural insight into the bulge-containing KRAS oncogene promoter G-quadruplex bound to berberine and coptisine" *Nat. Commun.* **2022**, *13*, 6016.

[90] S. Cogoi, L. E. Xodo, "G-quadruplex formation within the promoter of the KRAS proto-oncogene and its effect on transcription" *Nucleic Acids Res.*. **2006**, *34*, 2536–2549.

[91] J. Amato, T. W. Madanayake, N. Iaccarino, E. Novellino, A. Randazzo, L. H. Hurley, B. Pagano, "HMGB1 binds to the KRAS promoter G-quadruplex: a new player in oncogene transcriptional regulation?" *Chem. Commun.* **2018**, *54*, 9442–9445.

[92] S. Amrane, C. Jaubert, A. Bedrat, T. Rundstadler, P. Recordon-Pinson, C. Aknin, A. Guédin, A. D. Rache, L. Bartolucci, I. Diene, F. Lemoine, O. Gascuel, G. Pratviel, J.-L. Mergny, M.-L. Andreola, "Deciphering RNA G-quadruplex function during the early steps of HIV-1 infection" *Nucleic Acids Res.*. **2022**, *50*, 12328–12343.

[93] R. Perrone, M. Nadai, I. Frasson, J. A. Poe, E. Butovskaya, T. E. Smithgall, M. Palumbo, G. Palù, S. N. Richter, "A Dynamic G-Quadruplex Region Regulates the HIV-1 Long Terminal Repeat Promoter" *J. Med. Chem.* **2013**, *56*, 6521–6530.

[94] H. Cui, L. Zhang, "G-Quadruplexes Are Present in Human Coronaviruses Including SARS-CoV-2" *Front. Microbiol.* **2020**, *11*, 567317.

[95] J. Norseen, F. B. Johnson, P. M. Lieberman, "Role for G-Quadruplex RNA Binding by Epstein-Barr Virus Nuclear Antigen 1 in DNA Replication and Metaphase Chromosome Attachment" *J. Virol.* **2009**, *83*, 10336–10346.

[96] E. Butovskaya, B. Heddi, B. Bakalar, S. N. Richter, A. T. Phan, "Major G-Quadruplex Form of HIV-1 LTR Reveals a (3 + 1) Folding Topology Containing a Stem-Loop" *J. Am. Chem. Soc.* **2018**, *140*, 13654–13662.

[97] K. Niu, L. Xiang, X. Zhang, X. Li, T. Yao, J. Li, C. Zhang, J. Liu, Y. Peng, G. Xu, H. Xiang, H. Wang, Q. Song, Q. Feng, "DNA 5mC methylation inhibits the formation of G-quadruplex structures in the genome" *Genome Biol.* **2025**, *26*, 202.

[98] O. Mendoza, A. Bourdoncle, J.-B. Boulé, R. M. Brosh, J.-L. Mergny, "G-quadruplexes and helicases" *Nucleic Acids Res.* **2016**, *44*, 1989–2006.

[99] M. Caterino, K. Paeschke, "Action and function of helicases on RNA G-quadruplexes" *Methods* **2022**, *204*, 110–125.

[100] J. Frobel, R. Hänsel-Hertsch, "The age-related decline of helicase function—how G-quadruplex structures promote genome instability" *FEBS Lett.* **2025**, *599*, 267–274.

[101] S. Pepe, F. Guerra, M. Russo, R. C. Duardo, G. Capranico, "Genomic context influences translesion synthesis DNA polymerase-dependent mechanisms of micronuclei induction by G-quadruplexes" *Cell Rep.* **2025**, *44*, 115706.

[102] G. Miglietta, M. Russo, R. C. Duardo, G. Capranico, "G-quadruplex binders as cytostatic modulators of innate immune genes in cancer cells" *Nucleic Acids Res.*. **2021**, *49*, 6673–6686.

[103] Y. Wang, J. Yang, A. T. Wild, W. H. Wu, R. Shah, C. Danussi, G. J. Riggins, K. Kannan, E. P. Sulman, T. A. Chan, J. T. Huse, "G-quadruplex DNA drives genomic instability and represents a targetable molecular abnormality in ATRX-deficient malignant glioma" *Nat. Commun.* **2019**, *10*, 943.

[104] B. Zhou, C. Liu, Y. Geng, G. Zhu, "Topology of a G-quadruplex DNA formed by C9orf72 hexanucleotide repeats associated with ALS and FTD" *Sci. Rep.* **2015**, *5*, 16673.

[105] R. Simone, R. Balendra, T. G. Moens, E. Preza, K. M. Wilson, A. Heslegrave, N. S. Woodling, T. Niccoli, J. Gilbert-Jaramillo, S. Abdelkarim, E. L. Clayton, M. Clarke, M. Konrad, A. J. Nicoll, J. S. Mitchell, A. Calvo, A. Chio, H. Houlden, J. M. Polke, M. A. Ismail, C. E. Stephens, T. Vo, A. A. Farahat, W. D. Wilson, D. W. Boykin, H. Zetterberg, L. Partridge, S. Wray, G. Parkinson, S. Neidle, R. Patani, P. Fratta, A. M. Isaacs, "G-quadruplex-binding small molecules ameliorate C9orf72 FTD/ALS pathology in vitro and in vivo" *EMBO Mol. Med.* **2018**, *10*, 22–31.

[106] K. Reddy, B. Zamiri, S. Y. R. Stanley, R. B. Macgregor, C. E. Pearson, "The Disease-associated r(GGGGCC) n Repeat from the C9orf72 Gene Forms Tract Length-dependent Uni- and Multimolecular RNA G-quadruplex Structures*" *J. Biol. Chem.* **2013**, *288*, 9860–9866.

[107] V. J. Sahayasheela, Z. Yu, T. Hidaka, G. N. Pandian, H. Sugiyama, "Mitochondria and G-quadruplex evolution: an intertwined relationship" *Trends Genet.* **2023**, *39*, 15–30.

[108] M. Falabella, R. J. Fernandez, F. B. Johnson, B. A. Kaufman, "Potential Roles for G-Quadruplexes in Mitochondria" *Curr. Med. Chem.* **2019**, *26*, 2918–2932.

[109] M. Falabella, J. E. Kolesar, C. Wallace, D. de Jesus, L. Sun, Y. V. Taguchi, C. Wang, T. Wang, I. M. Xiang, J. K. Alder, R. Maheshan, W. Horne, J. Turek-Herman, P. J. Pagano, C. M. St. Croix, N. Sondheimer, L. A. Yatsunyk, F. B. Johnson, B. A. Kaufman, "G-quadruplex dynamics contribute to regulation of mitochondrial gene expression" *Sci. Rep.* **2019**, *9*, 5605.

[110] W.-C. Huang, T.-Y. Tseng, Y.-T. Chen, C.-C. Chang, Z.-F. Wang, C.-L. Wang, T.-N. Hsu, P.-T. Li, C.-T. Chen, J.-J. Lin, P.-J. Lou, T.-C. Chang, "Direct evidence of mitochondrial G-quadruplex DNA by using fluorescent anti-cancer agents" *Nucleic Acids Res.* **2015**, *43*, 10102–10113.

[111] D. Monchaud, M.-P. Teulade-Fichou, "A hitchhiker's guide to G-quadruplex ligands" *Org. Biomol. Chem.* **2007**, *6*, 627–636.

[112] A. R. Duarte, E. Cadoni, A. S. Ressurreição, R. Moreira, A. Paulo, "Design of Modular G-quadruplex Ligands" *ChemMedChem* **2018**, *13*, 869–893.

[113] E. Ruggiero, S. N. Richter, "G-quadruplexes and G-quadruplex ligands: targets and tools in antiviral therapy" *Nucleic Acids Res.*. **2018**, *46*, gky187-.

[114] H. Xu, M. D. Antonio, S. McKinney, V. Mathew, B. Ho, N. J. O'Neil, N. D. Santos, J. Silvester, V. Wei, J. Garcia, F. Kabeer, D. Lai, P. Soriano, J. Banáth, D. S. Chiu, D. Yap, D. D. Le, F. B. Ye, A. Zhang, K. Thu, J. Soong, S. Lin, A. H. C. Tsai, T. Osako, T. Algara, D. N. Saunders, J. Wong, J. Xian, M. B. Bally, J. D. Brenton, G. W. Brown, S. P. Shah, D. Cescon, T. W. Mak, C. Caldas, P. C. Stirling, P. Hieter, S. Balasubramanian, S. Aparicio, "CX-5461 is a DNA G-quadruplex stabilizer with selective lethality in BRCA1/2 deficient tumours" *Nat. Commun.* **2017**, *8*, 14432.

[115] H. Xu, L. H. Hurley, "A first-in-class clinical G-quadruplex-targeting drug. The bench-to-bedside translation of the fluoroquinolone QQ58 to CX-5461 (Pidnarulex)" *Bioorg. Med. Chem. Lett.* **2022**, *77*, 129016.

[116] H.-X. Li, Y.-M. He, J. Fei, M. Guo, C. Zeng, P.-J. Yan, Y. Xu, G. Qin, F.-Y. Teng, "The G-quadruplex ligand CX-5461: an innovative candidate for disease treatment" *J. Transl. Med.* **2025**, *23*, 457.

[117] K. P. Papadopoulos, D. W. Northfelt, D. M. Hufnagel, A. D. Ricart, P. P. Griffin, M. D. Oslund, D. D. V. Hoff, W. G. Rice, J. K. Lim, R. F. Marschke, "Phase I clinical trial of CX-3543, a protein-rDNA quadruplex inhibitor" *J. Clin. Oncol.* **2007**, *25*, 3585–3585.

[118] V. Sanchez-Martin, "Opportunities and challenges with G-quadruplexes as promising targets for drug design" *Expert Opin. Drug Discov.* **2024**, *19*, 1339–1353.

[119] S. Asamitsu, T. Bando, H. Sugiyama, "Ligand Design to Acquire Specificity to Intended G-Quadruplex Structures" *Chem. A Eur. J.* **2019**, *25*, 417–430.

[120] G. Qin, Z. Liu, J. Yang, X. Liao, C. Zhao, J. Ren, X. Qu, "Targeting specific DNA G-quadruplexes with CRISPR-guided G-quadruplex-binding proteins and ligands" *Nat. Cell Biol.* **2024**, *26*, 1212–1224.

[121] P. Maleki, J. B. Budhathoki, W. A. Roy, H. Balci, "A practical guide to studying G-quadruplex structures using single-molecule FRET" *Mol. Genet. Genom.* **2017**, *292*, 483–498.

[122] N. Kusi-Appauh, S. F. Ralph, A. M. van Oijen, L. M. Spenkelink, "Understanding G-Quadruplex Biology and Stability Using Single-Molecule Techniques" *The J. Phys. Chem. B* **2023**, DOI 10.1021/acs.jpcb.3c01708.

[123] B. Okumus, T. Ha, "G-Quadruplex DNA, Methods and Protocols" *Methods Mol. Biol.* **2009**, *608*, 81–96.

[124] Y. Dai, X. Teng, Q. Zhang, H. Hou, J. Li, "Advances and challenges in identifying and characterizing G-quadruplex–protein interactions" *Trends Biochem. Sci.* **2023**, *48*, 894–909.

[125] X. Zhang, J. Spiegel, S. M. Cuesta, S. Adhikari, S. Balasubramanian, "Chemical profiling of DNA G-quadruplex-interacting proteins in live cells" *Nat. Chem.* **2021**, *13*, 626–633.

[126] Z. Lu, S. Xie, H. Su, S. Han, H. Huang, X. Zhou, "Identification of G-quadruplex-interacting proteins in living cells using an artificial G4-targeting biotin ligase" *Nucleic Acids Res.* **2024**, *52*, e37–e37.

[127] V. Meier-Stephenson, "G4-quadruplex-binding proteins: review and insights into selectivity" *Biophysical Rev.* **2022**, 1–20.

[128] R. Duan, J. Zheng, Y. Hao, Z. Tan, "G-Quadruplex-Protein Interactome at Human Gene Promoters" *bioRxiv* **2025**, 2025.01.01.630896.

[129] R. Troisi, F. Sica, "Structural overview of DNA and RNA G-quadruplexes in their interaction with proteins" *Curr. Opin. Struct. Biol.* **2024**, *87*, 102846.

[130] S. Marzano, G. Pinto, A. D. Porzio, J. Amato, A. Randazzo, A. Amoresano, B. Pagano, "Identifying G-quadruplex-interacting proteins in cancer-related gene promoters" *Commun. Chem.* **2025**, *8*, 64.

[131] B. R. Sahoo, V. Kocman, N. Clark, N. Myers, X. Deng, E. L. Wong, H. J. Yang, A. Kotar, B. B. Guzman, D. Dominguez, J. Plavec, J. C. A. Bardwell, "Protein G-quadruplex interactions and their effects on phase transitions and protein aggregation" *Nucleic Acids Res.*. **2024**, *52*, 4702–4722.

[132] M. Abdelhaleem, "Helicases, Methods and Protocols" *Methods Mol. Biol.* **2009**, *587*, 1–12.

[133] R. M. Brosh, S. W. Matson, "History of DNA Helicases" *Genes* **2020**, *11*, 255.

[134] K. A. Bernstein, S. Gangloff, R. Rothstein, “The RecQ DNA Helicases in DNA Repair” *Genetics* **2010**, *44*, 393–417.

[135] H. Lu, A. J. Davis, “Human RecQ Helicases in DNA Double-Strand Break Repair” *Front. Cell Dev. Biol.* **2021**, *9*, 640755.

[136] J. A. Newman, O. Gileadi, “RecQ helicases in DNA repair and cancer targets” *Essays Biochem.* **2020**, *64*, 819–830.

[137] J. A. Smestad, L. J. Maher, “Relationships between putative G-quadruplex-forming sequences, RecQ helicases, and transcription” *BMC Méd. Genet.* **2015**, *16*, 91.

[138] W. Wu, N. Rokutanda, J. Takeuchi, Y. Lai, R. Maruyama, Y. Togashi, H. Nishikawa, N. Arai, Y. Miyoshi, N. Suzuki, Y. Saeki, K. Tanaka, T. Ohta, “HERC2 facilitates BLM and WRN helicase complex interaction with RPA to suppress G-quadruplex DNA” *Cancer Res.* **2018**, *78*, canres.1877.2018.

[139] A. O.-W. Leung, T.-C. Yiu, L. Liu, H.-Y. Tam, S. Gu, J. Tu, D. Pei, H.-H. Cheung, “Targeting G-quadruplex for rescuing impaired chondrogenesis in WRN-deficient stem cells” *Cell Biosci.* **2022**, *12*, 212.

[140] A. Ketkar, M. Voehler, T. Mukiza, R. L. Eoff, “Residues in the RecQ C-terminal Domain of the Human Werner Syndrome Helicase Are Involved in Unwinding G-quadruplex DNA.” *J. Biol. Chem.* **2017**, *292*, 3154–3163.

[141] W.-Q. Wu, X.-M. Hou, M. Li, S.-X. Dou, X.-G. Xi, “BLM unfolds G-quadruplexes in different structural environments through different mechanisms” *Nucleic Acids Res.*. **2015**, *43*, 4614–4626.

[142] G. H. Nguyen, W. Tang, A. I. Robles, R. P. Beyer, L. T. Gray, J. A. Welsh, A. J. Schetter, K. Kumamoto, X. W. Wang, I. D. Hickson, N. Maizels, R. J. Monnat, C. C. Harris, “Regulation of gene expression by the BLM helicase correlates with the presence of G-quadruplex DNA motifs” *Proc. Natl. Acad. Sci.* **2014**, *111*, 9905–9910.

[143] S. Chatterjee, J. Zagelbaum, P. Savitsky, A. Sturzenegger, D. Huttner, P. Janscak, I. D. Hickson, O. Gileadi, E. Rothenberg, “Mechanistic insight into the interaction of BLM helicase with intra-strand G-quadruplex structures” *Nat. Commun.* **2014**, *5*, 5556.

[144] N. van Wietmarschen, S. Merzouk, N. Halsema, D. C. J. Spierings, V. Guryev, P. M. Lansdorp, “BLM helicase suppresses recombination at G-quadruplex motifs in transcribed genes” *Nat. Commun.* **2018**, *9*, 271.

[145] K. Paeschke, M. L. Bochman, P. D. Garcia, P. Cejka, K. L. Friedman, S. C. Kowalczykowski, V. A. Zakian, “Pif1 family helicases suppress genome instability at G-quadruplex motifs” *Nature* **2013**, *497*, 458–462.

[146] C. M. Sanders, “Human Pif1 helicase is a G-quadruplex DNA-binding protein with G-quadruplex DNA-unwinding activity” *Biochem. J.* **2010**, *430*, 119–128.

[147] K. Paeschke, J. A. Capra, V. A. Zakian, “DNA Replication through G-Quadruplex Motifs Is Promoted by the Saccharomyces cerevisiae Pif1 DNA Helicase” *Cell* **2011**, *145*, 678–691.

[148] D. Dahan, I. Tsirkas, D. Dovrat, M. A. Sparks, S. P. Singh, R. Galletto, A. Aharoni, “Pif1 is essential for efficient replisome progression through lagging strand G-quadruplex DNA secondary structures” *Nucleic Acids Res.*. **2018**, *46*, 11847–11857.

[149] M. Varon, D. Dovrat, J. Heuzé, I. Tsirkas, S. P. Singh, P. Pasero, R. Galletto, A. Aharoni, “Rrm3 and Pif1 division of labor during replication through leading and lagging strand G-quadruplex” *Nucleic Acids Res.*. **2023**, gkad1205.

[150] X.-M. Hou, W.-Q. Wu, X.-L. Duan, N.-N. Liu, H.-H. Li, J. Fu, S.-X. Dou, M. Li, X.-G. Xi, “Molecular mechanism of G-quadruplex unwinding helicase: sequential and repetitive unfolding of G-quadruplex by Pif1 helicase” *Biochem. J.* **2015**, *466*, 189–199.

[151] Z. Hong, A. K. Byrd, J. Gao, P. Das, V. Q. Tan, E. G. Malone, B. Osei, J. C. Marecki, R. U. Protacio, W. P. Wahls, K. D. Raney, H. Song, “Eukaryotic Pif1 helicase unwinds G-quadruplex and dsDNA using a conserved wedge” *Nat. Commun.* **2024**, *15*, 6104.

[152] O. Andrisani, Q. Liu, P. Kehn, W. W. Leitner, K. Moon, N. Vazquez-Maldonado, I. Fingerman, M. Gale, “Biological functions of DEAD/DEAH-box RNA helicases in health and disease” *Nat. Immunol.* **2022**, *23*, 354–357.

[153] M. C. Chen, R. Tippana, N. A. Demeshkina, P. Murat, S. Balasubramanian, S. Myong, A. R. Ferré-D’Amaré, “Structural basis of G-quadruplex unfolding by the DEAH/RHA helicase DHX36” *Nature* **2018**, *558*, 465–469.

[154] R. Tippana, M. C. Chen, N. A. Demeshkina, A. R. Ferré-D’Amaré, S. Myong, “RNA G-quadruplex is resolved by repetitive and ATP-dependent mechanism of DHX36” *Nat. Commun.* **2019**, *10*, 1855.

[155] Z. Lu, J. Xu, Y. Chen, Y. Zhou, X. Zhou, Q. Wang, Q. Wei, S. Han, R. Zhao, X. Weng, X. Zhang, X. Zhou, “Rapid degradation of DHX36 revealing its transcriptional role by interacting with G-quadruplex” *Aggregate* **2025**, *6*, DOI 10.1002/agt2.647.

[156] P. M. Yangyuoru, D. A. Bradburn, Z. Liu, T. S. Xiao, R. Russell, “The G-quadruplex (G4) resolvase DHX36 efficiently and specifically disrupts DNA G4s via a translocation-based helicase mechanism” *J. Biol. Chem.* **2018**, *293*, 1924–1932.

[157] B. Chang-Gu, D. Bradburn, P. M. Yangyuoru, R. Russell, “The DHX36-specific-motif (DSM) enhances specificity by accelerating recruitment of DNA G-quadruplex structures” *Biol. Chem.* **2021**, *402*, 593–604.

[158] B. Heddi, V. V. Cheong, E. Schmitt, Y. Mechulam, A. T. Phan, “Recognition of different base tetrads by RHAU (DHX36): X-ray crystal structure of the G4 recognition motif bound to the 3′-end tetrad of a DNA G-quadruplex” *J. Struct. Biol.* **2020**, *209*, 107399.

[159] H. Ginisty, H. Sicard, B. Roger, P. Bouvet, “Structure and functions of nucleolin” *J. Cell Sci.* **1999**, *112*, 761–772.

[160] V. González, K. Guo, L. Hurley, D. Sun, "Identification and Characterization of Nucleolin as a c-myc G-quadruplex-binding Protein*" *J. Biol. Chem.* **2009**, *284*, 23622–23635.

[161] S. Lago, E. Tosoni, M. Nadai, M. Palumbo, S. N. Richter, "The cellular protein nucleolin preferentially binds long-looped G-quadruplex nucleic acids" *Biochim. Biophys. Acta (BBA) - Gen. Subj.* **2017**, *1861*, 1371–1381.

[162] A. Siddiqui-Jain, C. L. Grand, D. J. Bearss, L. H. Hurley, "Direct evidence for a G-quadruplex in a promoter region and its targeting with a small molecule to repress c-MYC transcription" *Proc National Acad Sci* **2002**, *99*, 11593–11598.

[163] S. Cogoi, S. Zorzet, V. Rapozzi, I. Géci, E. B. Pedersen, L. E. Xodo, "MAZ-binding G4-decoy with locked nucleic acid and twisted intercalating nucleic acid modifications suppresses KRAS in pancreatic cancer cells and delays tumor growth in mice" *Nucleic Acids Res.* **2013**, *41*, 4049–4064.

[164] S. Cogoi, A. E. Shchekotikhin, L. E. Xodo, "HRAS is silenced by two neighboring G-quadruplexes and activated by MAZ, a zinc-finger transcription factor with DNA unfolding property" *Nucleic Acids Res.* **2014**, *42*, 8379–8388.

[165] J. S. Hudson, L. Ding, V. Le, E. Lewis, D. Graves, "Recognition and Binding of Human Telomeric G-Quadruplex DNA by Unfolding Protein 1" *Biochemistry-us* **2014**, *53*, 3347–3356.

[166] H. Fukuda, M. Katahira, N. Tsuchiya, Y. Enokizono, T. Sugimura, M. Nagao, H. Nakagama, "Unfolding of quadruplex structure in the G-rich strand of the minisatellite repeat by the binding protein UP1" *Proc National Acad Sci* **2002**, *99*, 12685–12690.

[167] M. Paramasivam, A. Membrino, S. Cogoi, H. Fukuda, H. Nakagama, L. E. Xodo, "Protein hnRNP A1 and its derivative Up1 unfold quadruplex DNA in the human KRAS promoter: implications for transcription" *Nucleic Acids Res.* **2009**, *37*, 2841–2853.

[168] A. C. Krüger, M. K. Raarup, M. M. Nielsen, M. Kristensen, F. Besenbacher, J. Kjems, V. Birkedal, "Interaction of hnRNP A1 with telomere DNA G-quadruplex structures studied at the single molecule level" *Eur. Biophys. J.* **2010**, *39*, 1343–1350.

[169] M. Ghosh, M. Singh, "RGG-box in hnRNPA1 specifically recognizes the telomere G-quadruplex DNA and enhances the G-quadruplex unfolding ability of UP1 domain" *Nucleic Acids Res.* **2018**, *46*, 10246–10261.

[170] F. Tang, Y. Wang, Z. Gao, S. Guo, Y. Wang, "Polymerase η Recruits DHX9 Helicase to Promote Replication across Guanine Quadruplex Structures" *J. Am. Chem. Soc.* **2022**, *144*, 14016–14020.

[171] D. B. Oisen, S. S. Carroll, J. C. Culberson, J. A. Shafer, L. C. Kuo, "Effect of template secondary structure on the inhibition of HIV-1 reverse transcriptase by a pyridinone non-nucleoside inhibitor" *Nucleic Acids Res.*. **1994**, *22*, 1437–1443.

[172] L. Castells-Roca, E. Tejero, B. Rodríguez-Santiago, J. Surrallés, "CRISPR Screens in Synthetic Lethality and Combinatorial Therapies for Cancer" *Cancers* **2021**, *13*, 1591.

[173] D. Pradhan, L. H. Hansen, B. Vester, M. Petersen, "Selection of G-Quadruplex Folding Topology with LNA-Modified Human Telomeric Sequences in K+ Solution" *Chem. A Eur. J.* **2011**, *17*, 2405–2413.

[174] D. J. Y. Tan, P. Das, F. R. Winnerdy, K. W. Lim, A. T. Phan, "Guanine anchoring: a strategy for specific targeting of a G-quadruplex using short PNA, LNA and DNA molecules" *Chem Commun* **2020**, DOI 10.1039/d0cc01778g.

[175] L. Bonifacio, F. C. Church, M. B. Jarstfer, "Effect of Locked-Nucleic Acid on a Biologically Active G-Quadruplex. A Structure-Activity Relationship of the Thrombin Aptamer" *Int. J. Mol. Sci.* **2008**, *9*, 422–433.

[176] R. Hänsel-Hertsch, J. Spiegel, G. Marsico, D. Tannahill, S. Balasubramanian, "Genome-wide mapping of endogenous G-quadruplex DNA structures by chromatin immunoprecipitation and high-throughput sequencing" *Nat. Protoc.* **2018**, *13*, 551–564.

[177] X. Wang, G. Qin, J. Yang, C. Zhao, J. Ren, X. Qu, "A subcellular selective APEX2-based proximity labeling used for identifying mitochondrial G-quadruplex DNA binding proteins" *Nucleic Acids Res.*. **2024**, *53*, gkae1259.

[178] R. C. Monsen, E. Y. D. Chua, J. B. Hopkins, J. B. Chaires, J. O. Trent, "Structure of a 28.5 kDa duplex-embedded G-quadruplex system resolved to 7.4 Å resolution with cryo-EM" *Nucleic Acids Res.*. **2023**, *51*, 1943–1959.

[179] A. Hirschi, W. J. Martin, Z. Luka, L. V. Loukachevitch, N. J. Reiter, "G-quadruplex RNA binding and recognition by the lysine-specific histone demethylase-1 enzyme" *RNA* **2016**, *22*, 1250–1260.

[180] E. Stulz, G. Clever, M. Shionoya, C. Mao, "DNA in a modern world" *Chem. Soc. Rev.* **2011**, *40*, 5633–5635.

[181] G. H. Clever, C. Kaul, T. Carell, "DNA–Metal Base Pairs" *Angew. Chem. Int. Ed.* **2007**, *46*, 6226–6236.

[182] S. Katz, "The reversible reaction of Hg (II) and double-stranded polynucleotides a step-function theory and its significance" *Acta Biochim. Biophys. Sin.* **1963**, *68*, 240–253.

[183] A. Ono, S. Cao, H. Togashi, M. Tashiro, T. Fujimoto, T. Machinami, S. Oda, Y. Miyake, I. Okamoto, Y. Tanaka, "Specific interactions between silver(i) ions and cytosine – cytosine pairs in DNA duplexes" *Chem. Commun.* **2008**, *0*, 4825–4827.

[184] A. Ono, H. Togashi, "Highly Selective Oligonucleotide-Based Sensor for Mercury(II) in Aqueous Solutions" *Angew. Chem. Int. Ed.* **2004**, *43*, 4300–4302.

[185] J. Kondo, Y. Tada, T. Dairaku, Y. Hattori, H. Saneyoshi, A. Ono, Y. Tanaka, "A metallo-DNA nanowire with uninterrupted one-dimensional silver array" *Nat. Chem.* **2017**, *9*, 956–960.

[186] G. H. Clever, M. Shionoya, “Metal–base pairing in DNA” *Coord. Chem. Rev.* **2010**, *254*, 2391–2402.

[187] M. K. Schlegel, L.-O. Essen, E. Meggers, “Duplex Structure of a Minimal Nucleic Acid” *J. Am. Chem. Soc.* **2008**, *130*, 8158–8159.

[188] G. H. Clever, K. Polborn, T. Carell, “A Highly DNA-Duplex-Stabilizing Metal–Salen Base Pair” *Angew. Chem. Int. Ed.* **2005**, *44*, 7204–7208.

[189] K. Tanaka, A. Tengeiji, T. Kato, N. Toyama, M. Shionoya, “A Discrete Self-Assembled Metal Array in Artificial DNA” *Science* **2003**, *299*, 1212–1213.

[190] K. Tanaka, G. H. Clever, Y. Takezawa, Y. Yamada, C. Kaul, M. Shionoya, T. Carell, “Programmable self-assembly of metal ions inside artificial DNA duplexes” *Nat. Nanotechnol.* **2006**, *1*, nnano.2006.141.

[191] S. Johannsen, N. Megger, D. Böhme, R. K. O. Sigel, J. Müller, “Solution structure of a DNA double helix with consecutive metal-mediated base pairs” *Nat. Chem.* **2010**, *2*, 229.

[192] S. Liu, G. H. Clever, Y. Takezawa, M. Kaneko, K. Tanaka, X. Guo, M. Shionoya, “Direct Conductance Measurement of Individual Metallo-DNA Duplexes within Single-Molecule Break Junctions” *Angew. Chem. Int. Ed.* **2011**, *50*, 8886–8890.

[193] Y. Miyake, A. Ono, “Fluorescent sensor for redox environment: a redox controlled molecular device based on the reversible mercury mediated folded structure formation of oligothymidylate” *Tetrahedron Lett.* **2005**, *46*, 2441–2443.

[194] J. H. A. Duprey, Y. Takezawa, M. Shionoya, “Metal-Locked DNA Three-Way Junction ” *Angew. Chem. Int. Ed.* **2013**, *52*, 1212–1216.

[195] Y. Takezawa, S. Yoneda, J.-L. H. A. Duprey, T. Nakama, M. Shionoya, “Metal-responsive structural transformation between artificial DNA duplexes and three-way junctions” *Chem. Sci.* **2016**, *7*, 3006–3010.

[196] Y. Takezawa, W. Maeda, K. Tanaka, M. Shionoya, “Discrete Self-Assembly of Iron(III) Ions inside Triple-Stranded Artificial DNA” *Angewandte Chemie Int Ed* **2009**, *48*, 1081–1084.

[197] M. A. Abdelhamid, L. Fábián, C. J. MacDonald, M. R. Cheesman, A. J. Gates, Z. A. Waller, “Redox-dependent control of i-Motif DNA structure using copper cations” *Nucleic Acids Res.*. **2018**, *46*, gky390.

[198] N. M. Smith, S. Amrane, F. Rosu, V. Gabelica, J.-L. Mergny, “Mercury–thymine interaction with a chair type G-quadruplex architecture” *Chem. Commun.* **2012**, *48*, 11464–11466.

[199] D. M. Engelhard, R. Pievo, G. H. Clever, “Reversible Stabilization of Transition-Metal-Binding DNA G-Quadruplexes” *Angew. Chem. Int. Ed.* **2013**, *52*, 12843–12847.

[200] D. M. Engelhard, J. Nowack, G. H. Clever, "Copper-Induced Topology Switching and Thrombin Inhibition with Telomeric DNA G-Quadruplexes" *Angew. Chem. Int. Ed.* **2017**, *56*, 11640–11644.

[201] D. M. Engelhard, A. Meyer, A. Berndhäuser, O. Schiemann, G. H. Clever, "Di-copper(II) DNA G-quadruplexes as EPR distance rulers" *Chem. Commun.* **2018**, *54*, 7455–7458.

[202] L. M. Stratmann, Y. Kutin, M. Kasanmascheff, G. H. Clever, "Precise Distance Measurements in DNA G-Quadruplex Dimers and Sandwich Complexes by Pulsed Dipolar EPR Spectroscopy" *Angew. Chem. Int. Ed.* **2021**, *60*, 4939–4947.

[203] P. M. Punt, G. H. Clever, "Imidazole-modified G-quadruplex DNA as metal-triggered peroxidase" *Chem. Sci.* **2019**, *10*, 2513–2518.

[204] P. M. Punt, M. D. Langenberg, O. Altan, G. H. Clever, "Modular Design of G-Quadruplex MetalloDNAzymes for Catalytic C–C Bond Formations with Switchable Enantioselectivity" *J. Am. Chem. Soc.* **2021**, *143*, 3555–3561.

[205] A. E. Schneider, Metal-Based Modification of G Quadruplexes: An Approach for Targeted Protein Interactions, TU Dortmund, **2023**.

[206] P. M. Punt, L. M. Stratmann, S. Sevim, L. Knauer, C. Strohmann, G. H. Clever, "Heteroleptic Coordination Environments in Metal-Mediated DNA G-Quadruplexes" *Front. Chem.* **2020**, *8*, 26.

[207] P. M. Punt, G. H. Clever, "Tailored Transition-Metal Coordination Environments in Imidazole-Modified DNA G-Quadruplexes" *Chem. Eur. J.* **2019**, *25*, 13987–13993.

[208] D. M. Engelhard, L. M. Stratmann, G. H. Clever, "Structure-Property Relationships in Cu^{II} -Binding Tetramolecular G-Quadruplex DNA" *Chem. Eur. J.* **2018**, *24*, 2117–2125.

[209] C. Kaes, A. Katz, M. W. Hosseini, "Bipyridine: The Most Widely Used Ligand. A Review of Molecules Comprising at Least Two 2,2'-Bipyridine Units" *Chem. Rev.* **2000**, *100*, 3553–3590.

[210] V. Balzani, G. Bergamini, F. Marchioni, P. Ceroni, "Ru(II)-bipyridine complexes in supramolecular systems, devices and machines" *Coord. Chem. Rev.* **2006**, *250*, 1254–1266.

[211] Y. Xu, M. Komiyama, "G-Quadruplexes in Human Telomere: Structures, Properties, and Applications" *Molecules* **2023**, *29*, 174.

[212] H. Weizman, Y. Tor, "2,2'-Bipyridine Ligandoside: A Novel Building Block for Modifying DNA with Intra-Duplex Metal Complexes" *J. Am. Chem. Soc.* **2001**, *123*, 3375–3376.

[213] C. W. Greider, E. H. Blackburn, "A telomeric sequence in the RNA of Tetrahymena telomerase required for telomere repeat synthesis" *Nature* **1989**, *337*, 331–337.

[214] T. Laskowski, M. Kosno, W. Andrałojć, J. Pakuła, R. Stojałowski, J. Borzyszkowska-Bukowska, E. Paluszkiewicz, Z. Mazerska, "The interactions of Pu22 G-quadruplex, derived

from c-MYC promoter sequence, with antitumor acridine derivatives—An NMR/MD combined study" *Mol. Ther. Nucleic Acids* **2025**, *36*, 102513.

[215] S. Mohr, J. Jana, Y. M. Vianney, K. Weisz, "Expanding the Topological Landscape by a G-Column Flip of a Parallel G-Quadruplex" *Chem. A Eur. J.* **2021**, *27*, 10437–10447.

[216] W. D. Cornell, P. Cieplak, C. I. Bayly, I. R. Gould, K. M. Merz, D. M. Ferguson, D. C. Spellmeyer, T. Fox, J. W. Caldwell, P. A. Kollman, "A Second Generation Force Field for the Simulation of Proteins, Nucleic Acids, and Organic Molecules" *J. Am. Chem. Soc.* **1995**, *117*, 5179–5197.

[217] A. Pérez, I. Marchán, D. Svozil, J. Sponer, T. E. Cheatham, C. A. Laughton, M. Orozco, "Refinement of the AMBER Force Field for Nucleic Acids: Improving the Description of α/γ Conformers" *Biophys J* **2007**, *92*, 3817–3829.

[218] C. I. Bayly, P. Cieplak, W. Cornell, P. A. Kollman, "A well-behaved electrostatic potential based method using charge restraints for deriving atomic charges: the RESP model" *J Phys Chem* **1993**, *97*, 10269–10280.

[219] R. Mera-Adasme, K. Sadeghian, D. Sundholm, C. Ochsenfeld, "Effect of Including Torsional Parameters for Histidine–Metal Interactions in Classical Force Fields for Metalloproteins" *J Phys Chem B* **2014**, *118*, 13106–13111.

[220] J. Dai, M. Carver, C. Punchihewa, R. A. Jones, D. Yang, "Structure of the Hybrid-2 type intramolecular human telomeric G-quadruplex in K+ solution: insights into structure polymorphism of the human telomeric sequence" *Nucleic Acids Res.*. **2007**, *35*, 4927–4940.

[221] J. Dai, C. Punchihewa, A. Ambrus, D. Chen, R. A. Jones, D. Yang, "Structure of the intramolecular human telomeric G-quadruplex in potassium solution: a novel adenine triple formation" *Nucleic Acids Res.* **2007**, *35*, 2440–2450.

[222] D. N. Hague, A. R. White, "Kinetics of ternary complex formation between cobalt(II) species and 2,2′-bipyridine: parametrization of bound-ligand effects" *J. Chem. Soc., Dalton Trans.* **1995**, *0*, 449–453.

[223] D. N. Hague, A. R. White, "Kinetics of ternary complex formation between nickel species and 2,2′-bipyridine: parameterization of bound ligand effects" *J. Chem. Soc., Dalton Trans.* **1993**, *0*, 1337–1341.

[224] L. H. Kolopajlo, N. K. Hollis, I. Pendelton, "Kinetics of the Reaction between Ni(tetren)2+and Bipyridine" *J. Stud. Res.* **2012**, *1*, 39–45.

[225] J. T. Grün, A. Blümler, I. Burkhart, J. Wirmer-Bartoschek, A. Heckel, H. Schwalbe, "Unraveling the Kinetics of Spare-Tire DNA G-Quadruplex Folding" *J. Am. Chem. Soc.* **2021**, *143*, 6185–6193.

[226] S. Yamaguchi, N. Oyama, K. Ikeda, H. Matsuda, "The Complex Formation of the Copper(II) Ion with Ethylenediaminetetraacetic Acid and N-(2-Hydroxyethyl)ethylenediamine-N,N′,N′-triacetic Acid" *Bull. Chem. Soc. Jpn.* **2006**, *54*, 3753–3758.

[227] L. Aslanyan, J. Ko, B. G. Kim, I. Vardanyan, Y. B. Dalyan, T. V. Chalikian, "Effect of Urea on G-Quadruplex Stability" *J Phys Chem B* **2017**, *121*, 6511–6519.

[228] G. Auböck, M. Chergui, "Sub-50-fs photoinduced spin crossover in [Fe(bpy)3]2+" *Nat. Chem.* **2015**, *7*, 629–633.

[229] Z. R. Grabowski, K. Rotkiewicz, W. Rettig, "Structural Changes Accompanying Intramolecular Electron Transfer: Focus on Twisted Intramolecular Charge-Transfer States and Structures" *Chem. Rev.* **2003**, *103*, 3899–4032.

[230] J. R. Lakowciz, *Principles of Fluorescence Spectroscopy*, Springer New York, NY, **2006**.

[231] Prof. Dr. C. Reichardt, Prof. Dr. T. Welton, "Solvents and Solvent Effects in Organic Chemistry" **2022**, DOI 10.1002/9783527632220.

[232] K. S. Kjær, W. Zhang, R. Alonso-Mori, U. Bergmann, M. Chollet, R. G. Hadt, R. W. Hartsock, T. Harlang, T. Kroll, K. Kubiček, H. T. Lemke, H. W. Liang, Y. Liu, M. M. Nielsen, J. S. Robinson, E. I. Solomon, D. Sokaras, T. B. van Driel, T.-C. Weng, D. Zhu, P. Persson, K. Wärnmark, V. Sundström, K. J. Gaffney, "Ligand manipulation of charge transfer excited state relaxation and spin crossover in [Fe(2,2′-bipyridine)2(CN)2]" *Struct. Dyn.* **2017**, *4*, 044030.

[233] J. T. Malme, R. A. Clendening, R. Ash, T. Curry, T. Ren, J. Vura-Weis, "Nanosecond Metal-to-Ligand Charge-Transfer State in an Fe(II) Chromophore: Lifetime Enhancement via Nested Potentials" *J. Am. Chem. Soc.* **2023**, *145*, 6029–6034.

[234] A. Cléry, M. Blatter, F. H.-T. Allain, "RNA recognition motifs: boring? Not quite" *Curr. Opin. Struct. Biol.* **2008**, *18*, 290–298.

[235] C. Maris, C. Dominguez, F. H. -T. Allain, "The RNA recognition motif, a plastic RNA-binding platform to regulate post-transcriptional gene expression" *FEBS J.* **2005**, *272*, 2118–2131.

[236] J. Ding, M. K. Hayashi, Y. Zhang, L. Manche, A. R. Krainer, R.-M. Xu, "Crystal structure of the two-RRM domain of hnRNP A1 (UP1) complexed with single-stranded telomeric DNA" *Genes Dev.* **1999**, *13*, 1102–1115.

[237] L. Campbell, K. Lowran, E. Cismas, C. G. Wu, "8-Oxoguanine Disrupts G-Quadruplex DNA Stability and Modulates FANCJ AKKQ Peptide Binding" *Molecules* **2025**, *30*, 3424.

[238] A. K. Byrd, M. R. Bell, K. D. Raney, "Pif1 helicase unfolding of G-quadruplex DNA is highly dependent on sequence and reaction conditions" *J. Biol. Chem.* **2018**, *293*, 17792–17802.

[239] D. L. Yin, L. Pu, G. Pei, "Antisense oligonucleotide to insulin-like growth factor II induces apoptosis in human ovarian cancer AO cell line" *Cell Res.* **1998**, *8*, 159–165.

7. Appendix

Supporting Information

Experimental Section

Solvents were purified from higher boiling impurities on the rotational evaporator (RE). The solvent toluene was commercially purchased in 99.8% purity from Fischer Scientific Company L.L.C. and degassed using the freeze-pump-thaw method. The solvent dioxane was purchased in 99% purity from Fischer Scientific Company L.L.C. and degassed using the freeze-pump-thaw method. The solvents ethanol (EtOH), methanol (MeOH), dicholormethane (DCM) and ethylacetate (EtOAc) were used as technical and high performance liquid chromatography (HPLC) grade solvents.

Reactions involving substrates or reagents sensitive towards ambient air and/or hydrolysis were carried out in under vacuum heated glassware using the Schlenk technique under argon. Syringes and cannulas were washed with inert gas before usage.

Yields were determined via gravimetrical analysis using an analytical scale (variance: d = 0.1 mg). The yield was given as a weight percentage, relative to the amount of used substrate.

Reagents and substrates were either readily available from the groups chemical reservoir or were commercially purchased and used without further purification steps.

^{1}H-NMR-Spectra were obtained using Bruker *AV 400*, Bruker *AV 500*/ Agilent *DD2* und Bruker *AV 600* spectrometers manufactured by Bruker Physics and were carried out in deuterated chloroform ($CDCl_3$), deuterated acetonitrile (CD_3CN), deuterated dimethyl sulfoxide (DMSO-d_6), deuterated tetrahydrofuran (THF-d_8), deuterated methanol (MeOD), deuterated acetone (Aceton-d_6) and deuterated dimethylformamide (DMF-d_7). The chemical shifts δ were determined relative to a standard (trimethylsilane, δ = 0 ppm) in ppm.[x] All ^{1}H-NMR-spectra were calibrated on the residual proton signal of the respective deuterated solvents ($CDCl_3$: δ = 7.26 ppm, CD_3CN: δ = 1.93 ppm, DMSO-d_6 = 2.49 ppm). The coupling patterns were denoted with the following terms: s (singulet), d (doublet), t (triplet), m (multiplet).

^{13}C-NMR-Spectra were obtained using Bruker *AV 400*, Bruker *AV 500*/ Agilent *DD2* und Bruker *AV 600* spectrometers manufactured by Bruker Physics and were carried out in deuterated chloroform ($CDCl_3$), deuterated acetonitrile (CD_3CN) and deuterated dimethyl sulfoxide (DMSO-d_6). The chemical shifts δ were determined relative to a standard (trimethylsilane, δ = 77.0 ppm) in ppm.[x] All ^{1}H-NMR-spectra were calibrated on the residual proton signal of the respective deuterated solvents ($CDCl_3$: δ = 77.16 ppm, CD_3CN: δ = 1.3, 117.7 ppm, DMSO-d_6 = 39.7 ppm).

Oligonucleotide synthesis and purification

Table 1: Reagents for DNA synthesis

Name	Reagent	Composition
DCA	Detritylation	3% (v/v) dichloroacetic acid in anhydrous dichloromethane
ACT	Activator	0.3 M 5-(benzylthio)-1H-tetrazole in anhydrous acetonitrile
Cap A	Capping A	10% (v/v) N-methyl imidazole in anhydrous tetrahydrofurane
Cap B	Capping B	2,6-lutidine / acetic anhydride / anhydrous tetrahydrofurane 1:1:8 (v/v/v)
OXI	oxidizer	0.02 M iodine in tetrahydrofurane / pyridine / water 7:2:1 (v/v/v)
ACN	solvent	anhydrous acetonitrile

All oligonucleotides were synthesized on a K&A Laborgeraete GbR H-8 synthesizer on a 1 µmol scale using the standard phosphoramidite methods on controller pore glass (CPG) and following previously published procedures for synthesis. Standard phosphoramidites (DMT-dT-CEP, DMT-dG(iBu)-CEP, DMT-dA(bz)-CEP, DMT-dC(Ac)-CEP) were used and the cartridges with CPG solid supports (1000 Å, 25-35 µmol/g, DMT-dT-CPG and DMT-dG(iBu)-CPG) were manually packed. The oligonucleotide synthesis followed the built-in methods of the DNA synthesizer and was slightly modified. First, the cartridges were treated three times with DCA to deprotect the 5'-OH groups. Second, coupling was achieved by mixing the respective phosphoramidite building block (0.1 M in ACN) with ACT (1:1, v/v). The coupling time was ~0.5 min for standard phosphoramidites and ~3.5 min for the ligand-modified phosphoramidite. Third, the cartridge was treated with a 1:1 (v/v) mixture of Cap A and Cap B to acetylate unreacted 5'-OH groups, which was followed, by the oxidation with OXI. Here, an additional washing step with CAN was introduced compared to the standard routine. After each individual step of the cycle, the cartridge was washed with ACN followed by a drying step with argon. The described cycle was repeated for every incorporated nucleotide. After DNA synthesis, the solid supports were removed from the cartridges and treated with concentrated aqueous NH_3 solution at 55 °C overnight for cleavage and deprotection. The

supernatant solution was filtered (VWR Centrifugal filters) and the solid support was washed with 100 µL water. NH_3 was removed from the filtrate under reduced pressure using a H. Saur Laborbedarf S-Concentrator BA-VC-300H vacuum concentrator and the volume of the solution was reduced to ~300 µL. Purification of the oligonucleotides was performed with reversed-phase HPLC on an Agilent Technologies 1260 Infinity II HPLC system equipped with an autosampler, column oven, DAD detector and a Macherey-Nagel VP 250/10 Nucleodur 100-5 C18ec column (oven temperature: 60 °C, flow rate: 2.5 mL/min, solvent A: 50 mM TEAA pH 7, solvent B: 70:30 MeCN/50 mM TEAA pH 7, gradient: from 100% solvent A to 20% solvent A and 80% solvent B in 30 min). To remove ACN from the sample, the volume of the solution was again reduced to ~300 µL in the vacuum concentrator and then the sample was diluted with100 mM TEAA pH 7 to a volume of 2 mL. Subsequently, the cleavage of the 5′-OH DMT protecting groups (with 2% TFA) and desalting were accomplished using Waters Sep-Pak C18 cartridges. Desalted oligonucleotides were lyophilized using a Christ Alpha 2-4 LSC basic lyophilisation device and stored either as a solid or as 0.5–2.5 mM stock solutions in water (MQ water, pH 7.2) at 4 °C. The concentrations of all oligonucleotide stock solutions were determined via the absorbance at 260 nm at 25 °C with a Thermo Scientific Nanodrop One instrument and using revised extinction coefficients for the nucleosides.

UV-Vis experiments details

Both UV-VIS spectra and thermal denaturation profiles (melting curves) were recorded on a Jasco V-750 UV-Visible Spectrophotometer equipped with a PAC-743 6-cell thermostat for temperature control. The temperature was measured in the measurement cell in a water-filled cuvette. Quartz glass cuvettes (Hellma Analytics 114-QS, 1 cm path length) were used. In order to avoid condensation of water on the cuvette surface or cell window at low temperatures, a constant flow of air was pumped through the measurement cell. Evaporation of water at high temperatures and resulting changes in the absorption behaviour were minimized by a thin layer of silicon oil placed onto the sample and by tightly stoppering the cuvette. UV-VIS spectra were recorded from 350 to 220 nm with a scan rate of 200 nm/min both before (4 °C) and after thermal denaturation (95 °C). The data interval was set to 1 nm, bandwidth to 2.0 nm and the response time to 0.96 sec. All UV-VIS spectra were background corrected (cuvette, buffer and electrolyte) and zeroed using the absorption at 350 nm. To obtain the thermal difference spectra (TDS), the spectrum before denaturation (at 4 °C) was subtracted from the one after denaturation (at 95 °C). A negative band (hypochromic shift) at 295±2 nm and positive bands at 243±2 nm and 273±2 nm (hyperchromic shift) indicated G-quadruplex formation. For the thermal denaturation profiles (melting curves), absorption of the samples at 295 nm was recorded in a 0.5 °C interval with a temperature gradient set to

0.5 °C/min, which corresponds to ~0.174 °C/min including the measurement time. Data points were recorded from 4 °C to 90 °C. Melting curves were background corrected using the absorption at 350 nm and normalised from 0.0 to 1.0 absorption and a first order derivative calculated to determine the minimum which corresponded to the melting point (T_m).

Determination of binding constants of the individual metals (M^{2+} = Cu, Ni, Zn) with the respective G-quadruplexes was performed via titration experiments followed by UV-Vis spectroscopy. G-quadruplex samples were prepared identical to standard UV-Vis thermal denaturation studies. A concentrated solution of the metal salts was prepared (1 mM) and added in 0.1 eq steps until a total of 2.5 eq was reached. After each addition the sample was mixed thoroughly and incubated at r.t. for 15min to secure full complexation and subsequently a UV-Vis spectrum recorded. The absorbance of the metal-complex at 315 nm was then plotted against the increasing equivalents of metal cations to ensure that a saturation point had been reached. The binding constant was then calculated using the Benesi-Hildebrandt method by plotting the $1/\Delta A$ against $1/c(M^{2+})$ with $c(M^{2+})$ being the concentration of the metal cations in solution for each step. A linear fit through the data was performed and the slope determined from which the binding (association) constant could be extracted.

CD Spectroscopy further details

For the kinetic measurements by CD spectroscopy, the samples were prepared in the same way as for the UV-VIS-based thermal denaturation studies. The CD signal at 260 nm was chosen as this was indicative of the formation of an antiparallel G-quadruplex topology formed from the hybrid topology. The sample was kept at the desired temperature by the temperature control with an in-sample thermometer. At t = 0 s, 4.4 µL of 1 mM metal salt solution was added to the DNA sample and quickly mixed by pipetting. The measurement intervals were 15 s over a period of up to 20000 s. The recorded CD intensities were then plotted over time and fitted with an exponential decay curve which was used to calculate the concentration of the G-quadruplex without any metal (educt). To assess the order of this reaction we plotted the concentration of the G-quadruplex without any metal bound on a logarithmic scale over the recorded time. This was repeated for each metal cation (Cu^{2+}, Ni^{2+}, Zn^{2+}) and over four temperatures (284 K, 289 K, 298 K, 306 K). Out of the corresponding kinetic rate constants an Eyring plot was created to extract the enthalpy ($\Delta H^{\ddagger}$) and entropy ($\Delta S^{\ddagger}$) of activation as well as the activation energy at each temperature (E_a or $\Delta G^{\ddagger}$).

Molecular Dynamics simulations details

Force field parameters and RESP charges for the artificial nucleotide **BiPy-L** and its Cu^{2+} complex were generated in the identical manner as previously described.[53] The uncoordinated ligand nucleoside was split into fragments, according to the original AMBER force field implementation (dimethylphosphate)[60] and capped with 5' and 3' OH groups. For the linkage between the pyridine and the glycol backbone $–CH_3$ and $–OCH_3$ were used as caps, respectively. The standard $–CH_3$ and –OH approach resulted in less optimal RESP charge fits. All molecules were geometry optimized at the HF/6-31G(d)level using Gaussian '09. In case of the M^{2+} complex, metal bound to two of 4-(methoxymethyl)bipyridine units was used and was geometry optimized at the DFT B3LYPlevel of theory with the 6-31G(d) basis set. For all bipyridine containing molecules two different conformations were found with similar energies. Partial point charges were then derived by RESP charge fitting using the REDServer-Development.[61–63] Inter-molecular and intra-molecular charge constraints were used to maintain the correct total charge of the ligand. For the metal complex, the $–CH_3$ cap of the pyridine units was constrained to the same values obtained earlier for the uncoordinated ligand, to avoid problems arising from the different basis sets used. For the metal ion, a van-der-Waals radius of 1.7 Å was used. In all cases, the constrained charges were similar to the unconstrained values.

For the ligand alone, force field parameters missing in the AMBER force field ff99 bsc1 were generated with parmchk2 from the AmberTools, based on analogy to existing force field entries (see Table 4). Parameters for the copper complex were derived using the VFFDT program, which is based on the Seminario method, using a geometry-optimized model (B3LYP/6-311+G(d,p) (CHNO), def2-TZVPD (Cu) level of theory). To obtain a square-planar coordination environment for the Cu^{2+} ion, adjacent ligands were named differently, in order to avoid ambiguity in the parameterization. Improper dihedrals were used to maintain coplanarity between the pyridine plane and the pyridine – metal plane. The respective force constants were estimated based on literature values.

First, initial structures for the G-quadruplex (**htel22-L2a** and **htel22-L2b**) were constructed by using the solid-state or solution-sate structures of the respective parental G-quadruplex and the topologies observed by CD (PDB entries: 143D, 2JPZ, 2HY9).[64–66] All manipulations were carried out in UCSF Chimera.[67] Na^+ ions were replaced by K^+ ions. Redundant ions and redundant nucleotides were deleted, the geometry-optimized ligands or the respective Cu^{2+}-complex was inserted manually. The respective models obtained above were put in a periodic rhombic dodecahedron box (cut off 1.5 nm) and energy minimized 2000 steps of steepest descent (600 kJ/mol nm tolerance) in vacuum. PME and van-der-Waals cut off of 1.3 nm were used. The system was solvated with TIP3P water molecules and the negative charge of the system was neutralized with the corresponding amount of

randomly positioned K^+ ions. An additional 100 mmol/L KCl was added to simulate the ionic strength of the experiments. The system was then energy minimized in two steps, first 500 steps of steepest descent (500 kJ/mol nm tolerance) and then 3000 steps of conjugate gradient minimization (300 kJ/mol nm tolerance). The non-bonded Lennard-Jones cut off was set to 1.3 nm, the non-bonded pair list updated every 50 steps. For the coulombic interactions, Particle-mesh Ewald summation (PME) was used.[68] Next, the system was equilibrated with positional constraints on the model's heavy-atoms 100 ps in a first round (NVT ensemble, constraints 1000 kJ/mol $Å^2$, time step 2 fs; Temperature coupling modified Berendsen, 298 K); second round 100 ps with additional pressure coupling (isotropic, Berendsen, 1 bar, time constant for coupling 0.1 ps, compressibility 4.5 10−5) and a third round 100 ps but with lower constraints(100 kJ/mol $Å^2$, Nose-Hoover temperature coupling, 2 ps coupling, Parinello-Rahman isotropic pressure coupling, 2 ps coupling time). The equilibration phase was finished with 200 ps of an unconstraint DNA MD run (coupling times increased to 4 ps). A 100 ns MD production run was then performed. Coordinates were written every 10 ps, resulting in 10001 frames per trajectory. Trajectories were centered, aligned and fitted to the first frame using the built-in Gromacs tools and then analysed and visualized with UCSF Chimera. The depicted structures are representatives of the MD trajectories. For the RMSD plots, the first frame of the trajectory was used as the reference.

Reaction progress was determined via thin layer chromatography (TLC). Precoated aluminium plates with silicagel *DC-FERTIGFOLIEN* ALUGRAM® *XTRA SIL G/UV*$_{254}$ manufactured by MACHEREY NAGEL were used for this purpose. Investigation of the spots was carried out under UV light.

Purification was carried out via column chromatography. Silica gel KIESELGEL 60 manufactured by MACHEREY NAGEL (particle size: 40-63 µm) was used for this purpose. The column chromatography was performed under additional external pressure. The substance in need of purification was always directly adsorbed onto the silica gel. Additional purification was performed via gel permeation chromatography (GPC) with the LABOACE LC-5610 manufactured by JAPAN ANALYTICAL INDSUTRY Co., Ltd. and run with either dimethylformamide or chloroform, both in HPLC-grade purity, as solvent.

Native Electrospray Ionization Mass Spectrometry (ESI-MS) was conducted in negative ionization mode using Bruker timsTOF and Compact instruments. The TOF analyzer was calibrated with Agilent ESI-Low Concentration Tuning Mix. Oligonucleotide samples (5 µL, DNA concentration 25 µM in 10 mM TEAA, 1mM KCl, if present 27.5 µM MSO_4 (M = Cu, Ni, Zn) pH 7.0, annealed under standard conditions) were manually injected via (diluted 1:1 v/v

acetonitrile/DNA sample). All analyses utilized trifluoroacetate-free buffers to prevent ion suppression. Mass spectra were acquired under standard operating conditions with optimized capillary voltage (−4.5 kV) and nebulizer gas settings.

Cellular toxicity was determined via MTS Assays. MTS assays were conducted with a Assay kit reagents mix consisting of a MTS solution in MilliQ water at 2 mg/mL and a phenazine methosulfate (PMS) solution in MiliQ water at 0.92 mg/mL which were mixed in a 2:0.1 ration (MTS:PMS). This solution was then mixed with DMEM containing 10% FBS in a 1:4 ratio (MTS/PMS mix:medium). HeLa and U2OS cells were grown in high glucose Dulbecco's modified Eagle medium (DMEM) containing 10% fetal bovine serum (FBS) at 37 °C with 5% CO_2 in humidified air at 5000 cells per well in a 96-well plate over 16h after which media was replaced with fresh media and incubated with the respective oligonucleotide compound and again incubated under identical conditions for 16h. Lastly media was removed and replaced with MTS reagent/buffer mixture and incubated for 4h.
Absorbance of the MTS reagent mix was then measured at 490 nm from which absorbance at 630 nm was subtracted as background correction. The experiment was conducted in triplicate. Positive controls were conducted with DMSO to ensure no dehydrogenase activity. Negative controls were conducted with cells in just medium to ensure full dehydrogenase activity. The respective absorbance maximum and minimum absorbance values were then normalised to the negative and positive controls.

DNA transfection was performed with lipofectamine 2000 (Invitrogen) following the manufacturer's instructions: G4 DNA was incubated with lipofectamine at a 3:1 ratio of lipofectamine:DNA in DMEM (Gibco) for 15 min. The lipofectamine/DNA mixture was then incubated with cells for up to 24 hours and imaged every 4h using a Sartorius Incucyte S3 Live-Cell Analysis System from which total green count over all cells within each well was plotted over time to determine the optimal incubation time after which no more signal enhancement was present. All cell imaging experiments are an average of at least three independent biological repeats.

Confocal images of single fluorescently labelled G-quadruplex strands (FAM label) were acquired using a Leica SP5 II confocal microscope after incubation of U2OS/HeLa cells with the DNA samples for 16 hours. Images were taken with a 100× oil immersion objective (correction collar, NA = 1.2, Leica) after excitation using an internal Ar+ laser at 495 nm and detection at 500-700 nm.

For FRET based experimets, confocal images of U2OS and HeLa cells in 8 well chamber slides were acquired using a Leica Stellaris 8 inverted microscope equipped with a diode laser (405 nm) and a white light laser (440-790 nm). Images were collected using a 63x oil immersion objective (correction collar, NA = 1.4, Leica) at a resolution of 512 x 512 pixels. Samples were excited using the white light laser at 495 nm, and emission detected 505-650 nm, using Airy pinhole 1.

Protein Expression and Purification

Pif1

Pif1 stock solutions were kindly provided from the lab of Kathrin Paeschke and University of Bonn. Special thanks are extended to Dr. Lisa Weixler.

Recombinant Yeast RPA purified from Escherichia coli was a generous gift from P. Sung. The nuclear form of yeast Pif1p fused at its N-terminus to a 6-histidine tag was purified essentially as described. Briefly, the DNA coding for the nuclear form of hPif1 (amino acids 206–620) was cloned into vector pET28 (Novagen) and transformed into E. coli Rosetta strain, which is a derivative of the BL21(DE3) strain (Novagen). Protein expression was induced at 23°C by addition of 1 mM IPTG to a mid-log phase culture in rich media, and the culture was further grown for 16 h. hPif1 was purified by affinity chromatography to the 6-histidine tag, followed by cation exchange chromatography on a resource 15S column (GE Healthcare). Fractions containing pure hPif1 as assessed by Coomassie staining were pooled, concentrated and stored at –80°C in 25 mM HEPES pH 7.0, 100 mM NaCl, 25 mM, 25 mM Mg(OAc), 1 mM DTT, 50% glycerol.

His-thrombin-hPif1 amino acid sequence:
HHHHHHSSGL VPRGSHMQLS EEQAAVLRAV LKGQSIFFTG SAGTGKSYLL KRILGSLPPT GTVATASTGV AACHIGGTTL HAFAGIGSGQ APLAQCVALA QRPGVRQGWL NCQRLVIDEI SMVEADLFDK LEAVARAVRQ QNKPFGGIQL IICGDFLQLP PVTKGSQPPR FCFQSKSWKR CVPVTLELTK VWRQADQTFI SLLQAVRLGR CSDEVTRQLQ ATASHKVGRD GIVATRLCTH QDDVALTNER RLQELPGKVH RFEAMDSNPE LASTLDAQCP VSQLLQLKLG AQVMLVKNLS VSRGLVNGAR GVVVGFEAEG RGLPQVRFLC GVTEVIHADR WTVQATGGQL LSRQQLPLQL AWAMSIHKSQ GMTLDCVEIS LGRVFASGQA YVALSRARSL QGLRVLDFDP MAVRCDPRVL HFYATLRRGR SL.

DHX36

DHX36 stock solutions were kindly provided from the lab of Kathrin Paeschke and University of Bonn. Special thanks are extended to Dr. Lisa Weixler.

Recombinant proteins were produced by transformation of Escherichia coli strain Rosetta 2 (Novagen) with either TriEx-4 DHX36 or TriEx-4 vector alone. Recombinant proteins were initially purified by means of a His6 tag by utilizing the TALON purification kit (Clontech). Rosetta 2 cell lysates were isolated and bound to TALON cobalt resin as recommended by the manufacturer. TALON resin (1 ml bed volume) was eluted twice with 1 ml of histidine elution buffer (0.7 m histidine, pH 6.0, 8.6 mm βME, Sigma protease inhibitor mixture), followed by 1 ml of 250 mm EDTA, pH 6.0.

Fractions corresponding to monomeric DHX36 were pooled and further purified by size-exclusion chromatography on a Superdex 200 Increase 10/300 GL column equilibrated with SEC buffer (20 mM HEPES, pH 7.5; 150 mM KCl; 1 mM $MgCl_2$; 2 mM DTT). Peak fractions were collected, concentrated using a centrifugal concentrator (Amicon, 50 kDa cutoff), flash-frozen in liquid nitrogen, and stored at –80°C.

DHX36-His amino acid sequence:

MSYDYHQNWG RDGGPRSSGG GYGGGPAGGH GGNRGSGGGG GGGGGGRGGR GRHPGHLKGR EIGMWYAKKQ GQKNKEAERQ ERAVVHMDER REEQIVQLLN SVQAKNDKES EAQISWFAPE DHGYGTEVST KNTPCSENKL DIQEKKLINQ EKKMFRIRNR SYIDRDSEYL LQENEPDGTL DQKLLEDLQK KKNDLRYIEM QHFREKLPSY GMQKELVNLI DNHQVTVISG ETGCGKTTQV TQFILDNYIE RGKGSACRIV CTQPRRISAI SVAERVAAER AESCGSGNST GYQIRLQSRL PRKQGSILYC TTGIILQWLQ SDPYLSSVSH IVLDEIHERN LQSDVLMTVV KDLLNFRSDL KVILMSATLN AEKFSEYFGN CPMIHIPGFT FPVVEYLLED VIEKIRYVPE QKEHRSQFKR GFMQGHVNRQ EKEEKEAIYK ERWPDYVREL RRRYSASTVD VIEMMEDDKV DLNLIVALIR YIVLEEEDGA ILVFLPGWDN ISTLHDLLMS QVMFKSDKFL IIPLHSLMPT VNQTQVFKRT PPGVRKIVIA TNIAETSITI DDVVYVIDGG KIKETHFDTQ NNISTMSAEW VSKANAKQRK GRAGRVQPGH CYHLYNGLRA SLLDDYQLPE ILRTPLEELC LQIKILRLGG IAYFLSRLMD PPSNEAVLLS IRHLMELNAL DKQEELTPLG VHLARLPVEP HIGKMILFGA LFCCLDPVLT IAASLSFKDP FVIPLGKEKI ADARRKELAK DTRSDHLTVV NAFEGWEEAR RRGFRYEKDY CWEYFLSSNT LQMLHNMKGQ FAEHLLGAGF VSSRNPKDPE SNINSDNEKI IKAVICAGLY PKVAKIRLNL GKKRKMVKVY TKTDGLVAVH PKSVNVEQTD FHYNWLIYHL KMRTSSIYLY DCTEVSPYCL LFFGGDISIQ KDNDQETIAV DEWIVFQSPA RIAHLVKELR KELDILLQEK IESPHPVDWN DTKSRDCAVL SAIIDLIKTQ EKATPRNFPP RFQDGYYSLL EHHHHHH.

UP1/UP1RGG

UP1 stock solutions were kindly provided from the lab of Dr. Sebastian Jung at Ruhr University Bochum.

The N-terminal fragment of human hnRNP A1, corresponding to residues 1 – 196 (UP1) or corresponding to residues 1 – 249 (UP1RGG), encompassing the two RNA-recognition motifs (RRMs) and RGG motif, was cloned into a pET-derived expression vector containing an N-terminal His_6 tag followed by a TEV protease cleavage site. The construct was verified by Sanger sequencing and transformed into Escherichia coli BL21(DE3) cells for protein expression.

A single transformed colony was used to inoculate 50 mL LB medium containing 50 µg/mL kanamycin and grown overnight at 37°C with shaking (200 rpm). The overnight culture was diluted 1:100 into 1 L LB medium and grown at 37°C to an OD_{600} of 0.6–0.8. Recombinant UP1 expression was induced with 0.5 mM IPTG, followed by incubation for 16 h at 18°C. Cells were harvested by centrifugation at 4,000 × g for 20 min at 4°C, flash-frozen in liquid nitrogen, and stored at –80°C until purification.

Cell pellets were resuspended in lysis buffer containing 50 mM Tris-HCl, pH 7.5; 300 mM NaCl; 10% glycerol; 2 mM β-mercaptoethanol; 20 mM imidazole; and protease inhibitor cocktail. Cells were lysed by sonication on ice, and the lysate was clarified by centrifugation at 40,000 × g for 45 min at 4°C. The soluble fraction was applied to Ni-NTA HisTrap resin (Cytiva, 5 mL bed volume) pre-equilibrated with lysis buffer. After washing with 20 column volumes of wash buffer (50 mM Tris-HCl, pH 7.5; 300 mM NaCl; 20 mM imidazole), UP1/UP1RGG was eluted with 250 mM imidazole in lysis buffer. The His_6 tag was removed by overnight digestion with TEV protease at 4°C while dialyzing into low-salt buffer (25 mM Tris-HCl, pH 7.5; 150 mM NaCl; 2 mM DTT). Cleaved UP1/UP1RGG was further purified by size-exclusion chromatography on a Superdex 75 Increase 10/300 GL column equilibrated with SEC buffer (20 mM HEPES, pH 7.5; 150 mM NaCl; 1 mM DTT). Peak fractions corresponding to monomeric UP1 were collected, concentrated using an Amicon centrifugal concentrator (10 kDa cutoff), flash-frozen in liquid nitrogen, and stored at –80°C.

UP1 amino acid sequence:

MSKSESPKEP EQLRKLFIGG LSFETTDESL RSHFEQWGTL TDCVVMRDPN TKRSRGFGFV TYATVEEVDA AMNARPHKVD GRVVEPKRAV SREDSQRPGA HLTVKKIFVG GIKEDTEEHH LRDYFEQYGK IEVIEIMTDR GSGKKRGFAF VTFDDHDSVD KIVIQKYHTV NGHNCEVRK ALSKQEMASA SSSQRGR.

UP1RGG amino acid sequence:

MSKSESPKEP EQLRKLFIGG LSFETTDESL RSHFEQWGTL TDCVVMRDPN TKRSRGFGFV TYATVEEVDA AMNARPHKVD GRVVEPKRAV SREDSQRPGA HLTVKKIFVG GIKEDTEEHH LRDYFEQYGK IEVIEIMTDR GSGKKRGFAF VTFDDHDSVD KIVIQKYHTV NGHNCEVRK ALSKQEMASA SSSQRGRSGS GNFGGGRGGG FGGNDNFGRG GNFSGRGGFG GSRGGGGYGG SGDGYNGFGN

DNA G-quadruplex Protein Binding Assays

Fluorescence Polarisation (FP) Assays

Fluorescence polarization (FP) assays were performed to determine equilibrium dissociation constants (Kd) of proteins binding to DNA G-quadruplexes. In this assay, the smaller binding partner, in our case the DNA oligonucleotide, was fluorescently labelled (fluorescein (FAM), allowing free rotation and translation in solution and resulting in low fluorescence anisotropy. Upon addition of the larger binding partner (protein), complex formation increases the effective molecular weight of the bound species, slowing rotational diffusion and resulting in an increase in anisotropy.

FP measurements were performed in 384-well black, flat-bottom plates (Corning) using a Tecan Spark plate reader with excitation/emission wavelengths appropriate for the fluorophore. DNA G-quadruplexes were used at a fixed concentration of 1 nM per well, significantly lower than the expected Kd to ensure accurate titration curves. Protein titrations were performed over 15 concentrations ranging from 0.03 μM to 1 μM, covering the expected binding range. Each condition was prepared in triplicate to provide statistical significance. Incubation of DNA-protein mixture was performed at 37°C for 1h before measuring. Anisotropy values were plotted as a function of protein concentration and fitted to a single-site binding model using non-linear regression (sigmoidal function) in OriginLab to extract Kd values as second derivates of the corresponding fitted function. Care was taken to ensure that measurements remained within the linear dynamic range of the fluorophore and that fluorescence intensity did not significantly change during the titration, minimizing potential artifacts from inner filter effects or aggregation.

Ligand Synthesis

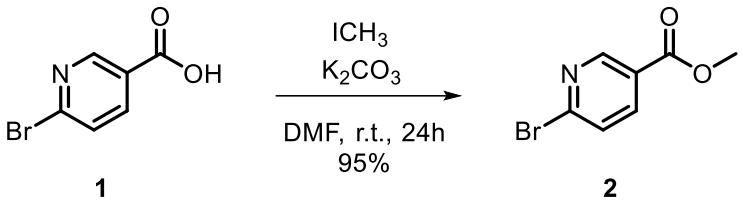

6-bromo-nicotinic acid (**1**) (1 g, 4.95 mmol, 1 eq.) or was dissolved in DMF (30 mL), methyl iodide (703.65 mg, 4.96 mmol,1.1 eq. for 3, 2.32 g, 16.34 mmol, 1.1 eq. for 4) and K_2CO_3 (1.03 g, 7.43 mmol, 1.5 eq.) were added, followed by stirring the solution overnight at room temperature (r.t.). The solution was diluted with water (100 mL), and the product was extracted with EtOAc (3 × 50 mL). The combined organic phases were washed with water (2 × 50 mL) and brine (2 × 50 mL), and the mixture was dried over $MgSO_4$. The solvent was evaporated under reduced pressure, and the substance was purified by column chromatography (SiO_2, pentane → pentane/EtOAc 10:1). Methyl-6-bromoisonicotinate (3) (1016.3 mg, 4.7 mmol, 95%) was obtained as a yellow oil.

^{1}H NMR (600 MHz, $CDCl_3$) δ (ppm) = 8.95 (dd, J = 2.4, 0.7 Hz, 1H, a), 8.12 (dd, J =8.3, 2.4 Hz, 1H, b), 7.58 (dd, J = 8.3, 0.8 Hz, 1H, c), 3.95 (s, 3H, d).

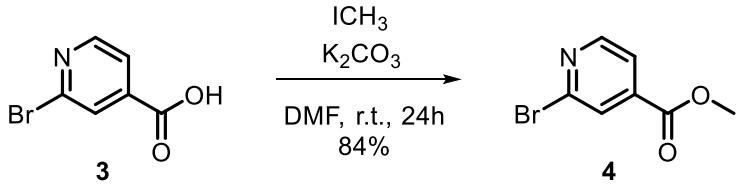

2-bromo-nicotinic acid (**2**) (1 g, 4.95 mmol, 1 eq.) was dissolved in DMF (30 mL), methyl iodide (2.32 g, 16.34 mmol, 1.1 eq.) and K_2CO_3 (1.03 g, 7.43 mmol, 1.5 eq.) were added, followed by stirring the solution overnight at room temperature (r.t.). The solution was diluted with water (100 mL), and the product was extracted with EtOAc (3 × 50 mL). The combined organic phases were washed with water (2 × 50 mL) and brine (2 × 50 mL), and the mixture was dried over $MgSO_4$. The solvent was evaporated under reduced pressure, and the substance was purified by column chromatography (SiO_2, pentane → pentane/EtOAc 10:1). Methyl 2-bromoisonicotinate (4) (2.7 g, 12.50 mmol, 84%) was obtained as white crystals.

^{1}H NMR (600 MHz, $CDCl_3$) δ (ppm) = 8.52 (d, J = 5.0 Hz, 1H, a), 8.04 (s, 1H, b), 7.80(dd, J = 5.0, 1.4 Hz, 1H, c), 3.96 (s, 3H, d).

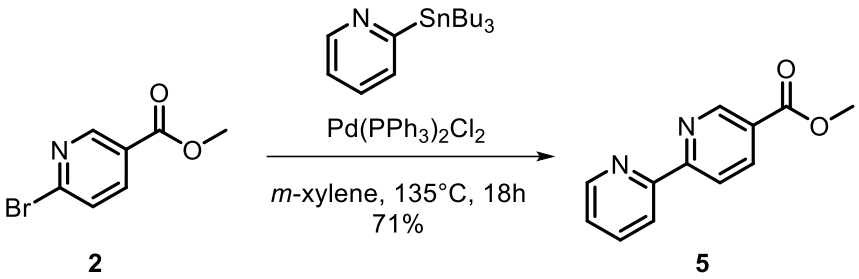

2 **5**

The reaction was carried out in degassed xylene (20 mL), which was subjected to the freeze-pump-thaw (FPT) method. Methyl 6-bromoisonicotinate (**2**) (3.0 g, 13.89 mmol, 1 eq.) was dissolved in the solvent. Subsequently, 2-(tributylstannyl)pyridine (5.11 g, 13.89 mmol, 1.1 eq.) and bis(triphenylphosphine)dichloropalladium(II) (487.36 mg, 694.34 µmol, 0.05 eq.) were added to the solution. The mixture was heated at 135°C for 18 hours. The resulting suspension was extracted with EtOAc, washed three times with aqueous potassium fluoride solution (1 M), and once with brine. The precipitated Bu_3SnF was removed by filtration through a KF/Celite mixture. The combined organic phases were dried over $MgSO_4$ and purified by column chromatography (SiO_2, pentane → pentane/EtOAc 10:1 → pentane/EtOAc 5:1). 5-(Methoxycarbonyl)-2,2'-bipyridine (**5**) (2.1 g, 9.72 mmol, 71%) was obtained as orange-brown oil.

^{1}H NMR (500 MHz, $CDCl_3$) δ (ppm) = 9.29 (s, 1H, a), 8.75 (d, J = 2.9 Hz, 1H, b), 8.59(d, J = 8.2 Hz, 1H, c), 8.53 (d, J = 8.1 Hz, 1H, d), 8.44 (dd, J = 8.4, 2.1 Hz, 1H, e), 7.93(td, J = 7.7, 1.8 Hz, 1H, f), 7.43 (dd, J = 7.9, 4.6 Hz, 1H, g), 3.98 (s, 3H, h).

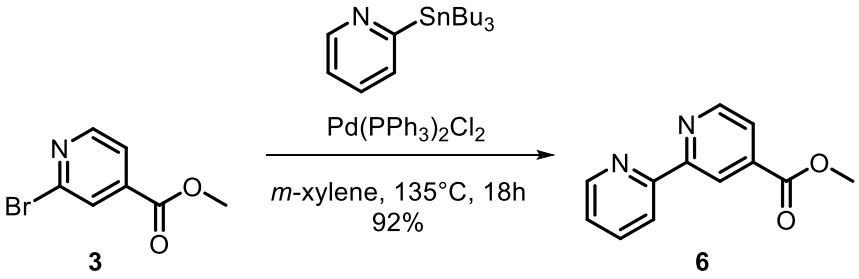

3 **6**

The reaction was carried out in degassed xylene (20 mL), which was subjected to the freeze-pump-thaw (FPT) method. Methyl 2-bromoisonicotinate (**4**) (2.7 g, 12.50 mmol, 1 eq.) was dissolved in the solvent. Subsequently, 2-(tributylstannyl)pyridine (4.60 g, 12.50 mmol, 1.1 eq.) and bis(triphenylphosphine)dichloropalladium(II) (487.36 mg, 694.34 µmol, 0.05 eq.)

were added to the solution. The mixture was heated at 135°C for 18 hours. The resulting suspension was extracted with EtOAc, washed three times with aqueous potassium fluoride solution (1 M), and once with brine. The precipitated Bu_3SnF was removed by filtration through a KF/Celite mixture. The combined organic phases were dried over $MgSO_4$ and purified by column chromatography (SiO_2, pentane → pentane/EtOAc 10:1 → pentane/EtOAc 5:1). 4-(methoxycarbonyl)-2,2'-bipyridine (**6**) (2.5 g, 11.50 mmol, 92%) was obtained as orange-brown oil.

^{1}H NMR (500 MHz, $CDCl_3$) δ (ppm) = 9.08 (s, 1H, a), 8.92 – 8.81 (m, 2H, b/c), 8.54(d, J = 8.1 Hz, 1H, d), 8.02 (t, J = 7.8 Hz, 1H, e), 7.95 (d, J = 3.5 Hz, 1H, f), 7.56 – 7.47(m, 1H, g), 4.01 (s, 3H, h).

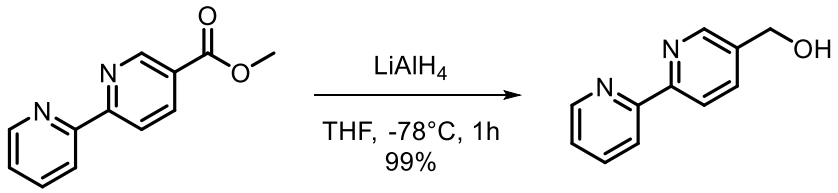

5 **7**

A solution of 5-(methoxycarbonyl)-2,2'-bipyridine (**5**) (420 mg, 1.96 mmol, 1 eq.) in anhydrous THF (50 mL) was cooled to –78 °C. A 1 M solution of lithium aluminum hydride in THF (2.16 mL, 2.16 mmol for 7; 12.32 mL, 12.32 mmol for 8) was added dropwise. The reaction mixture was warmed to –20 °C and stirred for 0.5 h until a homogeneous solution was formed. Subsequently, the mixture was cooled again to –78 °C and quenched dropwise with 30 mL of 10% aqueous THF. After reaching room temperature, the reaction mixture was stirred with dry Celite for 15 minutes, filtered, and the Celite was washed with approximately 100 mL of THF. The solvent was removed under reduced pressure after drying with $MgSO_4$. [2,2'-Bipyridin]-5-ylmethanol (**7**) (365.08 mg, 1.96 mmol, 100%) was obtained as a dark orange oil which was used directly in the subsequent reaction without further purification.

^{1}H NMR (500 MHz, $CDCl_3$) δ (ppm) = 8.73 (d, J = 4.6 Hz, 2H, a/a'), 8.48 (t, J = 9.2Hz, 2H, b/b'), 7.95 (d, J = 7.0 Hz, 1H, c), 7.91 (t, J = 7.6 Hz, 1H, d), 7.39 (t, J = 6.0 Hz,1H, e), 4.82 (s, 2H, f).

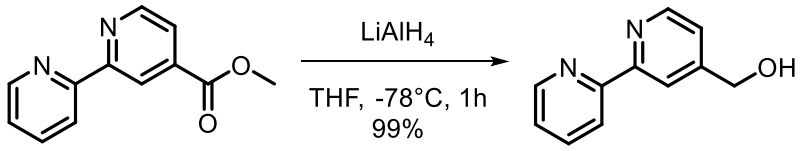

6 **8**

A solution of 4-(methoxycarbonyl)-2,2'-bipyridine (**6**) (2.40 g, 11.20 mmol, 1 eq.) in anhydrous THF (50 mL) was cooled to –78 °C. A 1 M solution of lithium aluminum hydride in THF (2.16 mL, 2.16 mmol for 7; 12.32 mL, 12.32 mmol for 8) was added dropwise. The reaction mixture was warmed to –20 °C and stirred for 0.5 h until a homogeneous solution was formed. Subsequently, the mixture was cooled again to –78 °C and quenched dropwise with 30 mL of 10% aqueous THF. After reaching room temperature, the reaction mixture was stirred with dry Celite for 15 minutes, filtered, and the Celite was washed with approximately 100 mL of THF. The solvent was removed under reduced pressure after drying with $MgSO_4$. [2,2'-bipyridin]-4-ylmethanol (8) (1.95 g, 10.43 mmol, 99%) was obtained as a yellow oil, which was used directly in the subsequent reaction without further purification.

^{1}H NMR (500 MHz, CDCl3) δ (ppm) = 8.69 (d, J = 4.9 Hz, 1H), 8.66 (d, J = 5.1 Hz,1H), 8.45 (d, J = 7.9 Hz, 1H), 8.41 (s, 1H), 7.86 (td, J = 7.8, 1.8 Hz, 1H), 7.40 (d, J = 4.3Hz, 1H), 7.36 (dd, J = 6.3, 4.8 Hz, 1H), 4.85 (s, 2H).

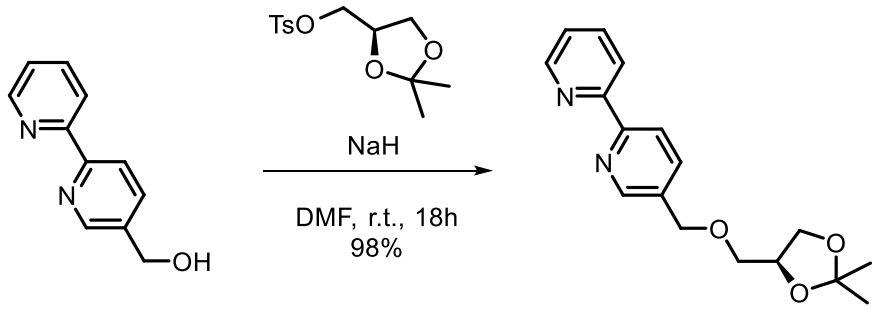

7 **9**

Sodium hydride (60% suspension in mineral oil, 136.41 mg, 5.68 mmol, 2.9 eq.) was washed three times with THF (10 mL) and dried under vacuum. Anhydrous DMF (10 mL) was then added, and the mixture was cooled to 0°C. A solution of [2,2'-bipyridin]-5-ylmethanol (**7**) (365 mg, 1.96 mmol, 1 eq.) in anhydrous DMF was added dropwise to the suspension, followed by stirring for 30 minutes at 0°C. Subsequently, (R)-(2,2-dimethyl-1,3-dioxolan-4-yl)methyl 4-methylbenzenesulfonate (645 mg, 781 µL, 2.25 mmol, 1.15 eq.) was added in portions (0.2

mL every 5 minutes). The reaction mixture was stirred at 0°C for an additional hour and then allowed to stir at room temperature overnight. The reaction was quenched by the careful addition of water (30–40 mL), and the product was extracted with EtOAc (3 × 50 mL). The combined organic phases were washed with water (4 × 80 mL) and brine (4 × 80 mL), dried over $MgSO_4$, and concentrated under reduced pressure and purified by column chromatography (SiO_2, pentane → pentane/EtOAc 10:1 → pentane/EtOAc 1:1). 5-(((2,2-dimethyl-1,3-dioxolan-4-yl)methoxy)methyl)-2,2'-bipyridine (**9**) (575.68 mg, 1.92 mmol, 98%) was obtained as orange oil.

^{1}H NMR (500 MHz, $CDCl_3$) δ (ppm) = 8.61 (ddd, *J* = 4.7, 1.9, 1.0 Hz, 1H, a), 8.57 (d, *J* = 3.1 Hz, 1H, b), 8.32 (d, *J* = 7.9 Hz, 1H, c), 7.78 – 7.73 (m, 2H, d/d'), 7.27 – 7.23 (m, 2H, e/e'), 4.64 – 4.55 (m, 2H, f), 4.29 – 4.18 (m, 1H, g), 3.99 (ddd, *J* = 12.7, 8.3, 6.5 Hz, 1H, h), 3.68 (ddd, *J* = 14.6, 8.2, 6.4 Hz, 1H, i), 3.57 – 3.45 (m, 2H, j), 1.36 (s, 6H, k/k').

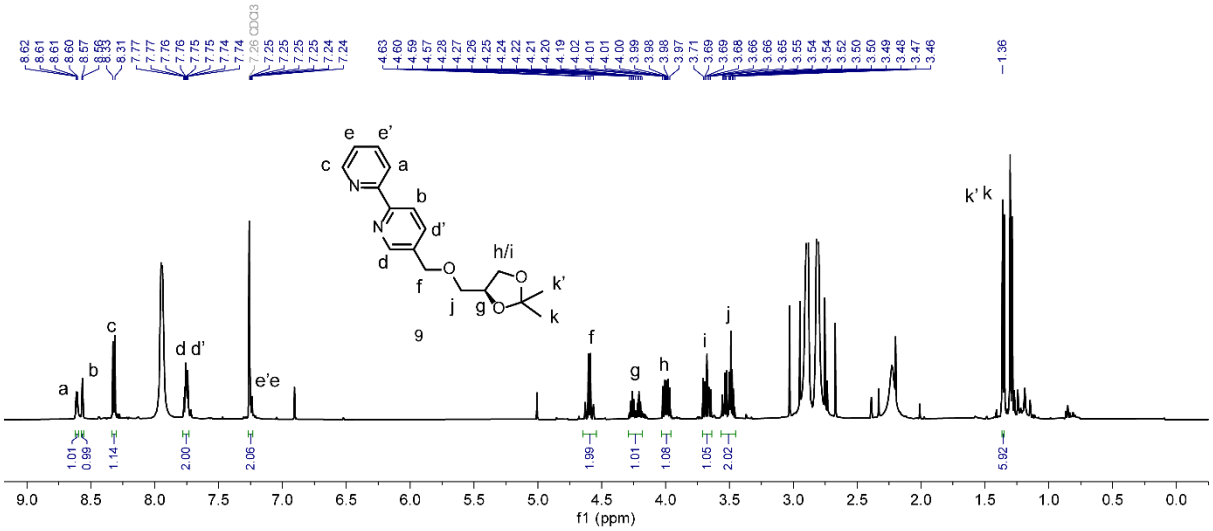

Figure S 1. ^{1}H-NMR spectrum of 5-(((2,2-dimethyl-1,3-dioxolan-4-yl)methoxy)methyl)-2,2'-bipyridine (9) in $CDCl_3$. 500MHz, 298K.

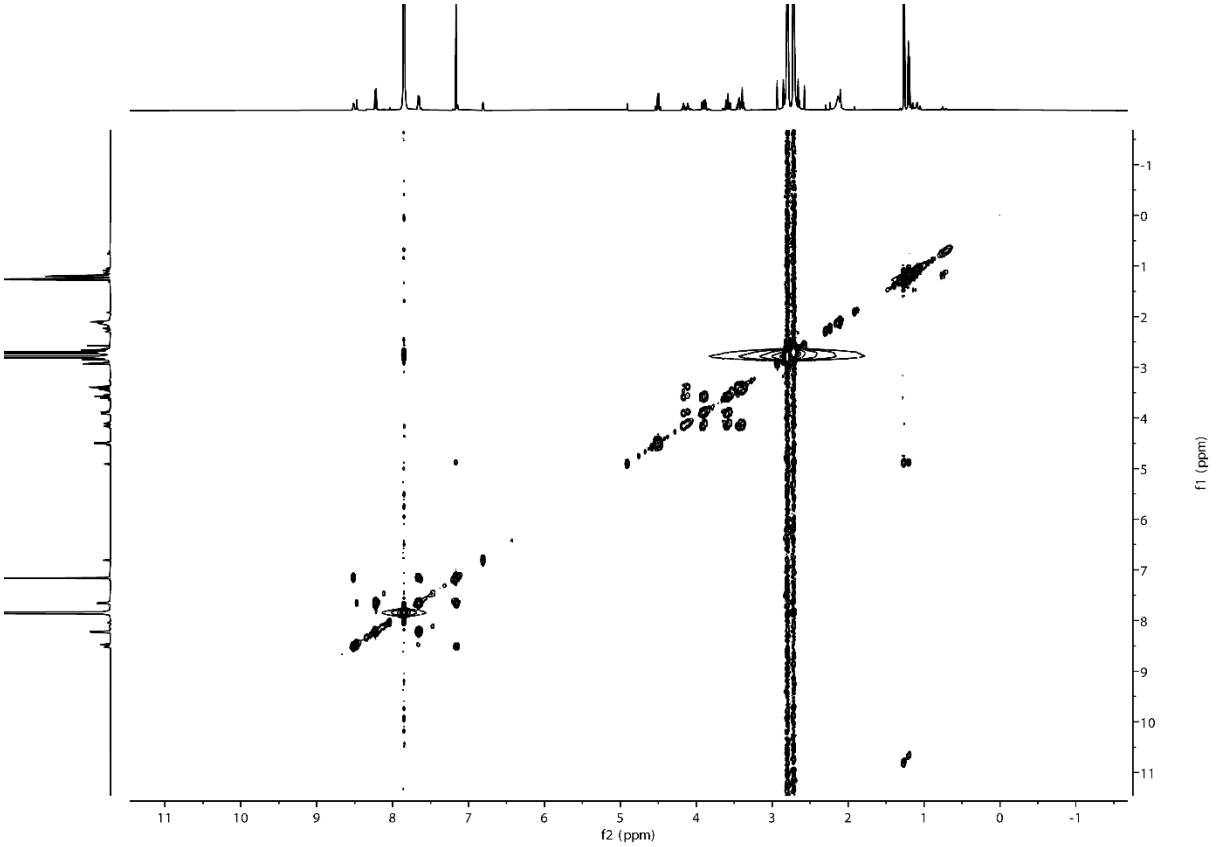

Figure S 2. COSY NMR spectrum of 5-(((2,2-dimethyl-1,3-dioxolan-4-yl)methoxy)methyl)-2,2'-bipyridine (9) in $CDCl_3$. 500MHz, 298K.

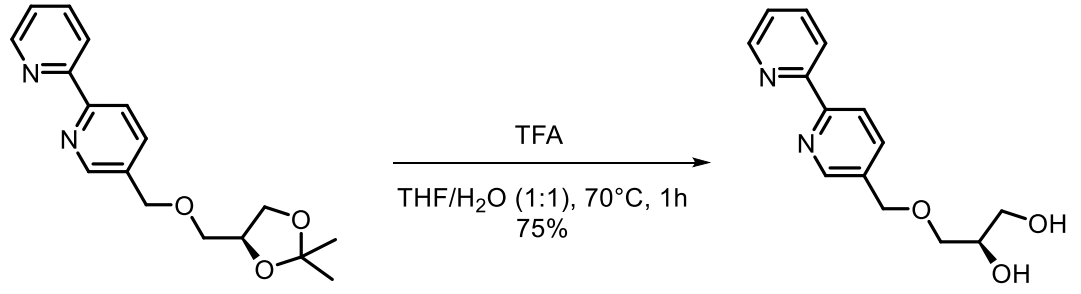

9 **11**

5-(((2,2-Dimethyl-1,3-dioxolan-4-yl)methoxy)methyl)-2,2'-bipyridine (**9**) (517 mg, 1.72 mmol, 1 eq.) was dissolved in a mixture of THF and water (4 mL, 1:1 v/v). Trifluoroacetic acid (215.89 mg, 144.99 µL, 1.89 mmol, 1.1 eq.) was added dropwise to the solution. The reaction mixture was heated to 70°C (reflux) for 1 hours, followed by stirring overnight at room temperature. The acidic suspension was neutralized with aqueous ammonia (25% v/v),

and the solvents were removed under reduced pressure. The residue was purified by column chromatography (SiO_2, chloroform/methanol 10:1), yielding 3-([2,2'-bipyridin]-5-ylmethoxy)propane-1,2-diol (**11**) (196.18 mg, 0.75 mmol, 75%) as yellow oil.

^{1}H NMR (600 MHz, $CDCl_3$) δ (ppm) = 8.72 (ddd, *J* = 4.9, 1.8, 0.9 Hz, 1H, a), 8.69 (d, *J* = 1.6 Hz, 1H, b), 8.47 (dd, *J* = 8.1, 6.1 Hz, 2H, c/c'), 7.92 – 7.82 (m, 2H, d/d'), 7.38 (ddd, *J* = 7.5, 4.9, 1.2 Hz, 1H, e), 4.66 (s, 2H, f), 3.98 – 3.92 (m, 1H, g), 3.75 (dd, *J* = 11.4, 3.9 Hz, 1H, h/i), 3.69 – 3.59 (m, 3H, i'), 3.48 (s, OH, j), 2.63 (s, OH, k).

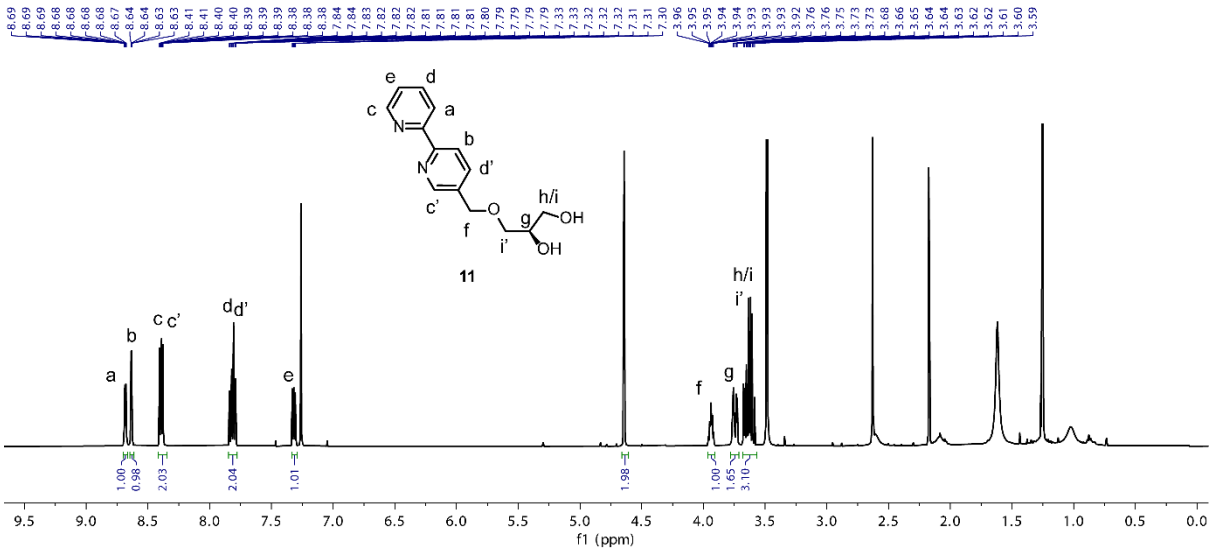

Figure S 3. ^{1}H-NMR spectrum of 3-([2,2'-bipyridin]-5-ylmethoxy)propane-1,2-diol (11) in $CDCl_3$. 500MHz, 298K.

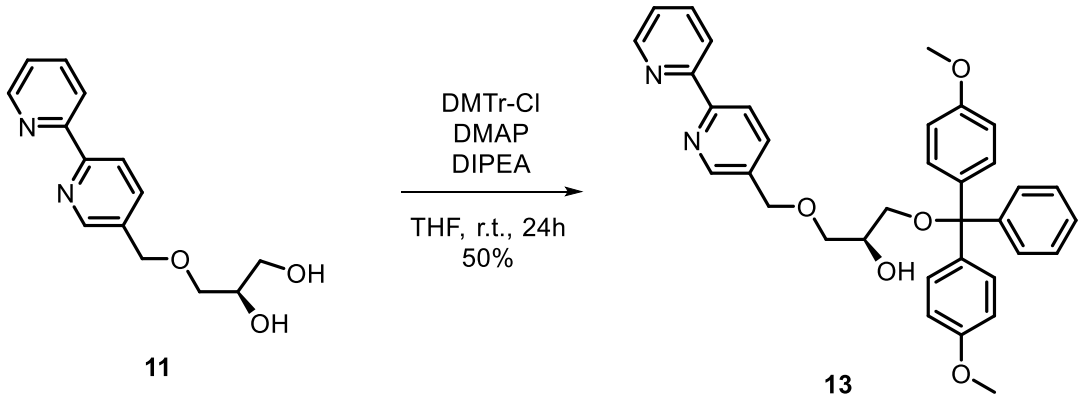

Under an inert atmosphere, 3-([2,2'-bipyridin]-5-ylmethoxy)propane-1,2-diol (**11**) (196.18 mg, 0.75 mmol, 1 eq.) was dissolved in anhydrous THF (3 mL). 4-Dimethylaminopyridine (5.52

mg, 45.18 µmol, 0.06 eq.) was added, followed by the slow addition of 4,4′-dimethoxytrityl chloride (280.65 mg, 828.30 µmol, 1.10 eq.) as a solid in portions. Diisopropylethylamine (194.65 mL, 256.11 µL, 1.51 mmol, 2.00 eq.) was then added to the mixture. The reaction was stirred overnight at room temperature. The suspension was diluted with methanol (1 mL) and ethyl acetate (50 mL), and the combined organic phases were washed with saturated aqueous sodium hydrogen carbonate solution (3 × 25 mL), water (3 × 25 mL), and brine (3 × 25 mL). The organic phase was dried over magnesium sulfate, and the solvents were removed under reduced pressure. Purification by column chromatography (SiO_2, ethyl acetate, 1% v/v triethylamine) yielded (S)-1-([2,2'-bipyridin]-5-ylmethoxy)-3-(bis(4-methoxyphenyl)(phenyl)methoxy)propan-2-ol (**13**) (210 mg, 373 µmol, 49%) as a white-gray solid.

^{1}H NMR (500 MHz, CD_2Cl_2) δ (ppm) = 8.61 (ddd, J = 4.7, 1.9, 1.0 Hz, 1H, a), 8.57 (d,J = 3.1 Hz, 1H, b), 8.32 (d, J = 7.9 Hz, 1H, c), 7.78 – 7.73 (m, 2H, d/d'), 7.27 – 7.23 (m,2H, e/e'), 4.64 – 4.55 (m, 2H, f), 4.29 – 4.18 (m, 1H, g), 3.99 (ddd, J = 12.7, 8.3, 6.5 Hz,1H, h), 3.68 (ddd, J = 14.6, 8.2, 6.4 Hz, 1H, i), 3.57 – 3.45 (m, 2H, j), 1.36 (s, 6H, k/k').

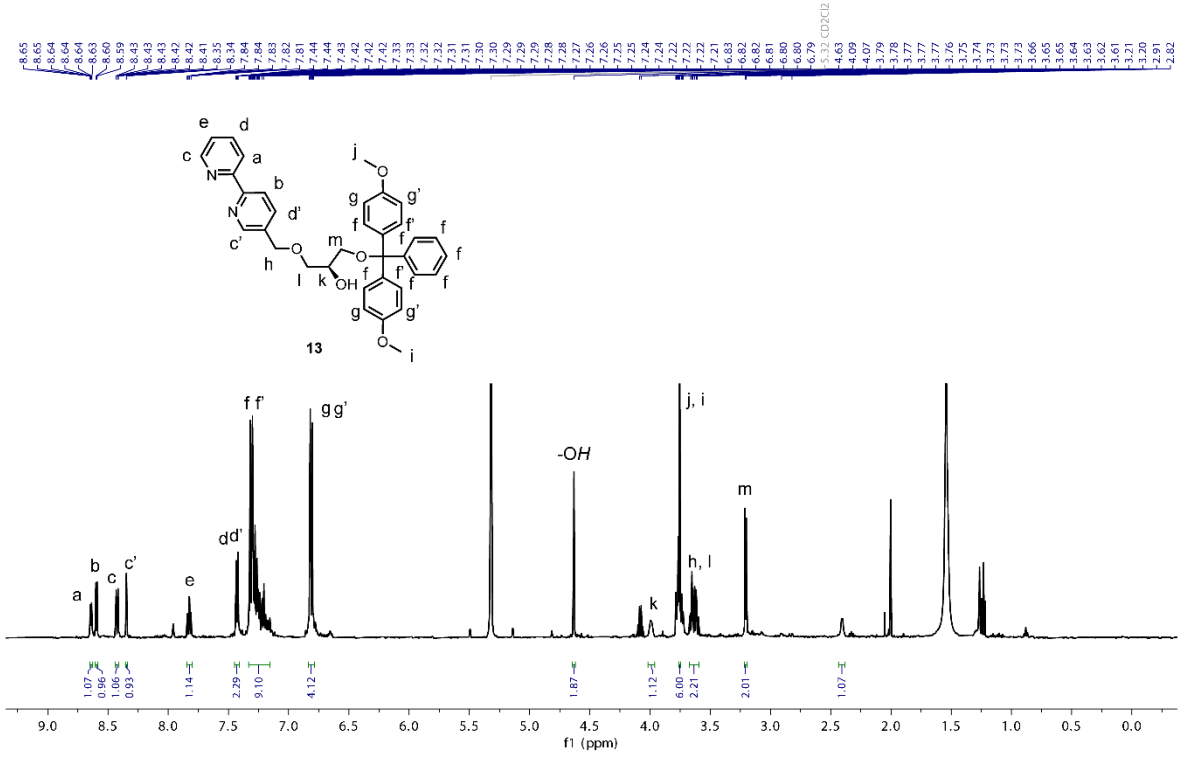

Figure S 4. ^{1}H-NMR spectrum of (S)-1-([2,2'-bipyridin]-5-ylmethoxy)-3-(bis(4-methoxyphenyl)(phenyl)methoxy)propan-2-ol (**13**) in CD_2Cl_2. 500MHz, 298K.

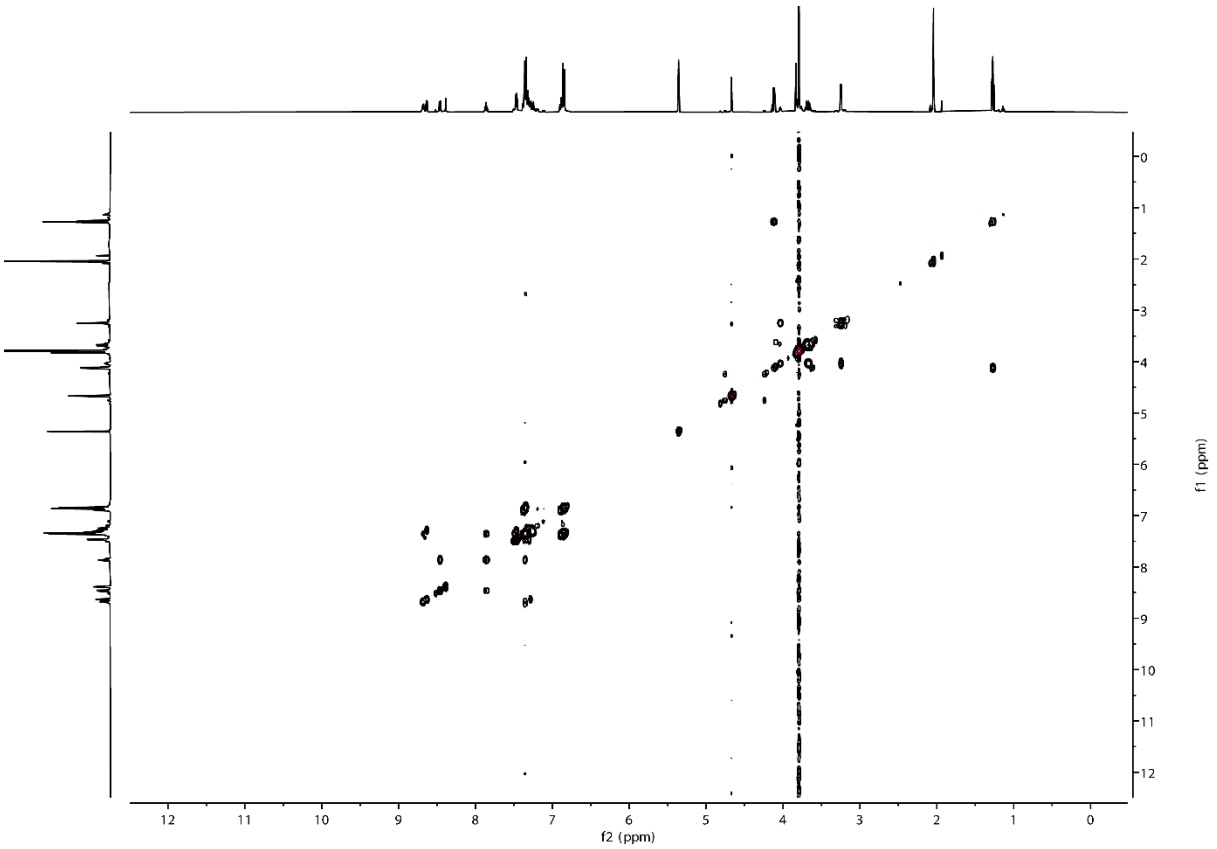

Figure S 5. COSY-NMR spectrum of (S)-1-([2,2'-bipyridin]-5-ylmethoxy)-3-(bis(4-methoxyphenyl)(phenyl)methoxy)propan-2-ol (**13**) in CD_2Cl_2. 500MHz, 298K.

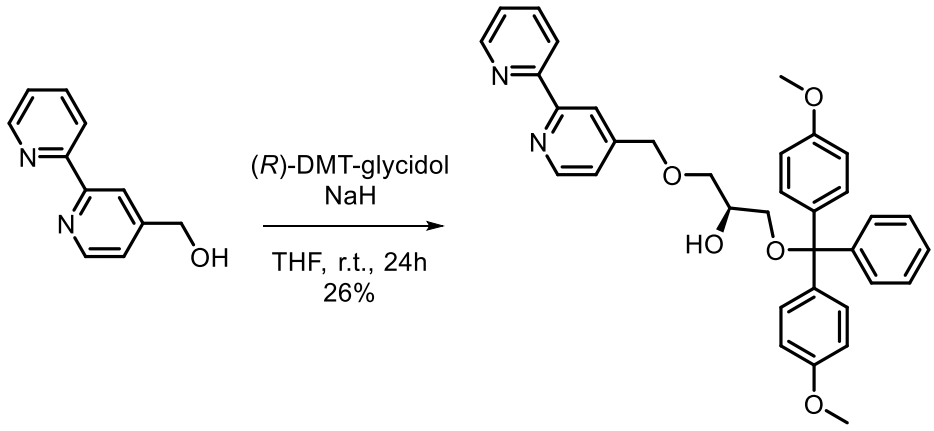

12 **14**

Sodium hydride (60% suspension in mineral oil, 2.90 eq.) washed with dry THF (2x20 mL) and shortly dried under vaccum. Subsequently dry THF was added (few mL) and the suspension cooled down to 0°C in an ice bath. To this [2,2'-bipyridine]-4-ylmethanol (**12**) dissolved in 2-3 mL dry THF was added dropwise through a syringe. This mixture was

further stirred at 0 °C for 1 h, and previously synthesised (*R*)-DMT-glycidol (1.3 eq.) solved in 3 mL THF was added dropwise. The ice bath was removed and the reaction was heated slowly r.t. and stirred over night. The reaction was stopped by slow addition of 30-40 mL of water, whereas 4 mL of brine was added for better phase separation. The reaction mixture was extracted three times with EtOAc, the combined fractions were washed three times with saturated aqueous sodium chloride solution and dried over $MgSO_4$. The organic phase was filtered and solvents were removed under reduced pressure. Purification was done by column chromatography followed by GPC (EtOAc, 1 % TEA).

^{1}H NMR (500 MHz, CD_2Cl_2) δ (ppm) = 8.69 (d, 1H, a), 8.62 (dz, J =4.9 Hz, 1H, b), 8.41(dt, J = 7.9, 1.2 Hz, 1H, c), 8.35 (s, 1H, d), 7.83 (td, J = 7.6, 1.8 Hz,1H, e), 7.76 (), 7.42 (dd, J = 8.5, 1.3 Hz, 2H, f), 7.34 – 7.16 (m, 7H, g), 6.84 – 6.80 (m, 4H, h), 4.61(s, 2H, i), 3.96 (s, 1H, j), 3.73 (s, 6H, k), 3.66 – 3.57 (m, 2H, l), 3.24f (d, J = 5.3 Hz,2H, m).

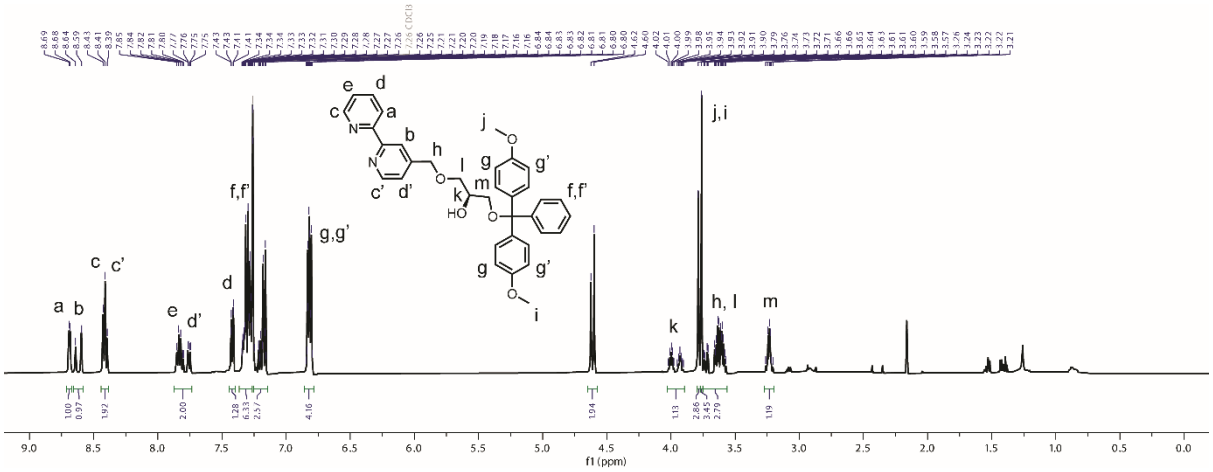

Figure S 6. ^{1}H-NMR spectrum of (*S*)-1-([2,2'-bipyridin]-4-ylmethoxy)-3-(bis(4-methoxyphenyl)(phenyl)methoxy)propan-2-ol (**14**) in CD_2Cl_2. 500MHz, 298K.

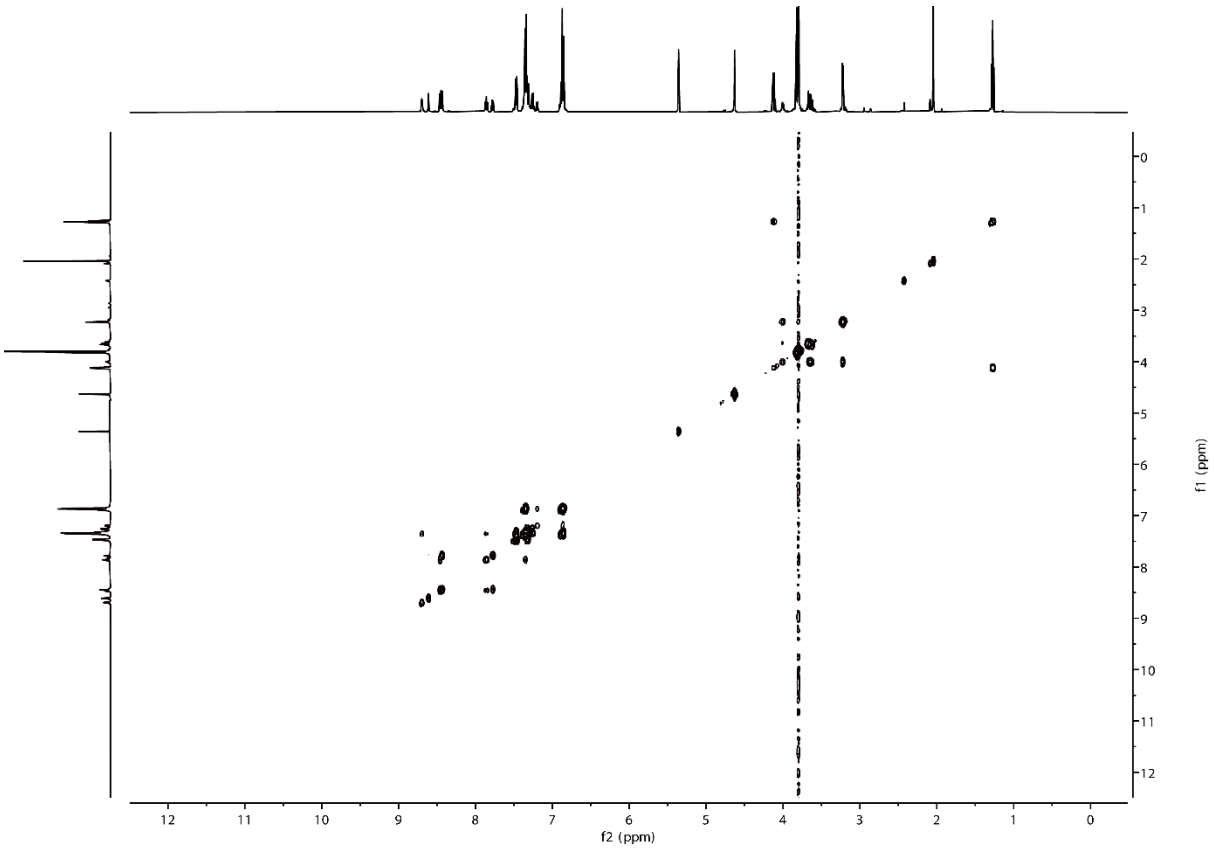

Figure S 7. COSY-NMR spectrum of (*S*)-1-([2,2'-bipyridin]-4-ylmethoxy)-3-(bis(4-methoxyphenyl)(phenyl)methoxy)propan-2-ol (**14**) in CD_2Cl_2. 500MHz, 298K.

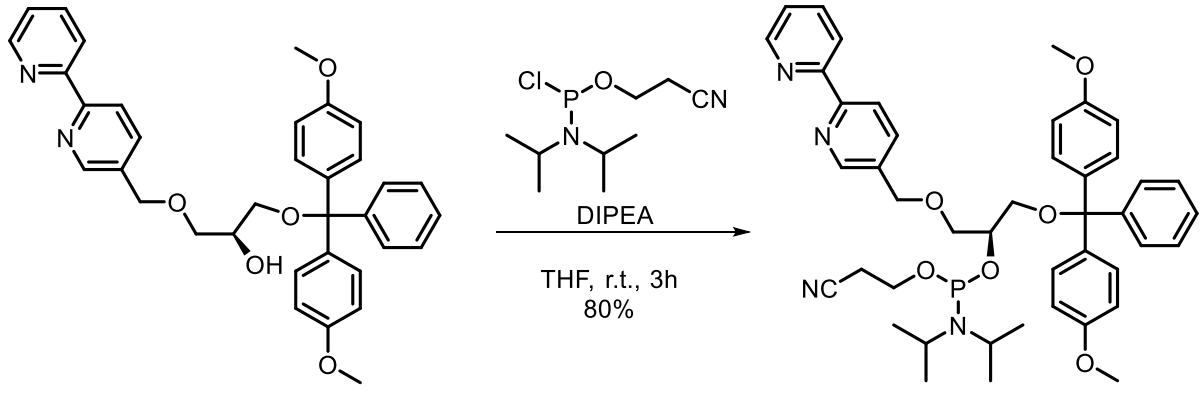

13 **15**

Compounds **13** was co-evaporated with anhydrous THF (2 × 1 mL) under an inert atmosphere and then dissolved in anhydrous THF (6 mL). DIPEA (4.00 eq.) was added dropwise, followed by the dropwise addition of 2-cyanoethyl-N,N-diisopropylchlorophosphoramidite (1.10 eq.). The resulting solution was stirred for 2–3 hours

at room temperature, during which a white precipitate formed. The reaction mixture was filtered through a syringe filter to remove the precipitated diisopropylethylammonium chloride. The solvent was removed under reduced pressure, yielding the final compounds **15** as yellow oils. The crude product was used without further purification, either directly or after storage at –25°C and was utilized within several days for automated DNA synthesis.

^{31}P NMR (202 MHz, CD_3CN) δ (ppm) = 148.91, 148.60, 13.76.

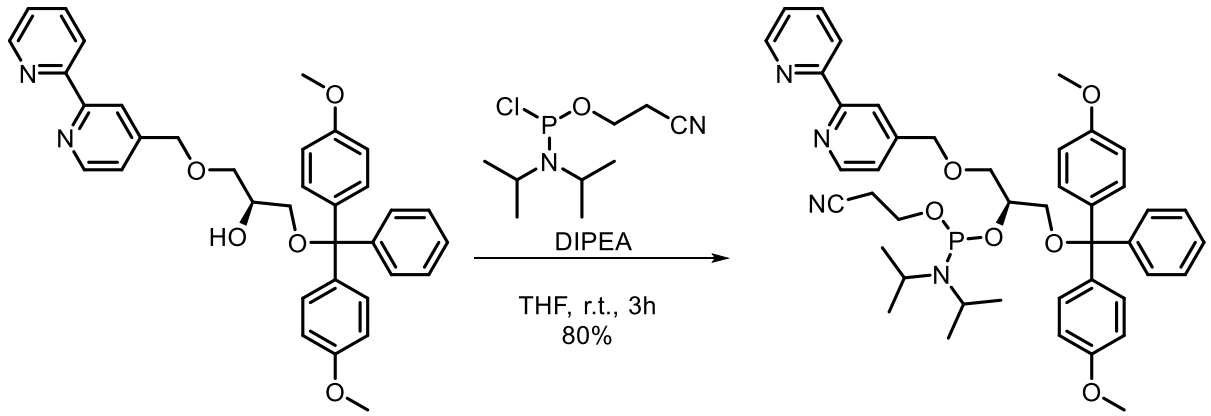

14 **16**

Compounds **14** was co-evaporated with anhydrous THF (2 × 1 mL) under an inert atmosphere and then dissolved in anhydrous THF (6 mL). DIPEA (4.00 eq.) was added dropwise, followed by the dropwise addition of 2-cyanoethyl-N,N-diisopropylchlorophosphoramidite (1.10 eq.). The resulting solution was stirred for 2–3 hours at room temperature, during which a white precipitate formed. The reaction mixture was filtered through a syringe filter to remove the precipitated diisopropylethylammonium chloride. The solvent was removed under reduced pressure, yielding the final compounds **16** as yellow oils. The crude product was used without further purification, either directly or after storage at –25°C and were utilized within several days for automated DNA synthesis.

^{31}P NMR (202 MHz, CD_3CN) δ (ppm) = 148.98, 148.63, 13.75.

Olignucleotide Sequence List

Name	Sequence 5'-3'
htel22-L2a	A GGG **L**TA GGG TTA GGG TT**L** GGG
htel22-L2b	A GG**L** TTA GGG TTA GG**L** TTA GGG
htel22-L3a	A GGG **L**TA GGG TTA GGG **L**T**L** GGG
ttel24-L2a	TTG GG**L** TTG GGG TTG GG**L** TTG GGG
ttel24-L2b	TTG GGG TT**L** GGG TTG GGG TT**L** GGG
pu22-L2a	TG**L** GGG TGG GTA GGG TGG G**L**A A
pu22-L2b	TG**L** GGG TTGG GTA GGG TGG G**L**A A
pu22-L2c	TG**L** GGG TTAGG GTA GGG TGG G**L**A A
FAM-htel22-L2a	FAM - A GGG **L**TA GGG TTA GGG TT**L** GGG
FAM-mut-htel22-L2a	FAM - A GTG **L**TA GTG TTA GTG TT**L** GTG
FAM-htel22-L2b	FAM - A GG**L** TTA GGG TTA GG**L** TTA GGG
FAM-ttel24-L2a	FAM - TTG GG**L** TTG GGG TTG GG**L** TTG GGG
FAM-T15-htel22-L2a	T^{FAM}TT TTT TTT TTT TTT A GGG **L**TA GGG TTA GGG TT**L** GGG
FAM-T15-htel22-L2b	T^{FAM}TT TTT TTT TTT TTT A GG**L** TTA GGG TTA GG**L** TTA GGG
FAM-T15-cmyc-L2a	T^{FAM}TT TTT TTT TTT TTT **L** GGG T GGG TA GGG T GGG **L**T
FAM-T15-pu22-L2a	T^{FAM}TT TTT TTT TTT TTT TG**L** GGG TTGG GTA GGG TGG G**L**A A
FAM-htel22-L2a-T15	A GGG **L**TA GGG TTA GGG TT**L** GGG TTT TTT TTT TTT TT^{FAM}T
FAM-htel22-L2b-T15	A GG**L** TTA GGG TTA GG**L** TTA GGG TTT TTT TTT TTT TT^{FAM}T
FAM-cmyc-L2a-T15	**L** GGG T GGG TA GGG T GGG **L** TTT TTT TTT TTT TT^{FAM}T
FAM-pu22-L2a-T15	TG**L** GGG TTGG GTA GGG TGG G**L**A A TTT TTT TTT TTT TT^{FAM}T
FAM-htel22-L2a-Cy3	FAM - A GGG **L**TA GGG TTA GGG TT**L** GGG – Cy3
FAM-htel22-L2b-Cy3	FAM - A GG**L** TTA GGG TTA GG**L** TTA GGG – Cy3

DNA G-quadruplex melting temperatures

Table S 1. Melting temperatures of bipyridine-modified DNA sequences in presence and absence of various transition metal cations in **K^+** containing buffer, measured by UV-Vis spectroscopy

Name	**T_m [°C]**	**ΔT_m ($+Cu^{2+}$)**	**ΔT_m ($+Ni^{2+}$)**	**ΔT_m ($+Zn^{2+}$)**	**ΔT_m ($+Co^{2+}$)**	**ΔT_m ($+Cd^{2+}$)**
htel22	64	n.d.	n.d.	n.d.	n.d.	n.d.
htel22-L2a (BiPy-L1)	68	79	84	83	81	83
htel22-L2a (BiPy-L2)	68	84	73	83	81	80
htel22-L2b (BiPy-L1)	44	72	75	74	74	71
htel22-L2b (BiPy-L2)	43	79	80	76	71	n.d.
ttel-24*	n.d.	n.d.	n.d.	n.d.	n.d.	n.d.
ttel24-L2a (BiPy-L1)	65	75	77	77	73	76
ttel24-L2a (BiPy-L2)	69	81	80	73	71	72
ttel24-L2b	65	76	79	77	71	74
pu22	85	n.d.	n.d.	n.d.	n.d.	n.d.
pu22-L2a	37 + >85**	>85	>85	>85	n.d.	n.d.
pu22-L2b	>85	>85	36 + >85	37 + >85	n.d.	n.d.
pu22-L2c	>85	>85	>85	>85	n.d.	n.d.

* Poorly defined melting transition. ** Two melting points identified.

Table S 2. Melting temperatures of bipyridine-modified DNA sequences in presence and absence of various transition metal cations in **Na^+** containing buffer, measured by UV-Vis spectroscopy

Name	T_m [°C]	ΔT_m (+Cu^{2+})	ΔT_m (+Ni^{2+})	ΔT_m (+Zn^{2+})	ΔT_m (+Co^{2+})	ΔT_m (+Cd^{2+})
htel22	64	n.d.	n.d.	n.d.	n.d.	n.d.
htel22-L2a (BiPy-L1)	52	72	74	73	71	71
htel22-L2a (BiPy-L2)	42	40 + 64**	54	31	28	46
htel22-L2b (BiPy-L1)	25	61	60	62	55	56
htel22-L2b (BiPy-L2)	19	21	18	20	n.d.	n.d.
ttel-24*	n.d.	n.d.	n.d.	n.d.	n.d.	n.d.
ttel24-L2a (BiPy-L1)	28	48	44	45	40	41
ttel24-L2a (BiPy-L2)	38	20	19	20	n.d.	n.d.
ttel24-L2b	40	42	48	56	35 + 63**	54
pu22	85	n.d.	n.d.	n.d.	n.d.	n.d.
pu22-L2a	18	n.d.***	n.d.***	n.d.***	n.d.***	n.d.***

* Poorly defined melting transition. ** Two melting points identified. ***Melting point could not be determined due to premature disturbance of G-quadruplex structure.

HPLC Oligonucleotides

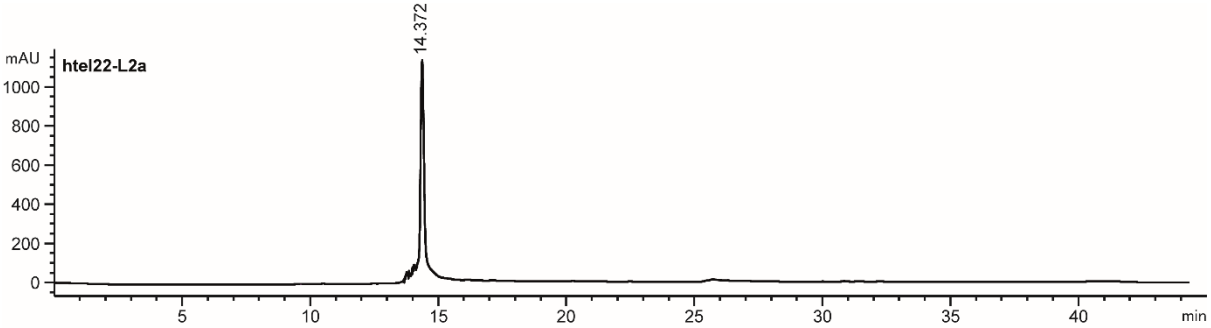

Figure S 8. HPLC-trace of oligonucleotide **htel22-L2a** with BiPy-L1 modification at 5µM concentration in 50mM TEAA buffer.

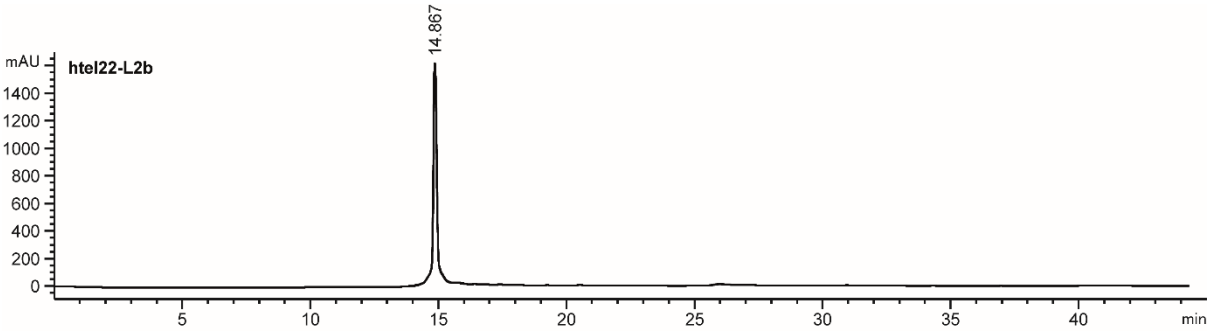

Figure S 9. HPLC-trace of oligonucleotide **htel22-L2b** with BiPy-L1 modification at 5μM concentration in 50mM TEAA buffer

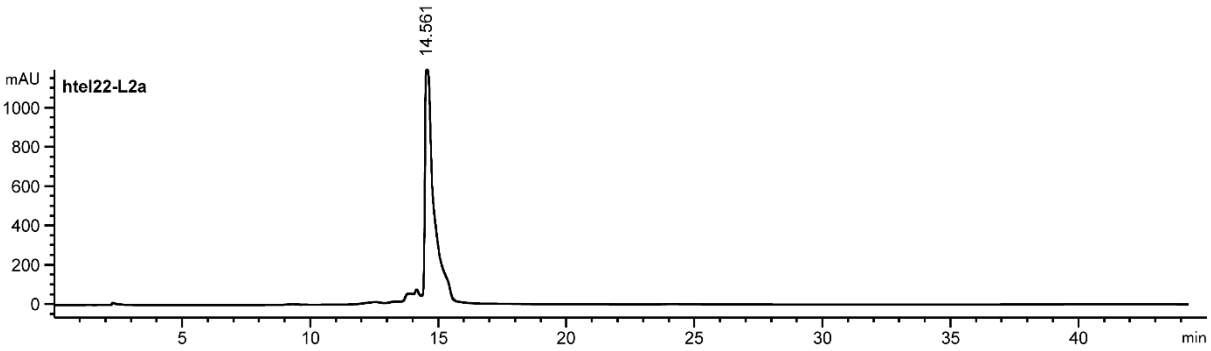

Figure S 10. HPLC-trace of oligonucleotide **htel22-L2a** with BiPy-L2 modification at 5μM concentration in 50mM TEAA buffer.

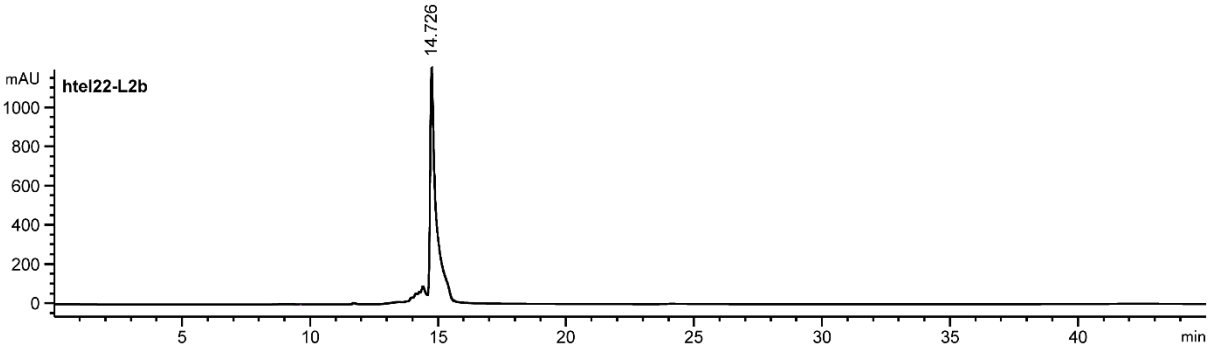

Figure S 11. HPLC-trace of oligonucleotide **htel22-L2b** with BiPy-L2 modification at 5μM concentration in 50mM TEAA buffer.

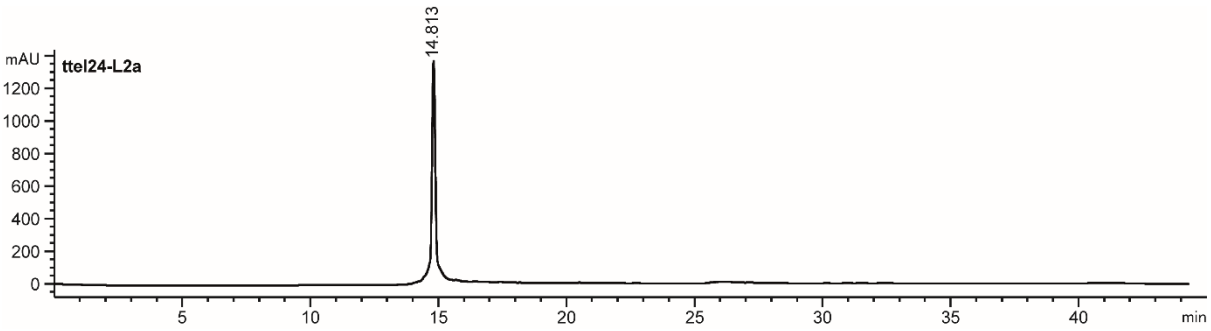

Figure S 12. HPLC-trace of oligonucleotide **ttel24-L2a** with BiPy-L1 modification at 5μM concentration in 50mM TEAA buffer.

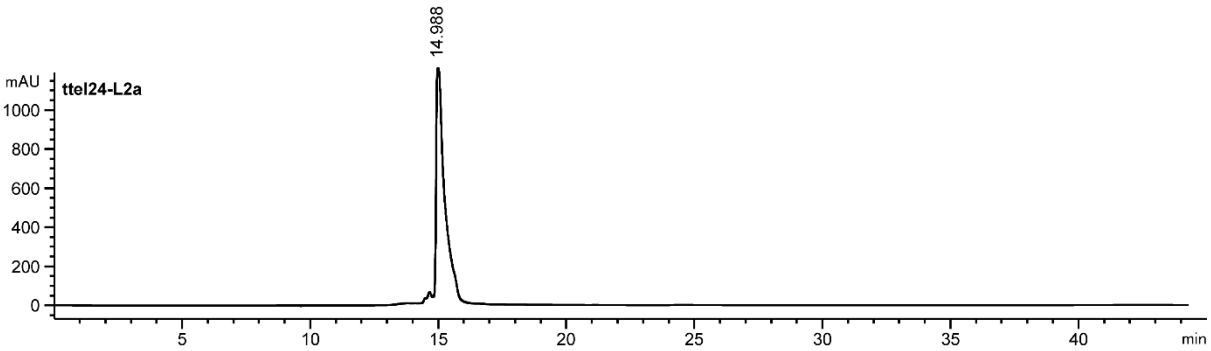

Figure S 13. HPLC-trace of oligonucleotide **ttel24-L2a** with BiPy-L2 modification at 5μM concentration in 50mM TEAA buffer.

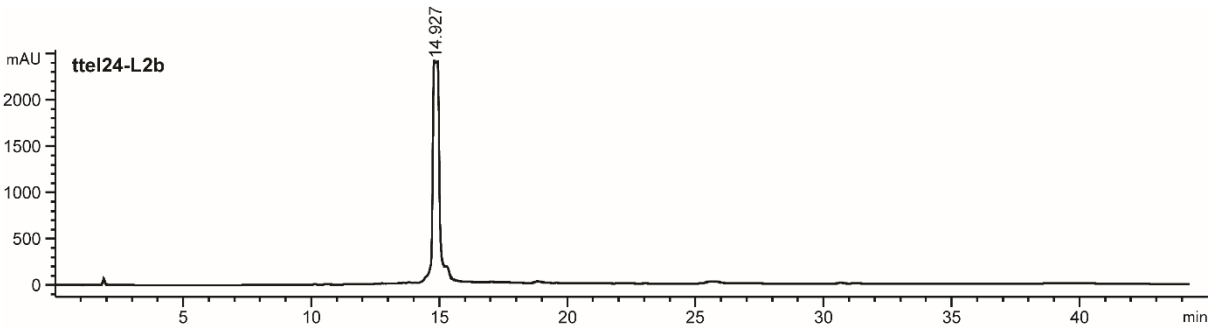

Figure S 14. HPLC-trace of oligonucleotide **ttel24-L2b** with BiPy-L1 modification at 5μM concentration in 50mM TEAA buffer.

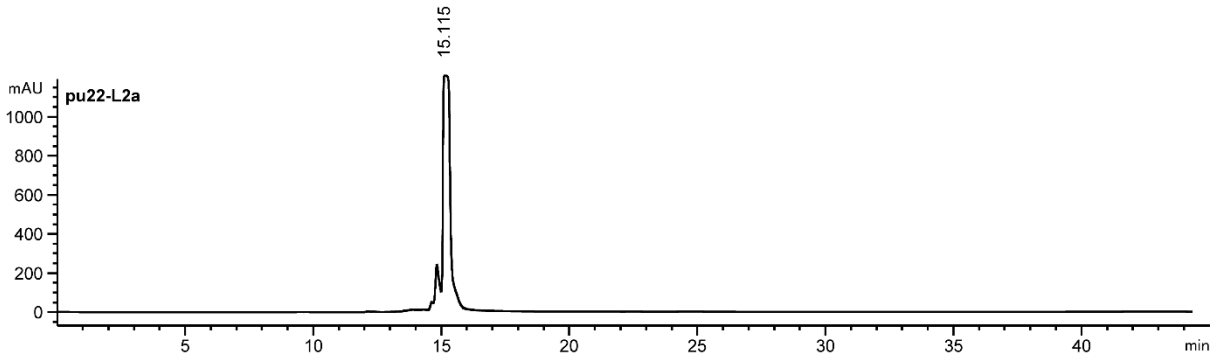

Figure S 15. HPLC-trace of oligonucleotide **pu22-L2a** with BiPy-L1 modification at 5μM concentration in 50mM TEAA buffer.

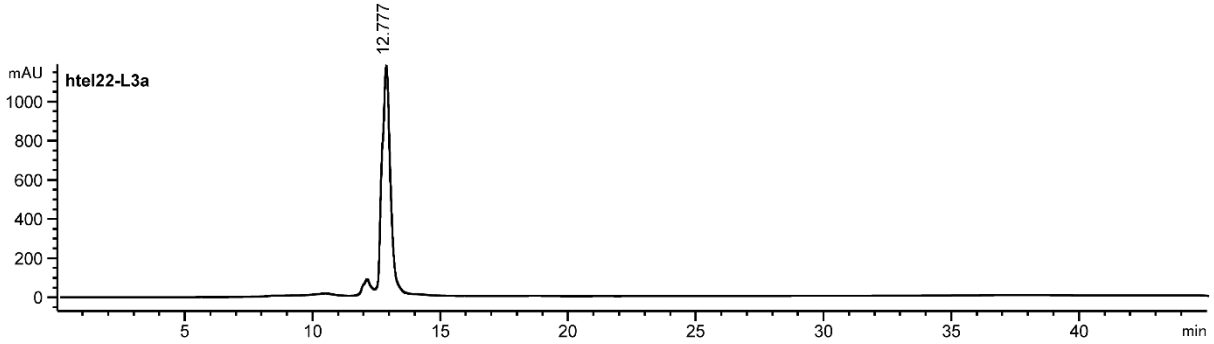

Figure S 16. HPLC-trace of oligonucleotide **htel22-L3a** at 5μM concentration in 50mM TEAA buffer.

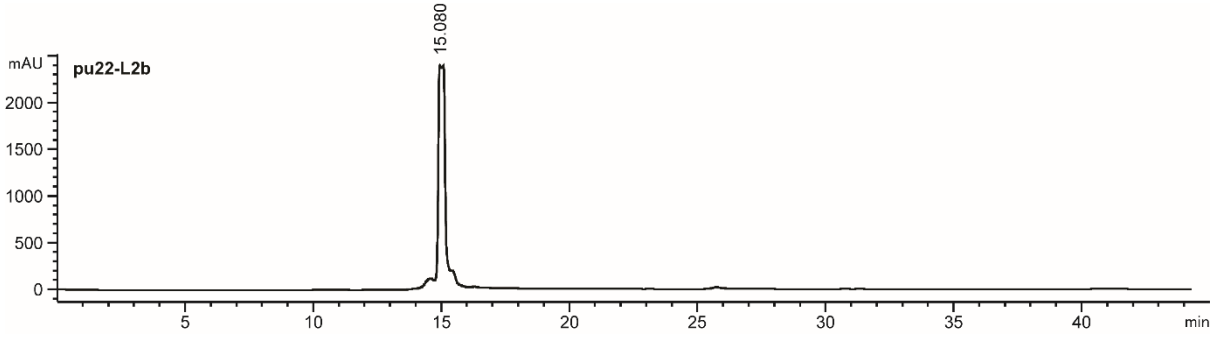

Figure S 17. HPLC-trace of oligonucleotide **pu22-L2b** at 5μM concentration in 50mM TEAA buffer.

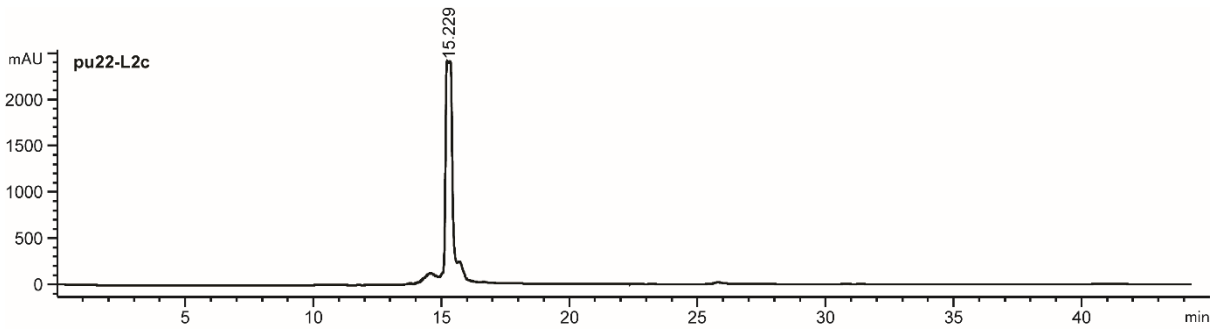

Figure S 18. HPLC-trace of oligonucleotide **pu22-L2c** at 5μM concentration in 50mM TEAA buffer.

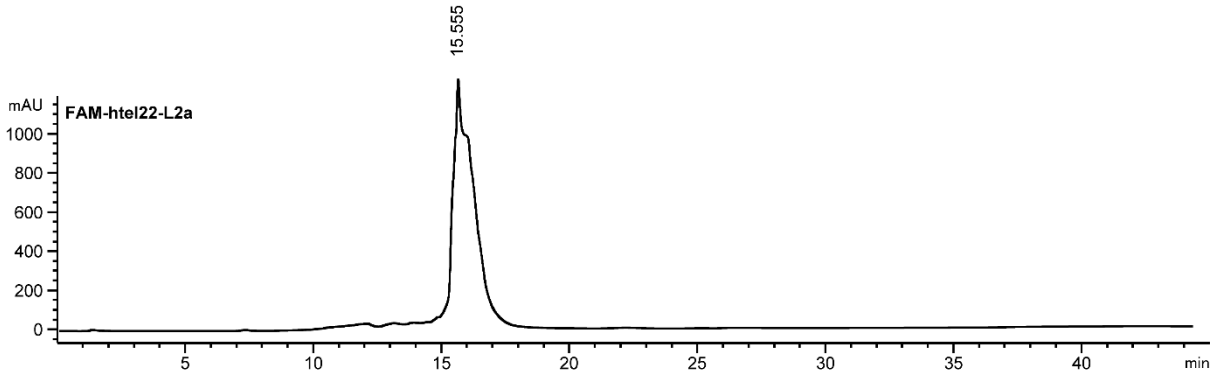

Figure S 19. HPLC-trace of oligonucleotide **FAM-htel22-L2a** at 5μM concentration in 50mM TEAA buffer.

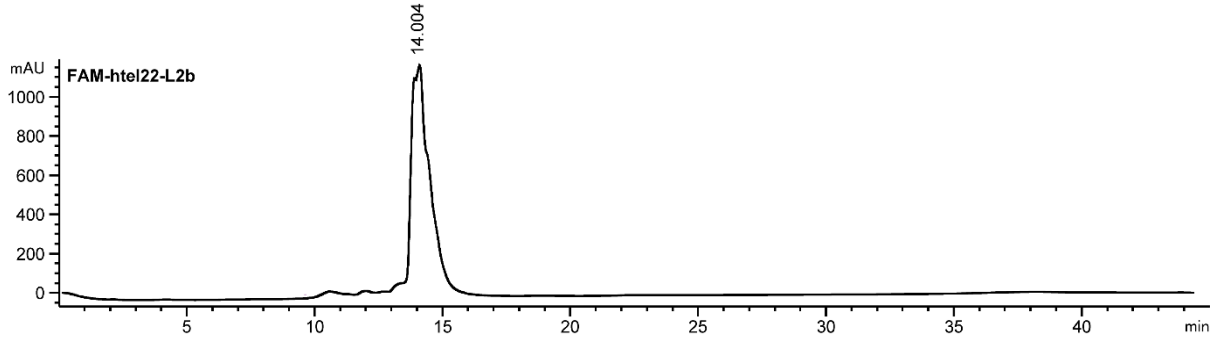

Figure S 20. HPLC-trace of oligonucleotide **FAM-htel22-L2b** at 5μM concentration in 50mM TEAA buffer.

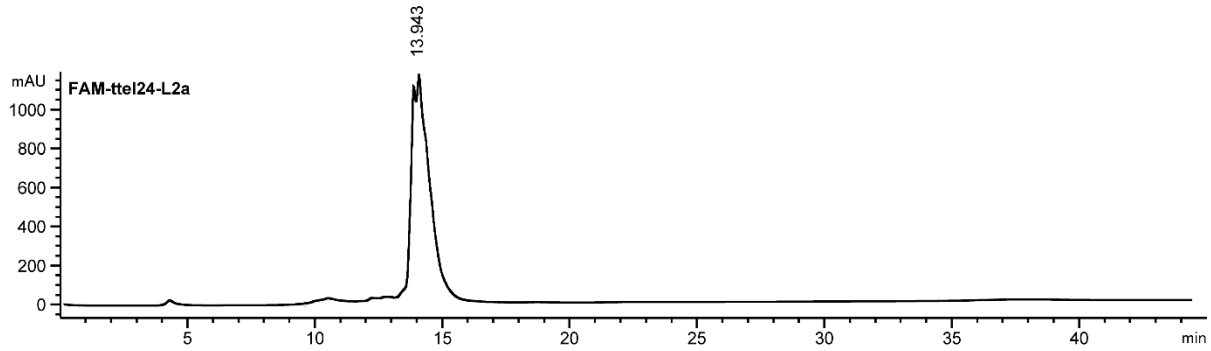

Figure S 21. HPLC-trace of oligonucleotide **FAM-ttel24-L2a** at 5μM concentration in 50mM TEAA buffer.

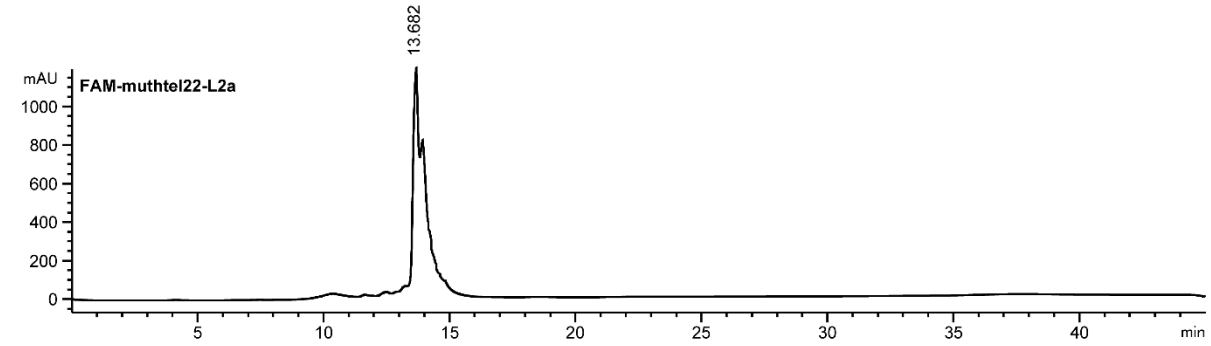

Figure S 22. HPLC-trace of oligonucleotide **FAM-muthtel22-L2a** at 5μM concentration in 50mM TEAA buffer.

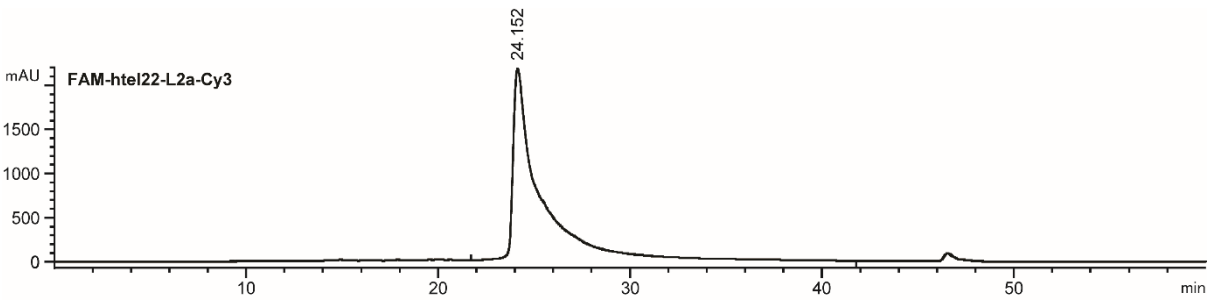

Figure S 23. HPLC-trace of oligonucleotide **FAM-htel22-L2a-Cy3** at 5μM concentration in 50mM TEAA buffer.

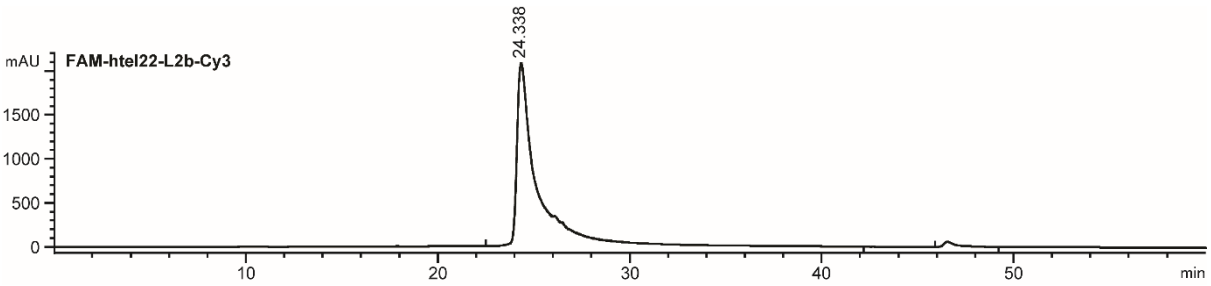

Figure S 24. HPLC-trace of oligonucleotide **FAM-htel22-L2b-Cy3** at 5µM concentration in 50mM TEAA buffer.

CD of folded G-Quadruplexes

CD

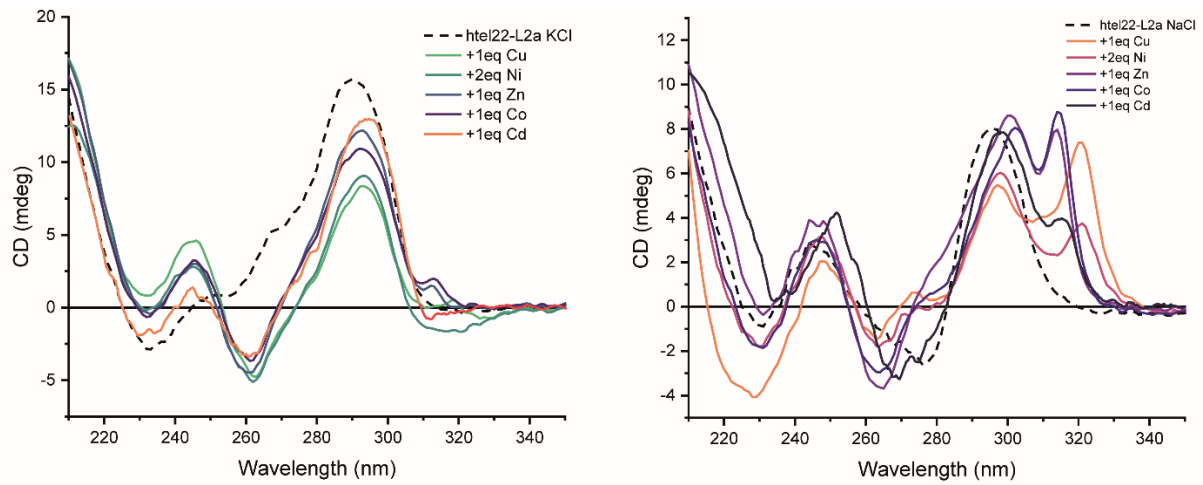

Figure S 25. CD spectra of htel22-L2a in absence or presence of various divalent metal cations. Conditions: 4μM DNA, 10mM HEPES, 100mM NaCl or KCl, 4.4 μM M^{2+} (M = Cu, Ni, Zn, Co, Cd).

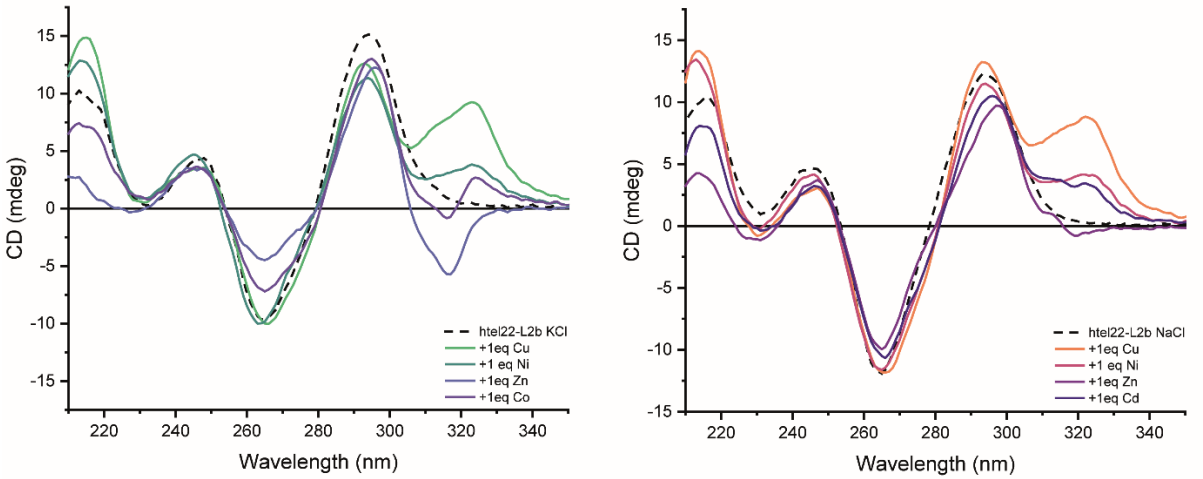

Figure S 26. CD spectra of htel22-L2b in absence or presence of various divalent metal cations. Conditions: 4μM DNA, 10mM HEPES, 100mM NaCl or KCl, 4.4 μM M^{2+} (M = Cu, Ni, Zn, Co).

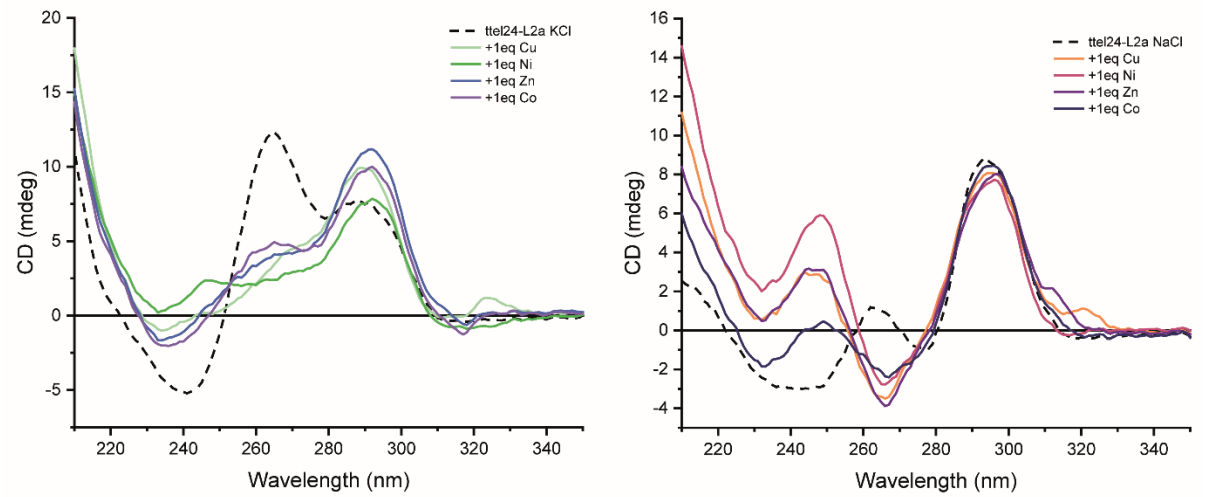

Figure S 27. CD spectra of ttel24-L2a in absence or presence of various divalent metal cations. Conditions: 4μM DNA, 10mM HEPES, 100mM NaCl or KCl, 4.4 μM M^{2+} (M = Cu, Ni, Zn, Co).

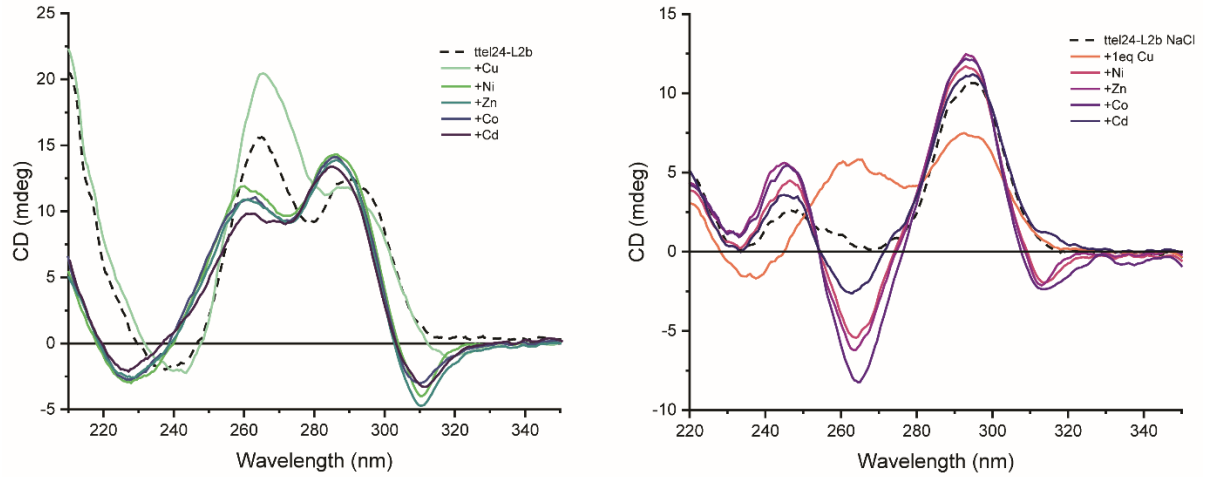

Figure S 28. CD spectra of ttel24-L2b in absence or presence of various divalent metal cations. Conditions: 4μM DNA, 10mM HEPES, 100mM NaCl or KCl, 4.4 μM M^{2+} (M = Cu, Ni, Zn, Co, Cd).

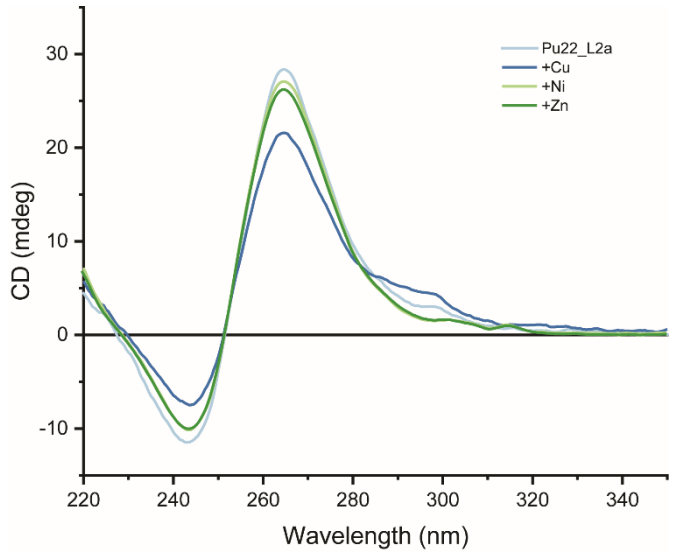

Figure S 29. CD spectrum of pu22-L2a in absence or presence of various divalent metal cations. Conditions: 4μM DNA, 10mM HEPES, 100mM KCl, 4.4 μM M^{2+} (M = Cu, Ni, Zn).

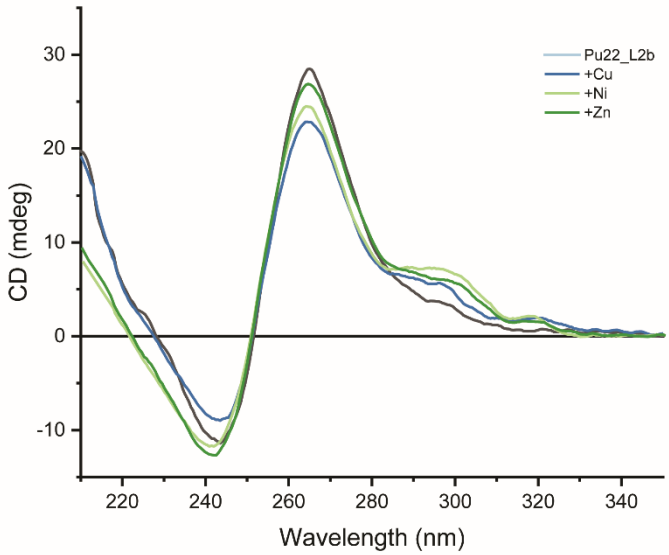

Figure S 30. CD spectrum of pu22-L2a in absence or presence of various divalent metal cations. Conditions: 4μM DNA, 10mM HEPES, 100mM KCl, 4.4 μM M^{2+} (M = Cu, Ni, Zn).

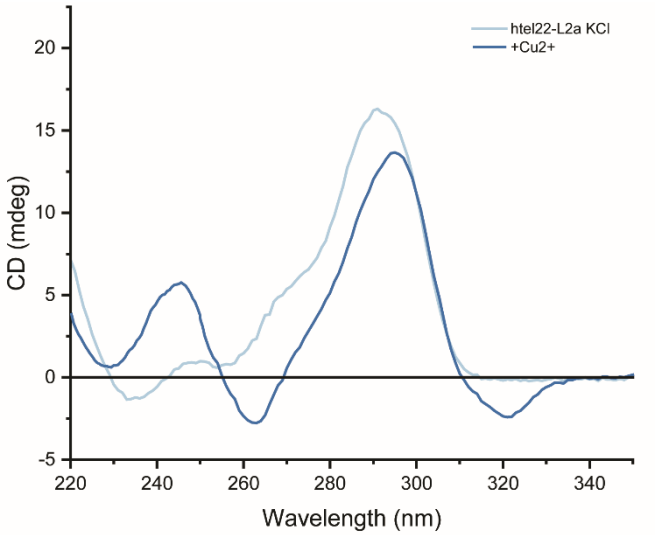

Figure S 31. CD spectrum of FAM-htel22-L2a in absence or presence of Cu^{2+}. Conditions: 4μM DNA, 10mM HEPES, 100mM KCl, 4.4 μM Cu^{2+}.

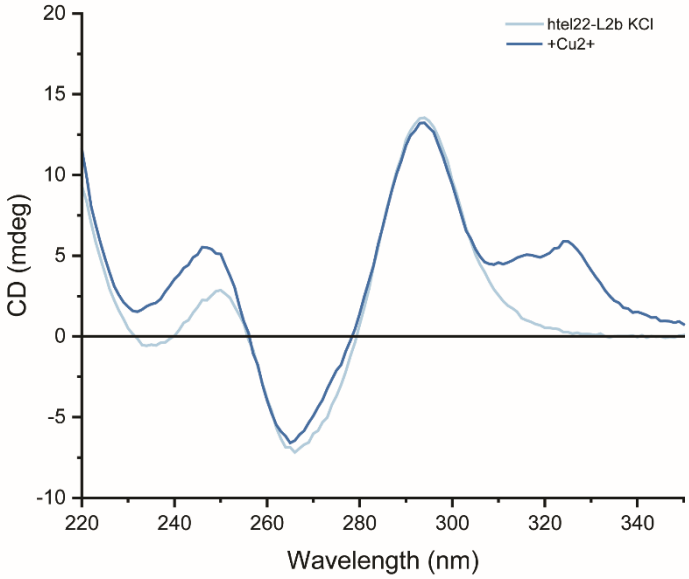

Figure S 32. CD spectrum of FAM-htel22-L2b in absence or presence of Cu^{2+}. Conditions: 4μM DNA, 10mM HEPES, 100mM KCl, 4.4 μM Cu^{2+}.

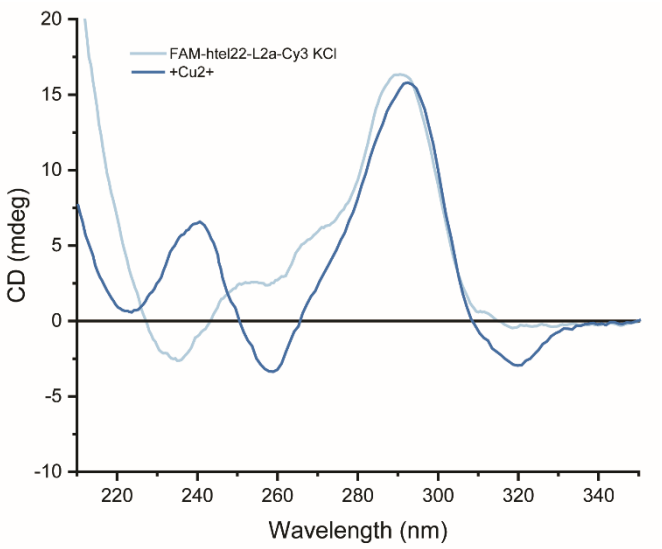

Figure S 33. CD spectrum of FAM-htel22-L2a-Cy3 in absence or presence of Cu^{2+}. Conditions: 4μM DNA, 10mM HEPES, 100mM KCl, 4.4 μM Cu^{2+}.

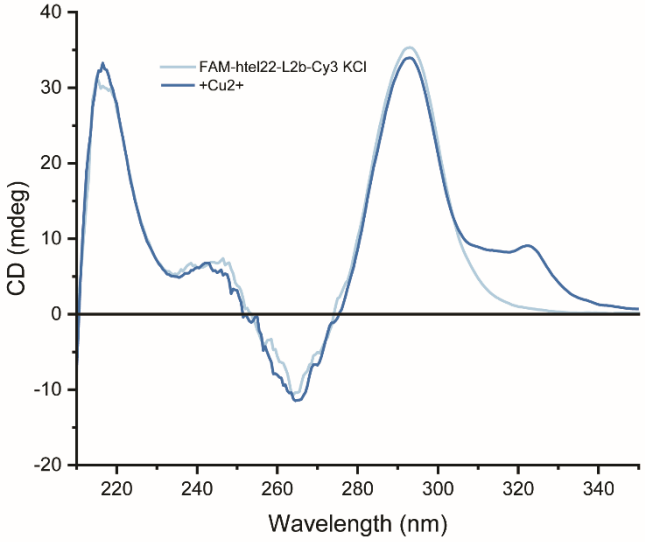

Figure S 34. CD spectrum of FAM-htel22-L2b-Cy3 in absence or presence of Cu^{2+}. Conditions: 4μM DNA, 10mM HEPES, 100mM KCl, 4.4 μM Cu^{2+}.

Htel22-L3a

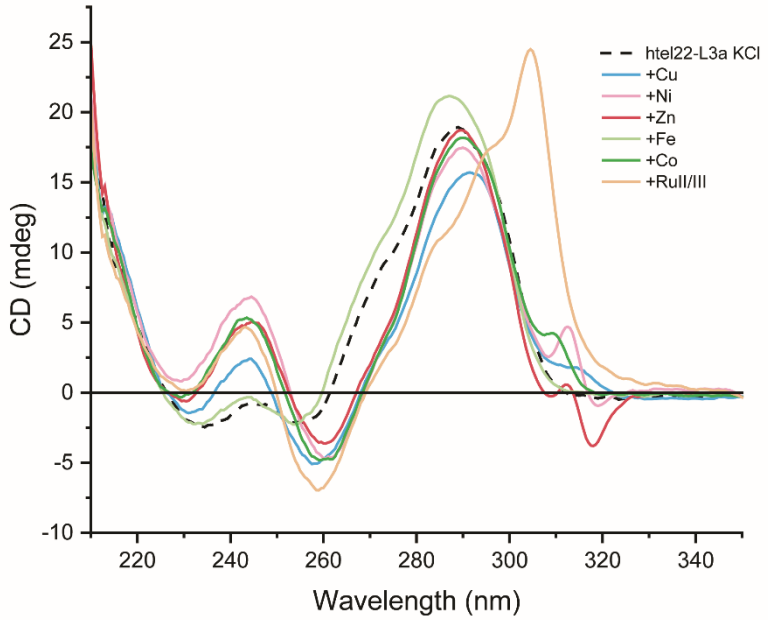

Figure S 35. CD spectrum of htel22-L3a in absence or presence of various divalent metal cations. Conditions: 4μM DNA, 10mM HEPES, 100mM KCl, 4.4 μM M^{2+} (M = Cu, Ni, Zn, Fe, Co, Ru).

Thymine modified cmyc G-quadruplexes

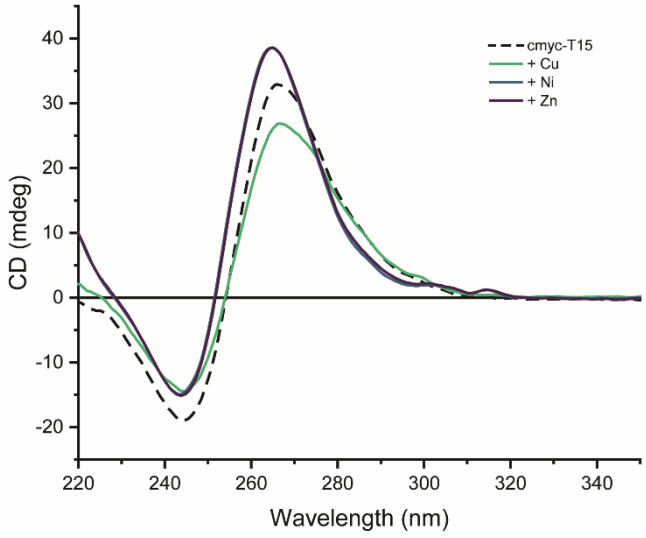

Figure S 36. CD spectrum of **cmyc-T15** in absence or presence of M^{2+} (M = Cu, Ni, Zn). Conditions: 4μM DNA, 10mM HEPES, 100mM KCl, 4.4 μM M^{2+}.

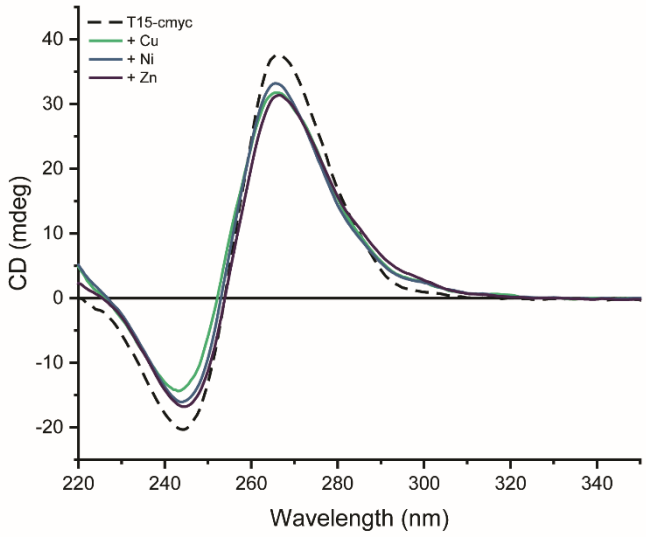

Figure S 37. CD spectrum of **T15-cmyc** in absence or presence of M^{2+} (M = Cu, Ni, Zn). Conditions: 4μM DNA, 10mM HEPES, 100mM KCl, 4.4 μM M^{2+}.

Thymine modified pu22 G-quadruplexes

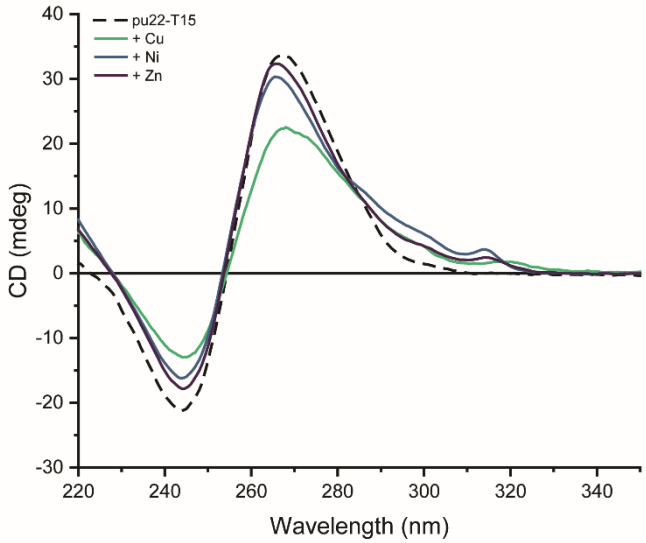

Figure S 38. CD spectrum of **pu22-T15** in absence or presence of M^{2+} (M = Cu, Ni, Zn). Conditions: 4μM DNA, 10mM HEPES, 100mM KCl, 4.4 μM M^{2+}.

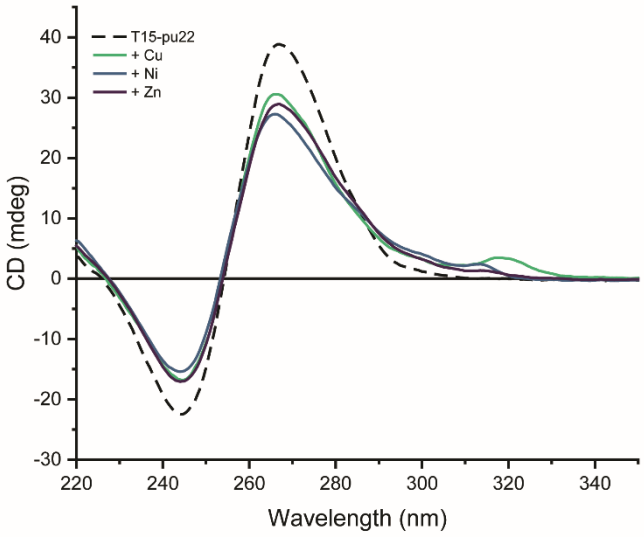

Figure S 39. CD spectrum of **T15-pu22** in absence or presence of M^{2+} (M = Cu, Ni, Zn). Conditions: 4μM DNA, 10mM HEPES, 100mM KCl, 4.4 μM M^{2+}.

Thymine modified htel22 G-quadruplexes

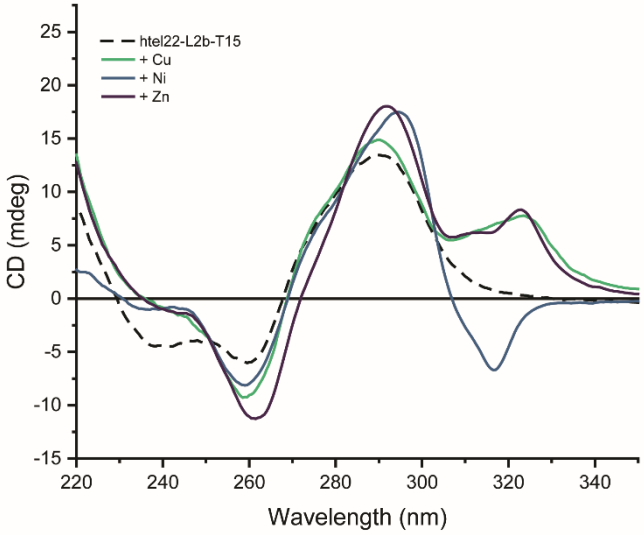

Figure S 40. CD spectrum of **htel22-L2b-T15** in absence or presence of M^{2+} (M = Cu, Ni, Zn). Conditions: 4μM DNA, 10mM HEPES, 100mM KCl, 4.4 μM M^{2+}.

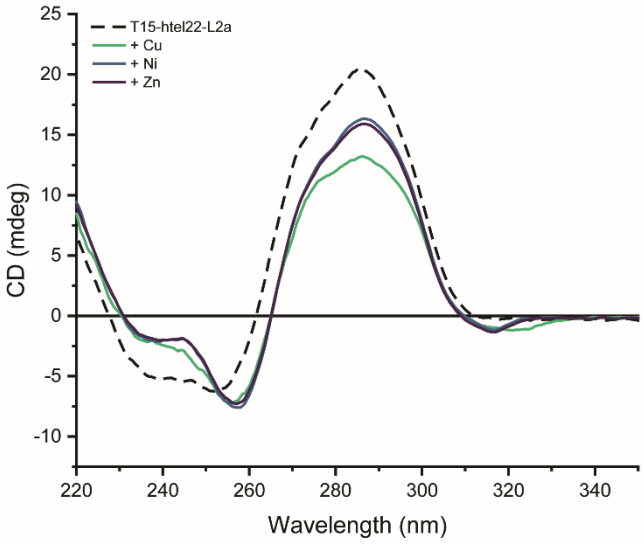

Figure S 41. CD spectrum of **T15-htel22-L2a** in absence or presence of M^{2+} (M = Cu, Ni, Zn). Conditions: 4μM DNA, 10mM HEPES, 100mM KCl, 4.4 μM M^{2+}.

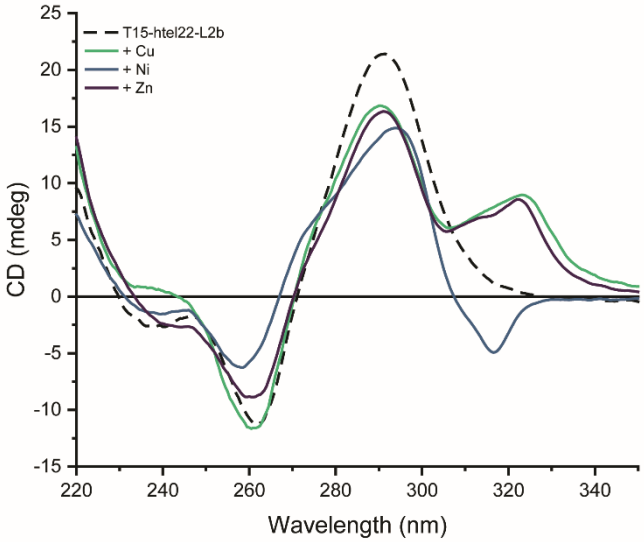

Figure S 42. CD spectrum of **T15-htel22-L2b** in absence or presence of M^{2+} (M = Cu, Ni, Zn). Conditions: 4μM DNA, 10mM HEPES, 100mM KCl, 4.4 μM M^{2+}.

Mass spectrometry

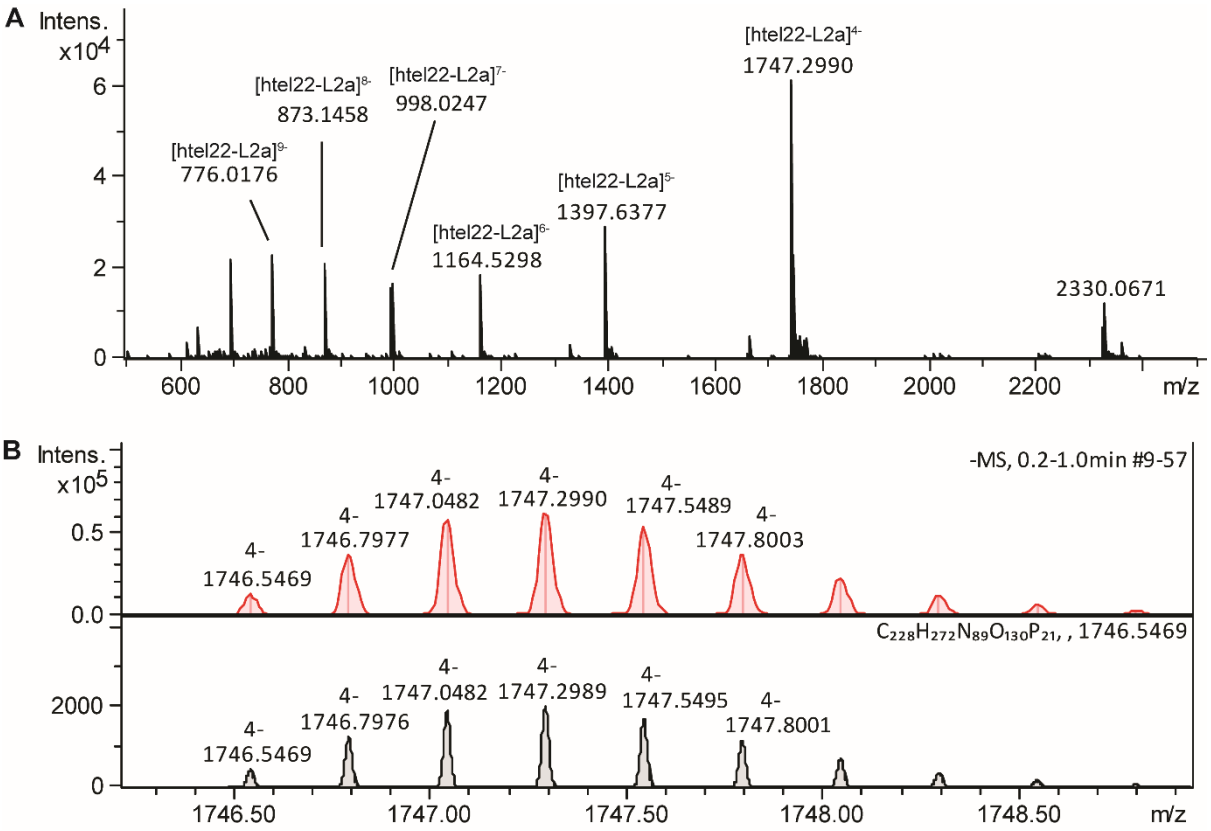

Figure S 43. LC-ESI-MS of htel22-L2a oligonucleotide with BiPy-L1 modification. Conditions: 5μM DNA, 100mM TMAA pH 7.1.

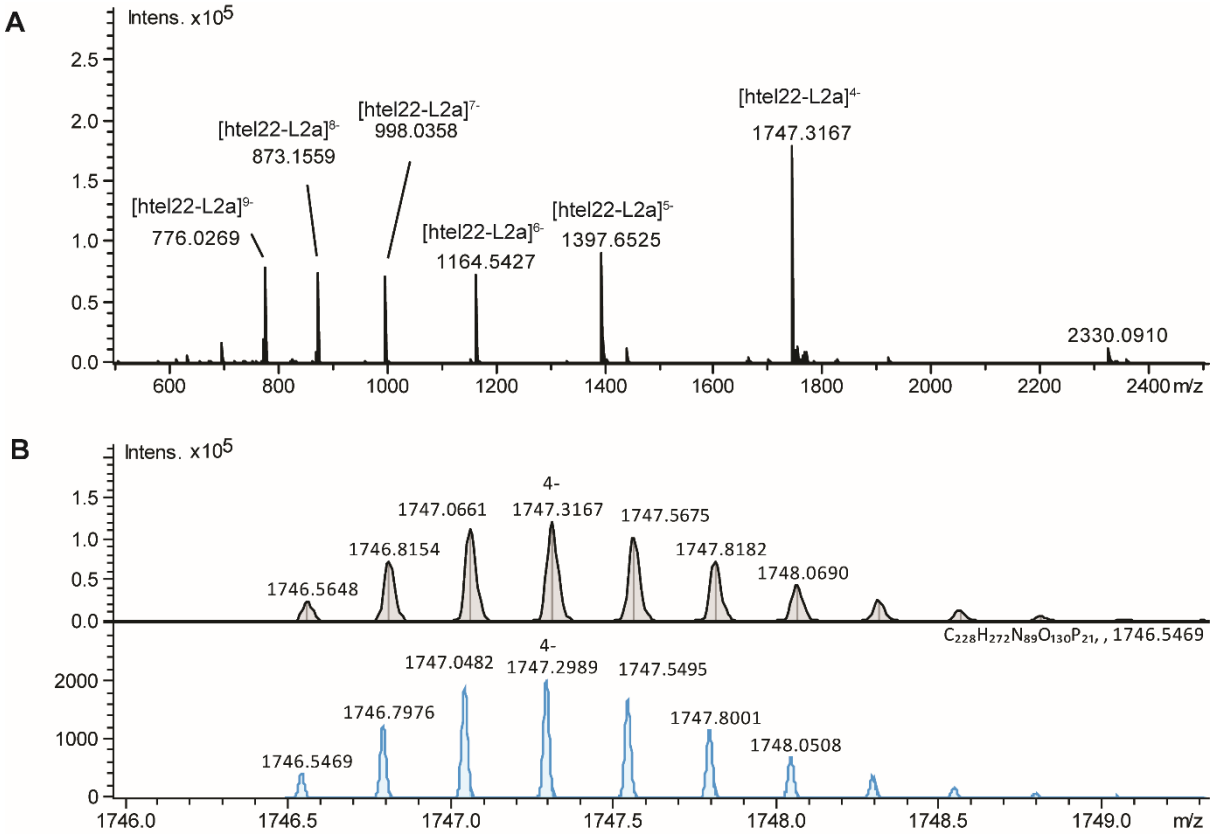

Figure S 44. LC-ESI-MS of htel22-L2a oligonucleotide with BiPy-L2 modification. Conditions: 5μM DNA, 100mM TMAA pH 7.1.

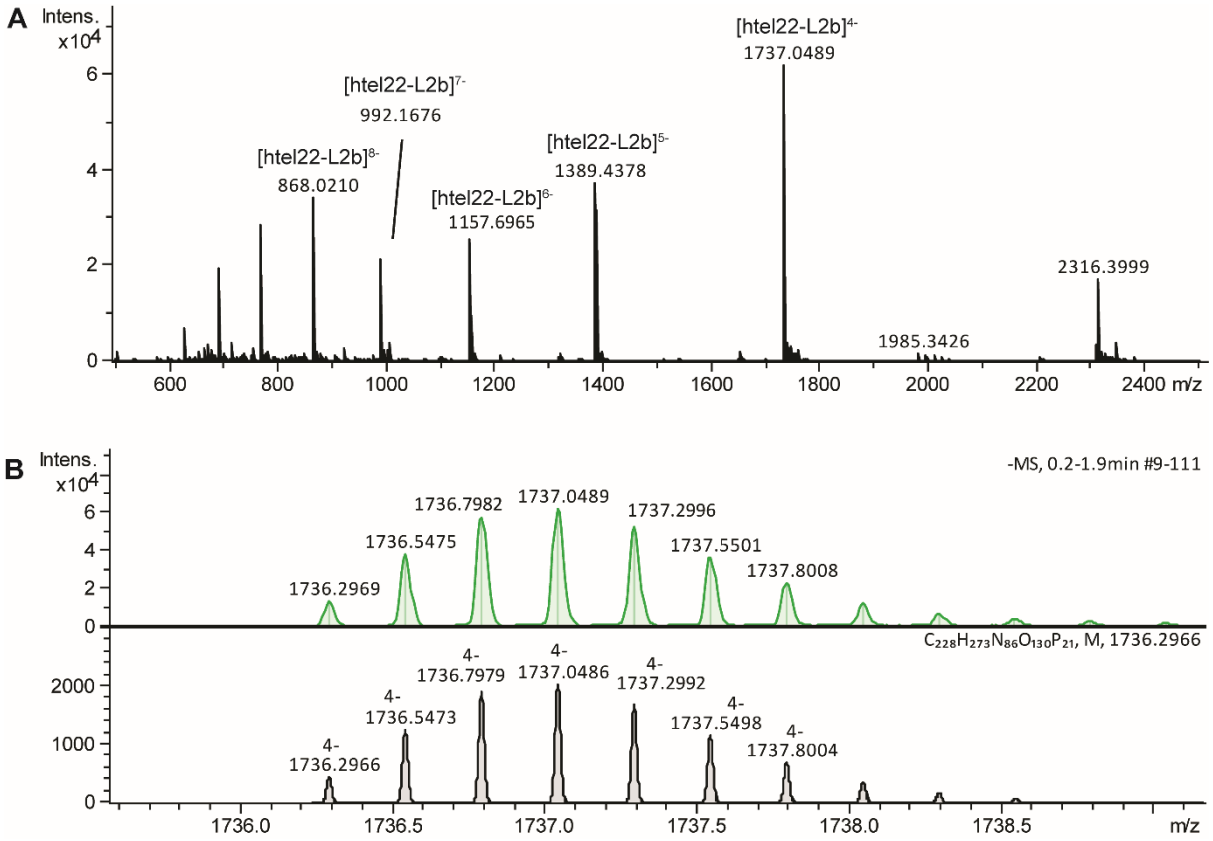

Figure S 45. LC-ESI-MS of htel22-L2b oligonucleotide with BiPy-L1 modification. Conditions: 5μM DNA, 100mM TMAA pH 7.1.

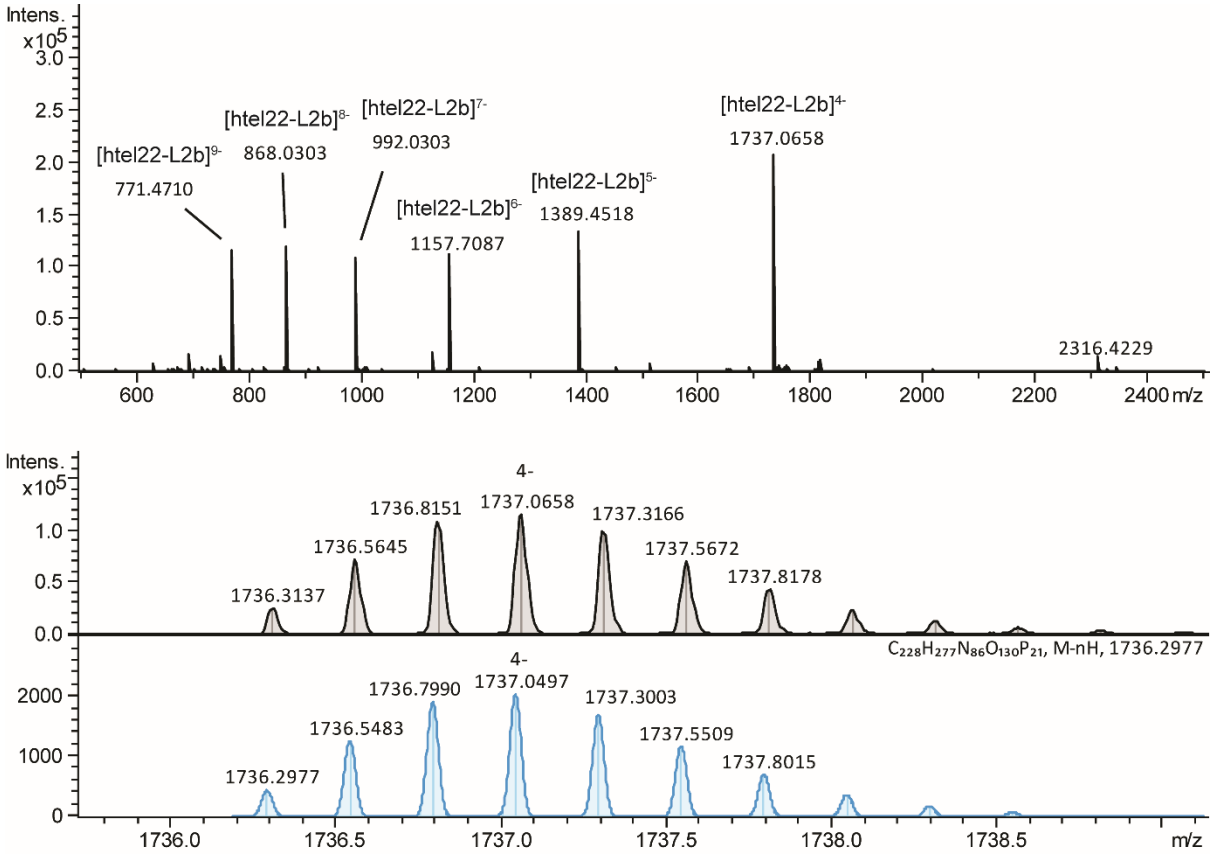

Figure S 46. LC-ESI-MS of htel22-L2b oligonucleotide with BiPy-L2 modification. Conditions: 5μM DNA, 100mM TMAA pH 7.1.

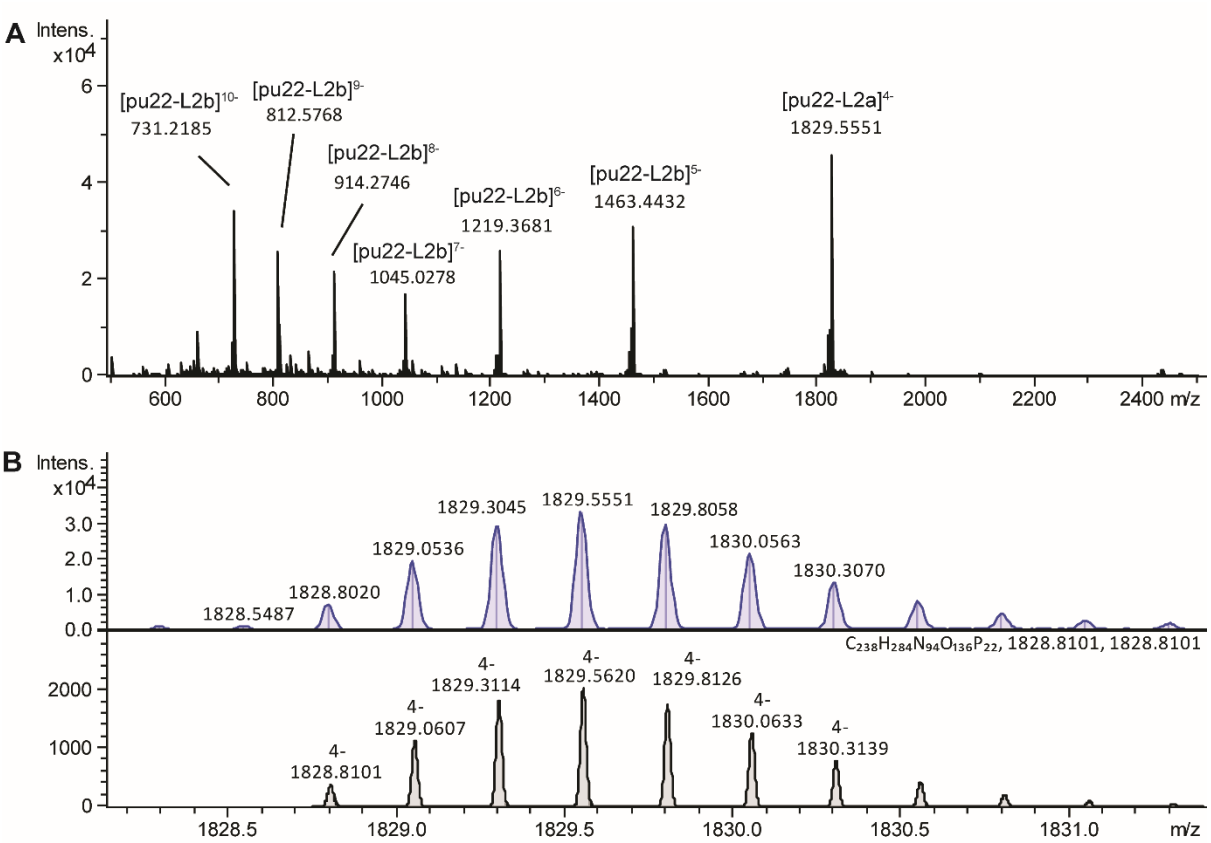

Figure S 47. LC-ESI-MS of pu22-L2a oligonucleotide. Conditions: 5μM DNA, 100mM TMAA pH 7.1.

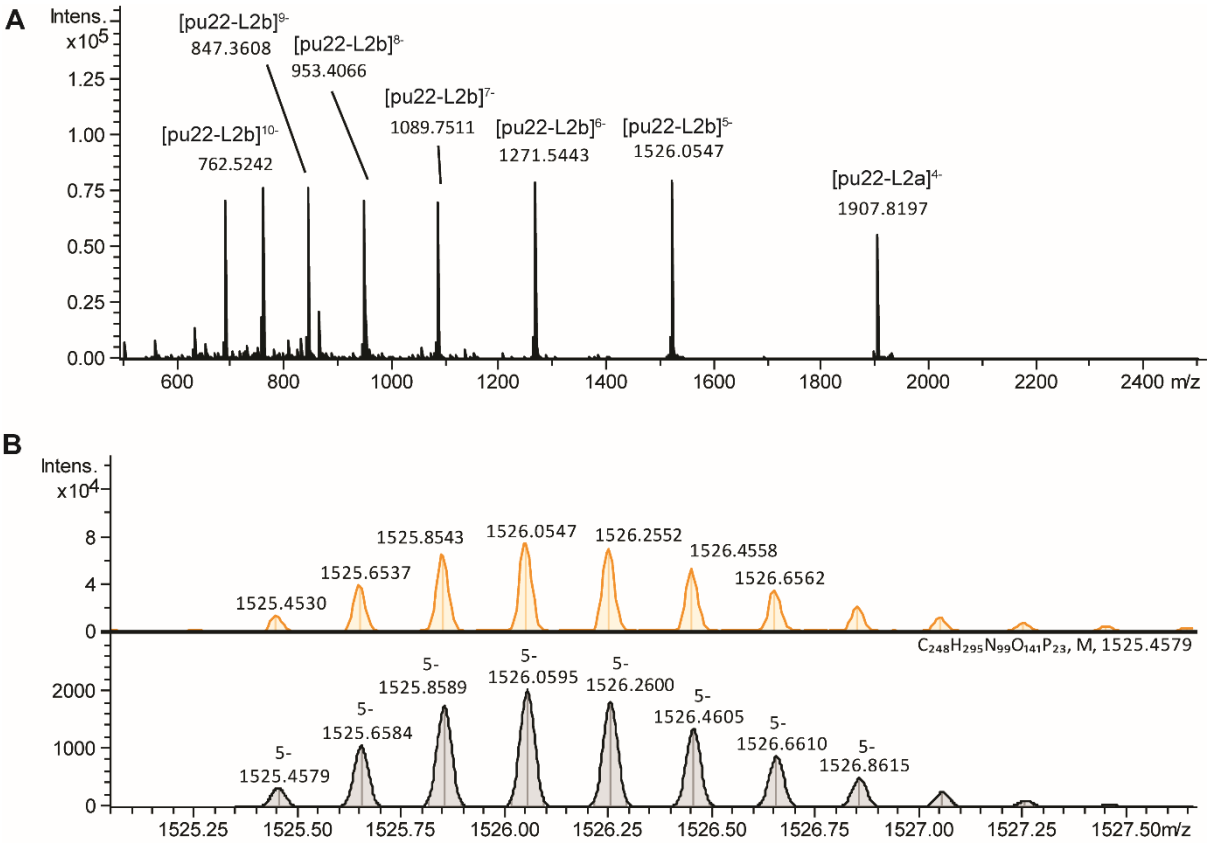

Figure S 48. LC-ESI-MS of pu22-L2b oligonucleotide. Conditions: 5μM DNA, 100mM TMAA pH 7.1

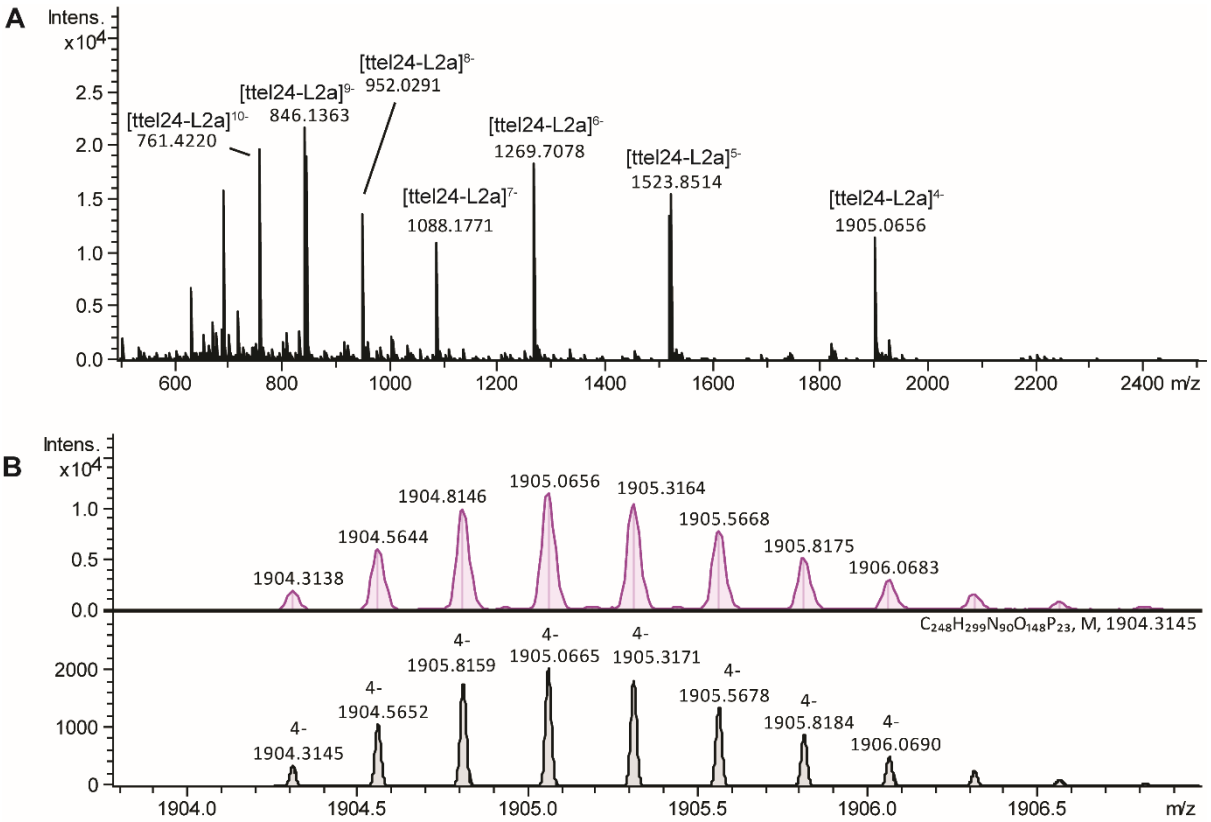

Figure S 49. LC-ESI-MS of ttel24-L2a oligonucleotide with BiPy-L1 modification. Conditions: 5μM DNA, 100mM TMAA pH 7.1.

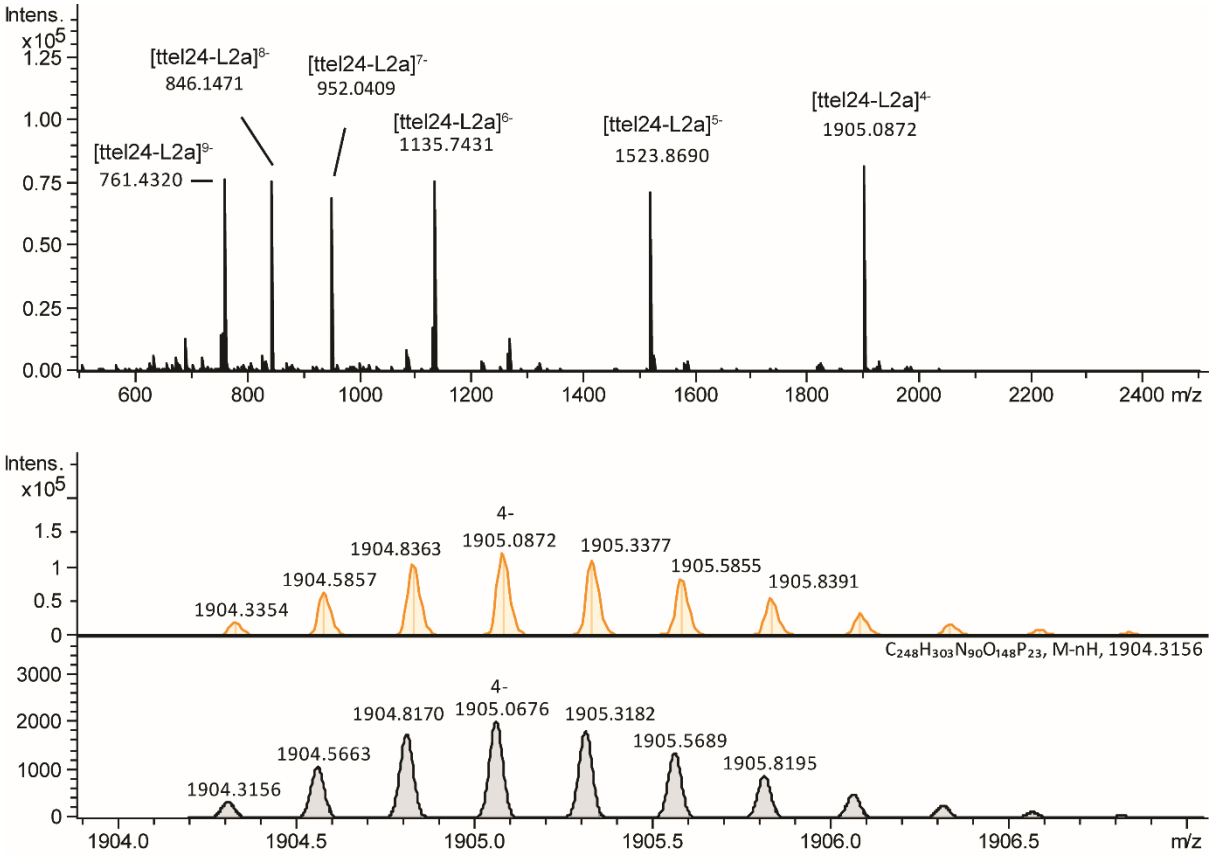

Figure S 50. LC-ESI-MS of ttel24-L2a oligonucleotide with BiPy-L2 modification. Conditions: 5μM DNA, 100mM TMAA pH 7.1.

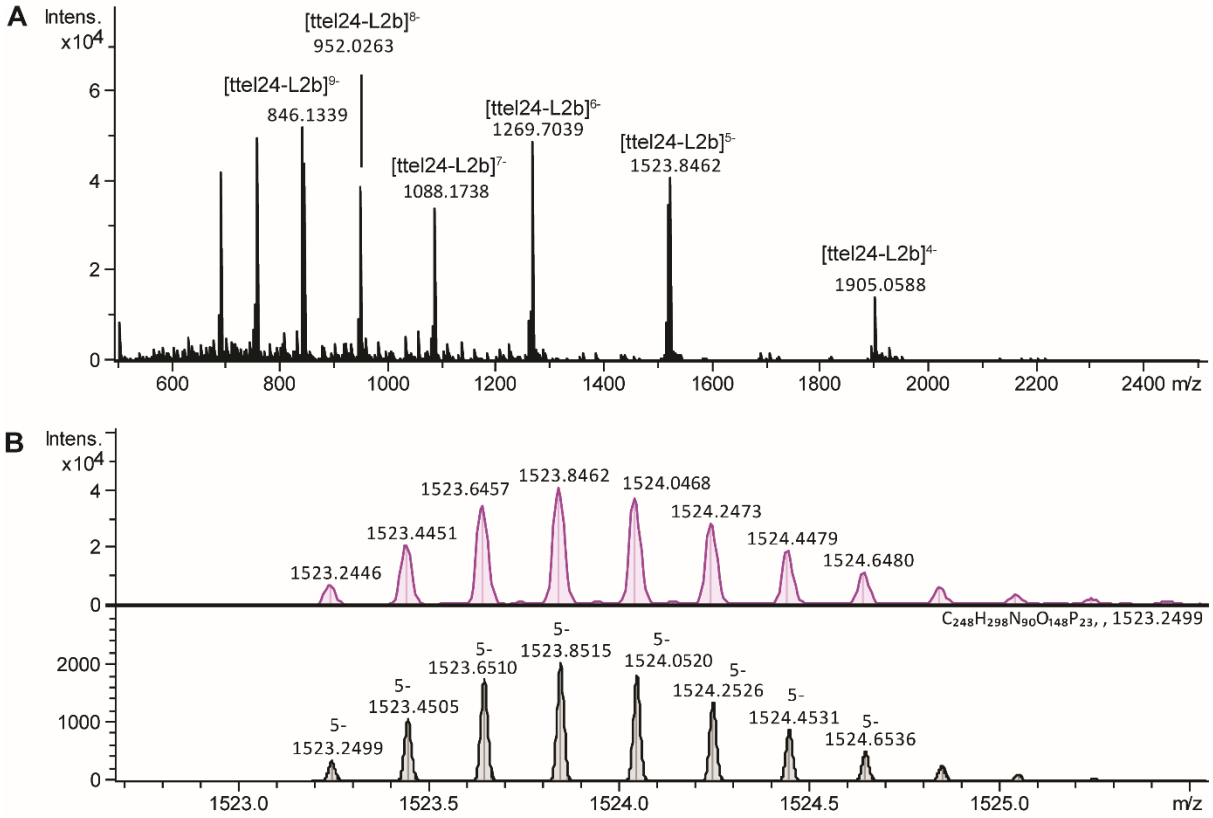

Figure S 51. LC-ESI-MS of ttel24-L2b oligonucleotide. Conditions: 5µM DNA, 100mM TMAA pH 7.1.

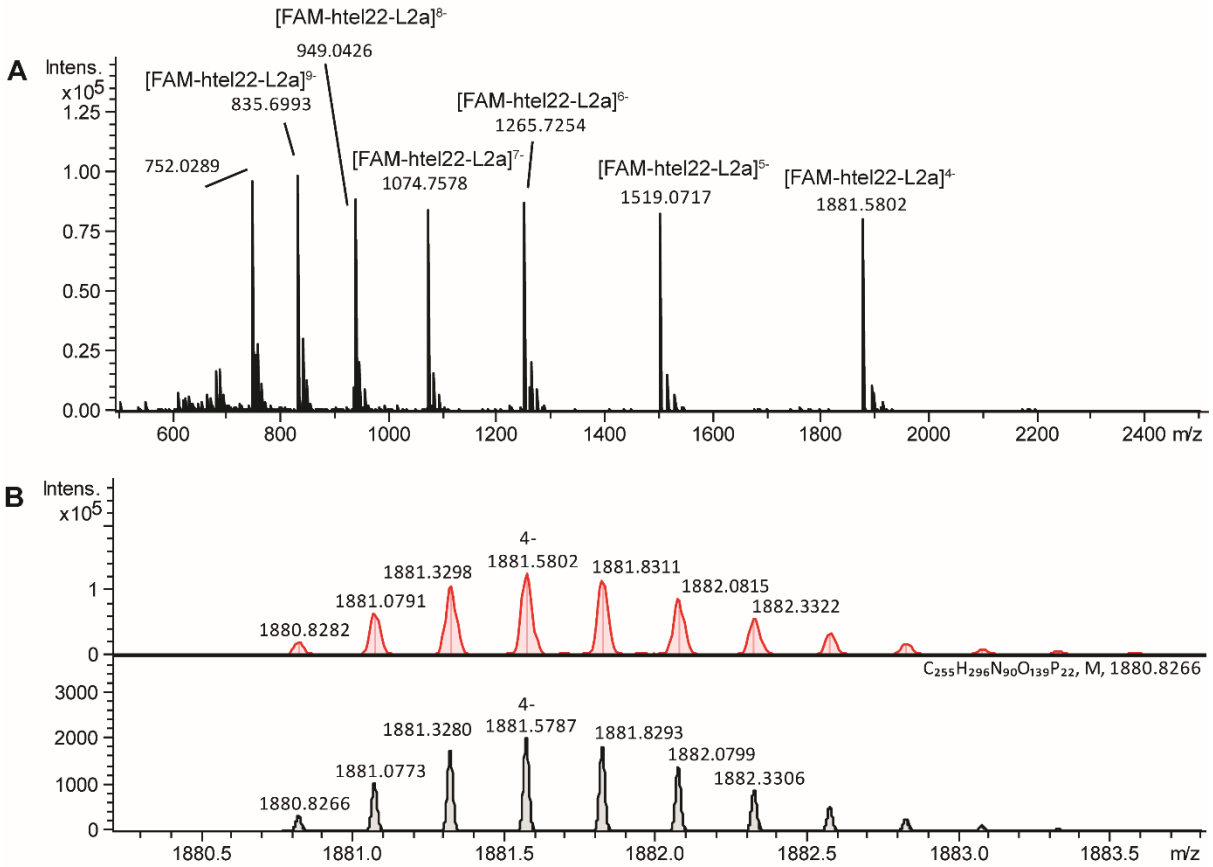

Figure S 52. LC-ESI-MS of FAM-htel22-L2a oligonucleotide. Conditions: 5μM DNA, 100mM TMAA pH 7.1.

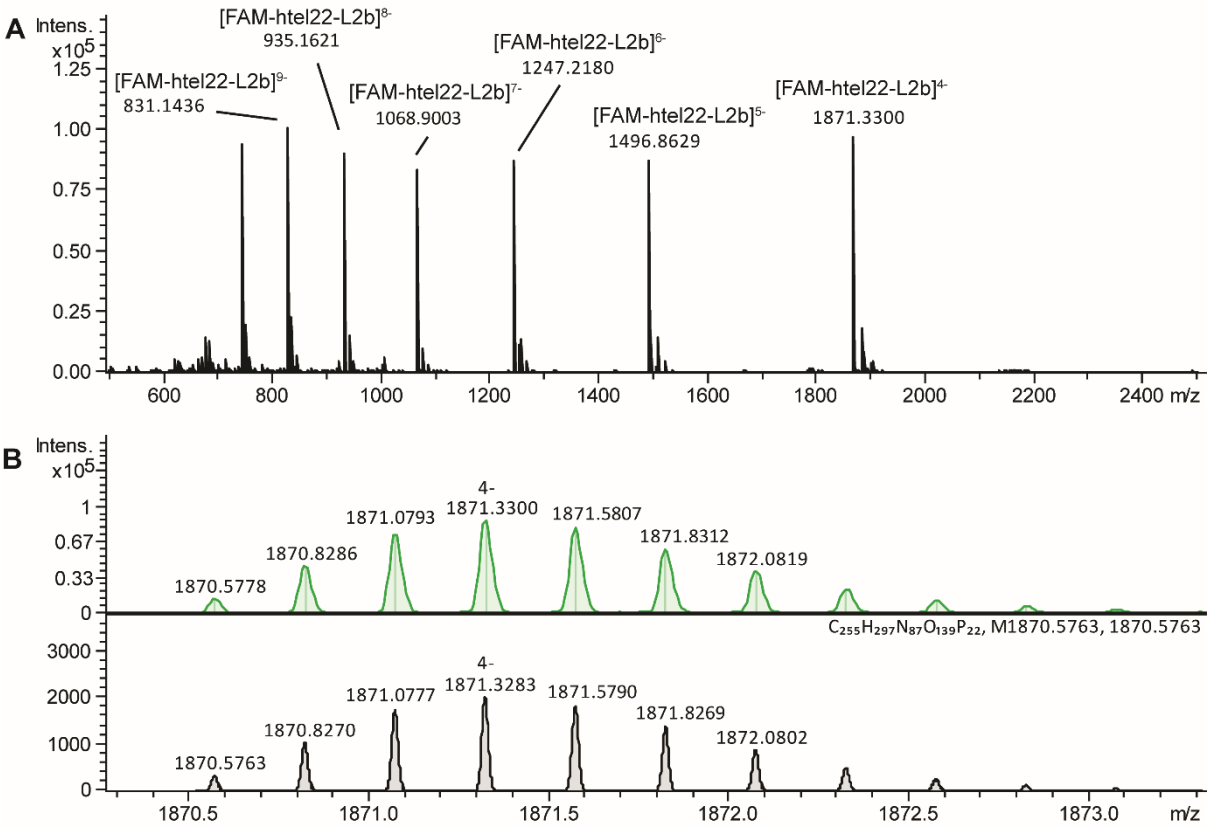

Figure S 53. LC-ESI-MS of FAM-htel22-L2b oligonucleotide. Conditions: 5µM DNA, 100mM TMAA pH 7.1.

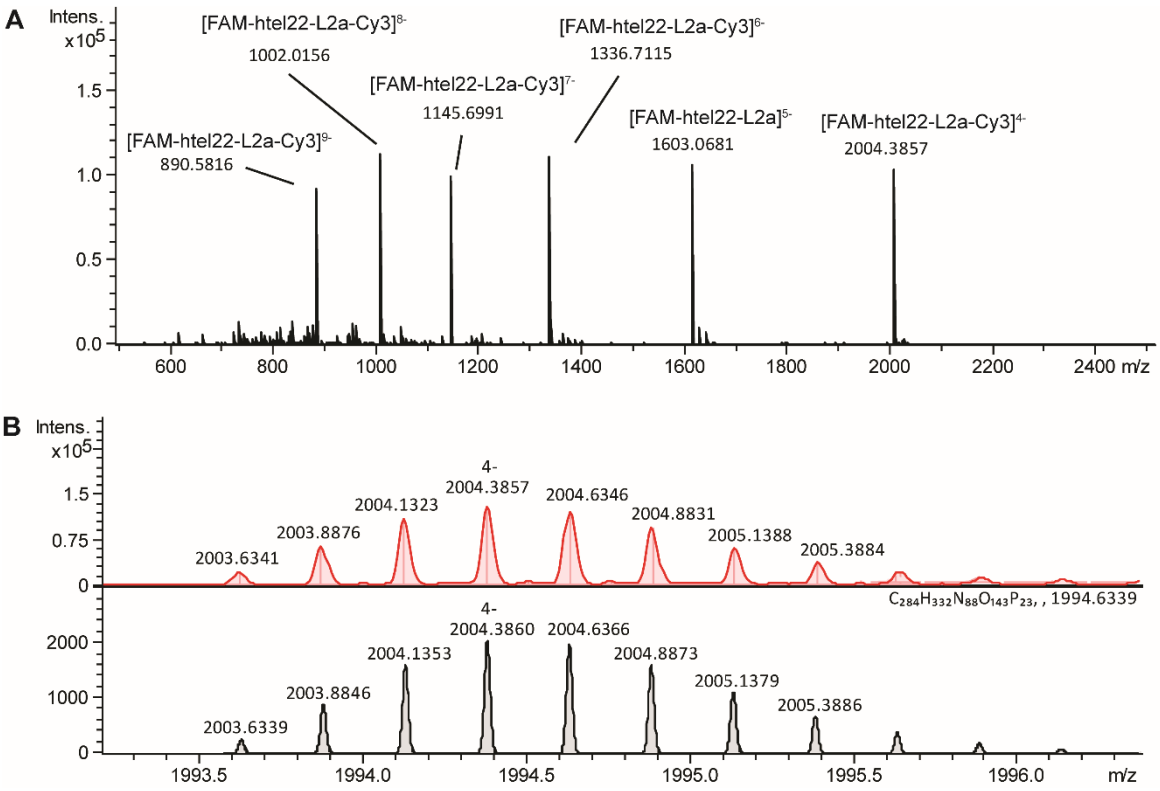

Figure S 54. LC-ESI-MS of FAM-htel22-L2a-Cy3 oligonucleotide. Conditions: 5µM DNA, 100mM TMAA pH 7.1.

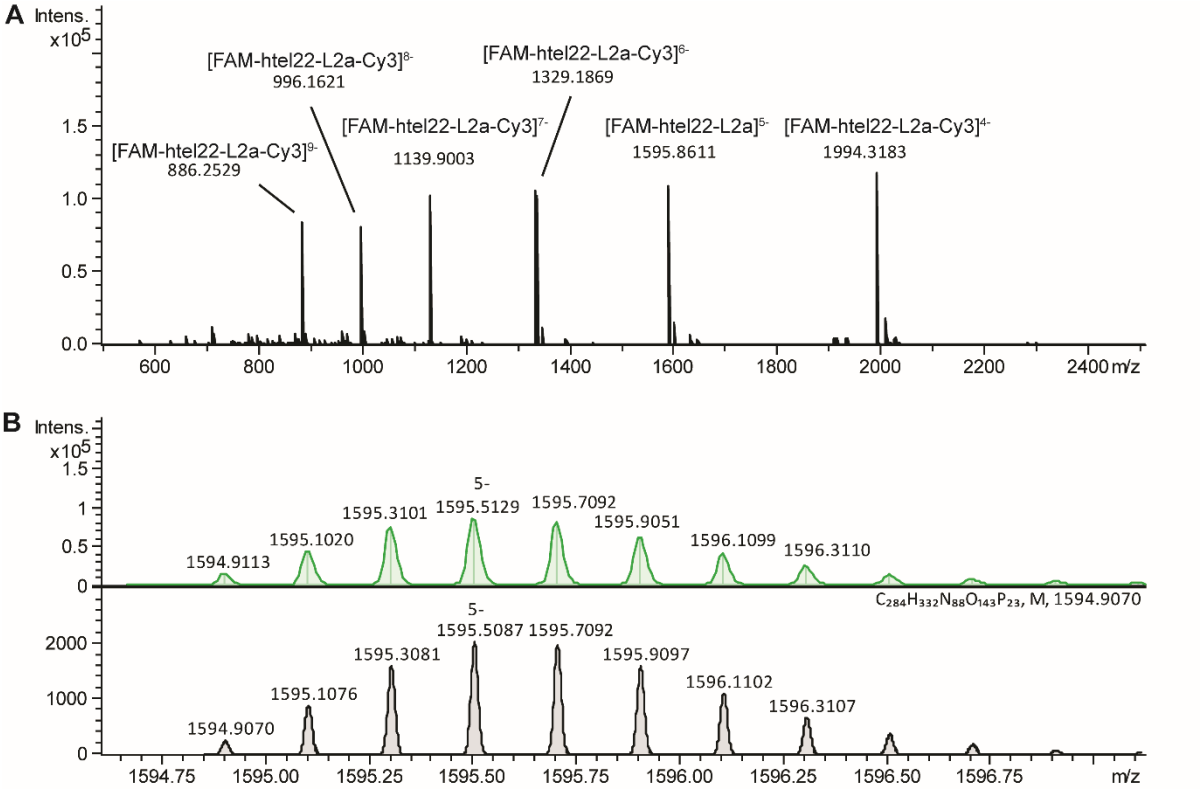

Figure S 55. LC-ESI-MS of FAM-htel22-L2b-Cy3 oligonucleotide. Conditions: 5µM DNA, 100mM TMAA pH 7.1.

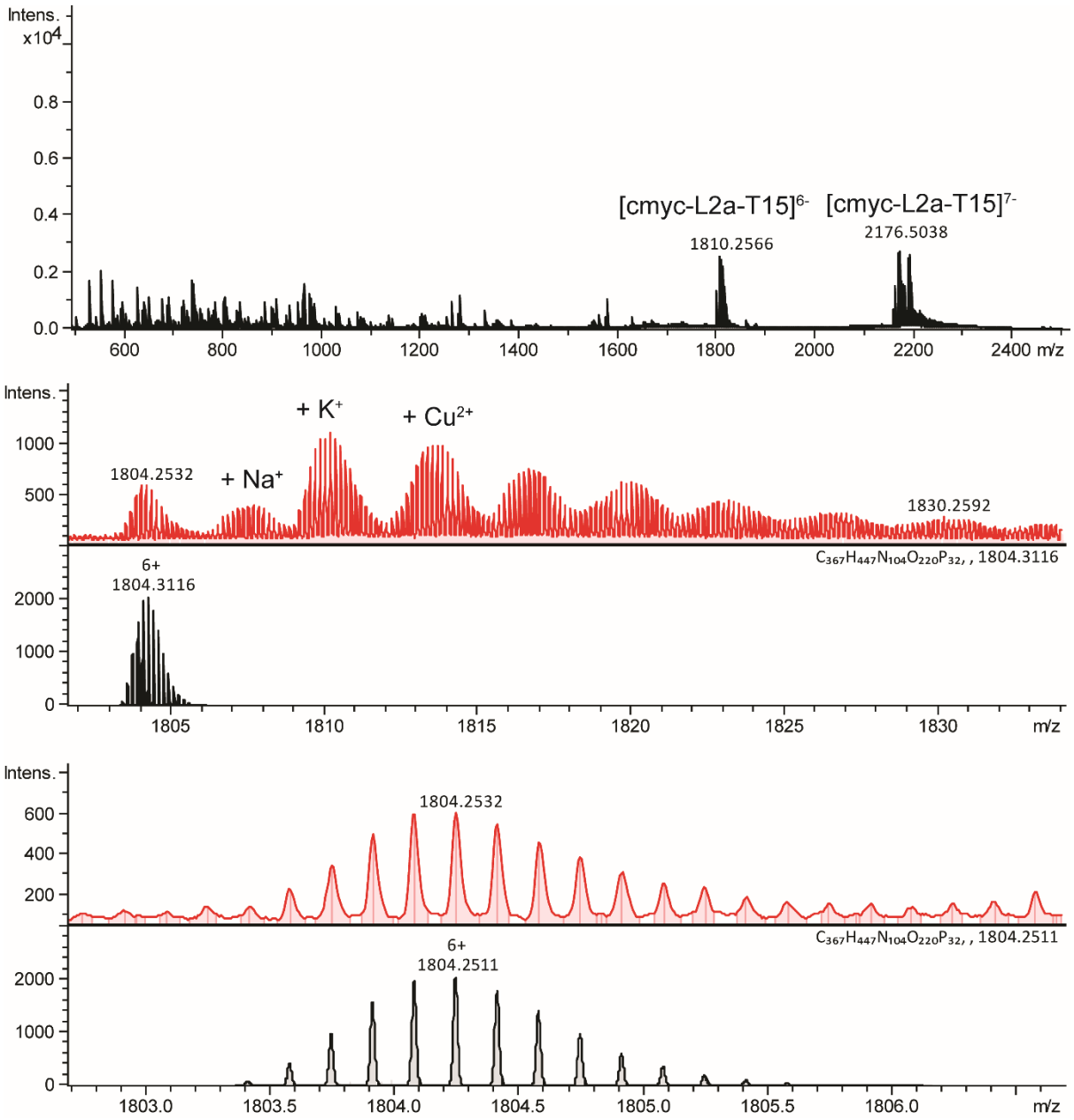

Figure S 56. LC-ESI-MS of cmyc-L2a-T15 oligonucleotide. Conditions: 5μM DNA, 100mM TMAA pH 7.1.

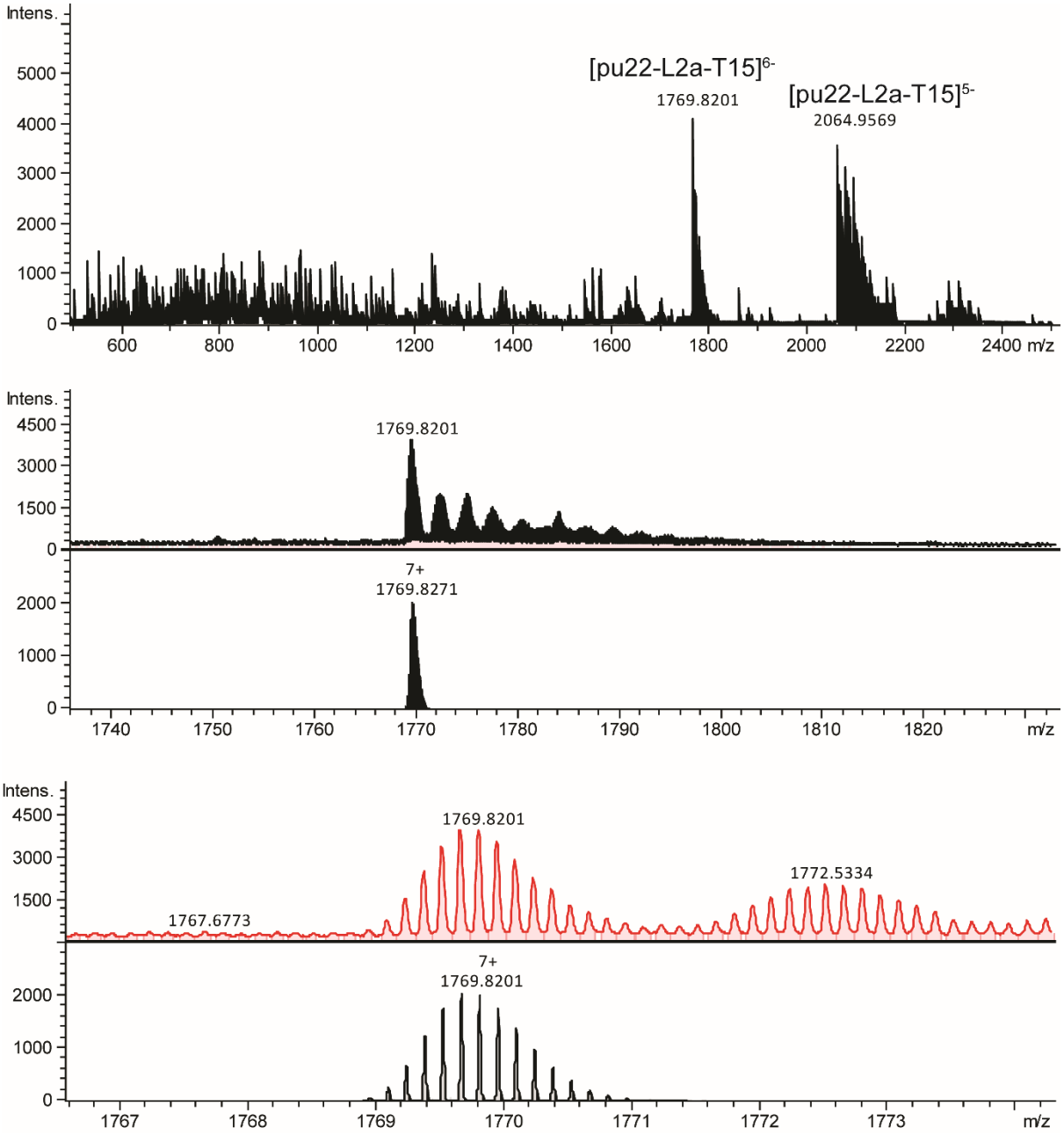

Figure S 57. LC-ESI-MS of pu22-L2a-T15 oligonucleotide. Conditions: 5μM DNA, 100mM TMAA pH 7.1.

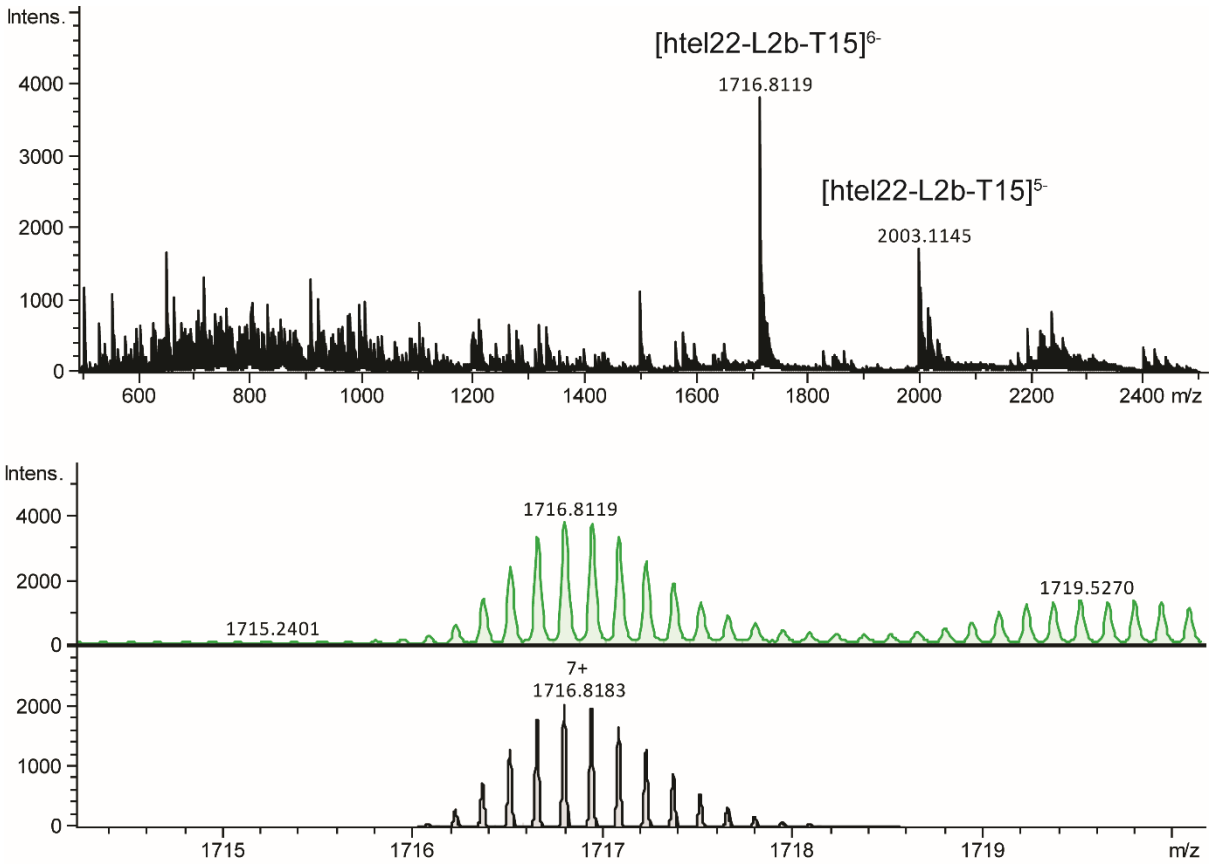

Figure S 58. LC-ESI-MS of htel22-L2b-T15 oligonucleotide. Conditions: 5μM DNA, 100mM TMAA pH 7.1.

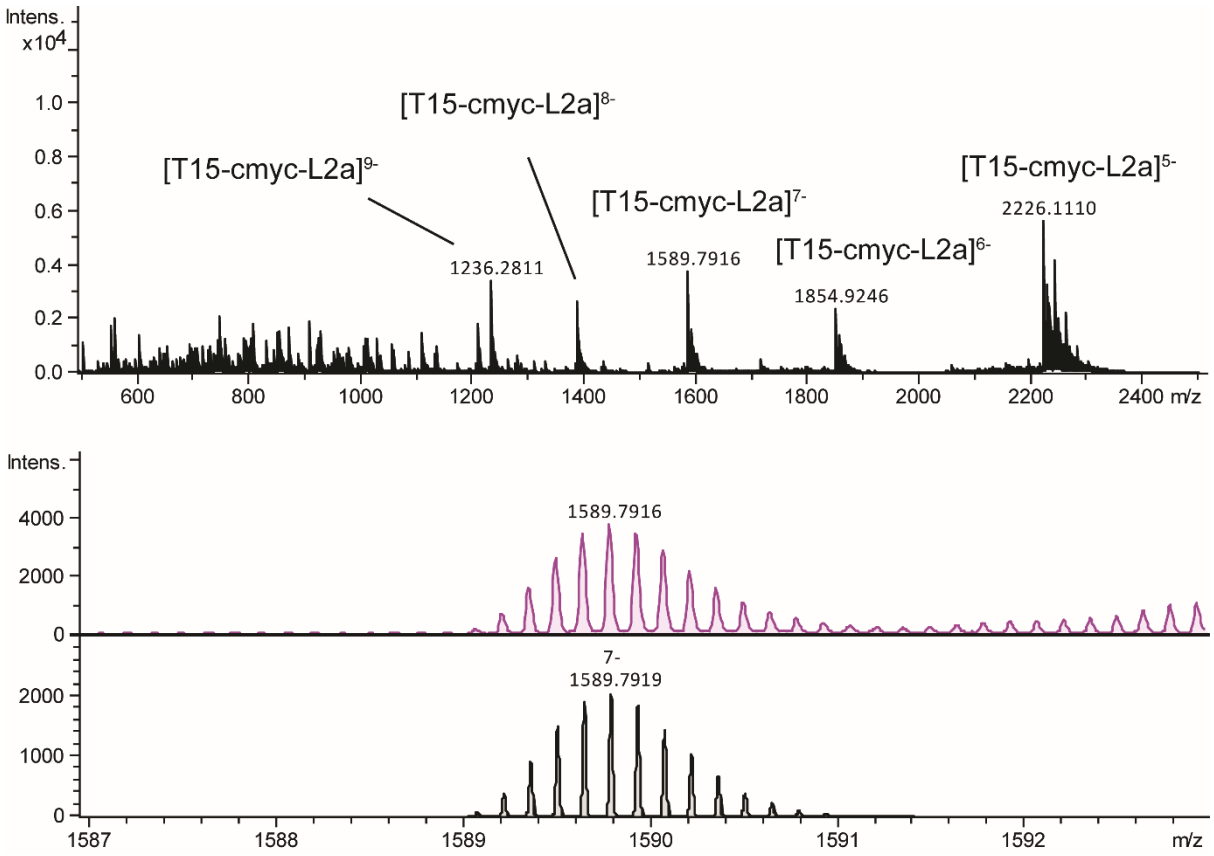

Figure S 59. LC-ESI-MS of T15-cmyc-L2a oligonucleotide. Conditions: 5μM DNA, 100mM TMAA pH 7.1.

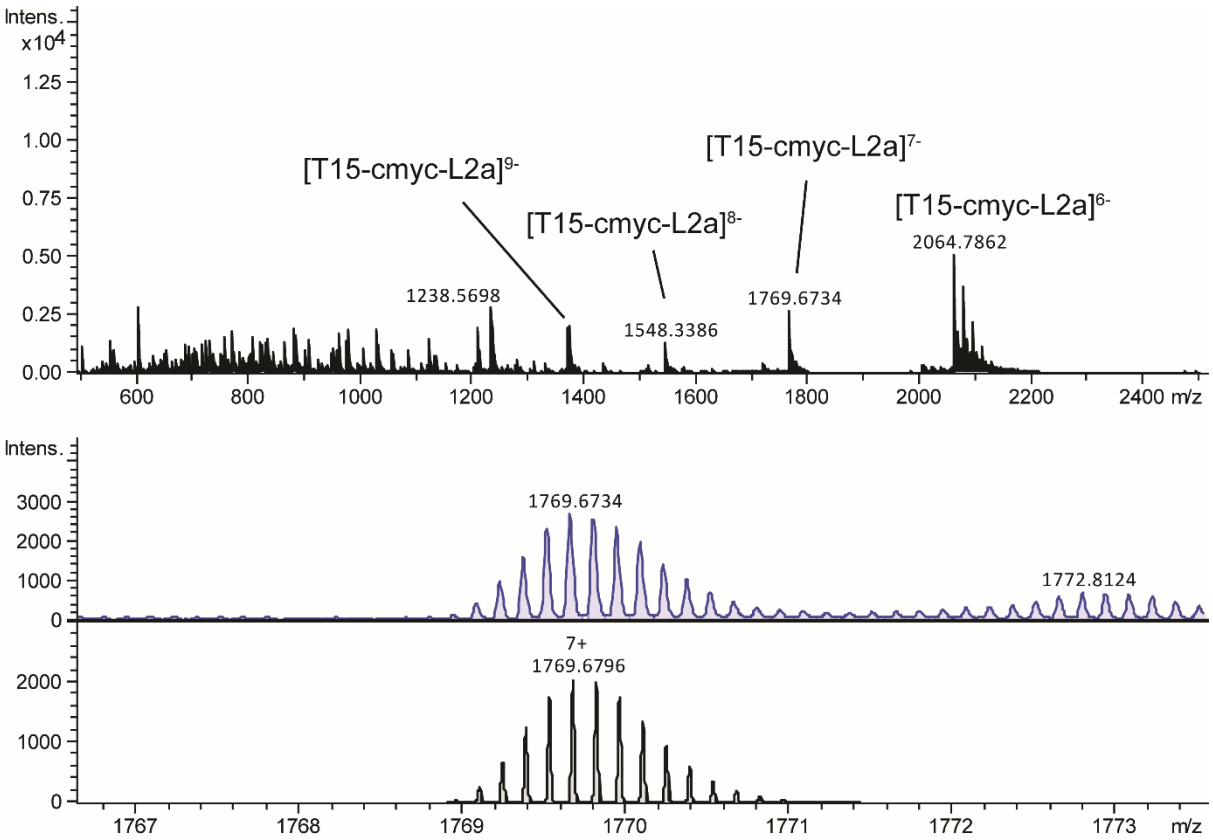

Figure S 60. LC-ESI-MS of T15-pu22-L2a oligonucleotide. Conditions: 5μM DNA, 100mM TMAA pH 7.1.

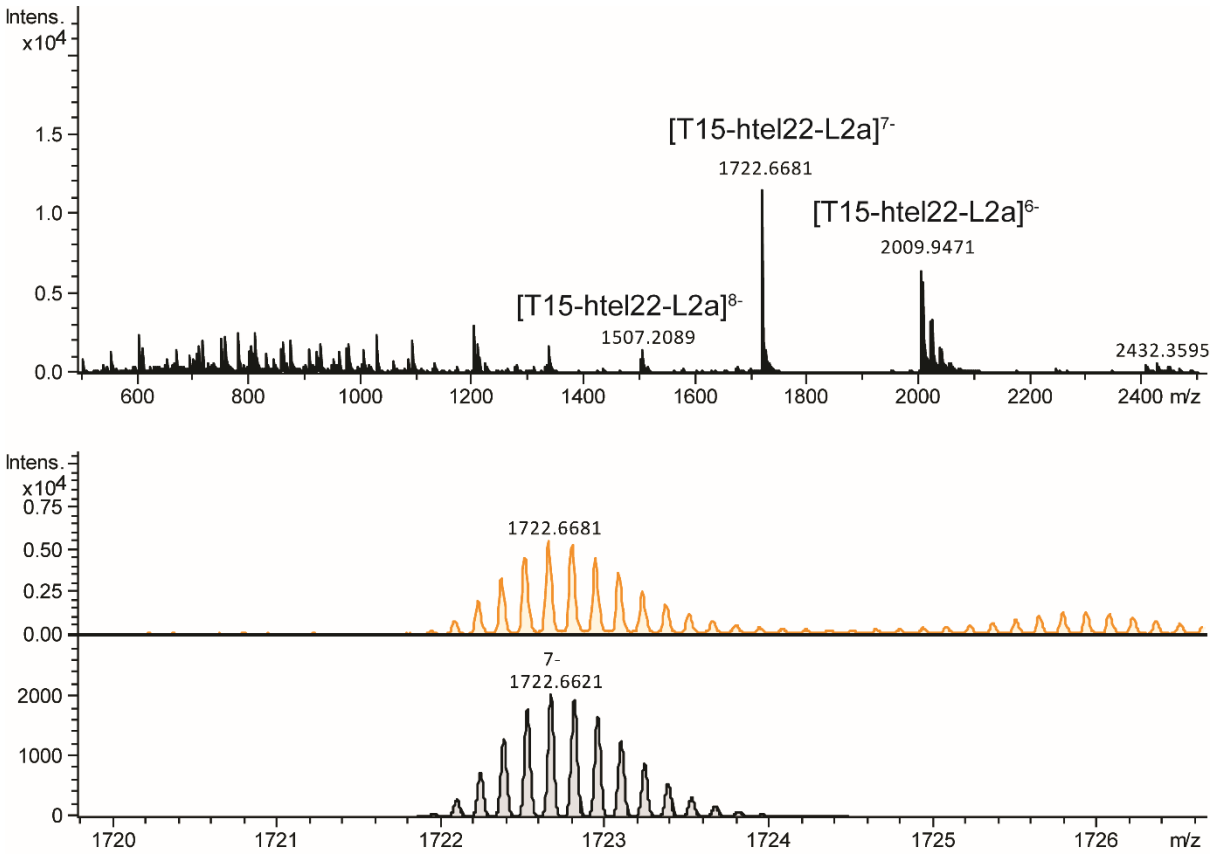

Figure S 61. LC-ESI-MS of T15-htel22-L2a oligonucleotide. Conditions: 5μM DNA, 100mM TMAA pH 7.1.

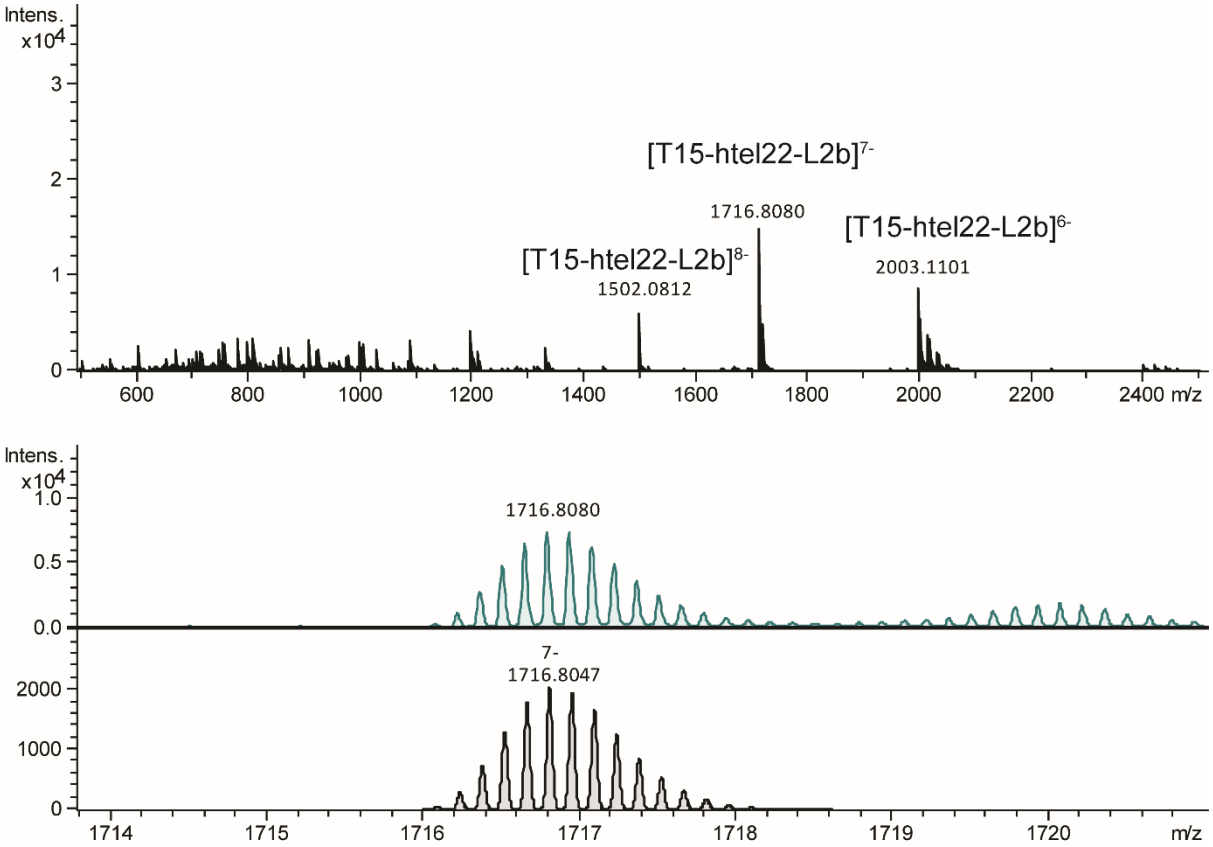

Figure S 62. LC-ESI-MS of T15-htel22-L2b oligonucleotide. Conditions: 5μM DNA, 100mM TMAA pH 7.1.

Native Mass spectrometry

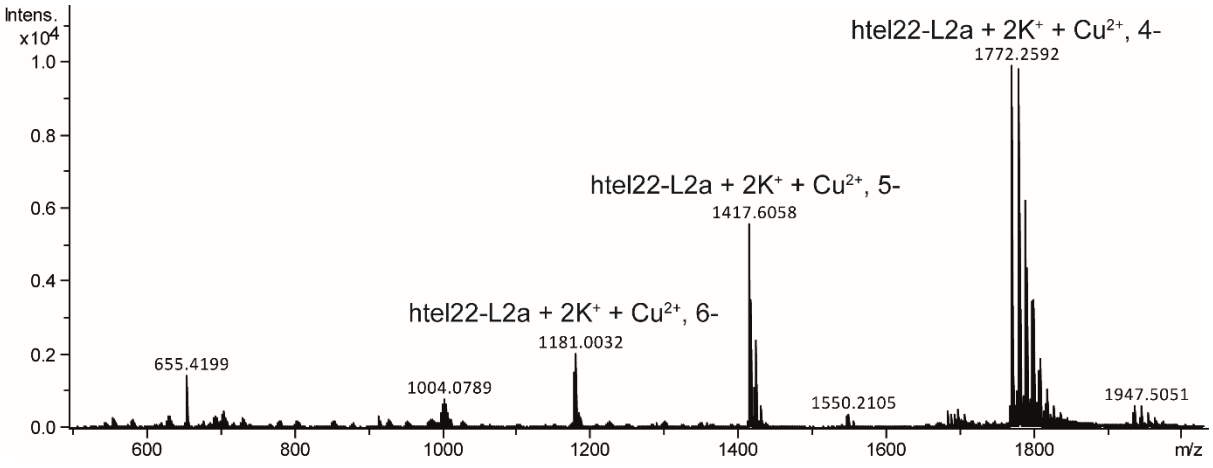

Figure S 63. Native ESI-MS of htel22-L2a with BiPy-L1 modification in presence of Cu^{2+}. Conditions: 12.5 μM DNA, 15 μM $CuSO_4$, 0.5 mM KCl, 50 mM TMAA pH 7.1, H_2O:ACN, 1:1.

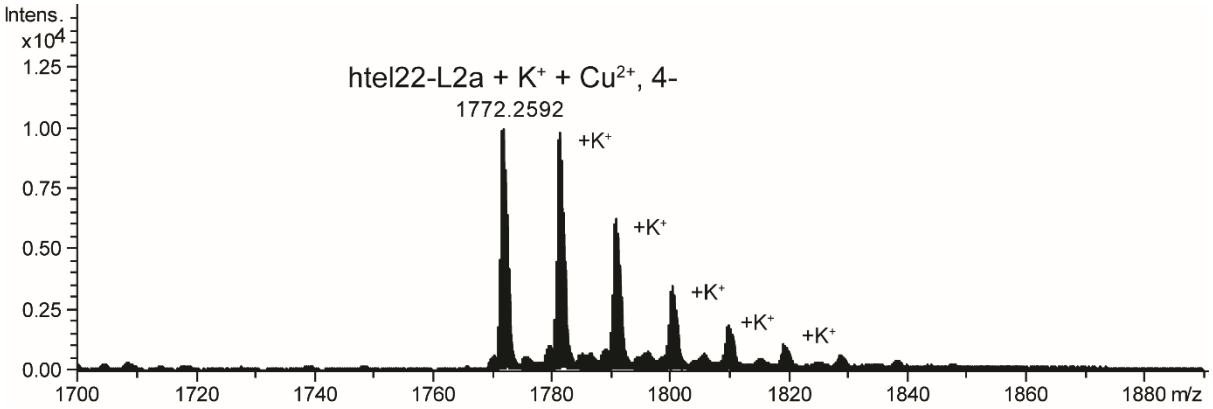

Figure S 64. Zoom of native ESI-MS of htel22-L2a with BiPy-L1 modification in presence of Cu^{2+}. Conditions: 12.5 µM DNA, 15 µM $CuSO_4$, 0.5 mM KCl, 50 mM TMAA pH 7.1, H_2O:ACN, 1:1.

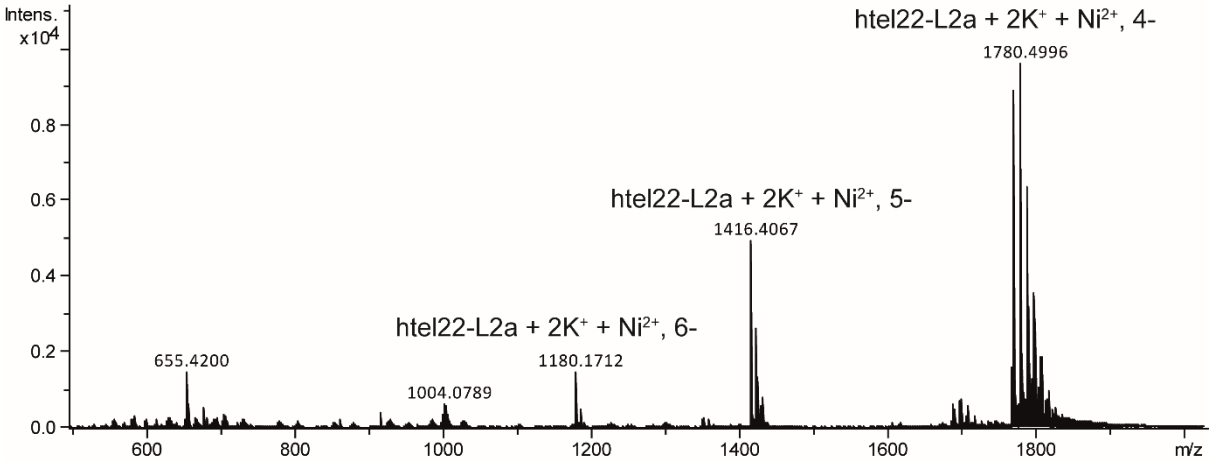

Figure S 65. Native ESI-MS of htel22-L2a with BiPy-L1 modification in presence of Ni^{2+}. Conditions: 12.5 µM DNA, 15 µM $CuSO_4$, 0.5 mM KCl, 50 mM TMAA pH 7.1, H_2O:ACN, 1:1.

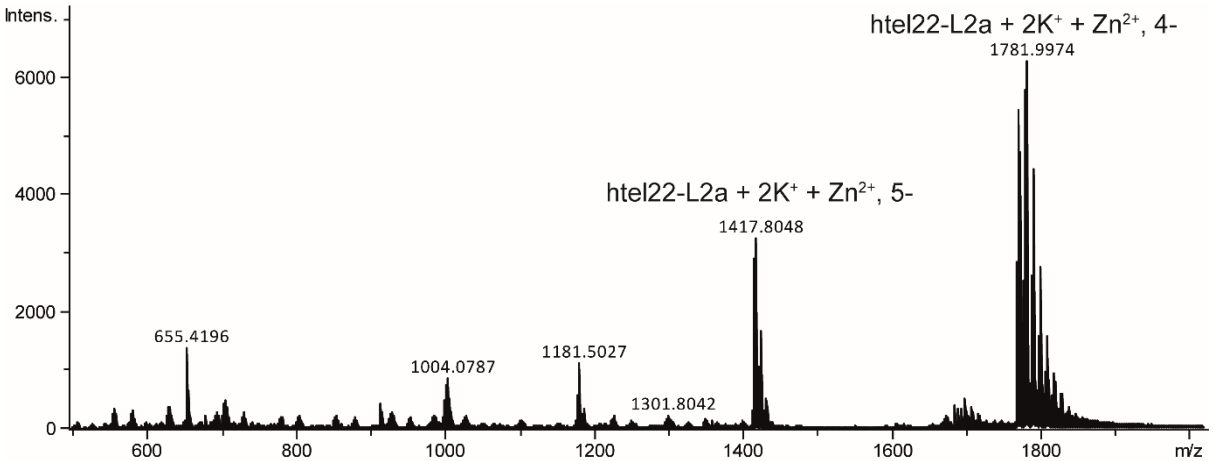

Figure S 66. Native ESI-MS of htel22-L2a with BiPy-L1 modification in presence of Zn^{2+}. Conditions: 12.5 µM DNA, 15 µM $CuSO_4$, 0.5 mM KCl, 50 mM TMAA pH 7.1, H_2O:ACN, 1:1.

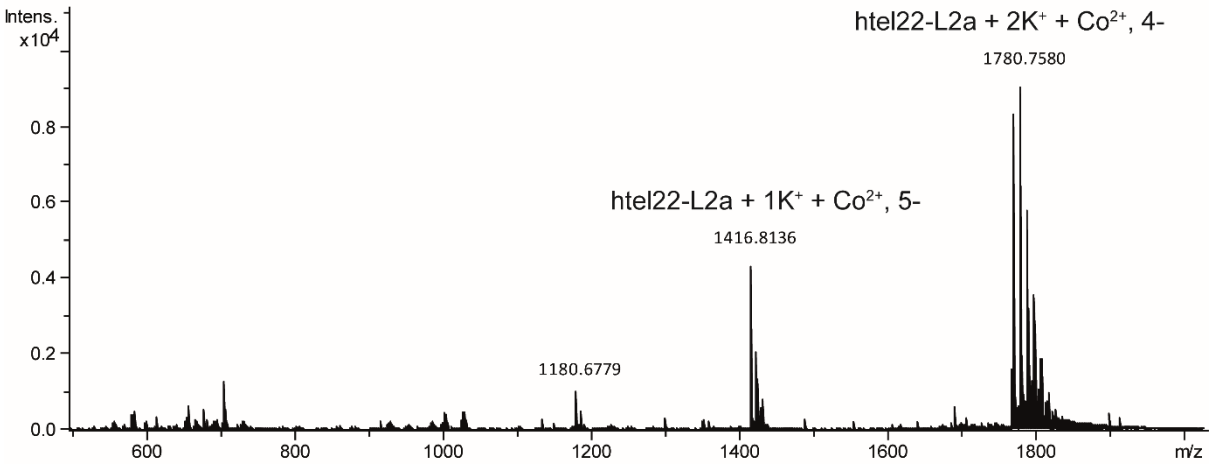

Figure S 67. Native ESI-MS of htel22-L2a with BiPy-L1 modification in presence of Co^{2+}. Conditions: 12.5 µM DNA, 15 µM $CuSO_4$, 0.5 mM KCl, 50 mM TMAA pH 7.1, H_2O:ACN, 1:1.

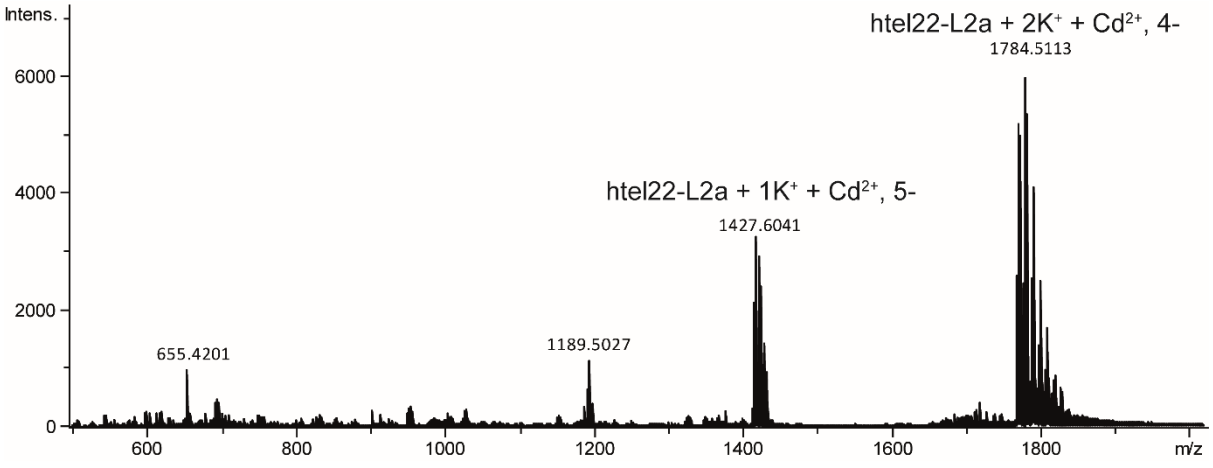

Figure S 68. Native ESI-MS of htel22-L2a with BiPy-L1 modification in presence of Cd^{2+}. Conditions: 12.5 µM DNA, 15 µM $CuSO_4$, 0.5 mM KCl, 50 mM TMAA pH 7.1, H_2O:ACN, 1:1.

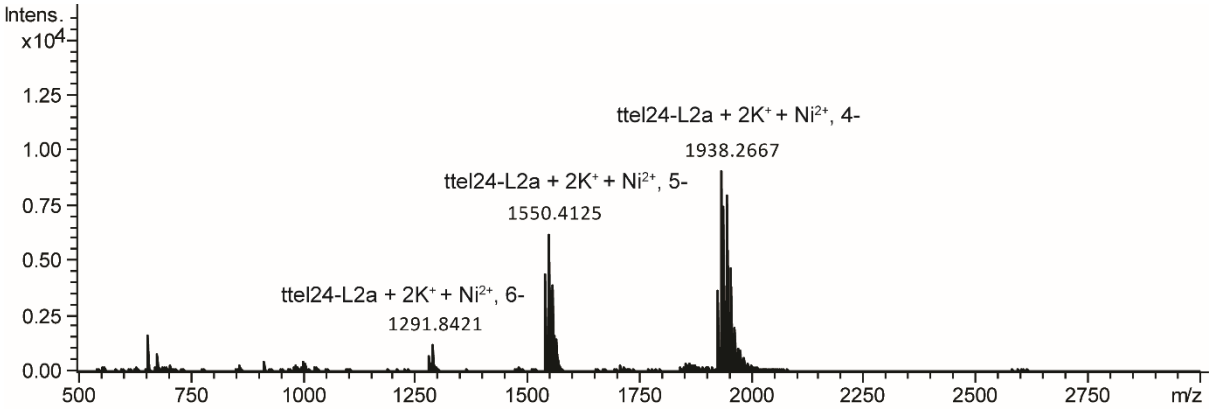

Figure S 69. Native ESI-MS of ttel24-L2a with BiPy-L1 modification in presence of Ni^{2+}. Conditions: 12.5 µM DNA, 15 µM $CuSO_4$, 0.5 mM KCl, 50 mM TMAA pH 7.1, H_2O:ACN, 1:1.

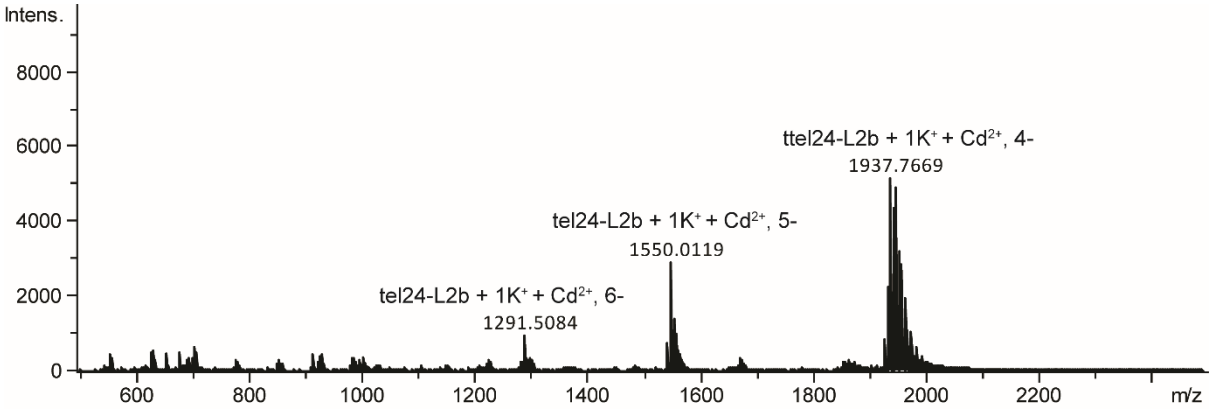

Figure S 70. Native ESI-MS of ttel24-L2b with BiPy-L1 modification in presence of Cd^{2+}. Conditions: 12.5 µM DNA, 15 µM $CuSO_4$, 0.5 mM KCl, 50 mM TMAA pH 7.1, H_2O:ACN, 1:1.

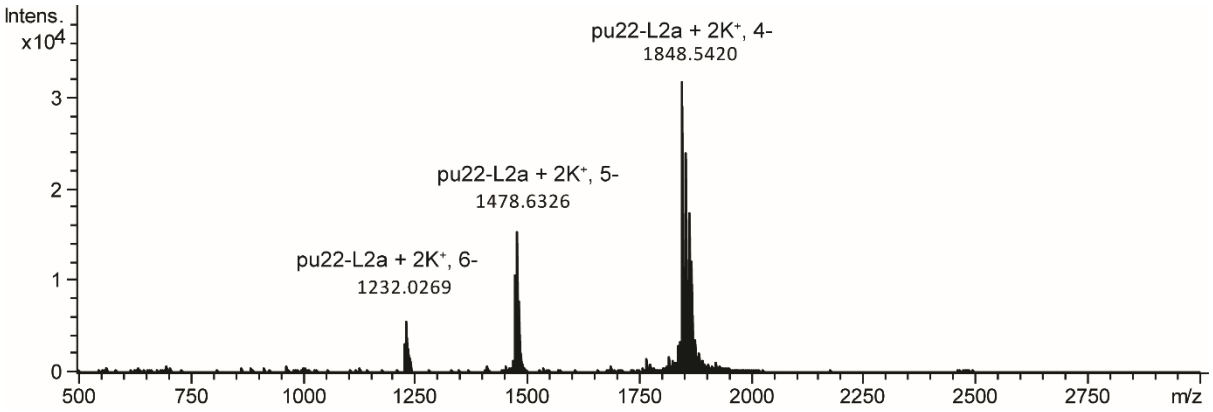

Figure S 71. Native ESI-MS of pu22-L2a with BiPy-L1 modification in absence of M^{2+} (Cu^{2+}, Ni^{2+}, Zn^{2+}). Conditions: 12.5 µM DNA, 0.5 mM KCl, 50 mM TMAA pH 7.1, H_2O:ACN, 1:1.

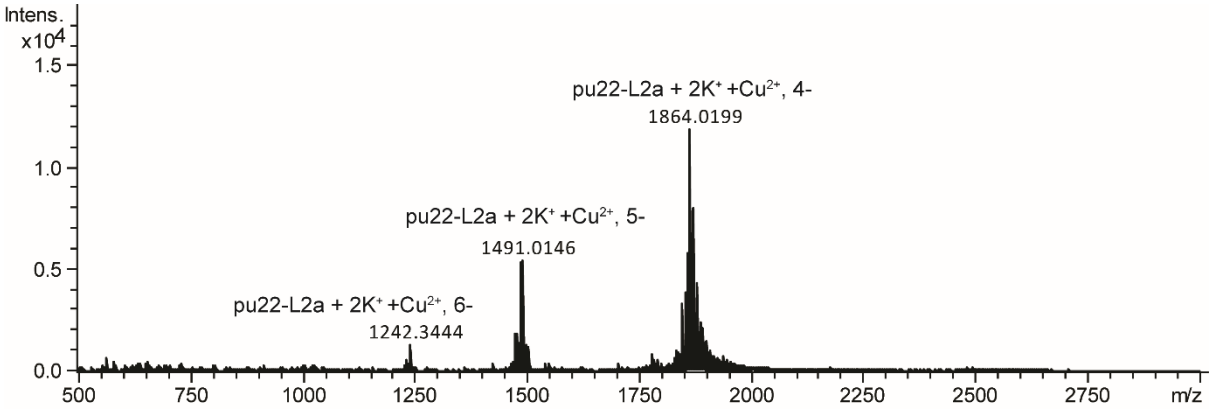

Figure S 72. Native ESI-MS of pu22-L2a with BiPy-L1 modification in presence of Cu^{2+}. Conditions: 12.5 µM DNA, 15 µM $CuSO_4$, 0.5 mM KCl, 50 mM TMAA pH 7.1, H_2O:ACN, 1:1.

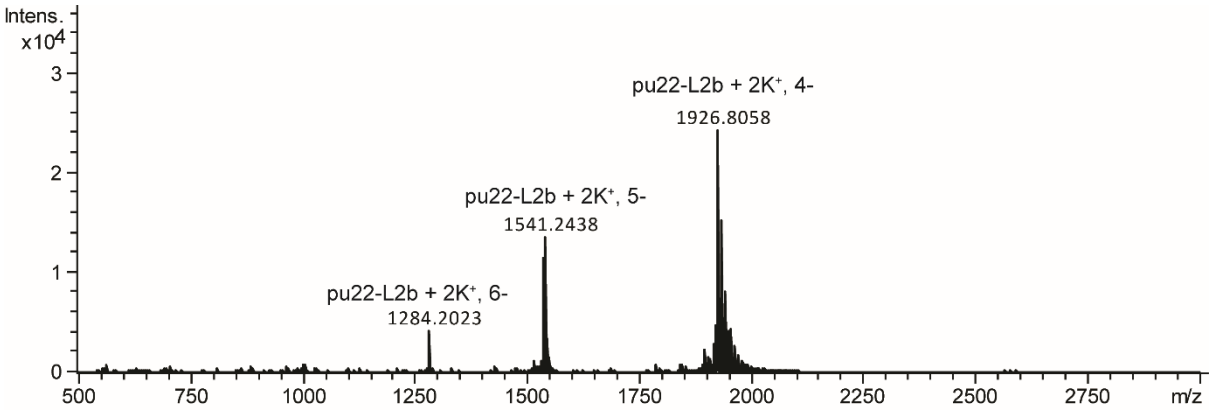

Figure S 73. Native ESI-MS of pu22-L2b with BiPy-L1 modification in absence of M2+ (Cu2+, Ni2+, Zn2+). Conditions: 12.5 µM DNA, 0.5 mM KCl, 50 mM TMAA pH 7.1, H2O:ACN, 1:1.

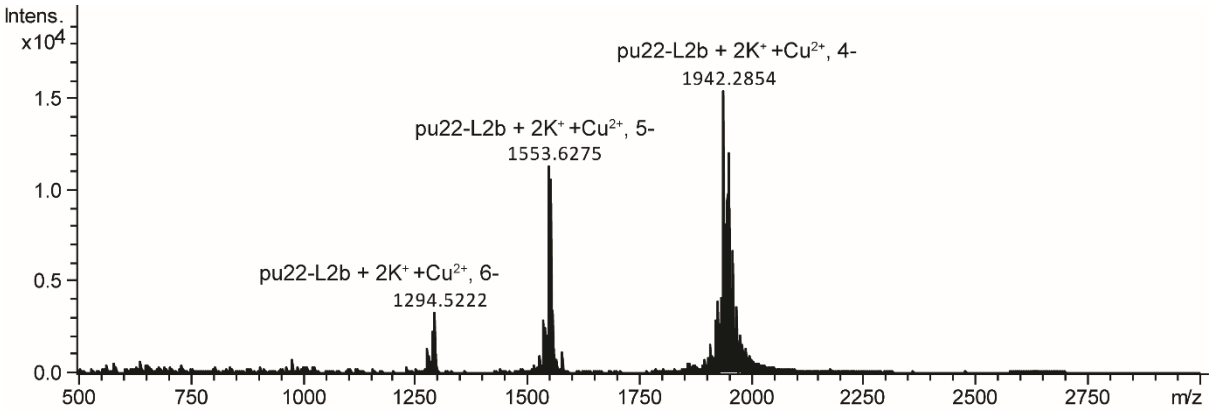

Figure S 74. Native ESI-MS of pu22-L2b with BiPy-L1 modification in presence of Cu^{2+}. Conditions: 12.5 µM DNA, 15 µM $CuSO_4$, 0.5 mM KCl, 50 mM TMAA pH 7.1, H_2O:ACN, 1:1.

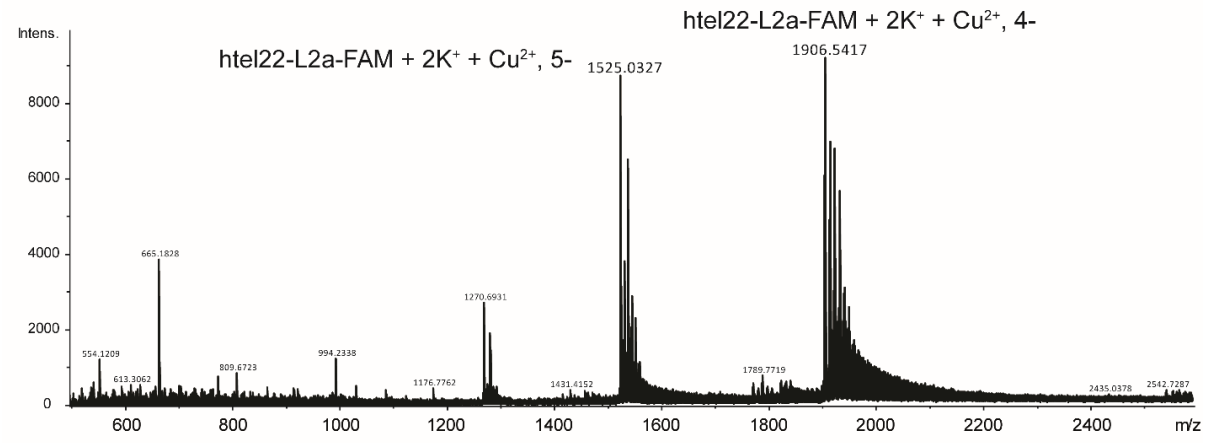

Figure S 75. Native ESI-MS of FAM-htel22-L2a with BiPy-L1 modification in presence of Cu^{2+}. Conditions: 12.5 μM DNA, 15 μM $CuSO_4$, 0.5 mM KCl, 50 mM TMAA pH 7.1, H_2O:ACN, 1:1.

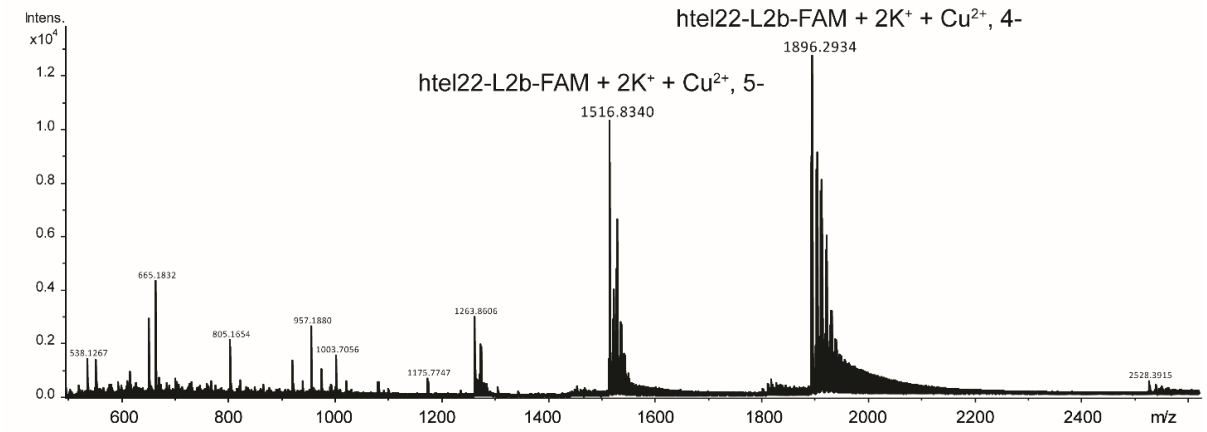

Figure S 76. Native ESI-MS of FAM-htel22-L2b with BiPy-L1 modification in presence of Cu^{2+}. Conditions: 12.5 μM DNA, 15 μM $CuSO_4$, 0.5 mM KCl, 50 mM TMAA pH 7.1, H_2O:ACN, 1:1.

TDS

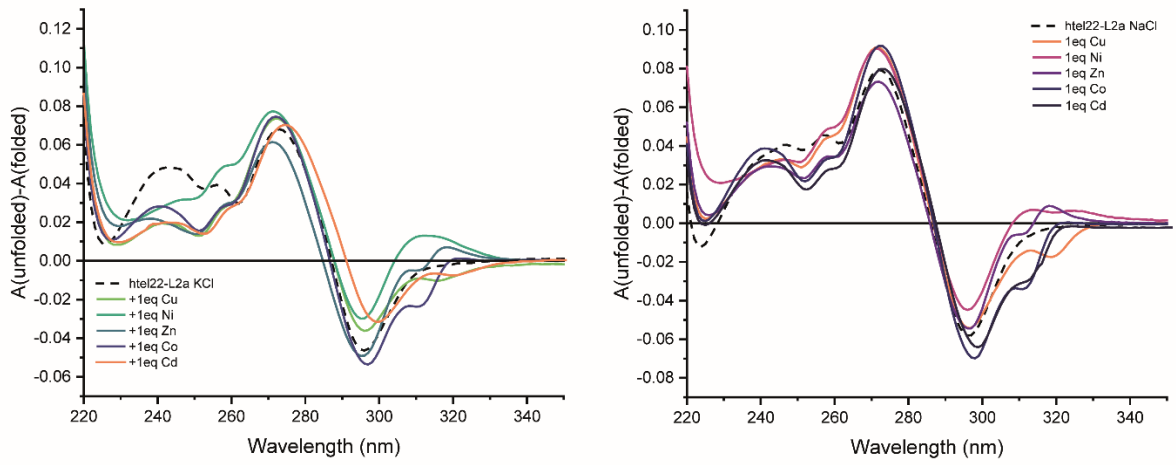

Figure S 77. TDS spectra of htel22-L2a in absence or presence of various divalent metal cations. Conditions: 4μM DNA, 10mM HEPES, 100mM KCl, 4.4 μM M^{2+} (M = Cu, Ni, Zn, Co, Cd).

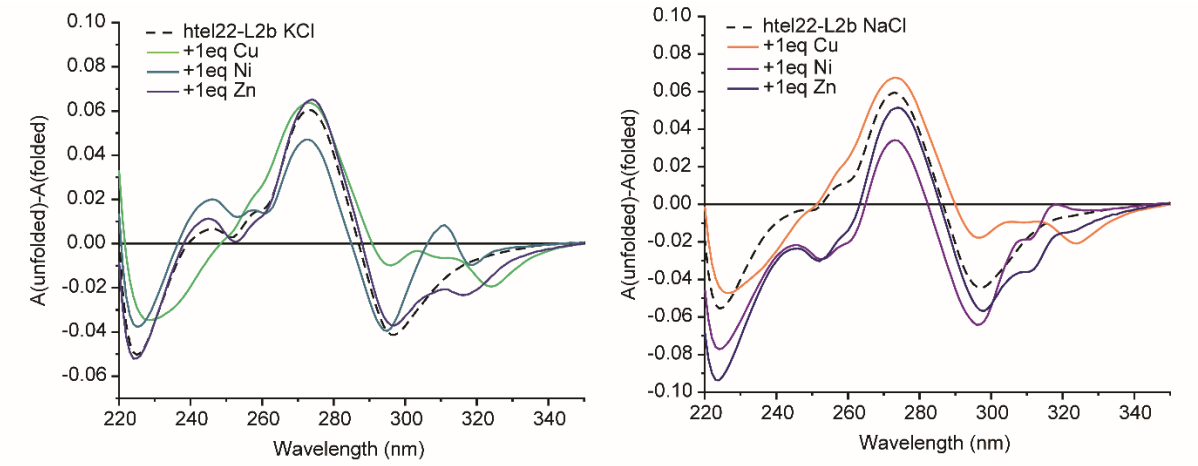

Figure S 78. TDS spectra of htel22-L2b in absence or presence of various divalent metal cations. Conditions: 4μM DNA, 10mM HEPES, 100mM KCl, 4.4 μM M^{2+} (M = Cu, Ni, Zn, Co).

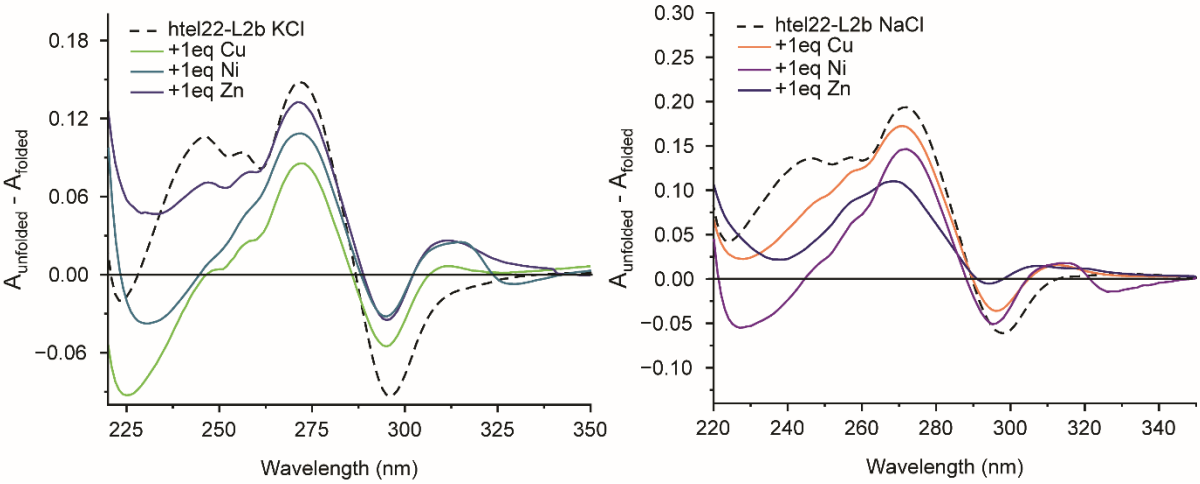

Figure S 79. TDS spectra of **htel22-L2b** with **BiPy-L2** modification in absence or presence of various divalent metal cations. Conditions: 4μM DNA, 10mM HEPES, 100mM KCl or NaCl, 4.4 μM M^{2+} (M = Cu, Ni, Zn

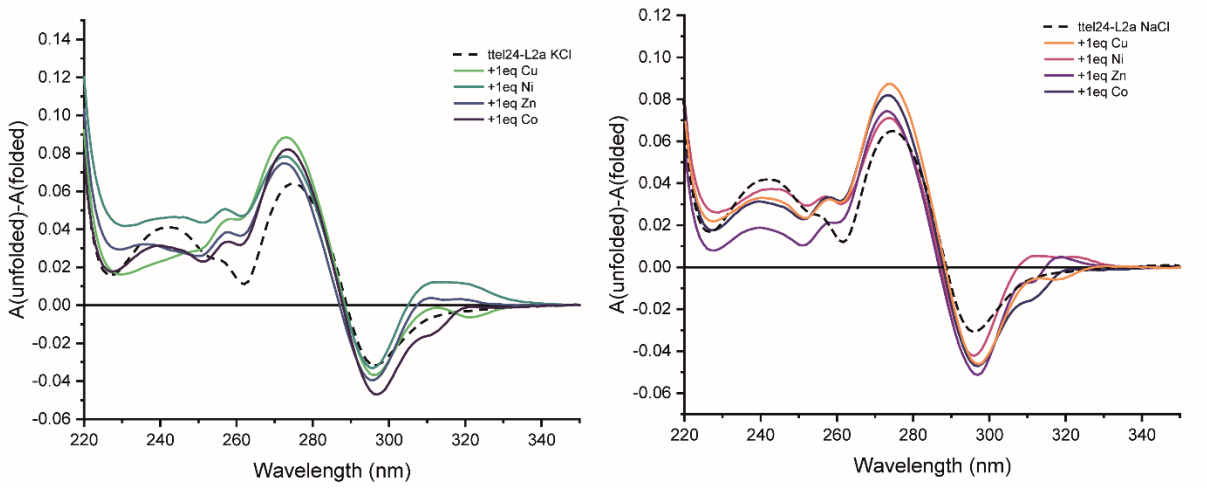

Figure S 80. TDS spectra of **ttel24-L2a** in absence or presence of various divalent metal cations. Conditions: 4μM DNA, 10mM HEPES, 100mM KCl, 4.4 μM M^{2+} (M = Cu, Ni, Zn, Co).

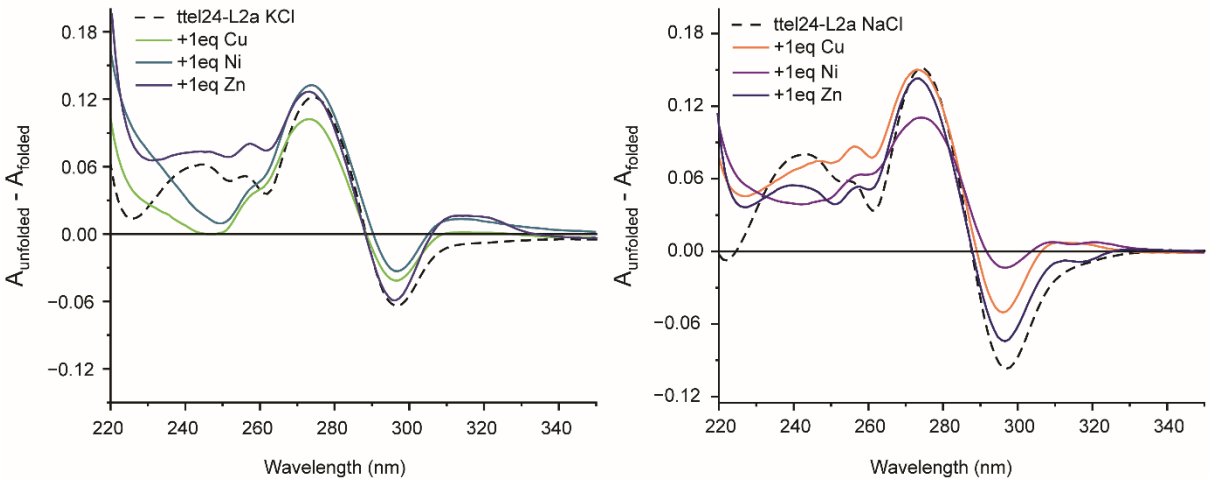

Figure S 81. TDS spectra of **ttel24-L2a** with BiPy-L2 modifications in absence or presence of various divalent metal cations. Conditions: 4μM DNA, 10mM HEPES, 100mM KCl or NaCl, 4.4 μM M^{2+} (M = Cu, Ni, Zn, Co).

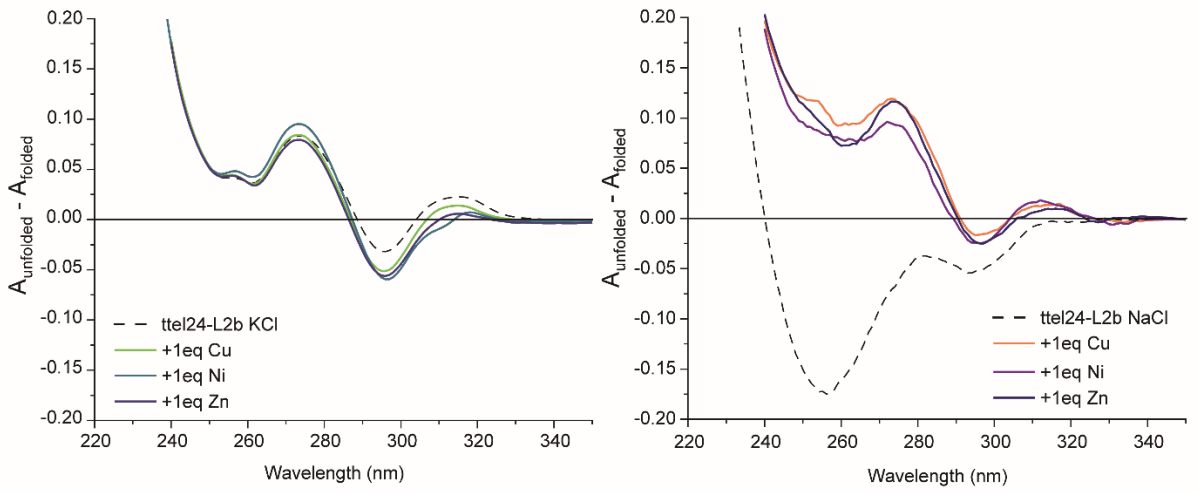

Figure S 82. TDS spectra of ttel24-L2b in absence or presence of various divalent metal cations. Conditions: 4μM DNA, 10mM HEPES, 100mM KCl, 4.4 μM M2+ (M = Cu, Ni, Zn, Co).

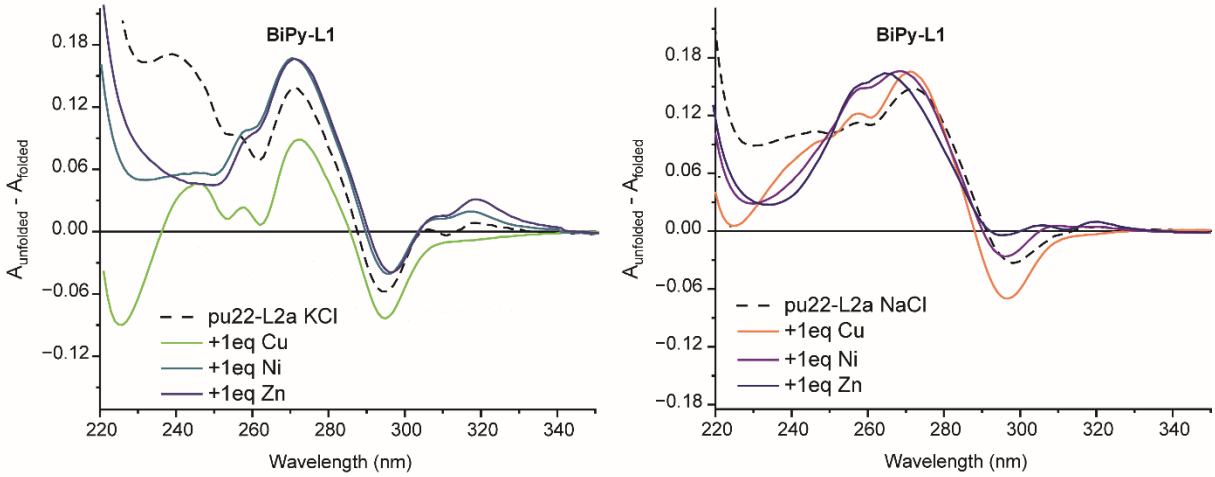

Figure S 83. TDS spectrum of pu22-L2a with BiPy-L1 modification in absence or presence of various divalent metal cations. Conditions: 4μM DNA, 10mM HEPES, 100mM KCl or NaCl, 4.4 μM M^{2+} (M = Cu, Ni, Zn).

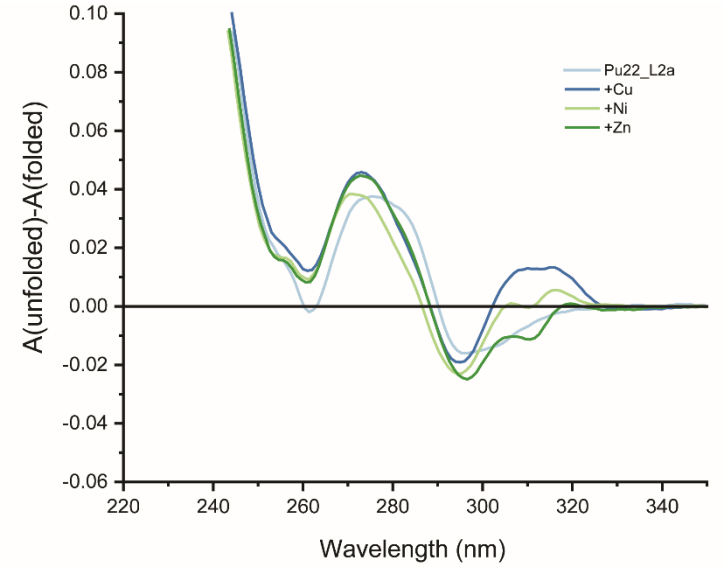

Figure S 84. TDS spectrum of pu22-L2b in absence or presence of various divalent metal cations. Conditions: 4μM DNA, 10mM HEPES, 100mM KCl, 4.4 μM M^{2+} (M = Cu, Ni, Zn).

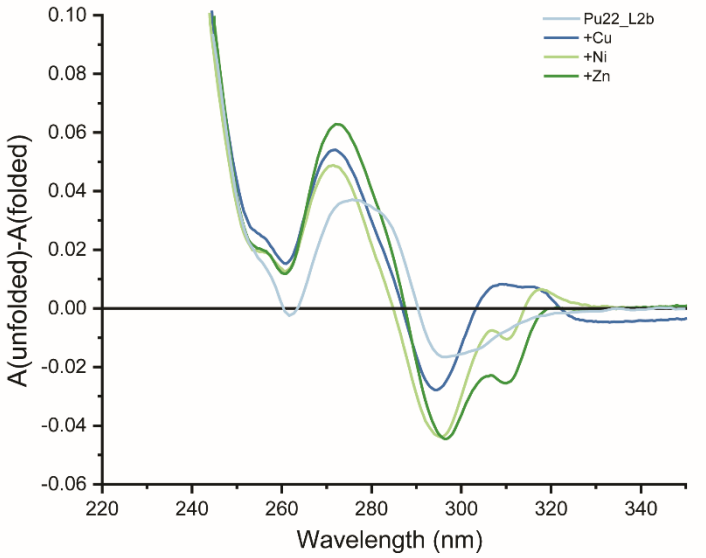

Figure S 85. TDS spectrum of pu22-L2c in absence or presence of various divalent metal cations. Conditions: 4μM DNA, 10mM HEPES, 100mM KCl, 4.4 μM M^{2+} (M = Cu, Ni, Zn).

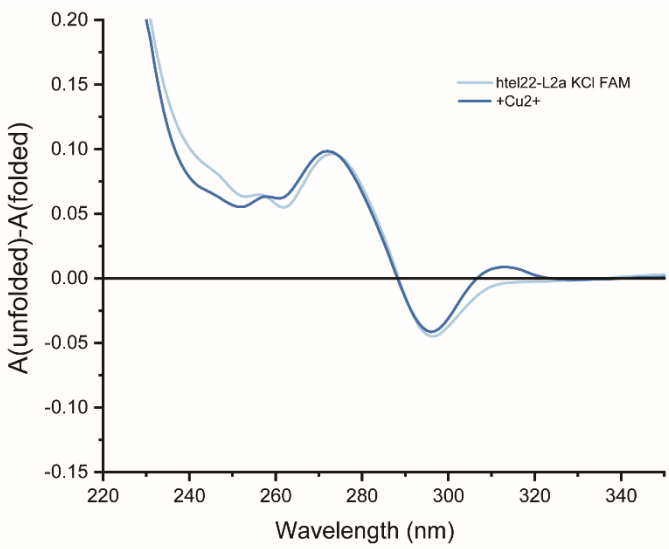

Figure S 86. TDS spectrum of FAM-htel22-L2a in absence or presence of various divalent metal cations. Conditions: 4μM DNA, 10mM HEPES, 100mM KCl, 4.4 μM Cu^{2+}.

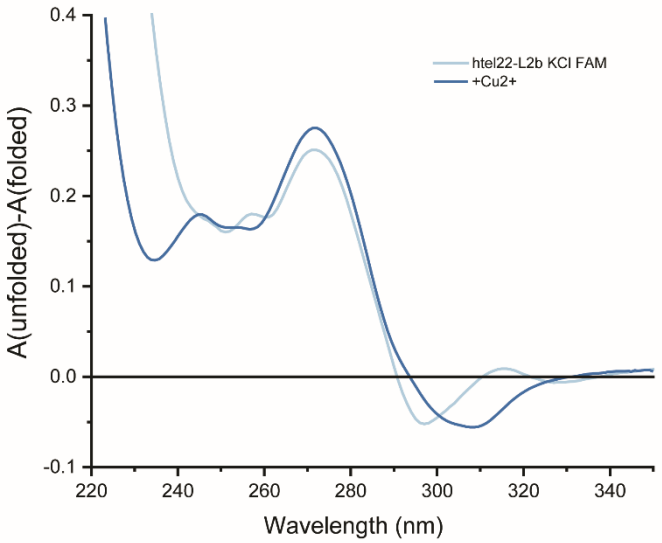

Figure S 87. TDS spectrum of FAM-htel22-L2b in absence or presence of various divalent metal cations. Conditions: 4μM DNA, 10mM HEPES, 100mM KCl, 4.4 μM Cu^{2+}.

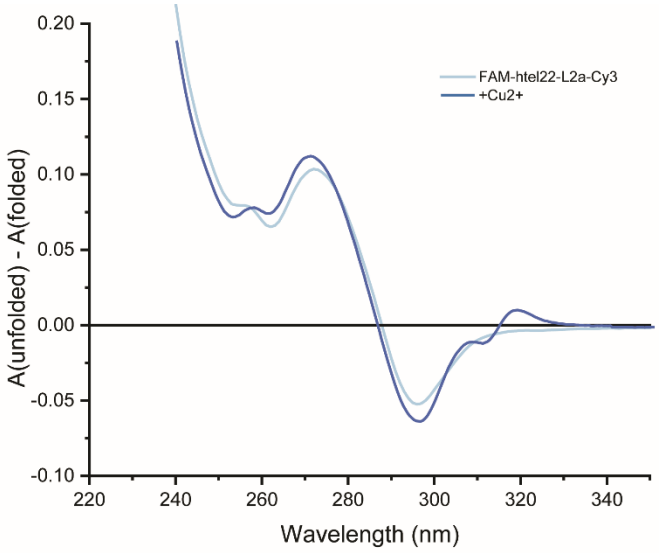

Figure S 88. TDS spectrum of FAM-htel22-L2a-Cy3 in absence or presence of various divalent metal cations. Conditions: 4μM DNA, 10mM HEPES, 100mM KCl, 4.4 μM Cu^{2+}.

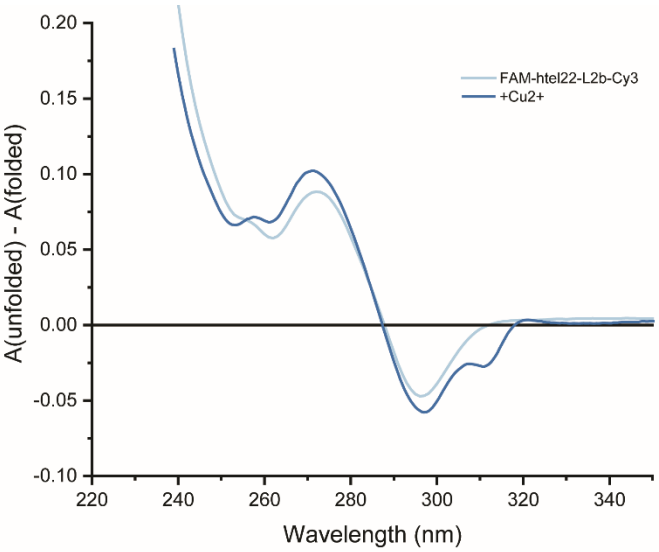

Figure S 89. TDS spectrum of FAM-htel22-L2b-Cy3 in absence or presence of various divalent metal cations. Conditions: 4μM DNA, 10mM HEPES, 100mM KCl, 4.4 μM Cu^{2+}.

UV-Vis Melting

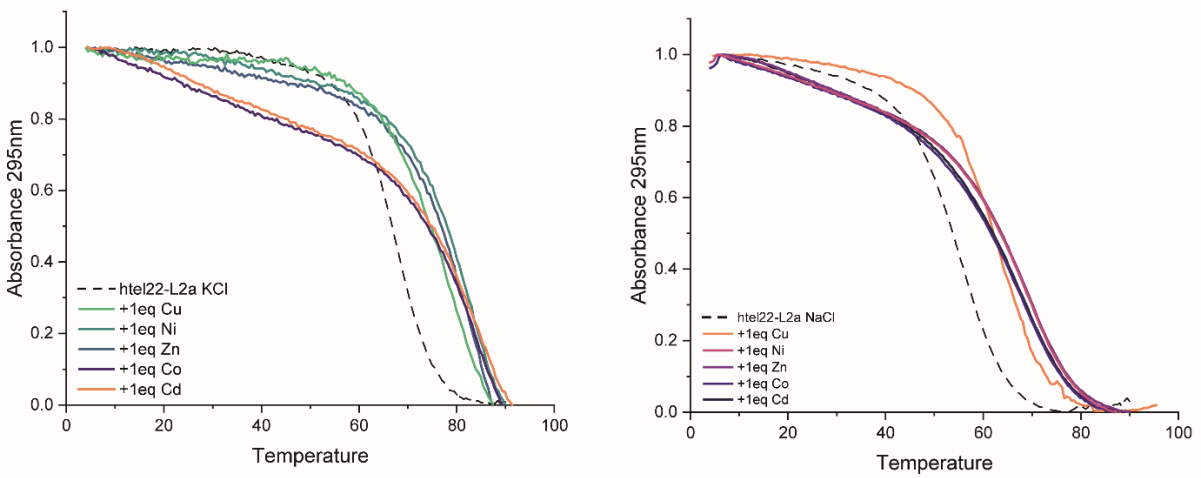

Figure S 90. UV-Vis melting spectra of htel22-L2a in absence or presence of various divalent metal cations. Conditions: 4μM DNA, 10mM HEPES, 100mM KCl, 4.4 μM M^{2+} (M = Cu, Ni, Zn, Co, Cd).

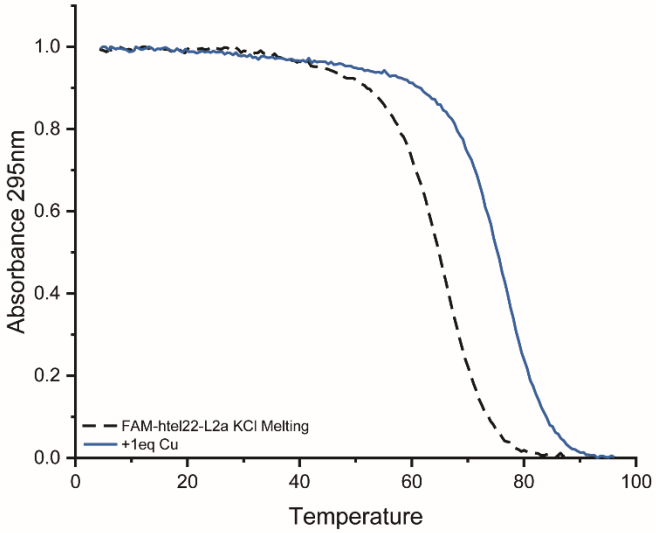

Figure S 91. UV-Vis melting spectra of FAM-htel22-L2a in absence or presence of Cu^{2+}. Conditions: 4μM DNA, 10mM HEPES, 100mM KCl, 4.4 μM Cu^{2+}.

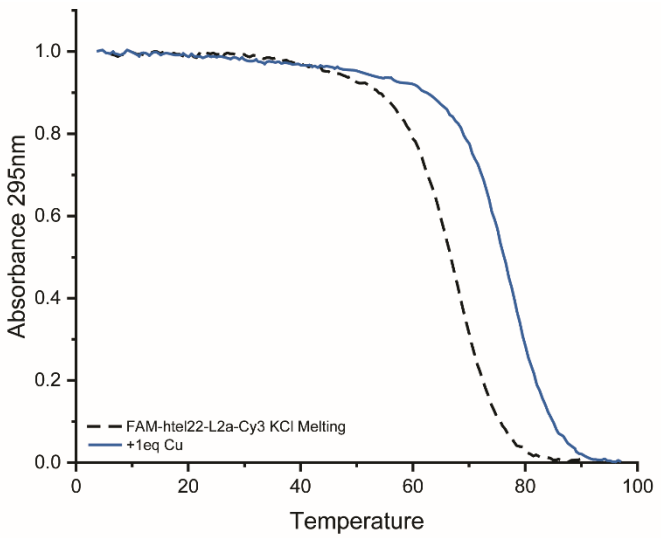

Figure S 92. UV-Vis melting spectra of FAM-htel22-L2a-Cy3 in absence or presence of Cu^{2+}. Conditions: 4μM DNA, 10mM HEPES, 100mM KCl, 4.4 μM Cu^{2+}.

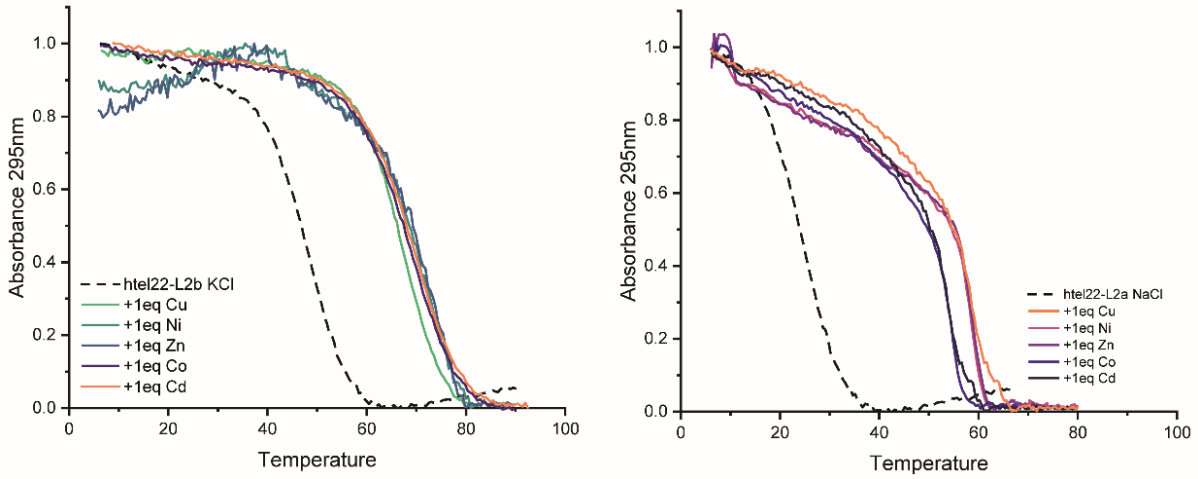

Figure S 93. UV-Vis melting spectra of htel22-L2b in absence or presence of various divalent metal cations. Conditions: 4μM DNA, 10mM HEPES, 100mM KCl or NaCl, 4.4 μM M^{2+} (M = Cu, Ni, Zn, Co, Cd).

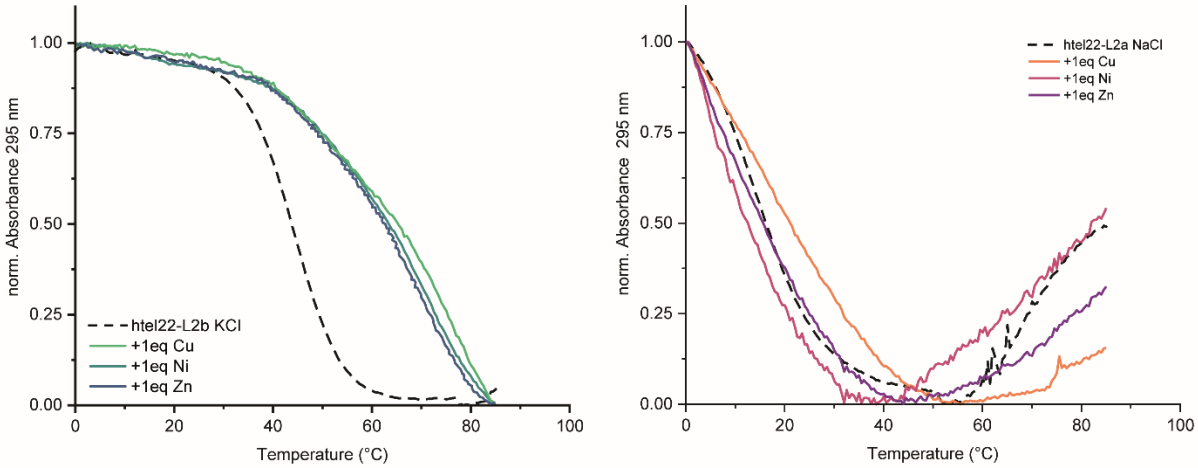

Figure S 94. UV-Vis melting spectra of htel22-L2b with BiPy-L2 modification in absence or presence of various divalent metal cations. Conditions: 4μM DNA, 10mM HEPES, 100mM KCl or NaCl, 4.4 μM M^{2+} (M = Cu, Ni, Zn).

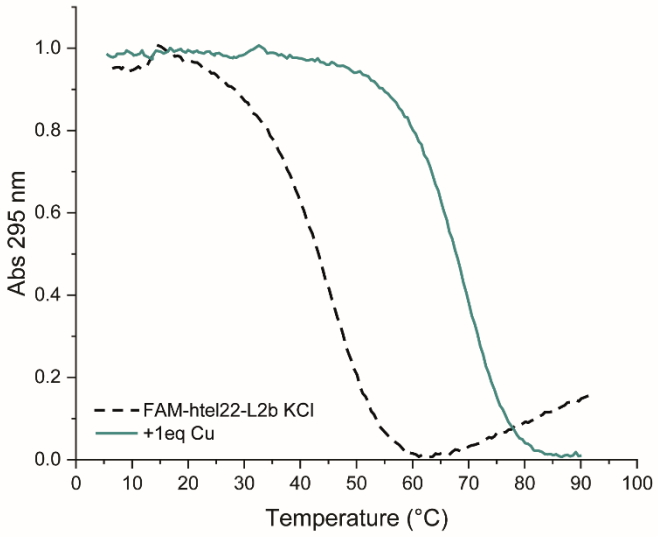

Figure S 95. UV-Vis melting spectra of FAM-htel22-L2b in absence or presence of Cu^{2+}. Conditions: 4μM DNA, 10mM HEPES, 100mM KCl, 4.4 μM Cu^{2+}.

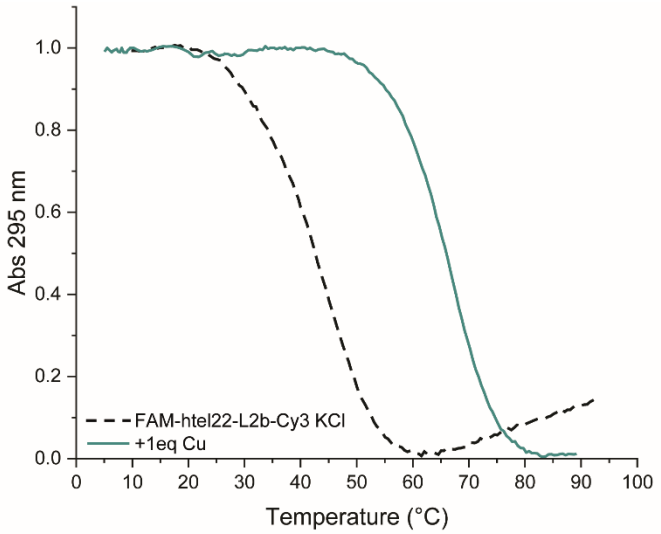

Figure S 96. UV-Vis melting spectra of FAM-htel22-L2b-Cy3 in absence or presence of Cu^{2+}. Conditions: 4µM DNA, 10mM HEPES, 100mM KCl, 4.4 µM Cu^{2+}.

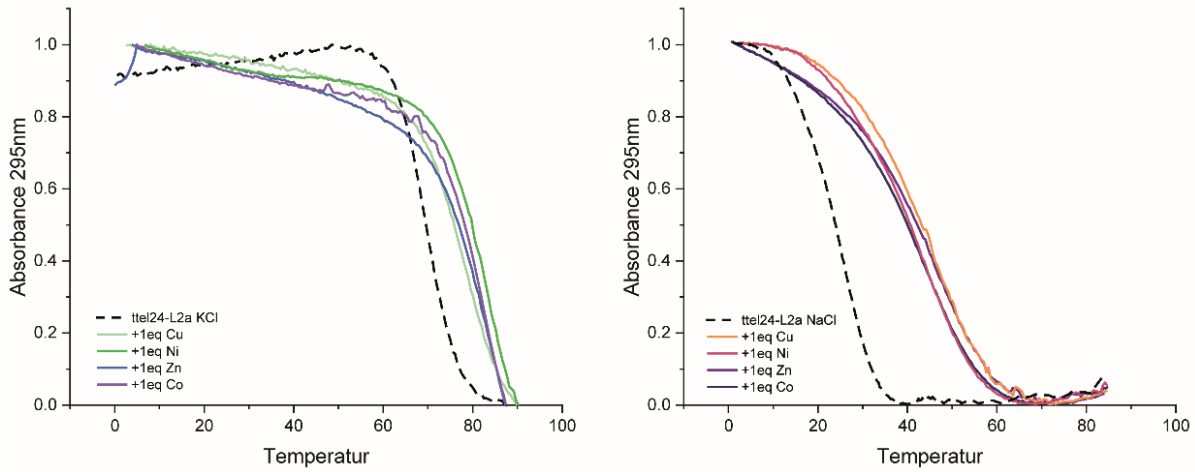

Figure S 97. UV-Vis melting spectra of ttel24-L2a in absence or presence of various divalent metal cations. Conditions: 4µM DNA, 10mM HEPES, 100mM KCl or NaCl, 4.4 µM M^{2+} (M = Cu, Ni, Zn, Co).

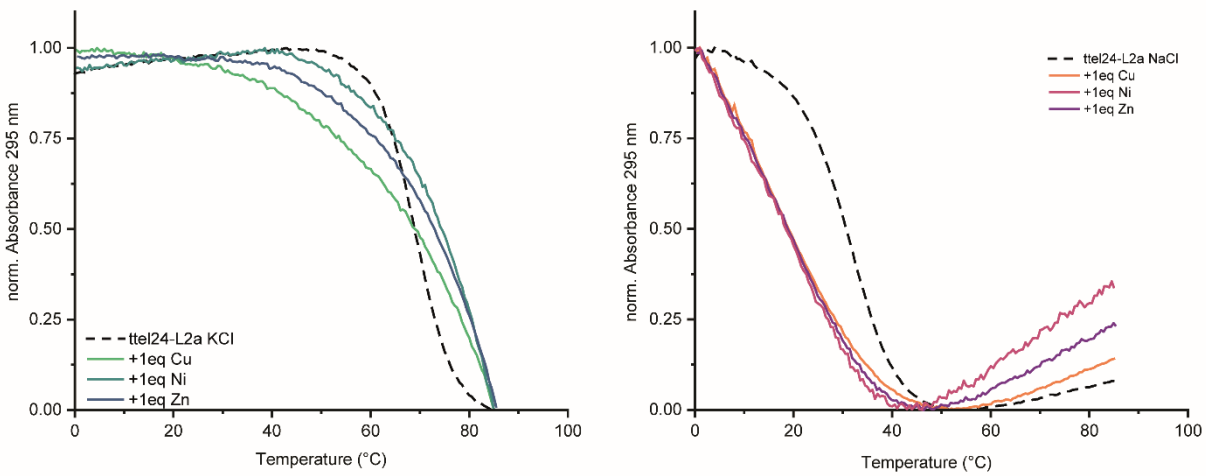

Figure S 98. UV-Vis melting spectra of **ttel24-L2a** with BiPy-L2 modification in absence or presence of various divalent metal cations. Conditions: 4μM DNA, 10mM HEPES, 100mM KCl or NaCl, 4.4 μM M^{2+} (M = Cu, Ni, Zn).

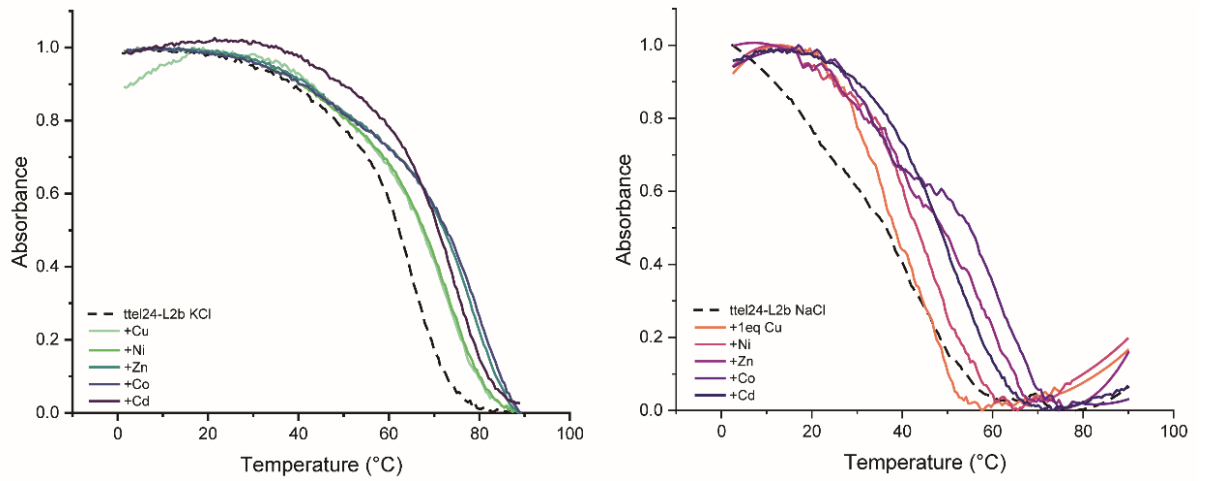

Figure S 99. UV-Vis melting spectra of ttel24-L2b with BiPy-L1 modification in absence or presence of various divalent metal cations. Conditions: 4μM DNA, 10mM HEPES, 100mM KCl or NaCl, 4.4 μM M^{2+} (M = Cu, Ni, Zn, Co, Cd).

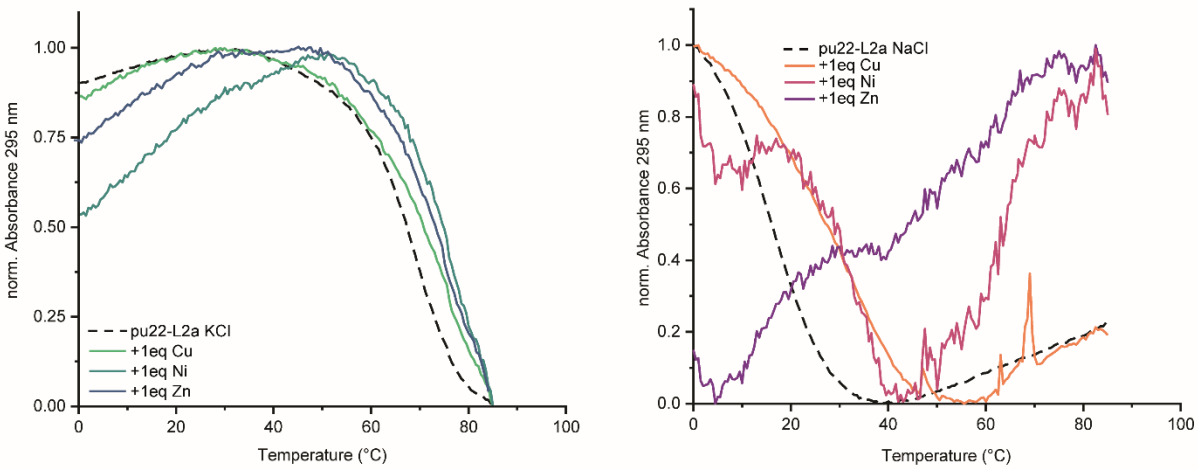

Figure S 100. UV-Vis melting spectra of pu22-L2a in absence or presence of various divalent metal cations. Conditions: 4μM DNA, 10mM HEPES, 100mM KCl or NaCl, 4.4 μM M^{2+} (M = Cu, Ni, Zn).

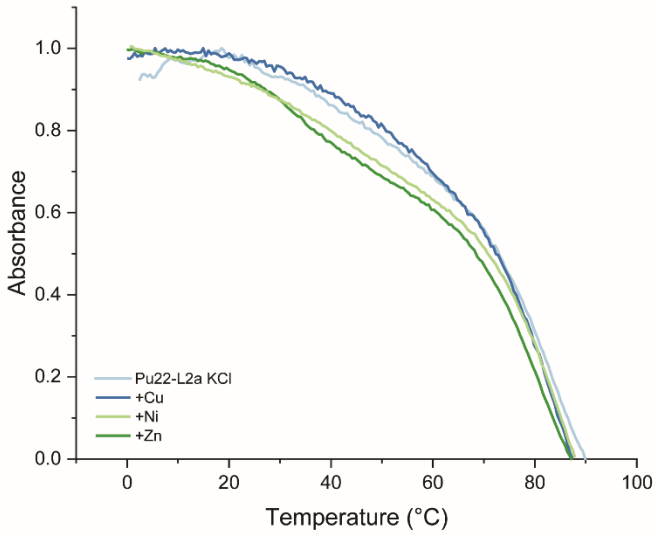

Figure S 101. UV-Vis melting spectra of pu22-L2b in absence or presence of various divalent metal cations. Conditions: 4μM DNA, 10mM HEPES, 100mM KCl, 4.4 μM M^{2+} (M = Cu, Ni, Zn).

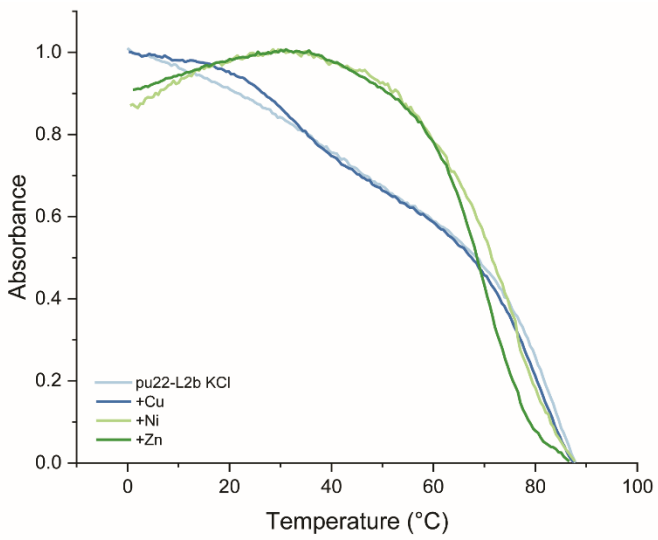

Figure S 102. UV-Vis melting spectra of pu22-L2c in absence or presence of various divalent metal cations. Conditions: 4 µM DNA, 10mM HEPES, 100mM KCl, 4.4 µM M^{2+} (M = Cu, Ni, Zn).

Cell studies

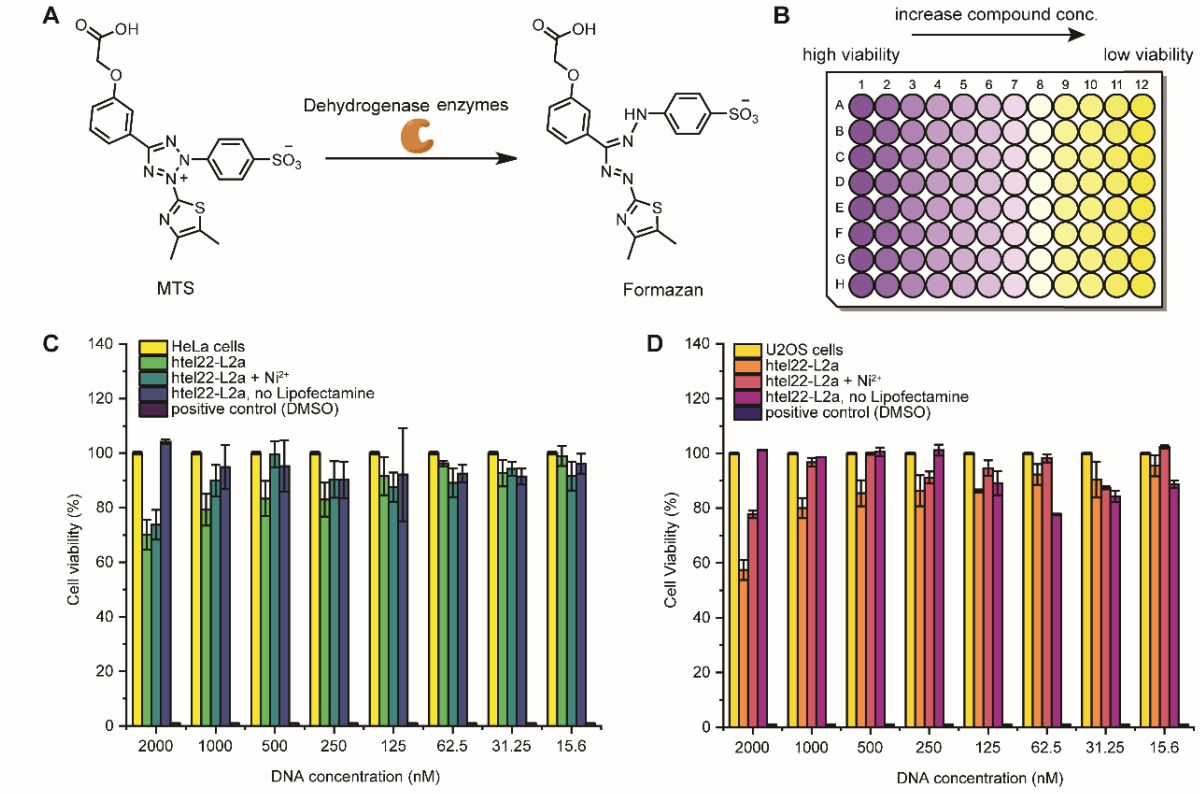

Figure S 103. MTS Assay of FAM-htel22-L2a in absence or presence of Ni^{2+} and in absence or presence of Lipofectamine2000. Negative control: 10000 cells per well in growth medium. Positive control: Incubation in medium with 50% DMSO over 16h at 37°C and 5% CO_2.

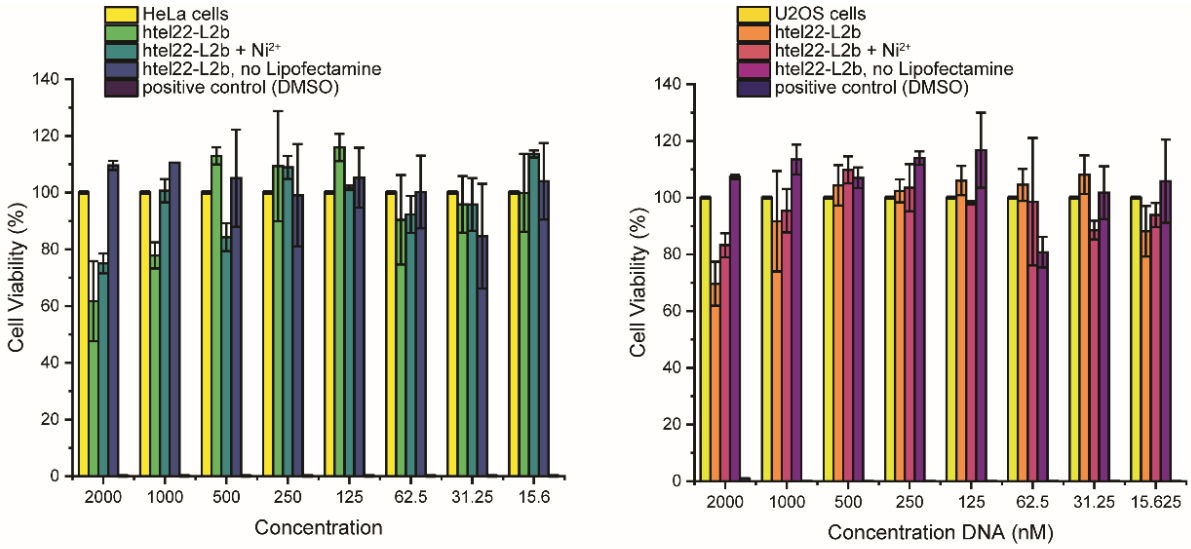

Figure S 104. MTS Assay of FAM-htel22-L2b in absence or presence of Ni^{2+} and in absence or presence of Lipofectamine2000. Negative control: 10000 cells per well in growth medium. Positive control: Incubation in medium with 50% DMSO over 16h at 37°C and 5% CO_2.

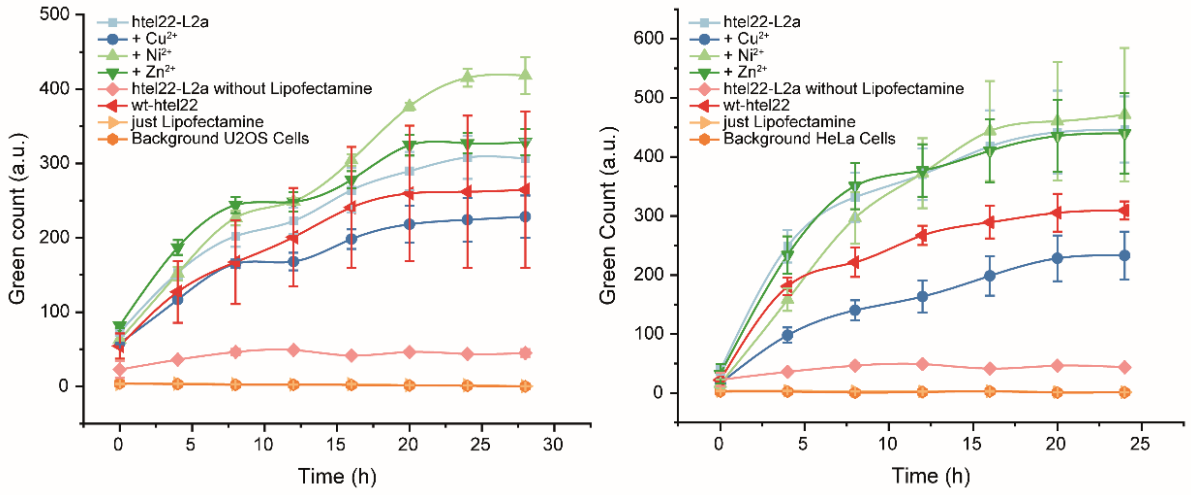

Figure S 105. Green fluorescence count ($\lambda_{ex.}$ = 490nm, $\lambda_{em.}$ = 520nm) of the cells transfected with htel22-L2a in absence and presence of M^{2+} (M = Cu, Ni, Zn) and in absence and presence of Lipofectamine2000.

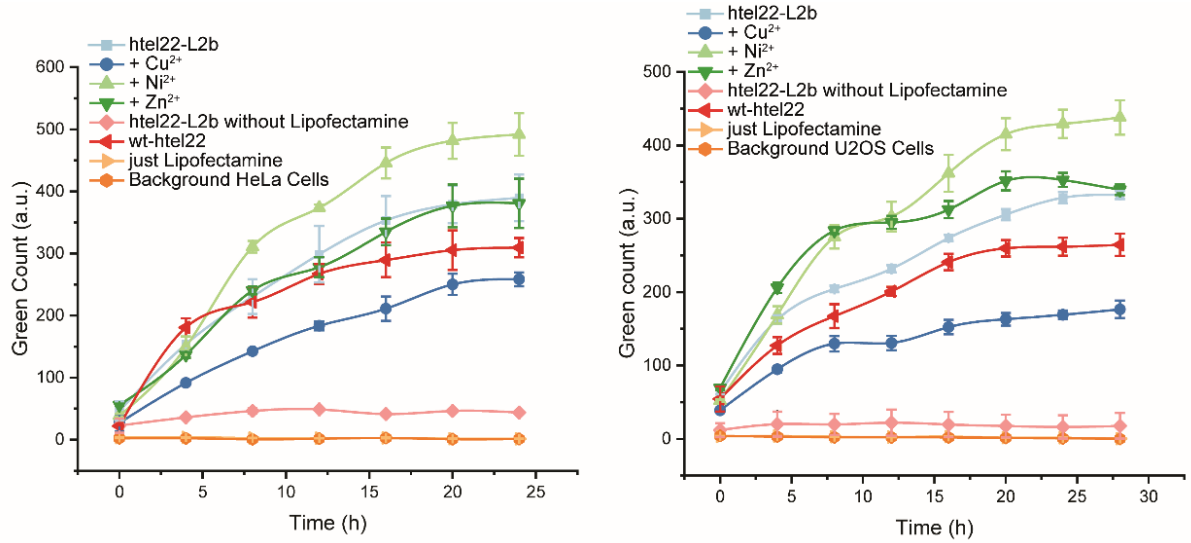

Figure S 106. Green fluorescence count ($\lambda_{ex.}$ = 490nm, $\lambda_{em.}$ = 520nm) of the cells transfected with htel22-L2b in absence and presence of M^{2+} (M = Cu, Ni, Zn) and in absence and presence of Lipofectamine2000.

Fluroescence

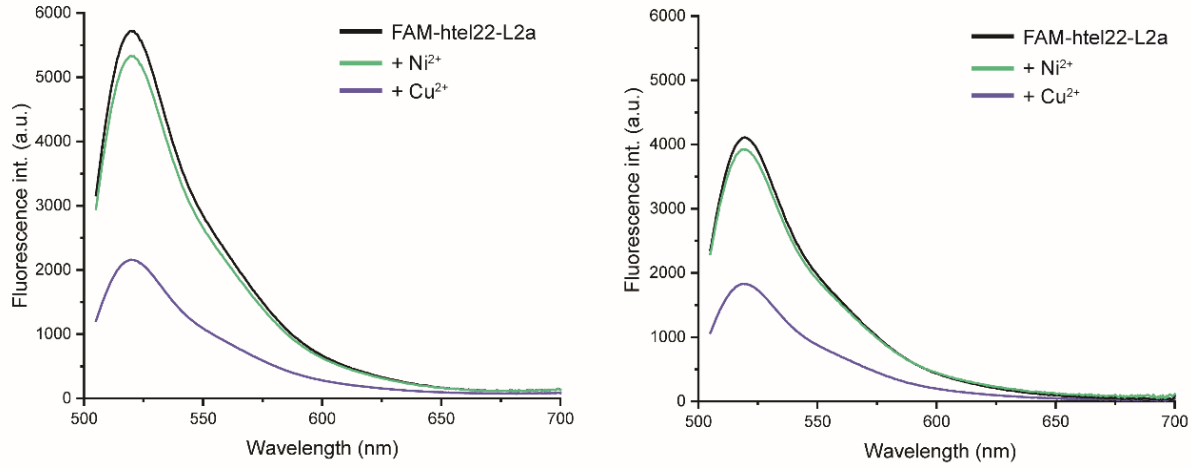

Figure S 107. Fluorescence spectra of FAM-htel22-L2a and FAM-htel22-L2b in absence and presence of either Ni^{2+} and Cu2+ showcasing metal dependent fluorescence quenching of the modified G-quadruplexes ($\lambda_{ex.}$ = 490nm).

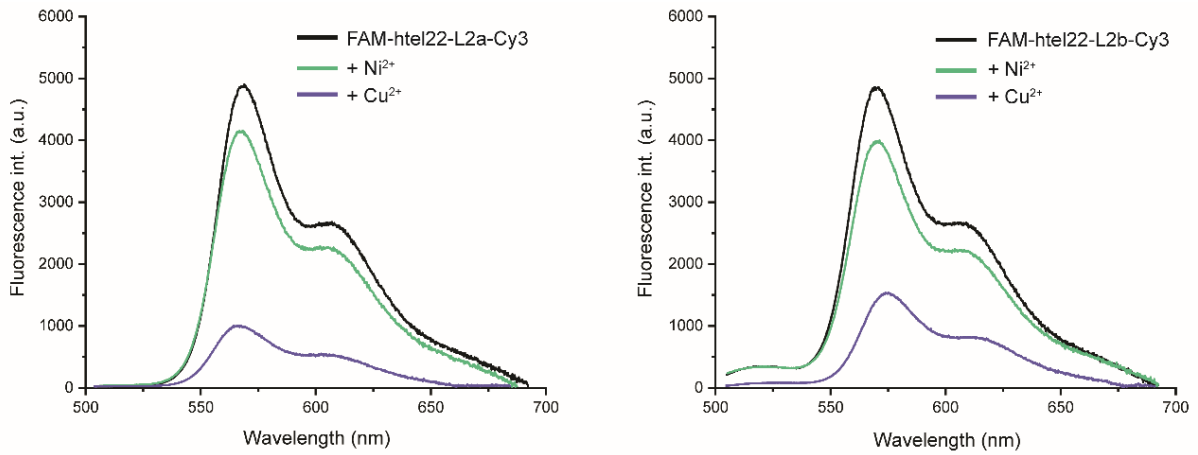

Figure S 108. Fluorescence spectra of FAM-htel22-L2a-Cy3 and FAM-htel22-L2b-Cy3 in absence and presence of either Ni^{2+} and Cu^{2+} showcasing metal dependent fluorescence quenching of the modified G-quadruplexes ($\lambda_{ex.}$ = 490nm).

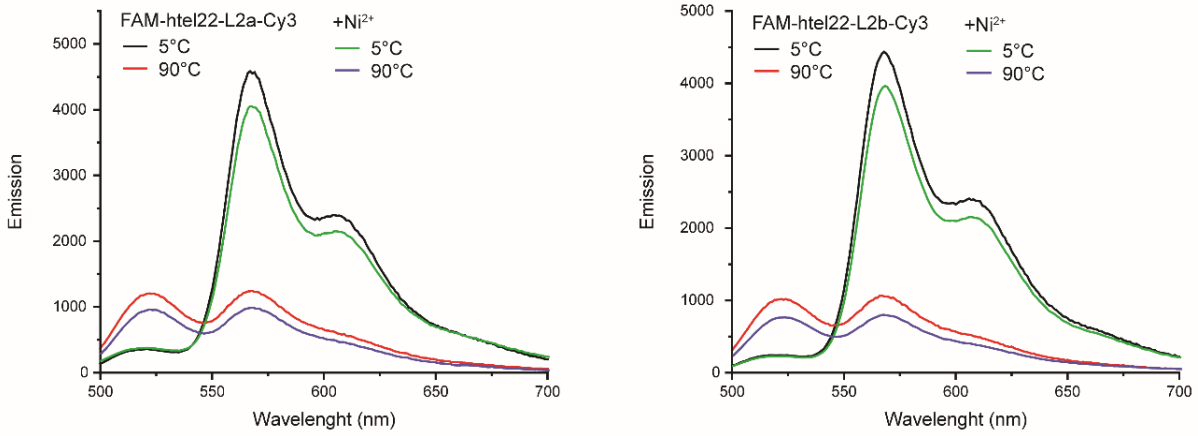

Figure S 109. Temperature dependent fluorescence spectra of FAM-htel22-L2a-Cy3 and FAM-htel22-L2b-Cy3 in absence and presence of either Ni^{2+} showcasing metal dependent as well as temperature dependent fluorescence quenching of the modified G-quadruplexes ($\lambda_{ex.}$ = 490nm).

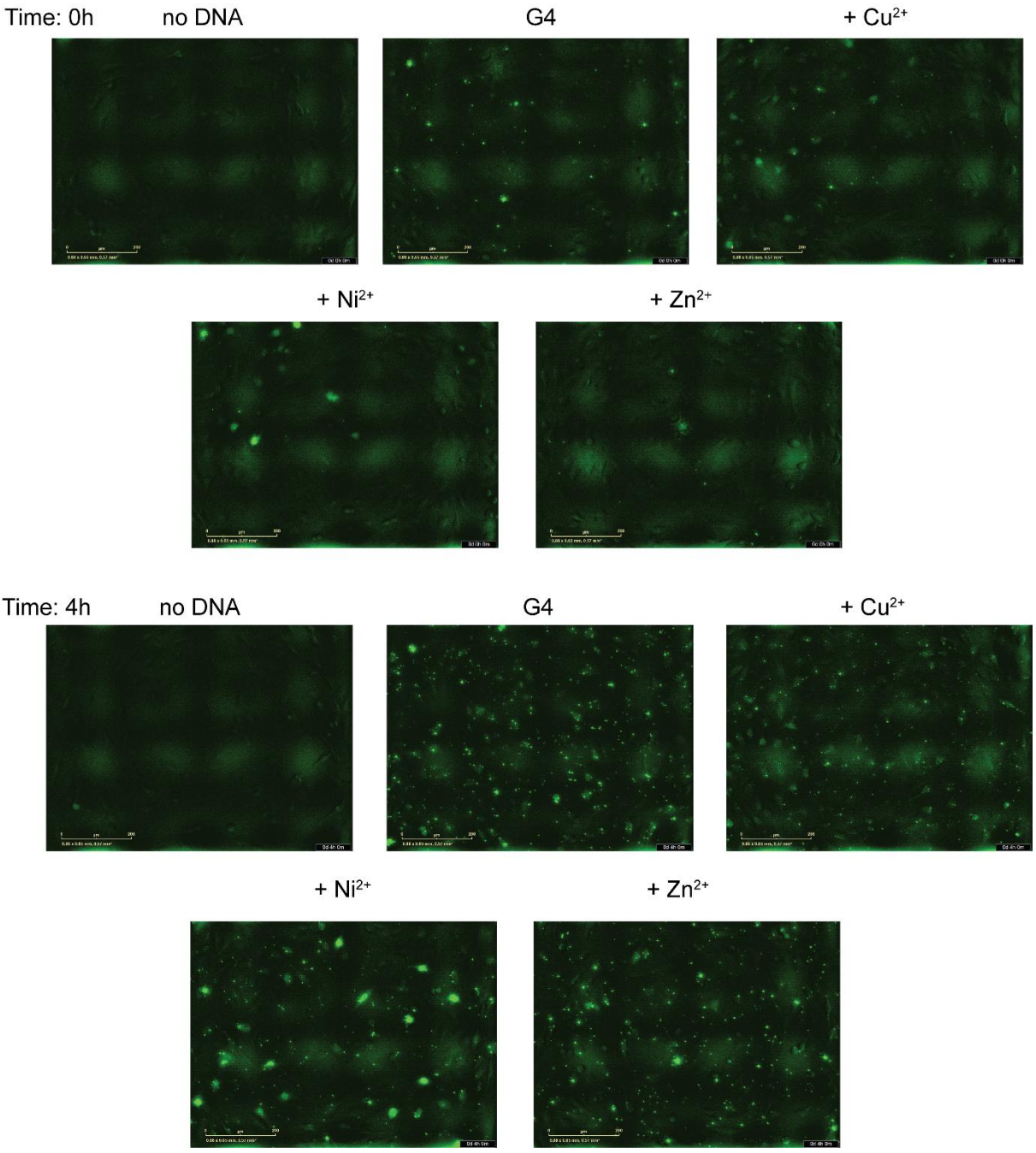

Figure S 110. Fluorescence microscopy of preformed htel22-L2a-FAM G-quadruplexes in HeLa cells after 0h post transfection and 4h post transfection in presence or absence of various M^{2+} (M = Cu, Ni, Zn).

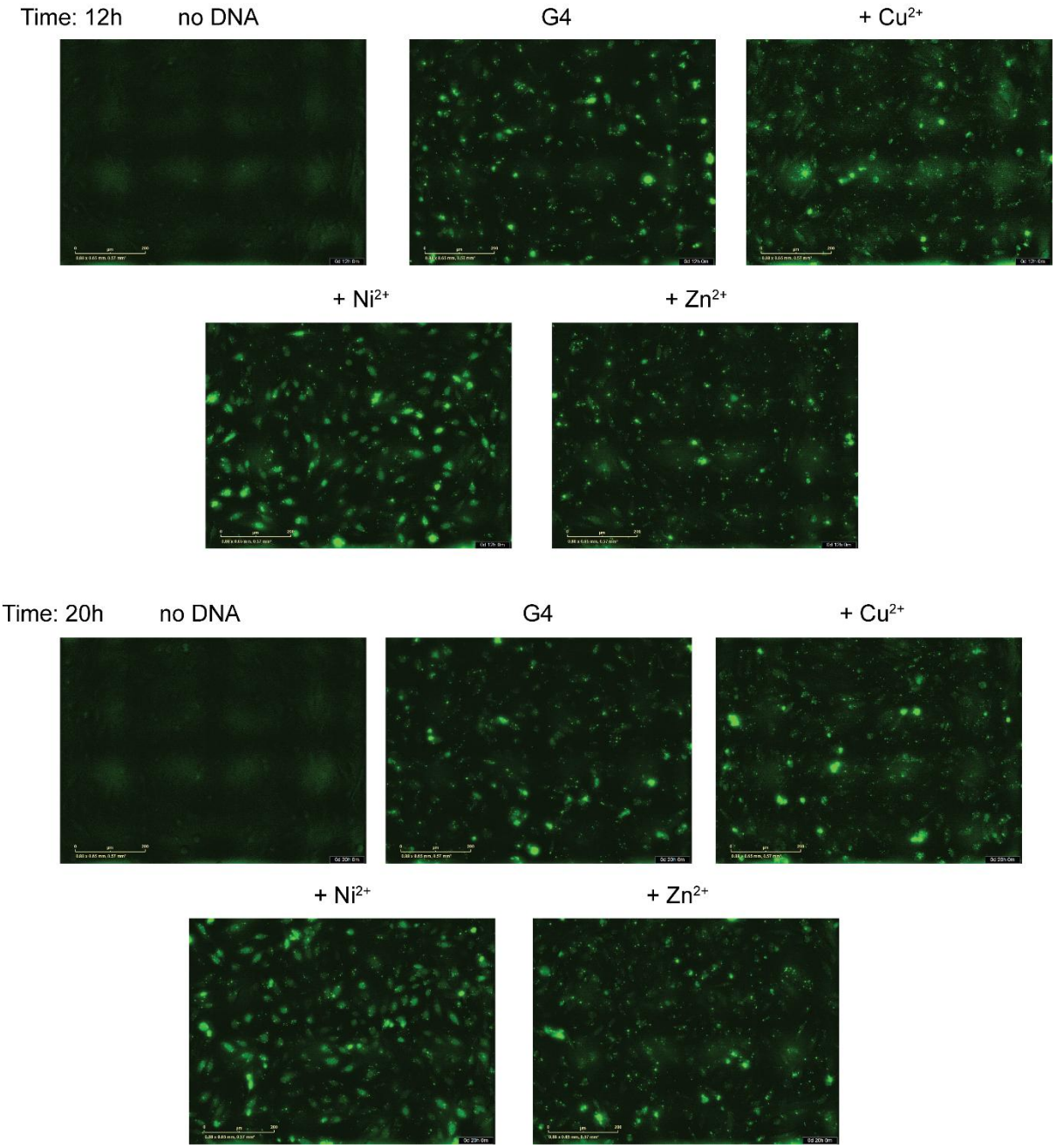

Figure S 111. Fluorescence microscopy of preformed htel22-L2a-FAM G-quadruplexes in HeLa cells after 12h post transfection and 20h post transfection in presence or absence of various M^{2+} (M = Cu, Ni, Zn).

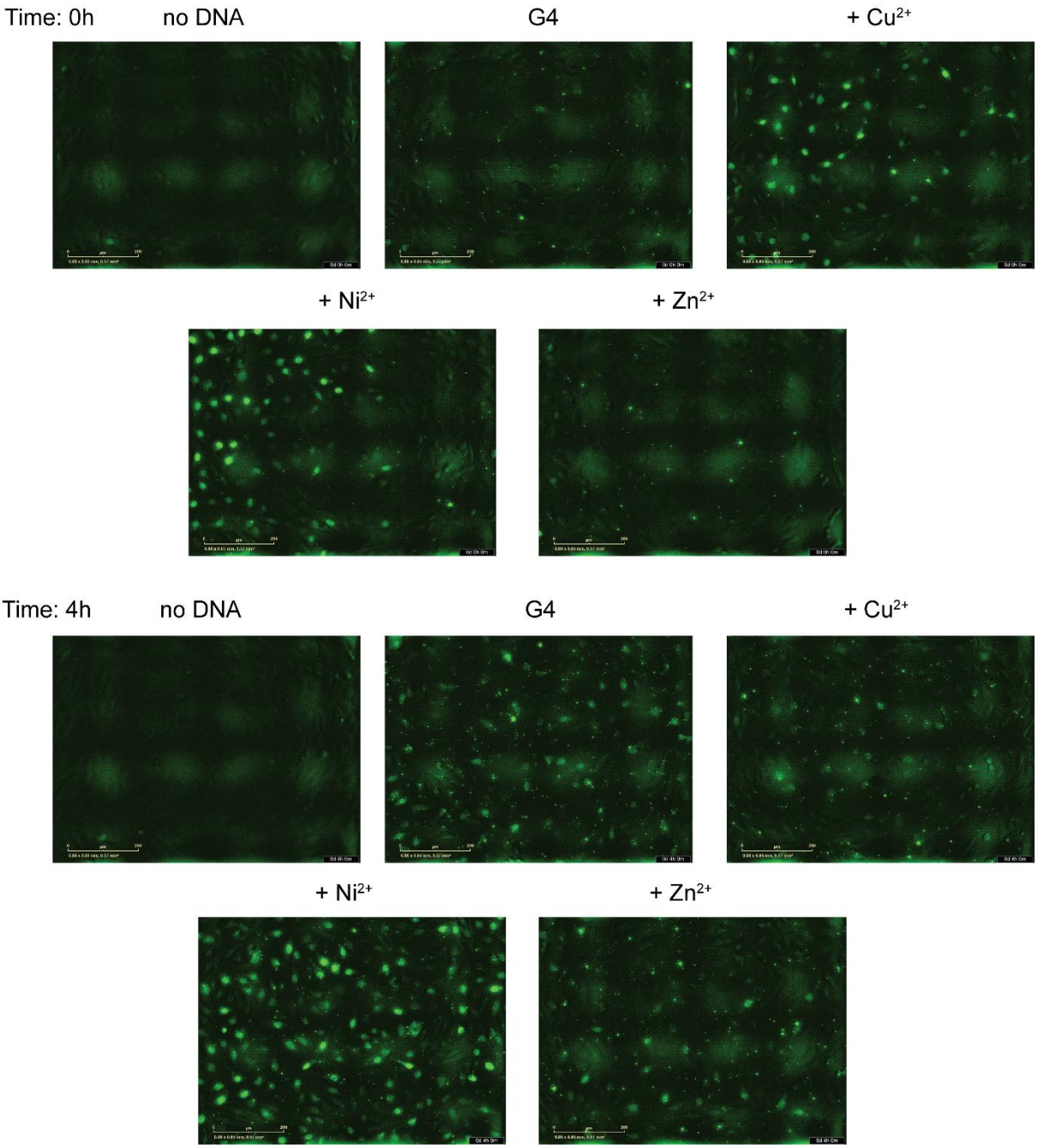

Figure S 112. Fluorescence microscopy of preformed htel22-L2b-FAM G-quadruplexes in HeLa cells after 0h post transfection and 4h post transfection in presence or absence of various M^{2+} (M = Cu, Ni, Zn).

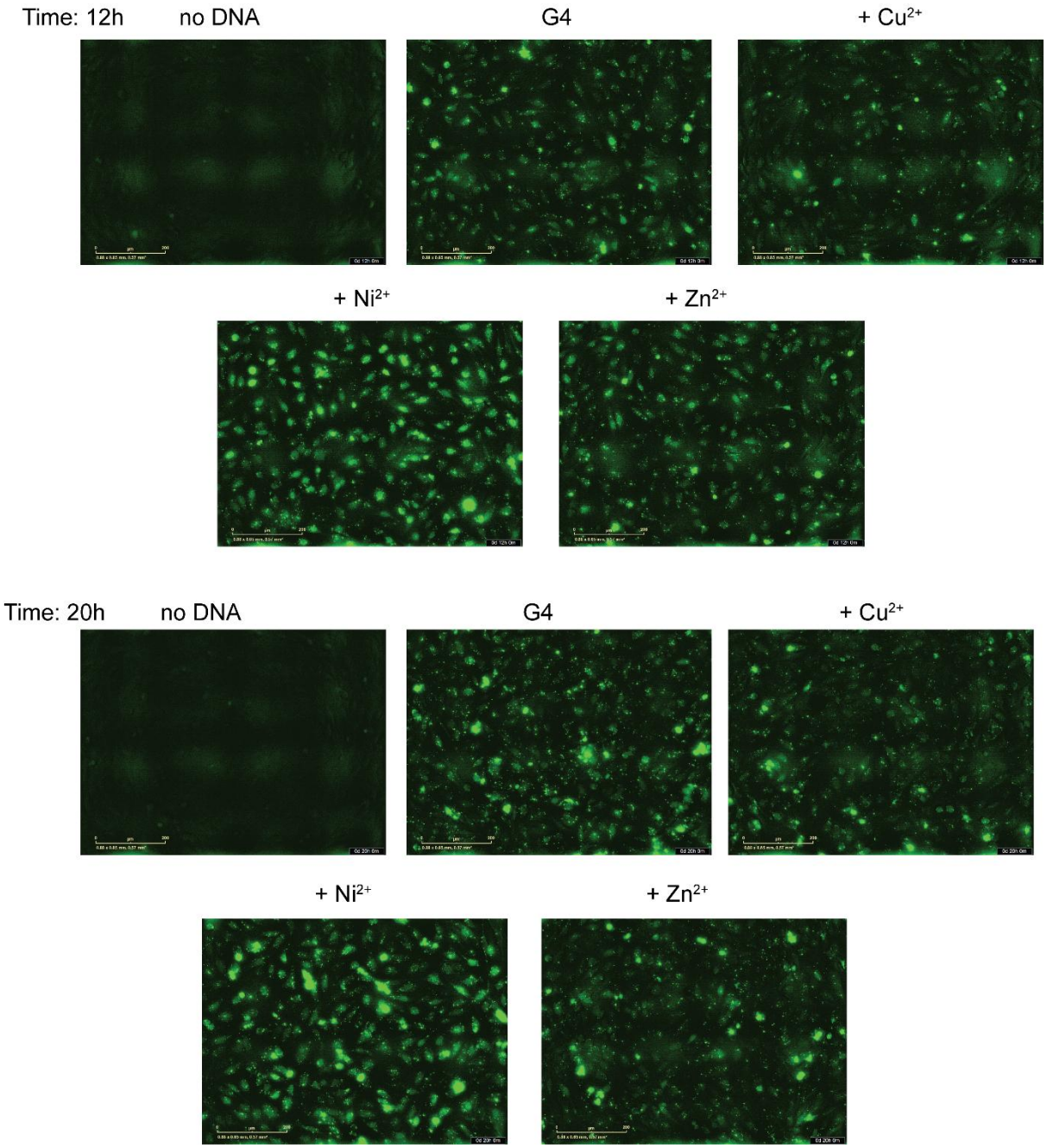

Figure S 113. Fluorescence microscopy of preformed htel22-L2b-FAM G-quadruplexes in HeLa cells after 12h post transfection and 20h post transfection in presence or absence of various M^{2+} (M = Cu, Ni, Zn).

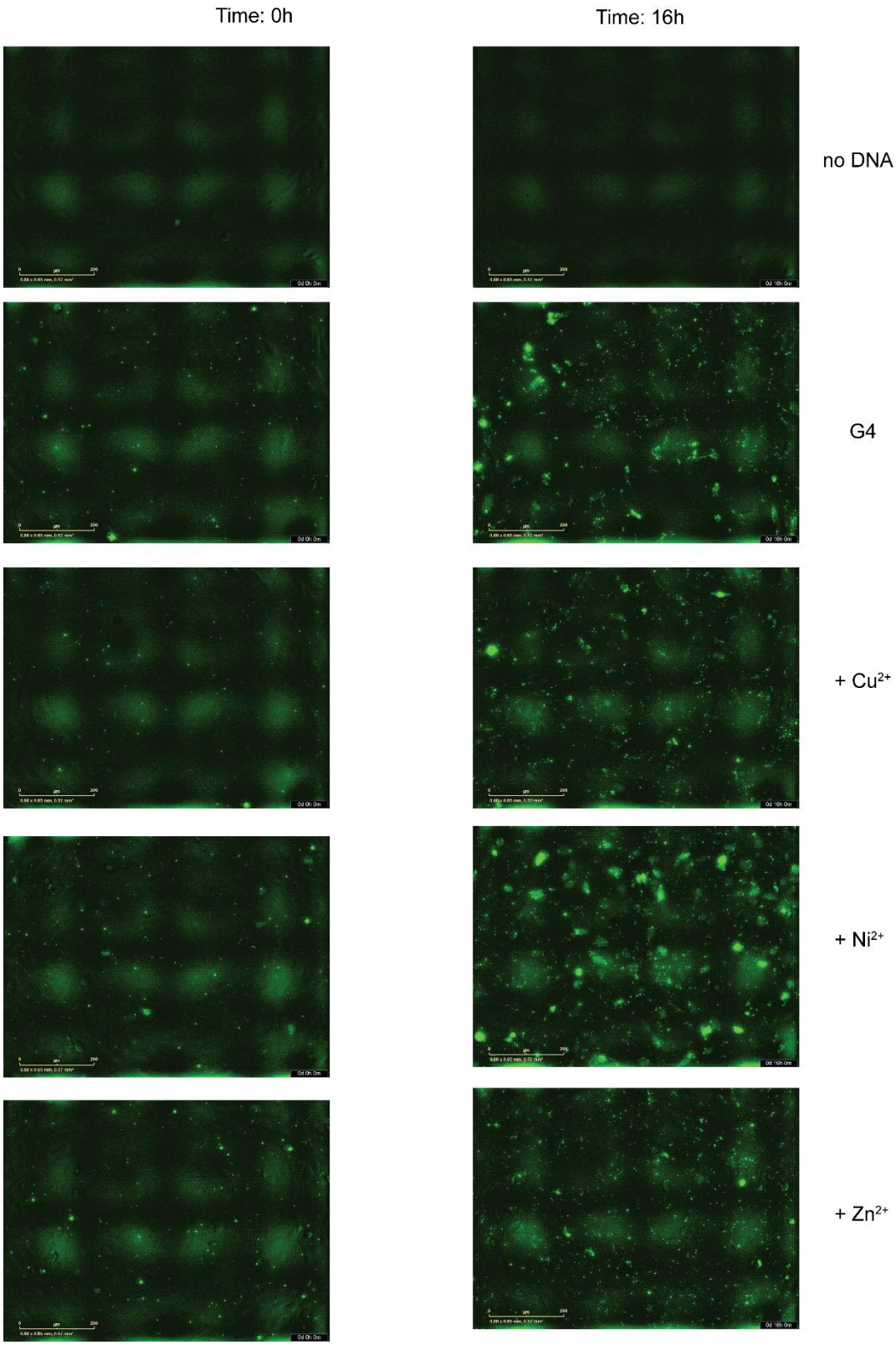

Figure S 114. Fluorescence microscopy of preformed htel22-L2a-FAM G-quadruplexes in U2OS cells after 0h post transfection and 16h post transfection in presence or absence of various M^{2+} (M = Cu, Ni, Zn).

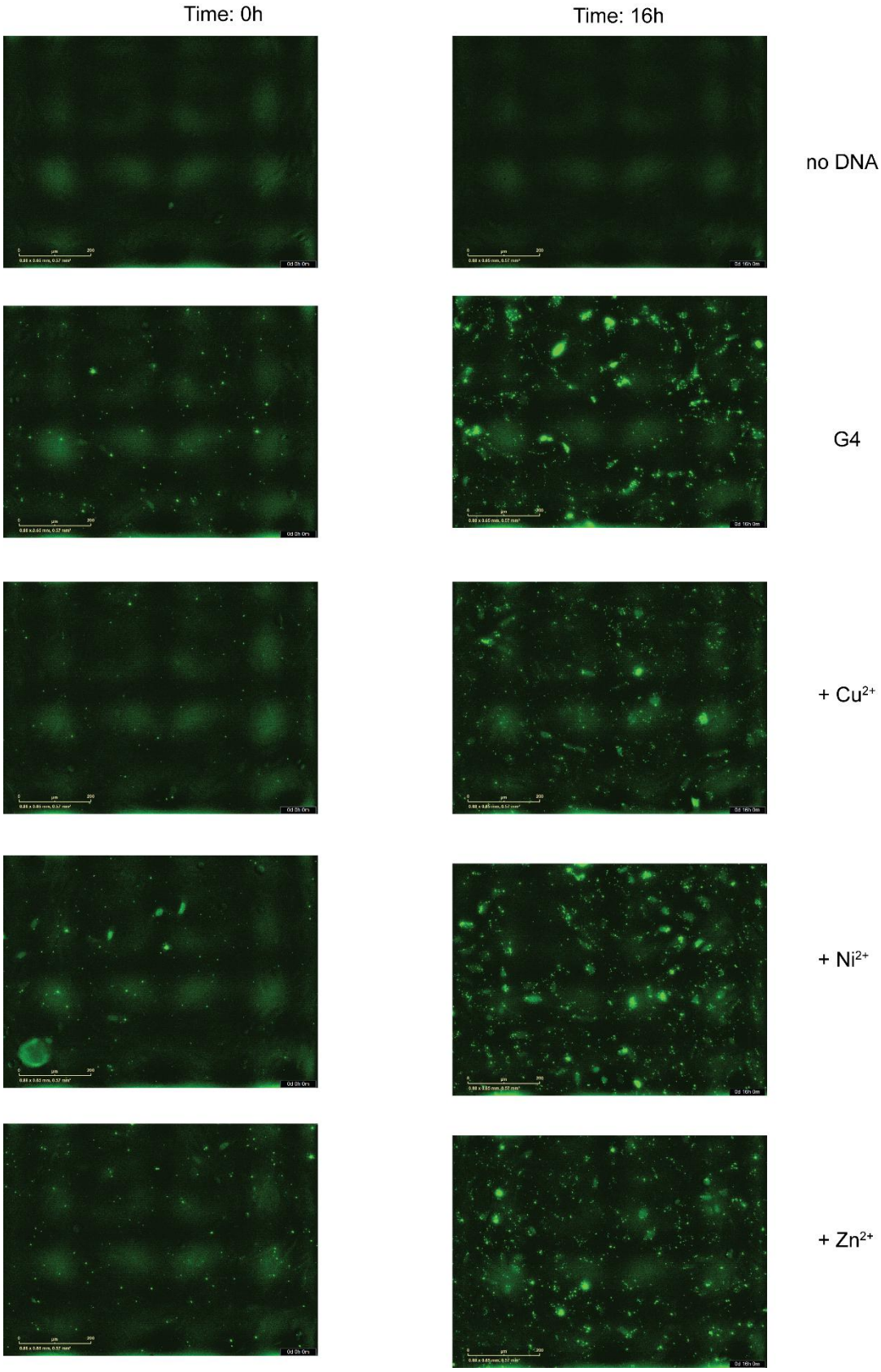

Figure S 115. Fluorescence microscopy of preformed htel22-L2a-FAM G-quadruplexes in U2OS cells after 0h post transfection and 16h post transfection in presence or absence of various M^{2+} (M = Cu, Ni, Zn).

Acknowledgment

I want to thank Prof. Dr. Guido Clever, my supervisor, for giving me the opportunity to conduct my research in his lab and under his supervision. You have a contagious excitement for science, which I really enjoy and which motivates me. Thank you for letting me chose my own project and giving me the freedom to work in my own very personal way. Thank you for all the inputs during this work, which are greatly appreciated and from which I have learned so much.

I would also like to thank Prof. Hannes Mutschler for taking over the role of co-examiner.

A huge thank you to my former mentor during my master thesis now Junior (!) Prof. Dr. Irene Regeni, for teaching me, guiding me through difficult times, inspiring me and motivating me to never give up when chemistry doesn't go the way I want it. You always had an open door and always made time to discuss what is happening and what I could do next if I was stuck. I am so happy for you, Lukas and Nora and I cannot wait to see her grow up with two wonderful parents.

A big thank you to the whole Clever Lab! Thank you for creating this awesome atmosphere with some many different people, nationalities and experiences. I feel just at home with all the people past and present and hopefully in the future too! I feel, that I can grow and learn here not only in a scientific way, but also in a personal and culture one. Thank you Robin (for the metal music in the lab), Jacopo, Philip, Lukas, Julian, Alexandre, Laura (Schneider and Neukirch), Lars, Sonja, Heari, Eri, Shota (or commonly known as Schorsch Hasengarten), Pedro (or Peter Berg), Qianqian, Subhadeep, Sudhakar, Ananya, Christoph, Maike, Birgit, Simon, Hannah, Kristina, André, Ertugrul, Ana, Wojtek, Shing and Gabi. I hope I didn't forget anybody, if so I am sorry, there were too many to list.

I made two very special friends during my time here, Elie and David (Ocki). My dear friends, without you I do not know how and if I would have survived these years. You were there for me through the ups and downs of a PhD thesis. We worked hard and we partied hard(er) and I am immensely grateful for all the experience I could share together with you. I feel I have made friends for life, a bond that connects us in a very special way. As you were there for me, so will I be there for you in times of need. Big love <3

Furthermore I was lucky to meet a special person, someone that unexpectedly entered my life when I wasn't searching for her. Christine, the past months have been more than wonderful with you and I am deeply in love with you and I see a bright future ahead of us. Never have I felt so heard and taken care of as I do in your arms. I can truly call you my partner, my equal, my love. Thank you for everything so far and all the support and thank you for everything that is coming! I cannot wait to live life with you.

Big thank you goes to all my family. Thank you for believing in me and supporting me from the first day. Without it, none of this would have been possible. Thank you (B)Onkel for

hanging out with me and being like a big brother. Thank you Sara for being the little sister I never had and good luck on your journey through the world. You will also have my support. Thank you Dzena and Robert for always being there for me, picking me up and driving me anywhere if I was again too late. Thank you also for feeding me throughout. Thank you for helping me move, even if you said it was the last time! :) Thank you also to Majka and Dido for washing my dirty laundry and feeding and loving me unconditionally at my start in Germany. Hvala Majka i Dido. Volim vas. I will always be there for you guys, doesn't matter where I will be in the world.

The love and support my parents have given me over the time has been one I wish upon everyone. You have made me into what I am now and what I will be in the future. Words can't describe how thankful I am for what you have done and continue to do, to provide me with a better future. I know the sacrifices you have gone through for me to reach this point. We haven't had it easy in life but we always had us and that's what mattered. What once felt like a burden, being foreign and different, is now my greatest asset. What you have achieved despite all the setbacks, fuels the fire in me to push on and achieve what seems impossible. And thank you for keeping me grounded. We have finally achieved the pin

Mama i Papa, volim vas naj vise na svijetu.